



Char formation, transportation and consumption in the blast furnace and its impact on coke rate

(Charfoco)

FINAL REPORT

Char formation, transportation and consumption in the blast furnace and its impact on coke rate (Charfoco)

European Commission

Directorate-General for Research and Innovation

Directorate D - Industrial Technologies

Unit D.4 — Coal and Steel

Contact Hervé Martin

E-mail RTD-PUBLICATIONS@ec.europa.eu

European Commission

B-1049 Brussels

Manuscript completed in 2019.

This document has been prepared for the European Commission however it reflects the views only of the authors, and the Commission cannot be held responsible for any use which may be made of the information contained therein.

More information on the European Union is available on the internet (<http://europa.eu>).

Luxembourg: Publications Office of the European Union, 2019

PDF

ISBN 978-92-79-98324-5

ISSN 1831-9424

doi: 10.2777/046097

KI-NA-29-548-EN-N

© European Union, 2019.

Reuse is authorised provided the source is acknowledged. The reuse policy of European Commission documents is regulated by Decision 2011/833/EU (OJ L 330, 14.12.2011, p. 39).

For any use or reproduction of photos or other material that is not under the EU copyright, permission must be sought directly from the copyright holders.

All pictures, figures and graphs © TATA STEEL NEDERLAND TECHNOLOGY B.V., RFSR-CT-2014-00001 Charfoco

European Commission

Research Fund for Coal and Steel

Char formation, transportation and consumption in the blast furnace and its impact on coke rate

(Charfoco)

S. Born, V. Pridhivi, J. van der Stel

TATA STEEL NEDERLAND TECHNOLOGY B.V., "TATA STEEL"
PO Box 10000, Building 3G.37, 1970 CA, IJmuiden, The Netherlands

A. Babich, H.T. Ho

RHEINISCH-WESTFÄLISCHE TECHNISCHE HOCHSCHULE AACHEN, "RWTH"
Intzestraße 1 – D-52056 Aachen

P. Gupta, D. Sert

ARCELORMITTAL MAIZIERES RESEARCH S.A. "AMMR"
Voie Romaine – BP 30320 – F-57283 Maizières-lès-Metz Cedex

J.-C. Pierret, O. Ansseau, C. Plancq

CENTRE DE RECHERCHES METALLURGIQUES ASBL, "CRM"
Boulevard de l'Imperatrice 6 - BE-1000 Bruxelles

Grant Agreement RFSR-CT-2014-00001
01.07.2014 –31.12.2017

Final report

Directorate-General for Research and Innovation

2019

EUR 29548 EN

Table of contents

1. ABSTRACT	5
2. FINAL SUMMARY	11
3. SCIENTIFIC AND TECHNICAL DESCRIPTION OF THE RESULTS.....	16
3.1 PROJECT OBJECTIVES	16
3.2 WORK PACKAGE 1: LABORATORY INVESTIGATIONS	16
3.2.1 <i>Task 1.1 Selection of coals and basic conditions for trials</i>	16
3.2.2 <i>Task 1.2 Investigation of coal devolatilisation and conversion</i>	26
3.2.3 <i>Task 1.3 Development of method to produce bigger amounts of char and char production</i>	39
3.2.4 <i>Task 1.4 Characterisation and laboratory investigations of char</i>	40
3.2.5 <i>Task 1.5 Char interaction with coke</i>	51
3.2.6 <i>Task 1.6 Study on char impact on the coke surface using the pilot plant COBESI</i>	52
3.2.7 <i>Task 1.7 Char interaction with ferrous burden and drainage in the dripping zone</i>	56
3.3 WORK PACKAGE 2: DEVELOPMENT OF ADVANCED MEASUREMENT TECHNIQUES FOR RACEWAY MONITORING	89
3.3.1 <i>Task 2.1 Development of tuyere instrumentation</i>	89
3.3.2 <i>Task 2.2 CFD calculations for evaluating the conditions at the instrumented tuyere</i>	97
3.3.3 <i>Task 2.3 Tests with instrumentation at COBESI for the tuyere instrumentation</i>	97
3.3.4 <i>Task 2.4 Commissioning of tuyere</i>	103
3.4 WORK PACKAGE 3: BLAST FURNACE TESTS.....	105
3.4.1 <i>Task 3.1 Blast furnace tests with instrumented tuyere</i>	105
3.4.2 <i>Task 3.2 Blast furnace trials</i>	126
3.4.3 <i>Task 3.3 Data analysis</i>	147
3.5 WORK PACKAGE 4: BLAST FURNACE MODELING	159
3.5.1 <i>Task 4.1 Implementation of char behaviour in the shaft in MOGADOR</i>	159
3.5.2 <i>Task 4.2 Evaluation of the amount of char leaving the raceway</i>	172
3.5.3 <i>Task 4.3 Process modelling with MOGADOR including char phenomena</i>	174
3.5.4 <i>Task 4.4 Simulation of char formation and conversion on the micro level</i>	176
3.6 WORK PACKAGE 5: COORDINATION, DOCUMENTATION, REPORTING.....	179
4. LIST OF FIGURES.....	181
5. LIST OF TABLES	188
6. LIST OF ACRONYMS AND ABBREVIATIONS.....	190
7. REFERENCES	192

1. ABSTRACT

In the past, blast furnace coal injection research mainly focused on combustion of injection coal in the raceway. However, it could be assumed that coal is anyway not able to fully combust, particularly at high injection rates, and unburnt residues leave the raceway as char.

The char evolution and subsequent consumption depends on the raceway characteristics, which depend on coal conversion. Both groups of factors were investigated with conversion tests, as well as raceway measurements. Generally, the char evolution is seen to manifest itself as a negative impact, but this may depend on the blast furnace conditions and injection coal characteristics. Char effects might deteriorate the blast furnace operation and stability (i.e. lower burden permeability or higher carbon losses in the flue dust). Nonetheless, char could also be advantageous by contributing toward the increase in coke reactivity thereby lowering the thermal reserve zone temperature. It was shown that the coal combustion highly depends on coal grain size and only marginally on oxygen enrichment. Effects of oxygen enrichment on maximum coal injection rate might be more related to char consumption, rather than coal conversion. Despite low conversion of granular coal under blast furnace raceway simulation conditions, granular coal injection is possible at high rates, obviously due to its consumption outside the raceway. Blast furnace operation experience with coals, like operational benefits or transport behaviour could be confirmed. Char impact on ferrous burden behaviour highly depends on temperature and gas composition and is difficult to predict from the performed tests.

Several raceway measurement techniques were successfully developed and applied at pilot scale and at a real blast furnace. Raceway size, temperature and changes in the gas composition could be shown. The raceway size depends on the location of the tuyère in relation to blast inlet and tap hole and changes significantly over time, indicating raceway collapses.

Gas and temperature measurements of the BF interior were performed: New insights regarding the impact of high coal injection rates on the blast furnace inner state were gained by gas and temperature measurements of the blast furnace inside and confirmed with mathematical modelling.

Work Undertaken:	<p>WP1</p> <ul style="list-style-type: none"> • Selection of coals for preliminary trials in granular (50 % <250 µm; 100 % <1mm) and pulverised (>90 µm, <200 µm) form • Conduction of preliminary trials using MIRI plant and microstructural analyses • Final selection of three coal types (2 PC, 1GC) for further investigation • Coal grinding at required size distribution for the next trials • MIRI-setup modified • Investigation of conversion behaviour of selected coal types at different oxygen rates at CANMET and RWTH • Development of a method for production of bigger amounts of char • Modification of Tammann furnace for the production of bigger amounts of char (Tammann-furnace DT setup) • Production of bigger amounts of char under two different reaction temperatures • Characterisation of char regarding its physical, chemical, microstructural and kinetic properties • Determination of activation energy of coke with addition of char using a modified Tammann-furnace setup (Tammann-furnace AE setup) • Revamping and maintenance of pilot plant COBESI (implementation of new exhausting system, new lining established) • Injection of selected coal types in the pilot plant COBESI, measurement of gas composition and temperature development • Determination of reduction degree of pellets with addition of char • Development of Tammann-furnace setup for simulation of dripping behaviour of hot metal and conduction of dripping tests • Method established for binding char to burden. • Study of influence of char on stack zone and cohesive zone <p>WP2</p> <ul style="list-style-type: none"> • Modification of COBESI access points for testing new developed instrumentations • Test of new developed instrumentation at COBESI pilot plant • Visits to blast furnaces in IJmuiden and Port Talbot to evaluate accessibility to equipment of tuyere instrumentation • Draft technical drawings of tuyere and access • Development and tests of measurement techniques • CAD evaluation with instruments • Prototype tests with distance measurements and calibration • Decision upon measurement techniques for pilot tests • Building of mechanical adaptations for the COBESI Trials • Laboratory tests to verify the measurement systems • Development of programs for data acquisition <p>WP3</p> <ul style="list-style-type: none"> • Design of FVP probe tip for dust sampling • Building mechanical and electrical adaptations for Blast Furnace trials • Development of programs for data processing • Test of dust sampling over the shaft by means of a Flexible Vertical Probe • Characterisation of coke degradation inside the BF shaft by means of coke core boring experiments • Characterisation of thermo-chemical conditions of AM Bremen BF2 at high injection rate by means of Multi-Point Vertical Probing trials • Measurement of temperature development in the raceway using a thermal vision camera (TVC) <p>WP4</p> <ul style="list-style-type: none"> • Modification of MOGADOR model • Preliminary investigation of the amount of char leaving the raceway (exemplary case) • Evaluation of the amount of char leaving the raceway by means of CFD calculations • Simulation of drainage behaviour on micro level with gas/char phase
------------------	---

	<p>WP5</p> <ul style="list-style-type: none">• Kick-off meeting in Port Talbot on 24./25.09.2014• Workshop on coal injection and coal and char research in Port Talbot on 24./25.09.2014 <p>Several WP and coordination meetings</p>
--	---

Main Results:	WP1	<ul style="list-style-type: none"> Preliminary trials show different coal conversion behaviour depending on their properties Microstructural analysis of char produced during preliminary results show different char particle structure Three coal types were selected (2 PC, 1 GC) , ground and distributed over the partners of the project for performing the lab tests About 1 kg of char was produced in the Tammann-furnace DT setup at two different scenarios Char structure types were categorised and allocated to the LOM images Reaction temperature has a significant influence on char properties Devolatilisation degree increases significantly with increased reaction temperature Microstructural properties changed accordingly (increase of more porous particles) Physical properties show significant change compared to parent coal however increase in reaction temperature shows only small changes (specific surface area, average particle size) Kinetic properties show a decreased activation energy of char compared to coal TG results show that char has a higher reactivity under different atmospheric conditions (CO_2, $\text{CO}_2/\text{CO}/\text{N}_2$ mixture and air) compared to coal Trials using the pilot plant COBESI show an significant change of gas composition when injecting coal as well as difference between injecting pulverised and granular coal Addition of char to pellet surface leads to higher reduction degree Regarding dripping zone trials, a low drainage rate was observed under examined conditions Sinter hood not usable for devolatilisation test Conversion of Coal C GC-form is not significantly influenced by O/C ratio Same conclusion is made for the gasification of the corresponding char in TGA Coal B led to blockages of the test rig due to low melting properties of its ash
	WP2	<ul style="list-style-type: none"> Idea generation for access to tuyere tip Decision about instrumentation and techniques Draft technical drawing tuyere Evaluation of possible accesses for instrumentation Distance measurement calibration Commissioning plan Different measurement techniques succeed and have been approved Data analysis for the COBESI trial has been realized
	WP3	<ul style="list-style-type: none"> Significant increase of raceway coke surface temperature was detected after shutting coal injection Temperature profiles taken by the TVC, mostly reflects BF parameters such as the flame temperature by changing PC rate Blast Furnace tests at blast furnaces in Port Talbot and Bremen Data analysis for BF tests was done Test of dust sampling by means of FVP not successful due to blockage of dust in the gas sampling pipe due to water condensation Dust recovered afterward from the pipe for SEM analysis, the result of which rendered it impossible to distinguish between char and coke A new probe was designed but could not be tested due to BF relining Measured coke degradation inside the blast furnace was ~ 30 mm Measured thermochemical conditions in the shaft of AM Bremen BF2 was assessed twice by means of MPVP trial. They were reproducible and very specific. They indicated a very central operation, reduction in a gradient at the wall and a low position of the root of the cohesive zone From coke core boring, it seems also likely that totally unreduced pellets arrive below the cohesive zone
	WP4	<ul style="list-style-type: none"> Around 50 % of the coal entering the raceway leaves it as char Results of the droplets model showed that the voidage is crucial for the dripping rate

Future work to be undertaken:	<p>WP1 NONE – Project completed</p> <p>WP2 NONE – Project completed</p> <p>WP3 NONE – Project completed</p> <p>WP4 NONE – Project completed</p> <p>WP5 NONE – Project completed</p>
On schedule (Yes /No):	Yes
Main problems encountered:	Long products UK and Teesside laboratory stepped out of the project. Port Talbot took over as lead hub.
Correction actions:	Commissioning, foreseen at the single tuyere rig was performed by RWTH.
Publications, patents:	

2. FINAL SUMMARY

Work package 1 (Laboratory investigations) comprises tests regarding coal conversion, char production, char characterization and its interaction with and impact on coke and iron ore reduction.

Four different coals were selected for preliminary investigations using conversion tests and microstructural analyses. Conversion tests were conducted for each coal in two different particle size distributions, called PC (90 - 125 µm) and GC (50 % <250 µm, 100 % <1000 µm). Results showed that the conversion degree of PC coals under conditions simulating the first part of the raceway was significantly higher compared to GC coals. Furthermore, conversion degrees differed depending on coal type. Especially chemical properties significantly influenced coal conversion. Thus a relatively low volatile matter content was not favorable for coal conversion. Micro-structure, ash content and specific surface area of the parent coal seemed to have a less crucial effect on conversion behavior although they only slightly differed. Char microstructure was analyzed and categorized into different groups. Char which experienced a low conversion was characterized by numerous dense particles which did not seem to have undergone reaction.

Three coal types were selected for further, in-depth investigation (2 PC, 1 GC). Selected coals were injected in order of AMMR in the CANMET injection Rig and in the MIRI plant at RWTH to investigate impact of oxygen enrichment on coal conversion. In the MIRI plant, char was collected and analyzed. Increase in oxygen content showed no significant effect on the conversion degree. Particularly, the effect of O/C ratio on the burnout rate of coal C in GC form was low. Thermogravimetric analyses (TGA) allowed the same conclusion for the gasification of the corresponding char. It should be mentioned that tests using the CANMET injection rig also showed that the effect of O/C atomic ratio on the burnout rate was quite limited. However the amount of CO₂ increased by increasing oxygen rate. Microstructural analysis revealed no significant difference in char structure types.

During the injection of coal B, blockages of the reaction tube/injection lance occurred. Based on further analyses, this phenomenon could be caused by low ash fusion temperature as well as high swelling index.

Pilot plant trials with the Coke Bed Simulator ("COBESI") at RWTH showed a lower evolution of CO₂ and CO during injection of granular coal (GC) than pulverised coal. Furthermore, oxygen depletes at a lower rate compared to PC. The injected particles were undetectable with the thermo-vision camera. However, the decrease in coke radiation during coal injection was determined.

Generally, complete conversion of coals (in both PC and GC form) could not be reached under conditions of very high injection rates. Char leaves the raceway for simulated raceway conditions. Consequently, consumption of char outside the raceway is crucial for stable and effective blast furnace operation.

A method for the production of larger amounts of char was developed. Preliminary trials using a muffle furnace and Tammann furnace were conducted. Consequently, the Tammann furnace DT (drop tube) setup was developed and used for the production of large amounts of char under two different temperatures producing six different char types. About 1 kg of each char type was produced and used for subsequent studies.

Char properties were determined and compared to its parent coal. Determined higher reaction temperature increases the conversion by devolatilisation. Regarding physical properties, a significant change in specific surface area, particle size distribution and microstructure from parent coal to char was observed. However, with increasing reaction temperature only minor changes were detected. A similar phenomena could also be detected at the CANMET rig. Change of O/C atomic ratio only had a marginal effect on the specific surface area. Char from GC coal showed an extremely high specific surface area caused by its wide particle size distribution. Kinetic investigation of char was conducted using a thermographic analyzer and Tammann furnace AE (Activation Energy) setup at RWTH. Results showed that the activation energy had a high correlation with volatile matter and specific surface area. A high increase in specific surface area can compensate for a significant loss of volatile matter regarding its activation energy. Due to its high specific surface area, the activation energy of GC char was low. Thermographic results showed that char had a high reactivity under CO₂ atmosphere, compared to the coal.

Furthermore, the influence of char on coke, pellets and sinter reaction and softening behavior was investigated. The activation energy of coke significantly decreased in the presence of char.

Based on the characterization of different char types, following conclusion could be drawn: Reactivity of coal seemed highly dependent on volatile matter whereas the reactivity of char relied more on its specific surface area.

The interaction of char with the burden in the stack zone and cohesive zone was studied in

metallurgical laboratory tests performed at Tata Steel and CRM. HOSIM tests were performed to simulate the stack zone of blast furnace in an interactive reducing gas mixture atmosphere with temperatures ranging from 430 °C to 910 °C. Free swelling tests at 900 °C and 1050 °C were done to study the pellet swelling behaviour in the presence of char. The cohesive zone of the blast furnace was studied in IJSST tests with isothermal reduction followed by softening and in separate isothermal reduction and softening test at CRM.

Dismissing char gasification, at temperatures lower than 900 °C, it was observed that char influenced the reduction behaviour by physically limiting gas flow into the sinter pores, thereby increasing the reduction time. This effect was higher at elevated test temperatures, at 900 °C, indicating that the temperature-dependant diffusion limitations were dominant. However, during the reduction and softening test performed at CRM with temperatures greater than 1000°C, it was noticed that reduction was enhanced in the presence of char for both sinter and pellets. The char preferentially stayed in the sinter macro-pores, as shown in the microstructure analysis, leading to higher reduction degrees for sinter compared to pellets. With respect to the swelling behaviour evaluated at 900°C and 1050°C, it could be observed that char coated pellets have lower swelling indices than pellets without coating. The possibility of the role of char acting as passivating layer to suppress swelling was speculative with respect to surrounding gas conditions experienced by the pellets. Additionally, higher metallic Fe content observed during swelling at 1050°C than at 900°C could be caused by the char's Boudouard Reaction on the surface of the pellets, regenerating the CO₂ from ore reduction.

From the softening tests of sinter and pellets, it was observed that in the absence of reducing gas, the presence of char aided in the reduction during the softening in inert atmosphere and under load. This was confirmed by the increased weight loss and subsequently, higher final reduction degree in the various tests performed at Tata Steel and CRM, respectively. The shorter reduction time for char coated pellets in IJSST could be attributed to Boudouard reaction. The softening behaviour of pellets coated with char was distinct from that of pellets without signified by the presence of char between the pellet boundaries to maintain higher gas permeability, thereby preventing intergrowth of pellets. Although higher bed shrinkage was noticed in the case of pellets coated with char, the ability of char to maintain thin channels along the pellet boundaries mitigated the loss of the majority of initial inter-pellet void up to higher temperature. Opposed to this phenomenon, was the coalescence of pellets at an earlier stage of deformation that lowered total void fraction and largely disabled gas flow.

In a nutshell, the impact of char could be distinguished based on temperature. At lower reduction test temperatures where char gasification did not occur, the effect of char was instrumental in forming a physical barrier to gas flow causing diffusion limitations, as noted in HOSIM. At higher temperatures, probable Boudouard reaction between char and CO₂ from ore reduction enhanced reduction degree as noted in Free Swelling, IJSST and reduction and softening tests at Tata Steel and CRM respectively.

The objective of **Work Package 2 (Development of advanced measuring techniques for raceway monitoring)** is to define and optimise the arrangement of the measurement methods for the instrumented tuyère/raceway.

Measuring techniques were developed to investigate the movement of the char, raceway depth, gas composition and temperature of the raceway.

The positioning of these instruments was investigated with mathematical modelling. Commissioning of the techniques on laboratory and pilot scale was considered essential and this was performed using the COBESI plant at RWTH and a cold-rig set-up consisting of a tuyère and the corresponding pipe-work at Tata Steel.

The coal movement was analysed with a high speed camera in the pilot plant. In the blast furnace, this camera should be used in combination with an endoscope. Four possible positions of the endoscope were identified and evaluated to their feasibility. It was concluded that the only possible option was the additional access on the opposite side of the coal injection pipe. On this basis, an endoscope and according cooling equipment was purchased. It was planned to build the necessary pipe work in the project to insert the probe on the opposite side of the coal injection pipe. However, due to time constraints for engineering a safe and operable system, the endoscope could not be used in the frame of the project.

The CFD calculation that AMMR was supposed to perform in **Work Package 2** as support of the design of the tuyère instrumentation was taken over by Tata Steel for confidentiality reasons.

The feasibility of the different measurement principles for the spectrometer (temperature, gas composition), laser (raceway size), radar (raceway size) and thermal-vision camera (temperature map) were demonstrated on pilot scale. Mathematical modelling was used to evaluate the impact of measurement techniques on operational conditions. **Work Package 3 (Blast Furnace trials)** comprises of blast furnace trials using the different measurement techniques developed and

commissioned in WP 2 at Tata Steel BF 4 in Port Talbot (task 3.1), as well as blast furnace trials with shaft dust and raceway coke sampling at AM Bremen BF 2 (task 3.2, task 3.3).

Two tests with raceway instrumentation were performed, leading to the following conclusions: The average gas temperature inside the raceway increases with decreasing granular coal injection rate. The alkali measurements showed a dependence on coal injection rate where a decrease led to an increase in the lithium concentration. However, sodium and potassium concentrations decreased with increase in coal injection rate. This may be explained by the different positions of the alkali cycles in the blast furnace, depending on boiling temperatures: Na and K cycles in the blast furnace might not reach that far down into the furnace, as that of lithium.

The raceway size was measured with a novel radar technique developed by Tata Steel, as well as with a laser – distance measurement, developed by CRM.

The radar was used during two measurement campaigns at Port Talbot Blast Furnace 4. After the first commissioning trial showing little effect of operational conditions on the raceway size, a second campaign was performed to measure the raceway size of all tuyeres, in order to evaluate the impact of the position and tuyère diameter. A method for quantification of the signal was developed and used to generate a raceway size profile.

Two distinct raceway size levels could be detected. The lower-level raceway fluctuated between 0.5 and 0.8 m, the higher one between 1.5 and 2.0 m. The raceway sizes and its changes depend on the position at the furnace with regards to blast inlet and tap hole position. At this BF, different tuyère diameters are in use: 125 mm and 115 mm: A bigger tuyere diameter led to a longer higher-level raceway (1.6 vs. 1.35 m). The impact on the lower-level raceway was however marginal (both approximately 0.6 m). For investigation of the reason of those two raceway size levels, a long-term measurement would be required.

Based on these results, continuous implementation of the radar sensors is planned in Port Talbot.

The raceway laser depth measurement showed promising results. The test also showed two distinct raceway size levels of 0.6 – 0.8 and 1.6 – 2.1 m, confirming the radar results.

Measurements of temperature distribution in the raceway were also performed under various blast furnace conditions, e. g. changing coal injection rates, blast temperature and oxygen enrichment. Different regions of interest were measured: small influence of other tuyère on the measured tuyere was detected, as well as parameters such as hot blast rate. When decreasing coal injection rate at one tuyere from 200 to 100 kg/t_{HM}, an increase of over 100 °C was detected. When stopping coal injection, temperature rose by 400 °C.

Mathematical modelling was performed at Tata Steel to correlate the raceway size to the kinetic energy of the hot blast. The size was calculated based on an empirical formula from literature. The low-level raceway size could be confirmed by the model data. The measured high-level size could however not be explained. The temperature of model and thermo-vision camera was compared and it showed similar temperature maps. However, the model calculated gas temperatures, whereas the temperature measured by the thermo-vision camera was the temperature of all compounds radiating in the recorded wavelength.

In **Work Package 3**, AMMR performed two trial campaigns at AM Bremen BF2. This furnace is regularly injecting ~240 kg/t_{HM} of a mixture of hard coal and lignite (75/25 share).

Three types of trials were performed:

- dust sampling over the shaft by means of a modified Flexible Vertical Probe. This test did show that fine dust was actually carried out with the gas, but was unfortunately condensed in the water in the gas sampling pipe. A new design of the probe was then proposed but could not be tested due to the stop for the intermediate relining of the furnace during the last quarter of 2017;
- two coke core boring and coke scrapping experiments at tuyeres were performed. They gave indications about the raceway depth (~1.0 m) and the coke size decrease between the charged coke and the raceway (~30 mm). They also indicated that unreduced material could reach the tuyere level, which was an interesting indication for the global interpretation of the blast furnace operation;
- in relation to the coke core boring experiments, two Multi-Point Vertical Probing trials were performed under comparable operating conditions. The reproducibility of the results was very good, which gave confidence in the conclusions drawn from these tests.

Additionally, data analysis including heat and mass balance calculations was conducted. A global picture could be derived from all results, showing a possibility for blast furnace operation at high

PCI rate. In the present case, it involved low gas flow at the wall and a strong central flow, leading to a marked inverted-V shape cohesive zone with a low position of its root, and reduction of the burden in a temperature gradient at the wall side leading to negative values of the defect to optimum of the reduction.

In **Work Package 4** (Blast furnace modelling), CRM tested the following effects within MOGADOR:

Kinetic data of Boudouard reaction in the BF shaft was modified in the MOGADOR model using the results obtained within WP1, taking into account the higher reactivity of coal char, compared to coke and impact of char on softening and melting characteristics of burden materials. Two complementary approaches were simulated:

- "Stick on burden": Considered coke and char together and modified coke reactivity, by changing the constant of equilibrium of the Boudouard reaction from coke to coke and char. Simulations showed that, with coke and char equilibrium, the cohesive zone was positioned slightly higher in the blast furnace. Indeed, char being more reactive than coke could start the gasification earlier.
- "Transported by gas" considered char particles independently and created a competition, by replacing the theoretical calculation of Boudouard kinetics by experimental data from WP1 (coke only) and adding the kinetics of char (CPC900) to simulate the consumption of char by Boudouard reaction. In the modified case, the Boudouard reaction took place in a larger area compared to the reference, impacting the shape of the cohesive zone.

Two different charging patterns of Bremen were simulated in MOGADOR. The results were in good agreement to the MPVP.

AMMR performed CFD calculations to evaluate the amount of char leaving the raceway. Calculations done based on a hard coal operation at 240 kg/t_{HM} of PCI did show that ~50 % of the coal entering the raceway was leaving as char. This information was taken into account for MOGADOR simulations.

3. SCIENTIFIC AND TECHNICAL DESCRIPTION OF THE RESULTS

The tasks in the RFCS project CharFoCo are distributed into five work packages as shown in **Figure 3.1**.

The work performed in the work packages is being presented for each of the tasks, in which the work packages are divided into

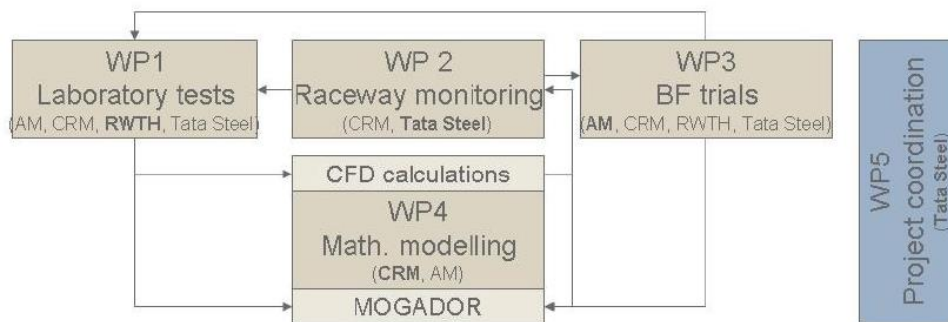


Figure 3.1: Interaction between work packages

3.1 Project objectives

The main objective of this project is to investigate the appropriateness of coals or coal blends for blast furnace injection. To do so, the correlations between coal characteristics, raceway conditions and overall blast furnace parameters, also including impact on melting, smelting and permeability of the burden will be investigated. The focus will be on the unconverted coal char in the raceway and its effects on the blast furnace operation, depending on process conditions and coal properties.

3.2 Work Package 1: Laboratory investigations

3.2.1 TASK 1.1 SELECTION OF COALS AND BASIC CONDITIONS FOR TRIALS

3.2.1.1 COAL SELECTION

Before selecting the final coals to be used for the different trials to be performed in the course of CharFoCo, a preselection stage was organised, with preliminary trials performed at the MIRI at RWTH Aachen. Tata Steel and ArcelorMittal proposed different candidate coals for these trials.

Based on plant experience, coal selection was done in such a way to accommodate both good (A & C) and bad (B) coals. Typical size, hardness, proximate, ultimate and ash analysis of the coals proposed by ArcelorMittal are given in **Table 3.2**.

In addition, another coal referred to as Coal D, was proposed by Tata Steel. All 4 coals were then treated in the MIRI furnace of IEHK RWTH Aachen.

Preliminary trials were conducted at the Dept. of Ferrous Metallurgy (IEHK) at RWTH Aachen University and consisted of conversion trials using the Multifunctional Injection Rig for Ironmaking (MIRI) as well as morphologic analyses of coals and char produced from these coals. All four coals were aimed to be investigated at two grain size fractions, called PC (pulverised coal) and GC (granular coal): PC 90 - 125 µm; GC 50 % <250 µm, 100 % <1000 µm.

The results of MIRI trials and microscopic investigations should deliver needed information for final selection of coals for the investigations in the following tasks. **Table 3.1** summarizes the coals and size fractions used for preliminary trials. In total, 8 coal samples were examined.

Table 3.1: Coals and size fractions used for preliminary trials

Coal	A		B		C		D	
Size Fraction	PC	GC	PC	GC	PC	GC	PC	GC

The chemical analyses of the coals were conducted multiple times and are shown in **Table 3.2**. Ultimate and proximate analysis were performed at RWTH Aachen.

Table 3.2: Chemical analysis for coals chosen for preliminary trials (wt.-%) (db)

Coal	A	B	C	D
HGI	48	95	78	62
Ultimate analysis				
%C	79.4	83.9	82.5	78.6
%O	4.9	3.0	3.5	4.8
%N	2.1	1.2	1.5	1.9
%H	3.9	4.1	3.6	3.9
%S	0.3	0.7	0.2	0.3
Proximate analysis				
%VM	19.1	16.3	11.8	20.4
%Ash	8.15	6.21	8.05	8.34
%C _{FIX}	71.3	76.2	79.1	69.6
Ash composition				
%SiO ₂	45.3	31.8	43.8	54.1
%Al ₂ O ₃	23.6	20.7	36.5	24.3
%CaO	7.1	10.5	3.2	3.4
%MgO	3.1	2.0	1.0	1.5

3.2.1.2 COAL PREPARATION

The next stage concerned the preparation of the different coals for the lab trials to be performed during the project.

Actually, it came out that this task had been underestimated in the preparation of the proposal. As a matter of fact, due to the yield of the grinding operation, relatively huge amount of coals had to be handled at this stage (up to 1 t of raw coal).

As AMMR had recently bought a Rotor Beater mill SR300 from the Retsch company for treating relatively large quantities of material, it was asked to make the preparation of the coals for the trials. However, it should be noticed that this task was not planned at the time the budget proposal was prepared, so it induced an extra operating cost of over 40 k€ for AMMR.

More information about the grinder can be obtained at:

<http://www.retsch.com/products/milling/rotor-mills/sr-300/>.

After a rather long commissioning phase, which led to some delay in the start-up of the lab trials afterwards, the grinding of the coals was performed. The two fractions to be obtained were aimed to reach following size distributions:

- granular coal (coal C): < 1 mm coal, with a d₅₀ size of 250 µm
- pulverised coal (coal B & C): 90-125 µm fraction of the coal

The granular coal (GC) preparation could be done in one step, after having determined the final characteristics of the coal depending on the mill screen mesh and the feeding rate of the coal into the mill. The coal size distributions obtained as a function of the rotation speed of the rotor for the minimum and maximum (90 % of flooding flow rate of the mill) feeding rate of the coal are given in **Figure 3.2**. The minimum rotation speed and maximum feeding rate were finally selected for the preparation of the granular coal. The corresponding size distribution is given in the table in the same **Figure 3.2**.

Regarding the preparation of the coals under pulverised form (PC), screening of coal C was easier when compared to coal B .For Coal B, it turned out that the coal obtained after grinding with the 500 µm screen was too sticky for an easy screening at 90 and 125 µm. The second stage of grinding with the 500 µm screen had then to be given up in order to speed up the preparation of this sample. This behaviour then corresponded to a first specific characteristic of this coal.

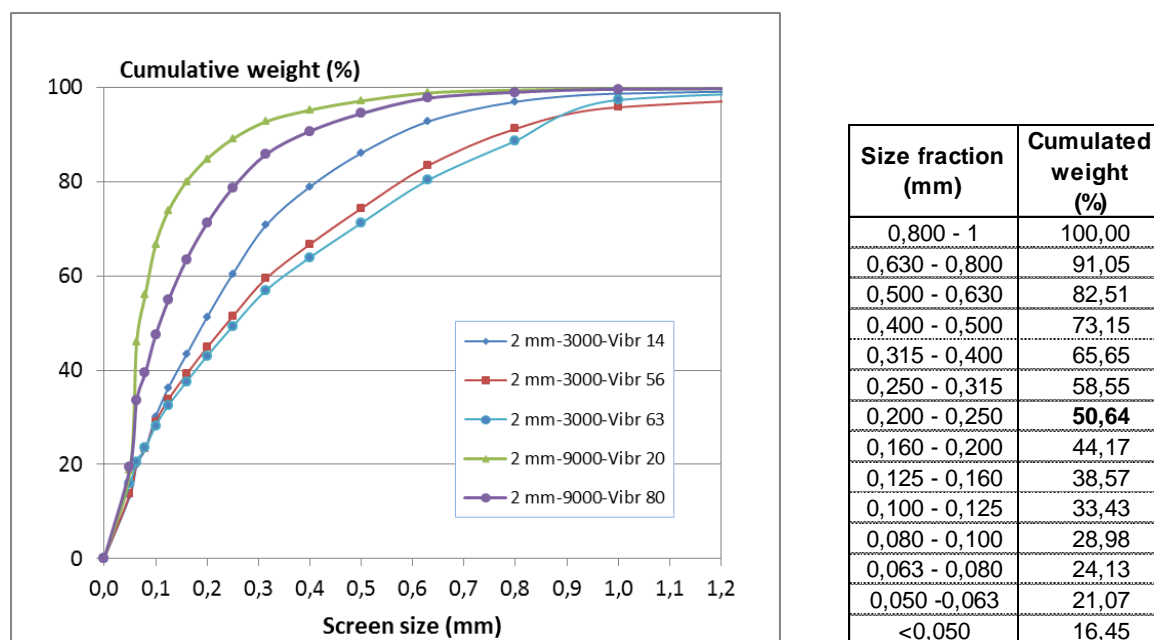


Figure 3.2: Size distribution curves of Coal C-GC form prepared under various grinding conditions and final size distribution of Coal C-GC form sample after screening at 1 mm; cumulative wt. %

Following facilities and analytical methods were used for the characterisation of coal/char.

Microstructural analyses

Light Optical Microscopy (LOM) was used to take images at different magnifications. These images were processed by an imaging analysis software, which detects various particle surfaces. Based on this technique cross section porosity, form factor and micro-size distribution could be analysed.

Scanning Electron Microscopy (SEM) was conducted to examine the texture of the surface area of grinded coal at various magnifications.

Injection facility

Multifunctional Injection Rig for Ironmaking (MIRI) was developed in scope of the ULCOS TGRBF project (RFSR-CT-2009-00002). This plant simulated the conversion behaviour of solid fines in the raceway. In scope of this project pulverised and granular coals were injected through an injection lance in a reaction chamber. Injection rates and composition of gas (oxygen enrichment) could be set and adjusted. The injected gas was preheated through a preheating furnace. The char, which was generated in the reaction chamber, was separated from the off-gas stream in a cyclone. The off-gas which was produced during the reaction was analysis in-situ.

In scope of CharFoCo a second preheating furnace ("preheating furnace 2") was established in

order to ensure a more stable process. A schematic drawing is shown in **Figure 3.3**.

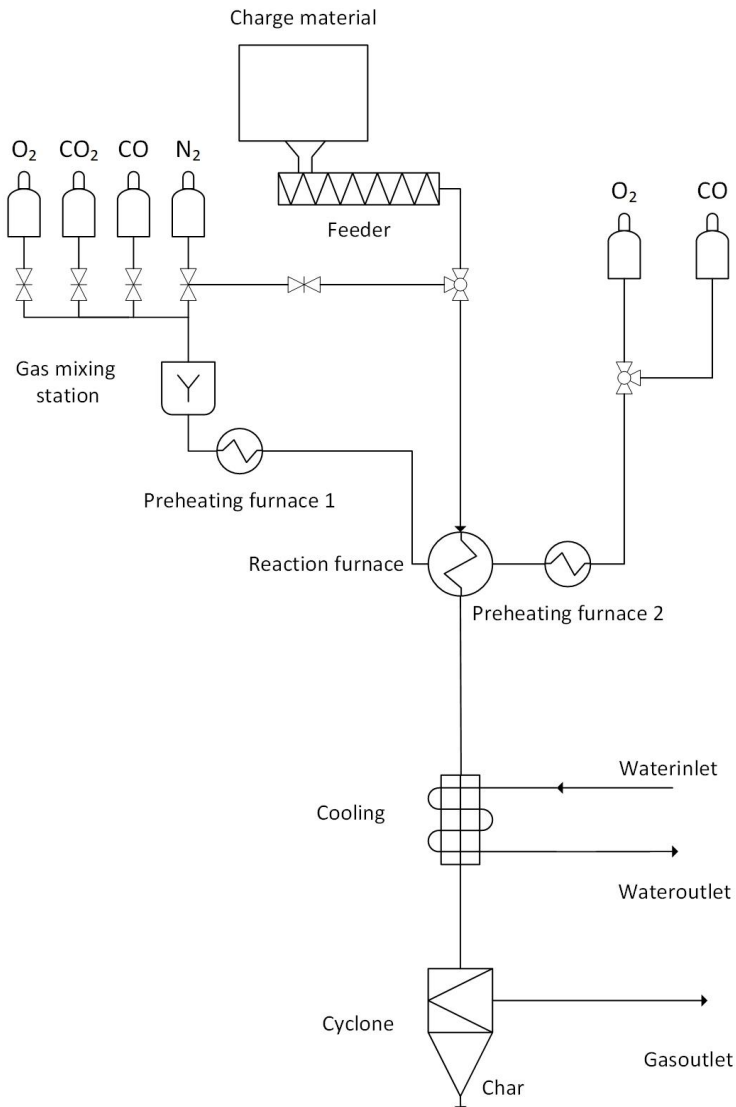


Figure 3.3: Schematic drawing of MIRI experimental setup

The conversion degree was determined based on the off-gas analysis:

$$\eta_{\text{gas}} = 100 * \frac{CO_2 + CO + CH_4}{\varphi_{CO_2}}$$

η_{gas} conversion degree based on off-gas

CO_2 carbon dioxide content in off-gas [vol-%]

φ_{CO_2} theoretical maximum amount of CO₂ produced

CO carbon monoxide in off-gas [vol-%]

CH_4 methane content in off-gas [vol-%]

Delivered coals were grinded and sieved in two particle size fractions, PC and in GC form. Microstructure analysis of a raw coal (before grinding and sieving) and grinded coal in PC and GC form was conducted. Coal A in GC form was not meant to be analysed in scope of the preliminary trials. Injection trials using the MIRI were conducted for each coal in both size fractions. An oxygen concentration of 26 vol.-% and an injection rate of 700 g/h was set.

The char generated during these trials was collected. Ash content of the char was determined. The conversion degree based on the off-gas analysis and the ash analysis was calculated. Furthermore a microstructural analysis of the char was conducted.

3.2.1.3 RESULTS

In this section, the results of microstructural analysis of raw coals and conversion trials are introduced. These analyses were conducted in scope of task 1.4. Based on these results, coals and size fraction were chosen for further investigations.

Microstructural analysis of coals

Several images with different magnifications were taken by LOM. The image analysis software processed these images. Average pore diameters and cross-sectional porosity were determined and are presented in **Figure 3.4**. In term of porosity and pore diameter, coal D showed the highest values. Coal C was characterized by the lowest porosity. In terms of average pore diameter, all coals except for coal D, showed similar values.

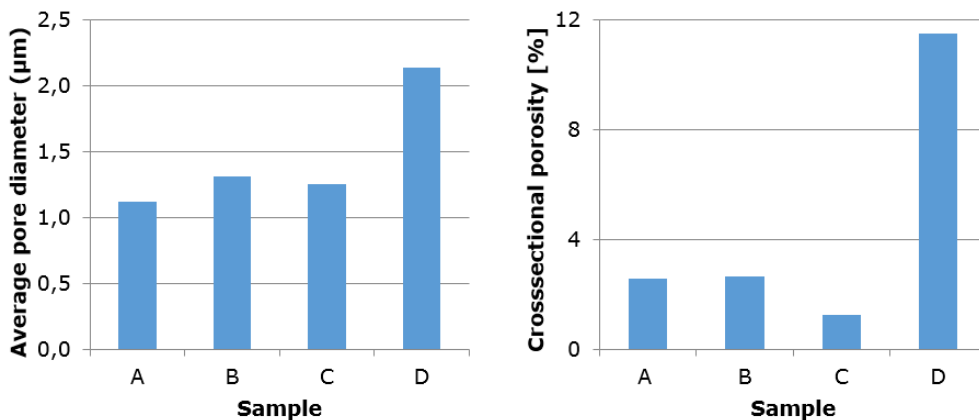


Figure 3.4: Average pore diameter (left) and cross-sectional porosity (right) of raw coal

After grinding, PC and GC were examined by LOM, as well as SEM. Micro-size distribution, as well as shape factors were determined and are shown in **Figure 3.5**. All coals showed similar size distribution except for coal B. Due to a high HGI value, coal B broke very easily and therefore was very easy to grind. However breakage also occurred during transportation resulting in further breakdown of the coal after sieving.

Regarding shape factor, coal A presented the lowest value. The other coals resembled similar shape factors. The shape factor could be an indication for the specific surface area. A low shape factor indicates a higher specific surface area.

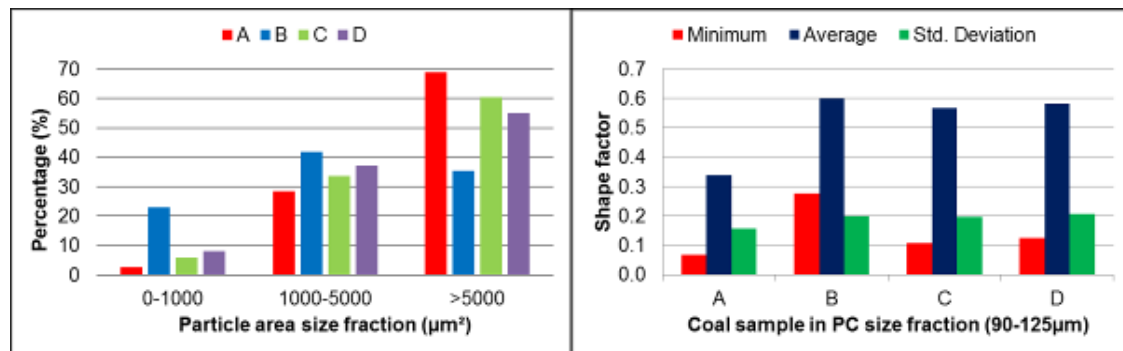


Figure 3.5: Particle size distribution (left) and shape factor of PC coals (90 - 125 μm)

In order to examine the surface texture of coals, SEM was used. As already seen by LOM analysis, coal B consisted of greater amount of smaller particles compared to other coals. This analysis was also used to compare the char generated.

The microstructural analyses were also conducted for granular coals. However, the results varied too much due to the wide grain size distribution. Consequently, LOM analyses were only conducted qualitatively. **Figure 3.6** shows the LOM images of the granular coal. In addition, SEM analysis was conducted and the results are shown in **Figure 3.7**. Analyses show a wider range of particle sizes compared to PC coal.

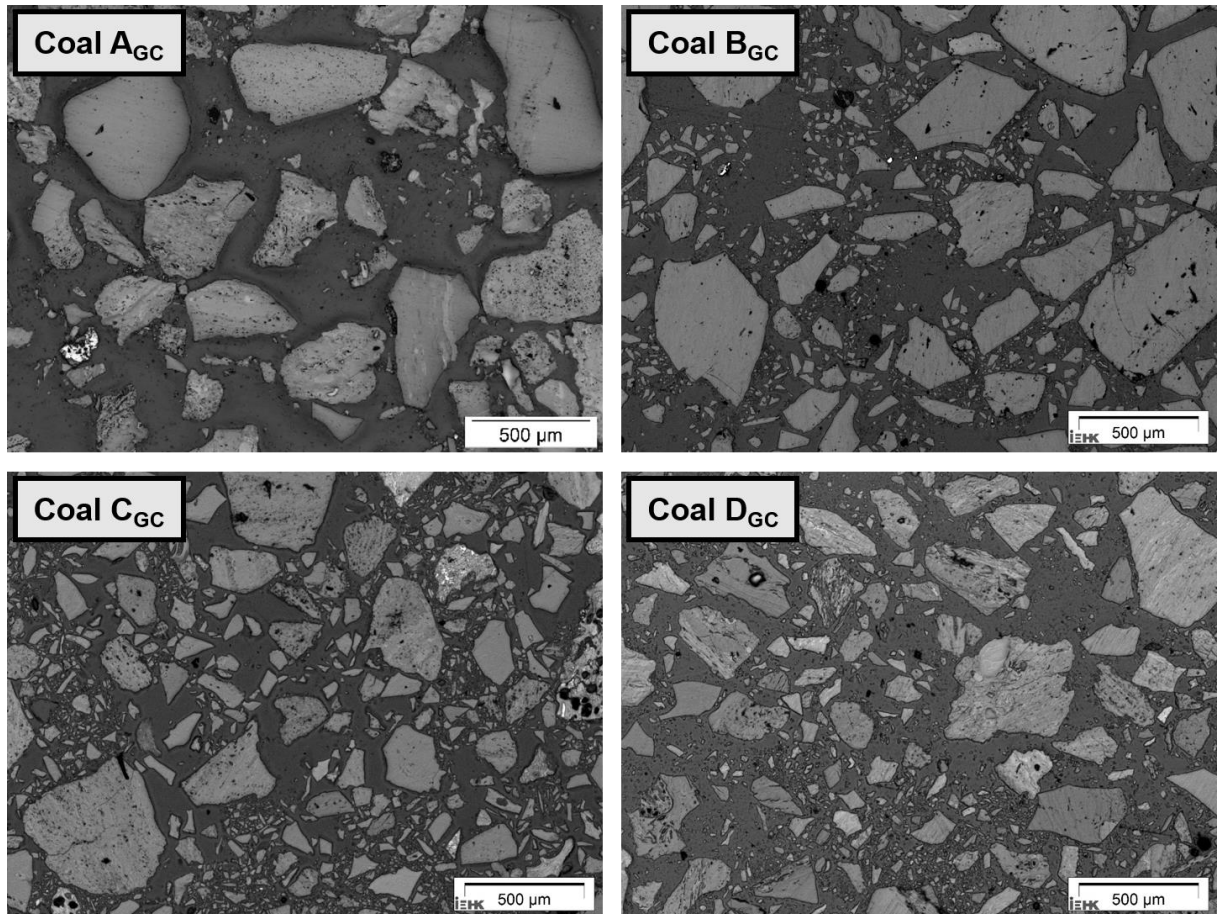


Figure 3.6: LOM images of GC coal (50% <250 μm) (x50)

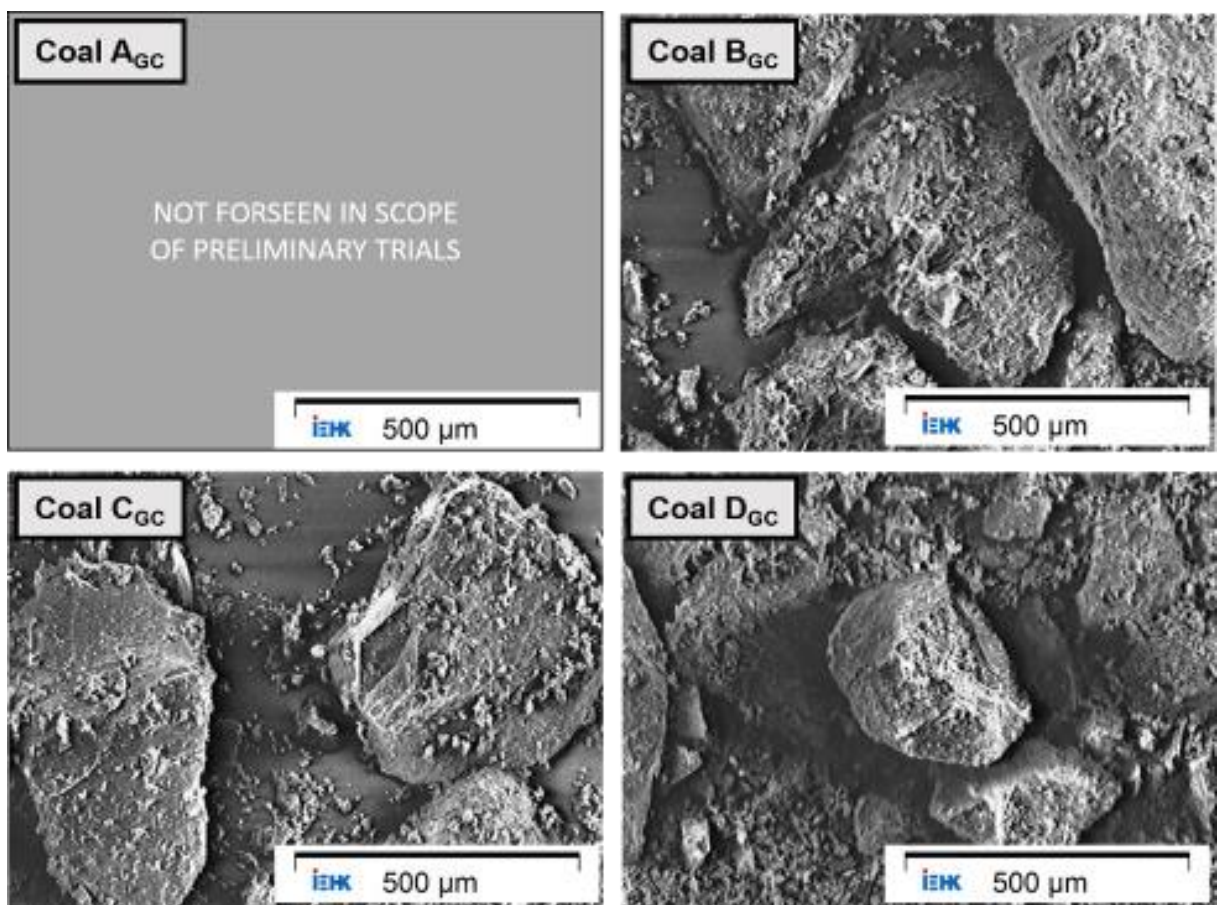


Figure 3.7: SEM images of GC coal (50 <250 μm) (x100)

Conversion trials

With respect to the char formation behavior, trials using the Multifunctional Injection Rig for Ironmaking were conducted. All coals in PC as well as in GC form were tested. Coal A_{GC} form was added to the test program on the request of project partners.

The obtained conversion degrees are presented in **Table 3.3**. Trials regarding the coal in PC form could be executed with no problems. For the coal in GC form, problems occurred. For coal B and D, clogging of the injection lance occurred. Multiple attempts were carried out before obtaining reliable results. The char generated from trials using coal B and D was very inhomogeneous.

Coal in PC size fraction showed a significantly higher conversion degree. The low volatile matter content of coal C reflected on the conversion degree of PC coals. Although coal B_{PC} and D_{PC} had a lower content in volatile matter the conversion degree was higher compared to coal A, which had the highest volatile matter content. Coal B and D showed similar conversion degrees for PC as well as GC coal. Particle size had a lower impact on coal C compared to the other coals. However in granular form coal A had the lowest conversion degree.

Table 3.3: Coal conversion degrees based on MIRI trials

Coal	A		B		C		D	
Size fraction	PC	GC	PC	GC	PC	GC	PC	GC
$\eta_{\text{gas}} [\%]$	38.5	8.7	52.3	23.9	22.4	12.6	47.5	23.3

First injection trials of coal B showed no successful injection of the coal. Blockages in the injection lance occurred. During a successful injection trial with coal B_{GC}, big ash particles appeared in the cyclone. This phenomenon could be caused by a low ash fusion temperature of coal. During coal conversion, high temperatures led to coal ash particles reaching liquid state. These then condensed at the gas cooling system and were collected in the cyclone together with the char. Residues of coal B_{GC} are shown in **Figure 3.8**. Two different types of particles could be identified. One was similar to the residues found in other samples. The other particle type appeared as thin plates with metallic shining look.

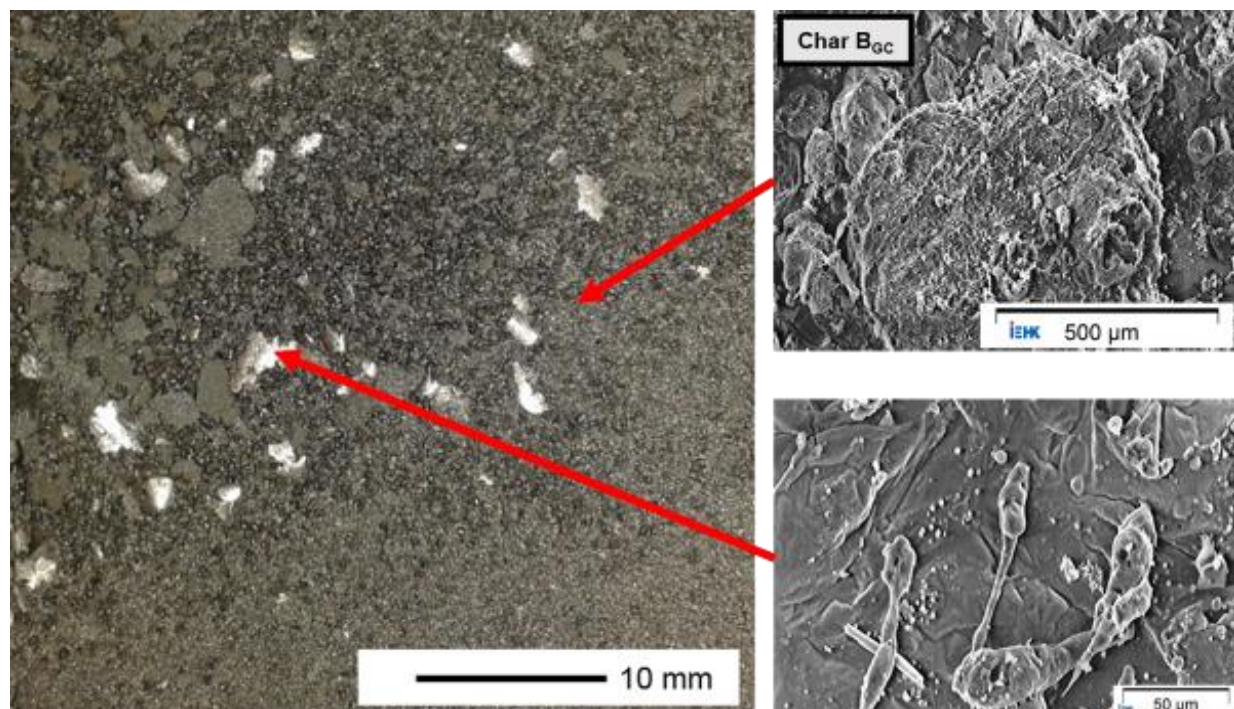


Figure 3.8: Occurrence of inhomogeneous char (left), char particle by SEM (right top) and ash particles by SEM (right bottom)

The ash analysis, which was accompanying with the coals was simplified shown in **Table 3.4** and transferred to a ternary system (SiO₂-Al₂O₃-CaO). Based on this ternary system shown in **Figure 3.9** coal A, C and D were located in mullite (Al₂Si₂O₅) area whereas coal B was located in anorthite (CaAl₂O₄) due its high calcium oxide content in comparison to the other coals.

Table 3.4: Ash composition of coals and calculation of pseudo ash composition

Coal	%SiO ₂	%Al ₂ O ₃	%CaO	Sum	%SiO ₂ '	%Al ₂ O ₃ '	%CaO'	Sum	
A	45.3	23.6	7.1	76.0	59.6	31.1	9.3	100	
B	31.8	20.7	10.5	63.0	50.5	32.9	16.7	100	
C	43.8	36.5	3.2	83.5	52.5	43.7	3.8	100	
D	54.1	24.3	3.4	81.8	66.1	29.7	4.2	100	

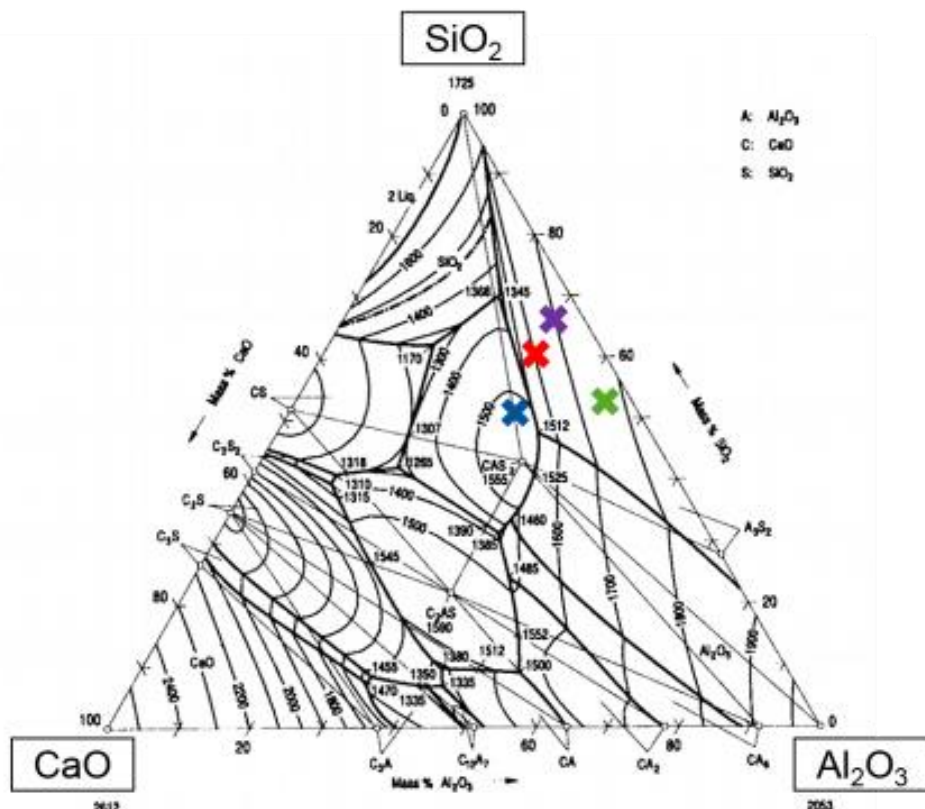


Figure 3.9: Location of coal ash in ternary system (CaO-SiO₂-Al₂O₃)

However this simplification did not consider the influence of iron oxides, which also may have a considerable percentage in the ash.

In addition the free swelling index was determined for all preselected coals. Coal A and C showed no swelling behavior whereas coal D showed a minor swelling degree of 1. However coal B showed a very high swelling degree of 5. This high swelling behavior could be responsible for blockage of the injection lane regarding coal B.

Char microstructural analysis

The microstructure of the char was analyzed using LOM (**Figure 3.10**) and SEM (**Figure 3.11**). Due to the highly porous nature of the char, the imaging software of the LOM could not be applied automatically. Qualitative analysis showed that Char B_{PC} and D_{PC} were more porous compared to char A_{PC} and especially C_{PC}. This observation corresponded with the conversion degree determined based on the injection trials.

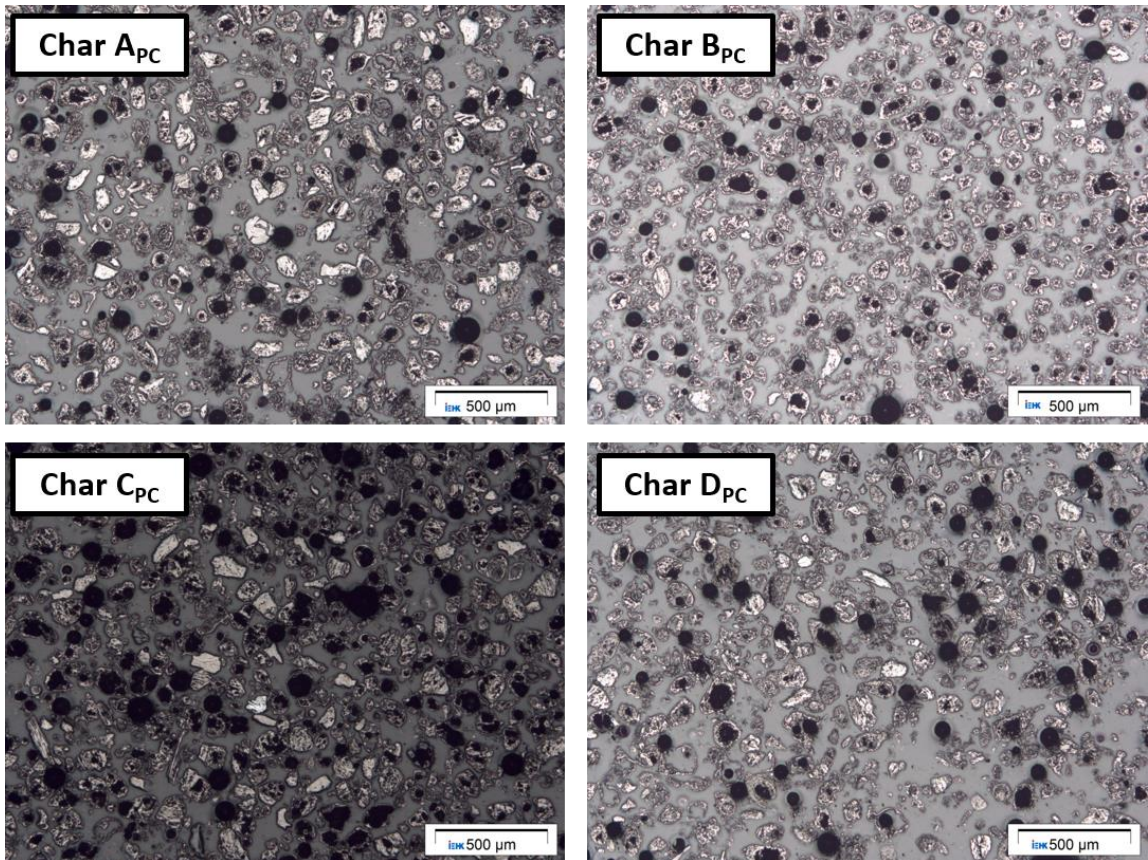


Figure 3.10: LOM image of PC char (90 -125 μm) (x50)

In addition, the surface texture of the char was analyzed by SEM. The surface of char C_{PC} was very smooth in comparison to the other coals. All PCchars showed a rather homogenous particle size distribution which may be caused due to the narrow grain size distribution.

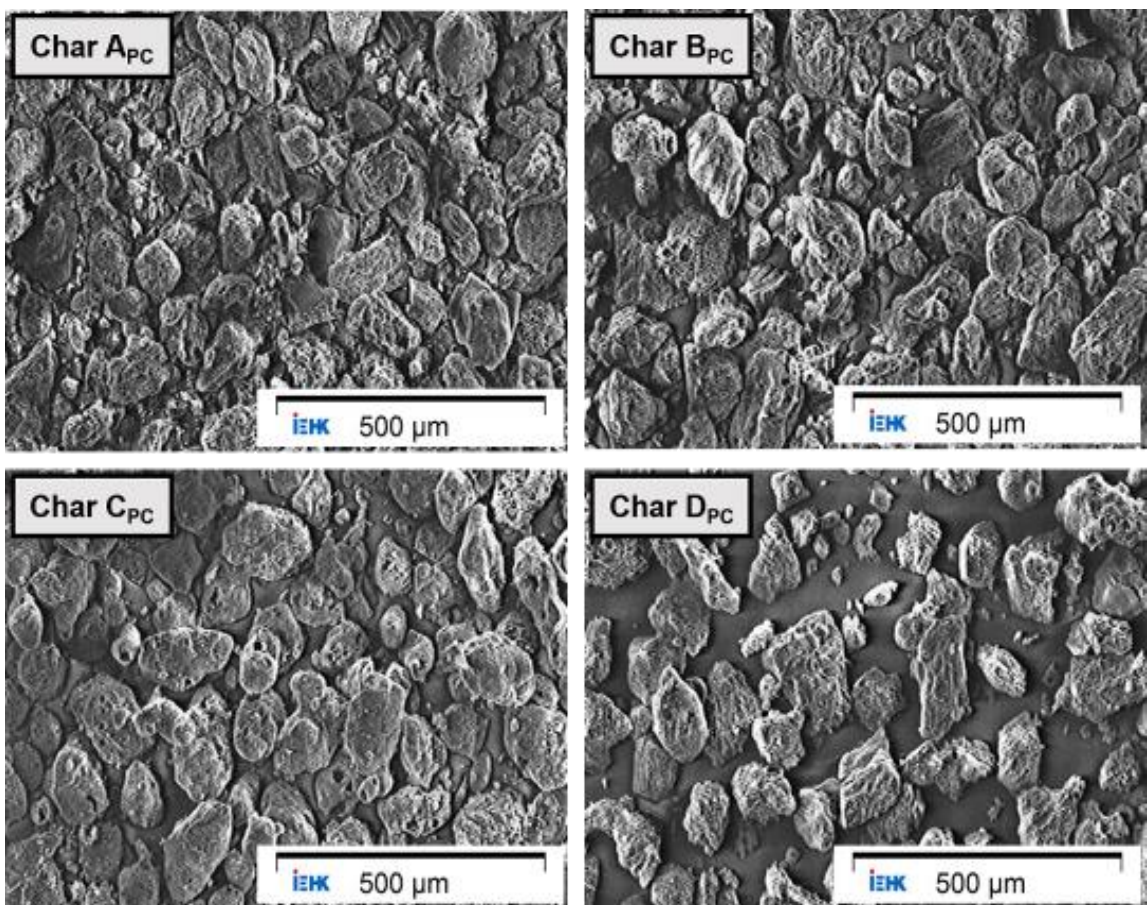


Figure 3.11: SEM image of PC char (90 -125 μm) (x100)

The microstructural analysis of the granular coals shown in **Figure 3.12** confirmed the low conversion degree of coal C_{GC} ; the char porosity was low. Char B and D both showed high porous structure. However the char particle size distribution was much wider compared to PC-char. A mix of porous and dense unreacted particles could be found. Unreacted particle appeared in a greater particle size than reacted porous particle.

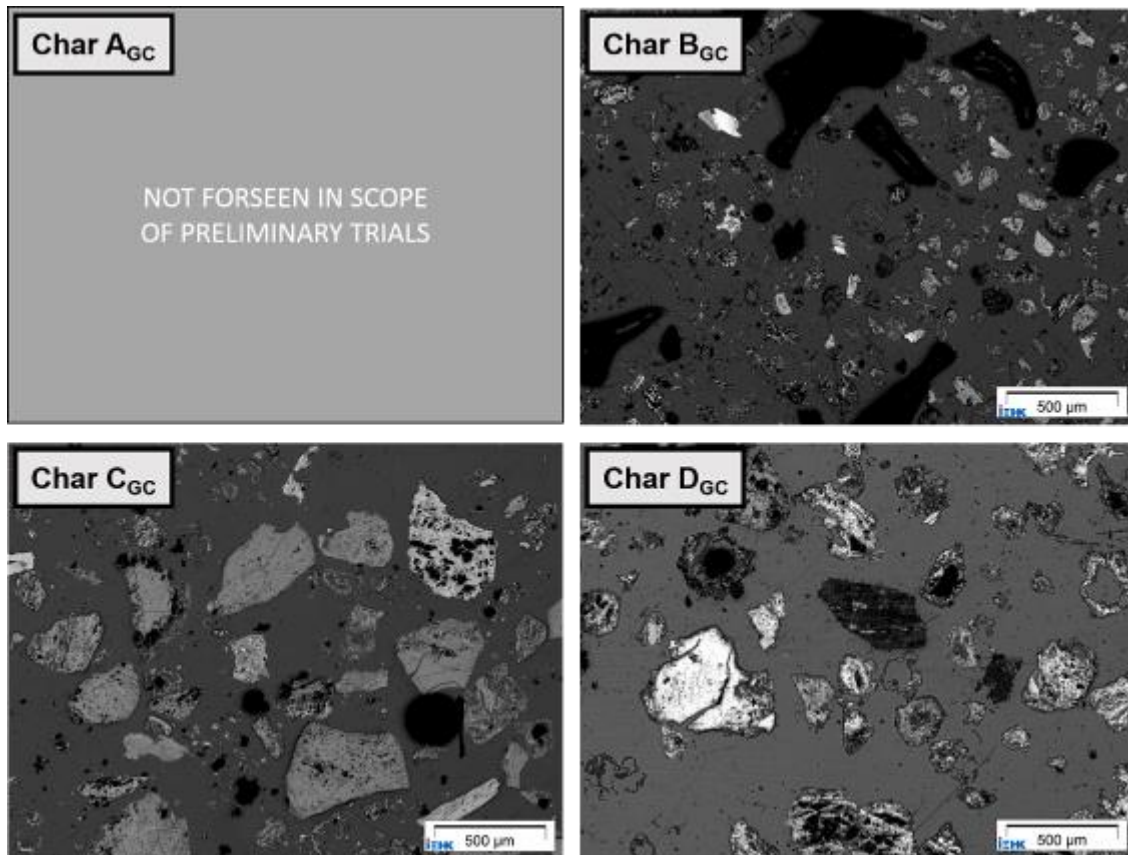


Figure 3.12: LOM images of GC char (50% <250 µm) (x50)

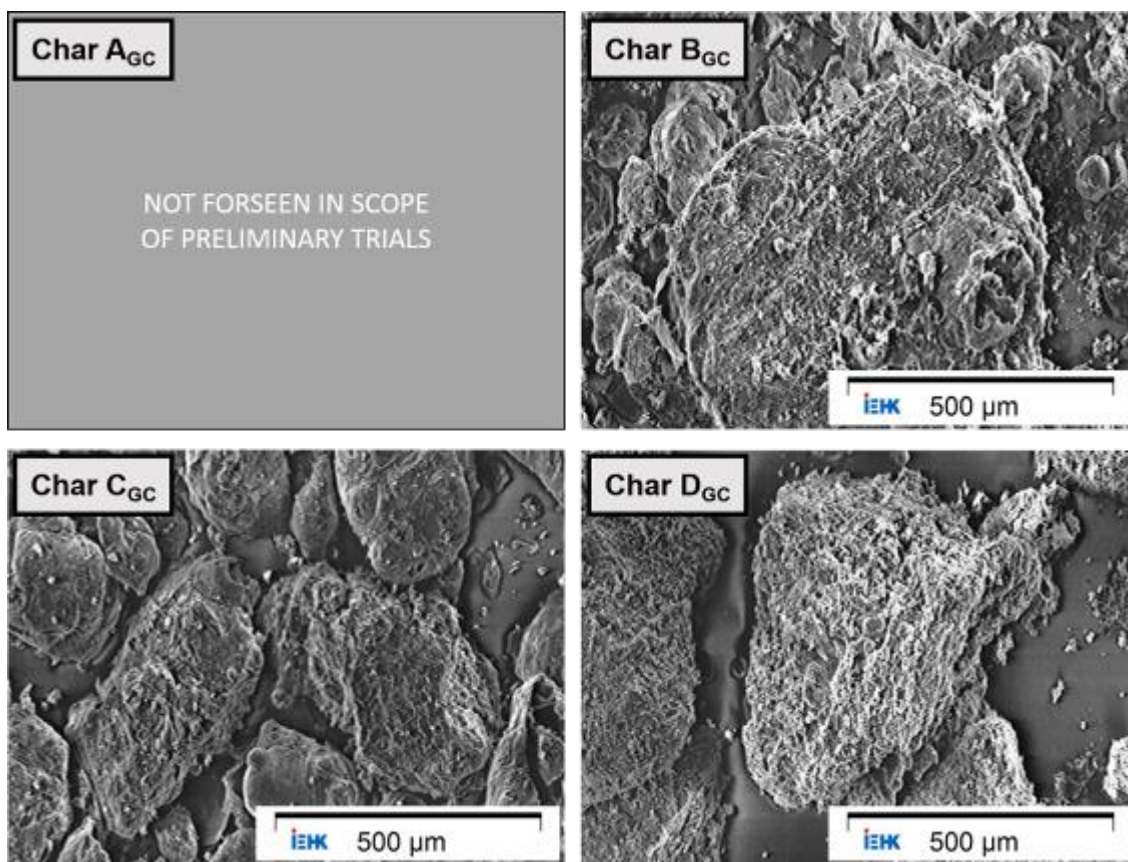


Figure 3.13: SEM images of GC char (50% <250 µm) (x50)

The particle surface image conducted via SEM (**Figure 3.13**) showed for Char B_{GC} and D_{GC} a fissured surface. Char C_{GC} appeared to be consisting of smooth particle surfaces (as seen in PC form) as well as fissured surfaces.

Further discussion of the microstructural analysis will be done in Task 1.4.

3.2.1.4 CONCLUSION OF SELECTION OF COALS

The preliminary results obtained by RWTH Aachen at the MIRI for coals A, B, C and D were used to define the coals for the further program: Based on the above discussed results, three types of two coals were selected for studies in further project tasks: C_{PC} , C_{GC} and B_{PC} . Coal C was chosen in PC as well as in GC grain size fraction due to its homogenous char. Coal B was chosen in PC size fraction. Amounts of coal and char needed by each project partner were determined. A method for grinding and sieving greater amount of coal with chosen particle size distribution has been developed.

3.2.2 TASK 1.2 INVESTIGATION OF COAL DEVOLATILISATION AND CONVERSION

These aspects were investigated by RWTH and AMMR.

Trials with the MIRI plant at different oxygen enrichment were conducted with selected coals. Char produced was collected and analysed by different means.

ArcelorMittal on its side focussed on the devolatilisation process of the selected coals. In particular, the intention was to use devices with heating rates of the coal similar to the one it encounters when entering the blast furnace raceway. The foreseen devices when the CharFoCo proposal was submitted were: a Gleeble test apparatus, a sinter pot hood and a laboratory plasma torch. Afterwards, access was obtained to a combustion test facility at CANMET, which offered a new possibility.

3.2.2.1 MIRI CONVERSION TRIALS

Coals C_{PC} , C_{GC} and B_{PC} were injected at various oxygen content in blast: 26 vol.%, 28 vol.% and 30 vol.-%. Injection of coal B_{PC} was not possible due to clogging of coal in the injection lance leading to blockage before reaching stable reaction conditions.

Table 3.5: Results of injection trials with various oxygen enrichments

		η for coal C_{GC}	η for coal C_{PC}	η for coal B_{PC}
Immediate analysis	V. M. (wt.-%)	11.90	11.90	17.65
	C_{fix} (wt.-%)	79.95	79.95	76.45
	ash (wt.-%)	8.15	8.15	5.90
Conversion degree η	26 Vol.-% O ₂	11.37	24.82	-
	28 Vol.-% O ₂	10.77	23.77	-
	30 Vol.-% O ₂	9.78	24.19	-
Stable CO₂ content during trial	26 Vol.-% O ₂	2.48	5.59	-
	28 Vol.-% O ₂	2.52	5.75	-
	30 Vol.-% O ₂	2.43	6.26	-

Table 3.5 presents the results of the injection trials with increasing oxygen enrichment of blast. Similar to the preliminary trials, the conversion degree of granular coals was much lower compared to pulverised coal. However conversion of char might be higher which is investigated in task 1.4. The increase of oxygen content showed no significant effect on the conversion degree. An almost decreasing tendency of the conversion degree was detected although the CO₂ content in off-gas

rose. In conclusion, the increase in CO₂ content was lower than the theoretical maximum CO₂ production. The increase in oxygen content was realised by a coaxial injection lance. By increasing oxygen content, the gas speed of the outer injection lance increases significantly which could result in a shortened residence time of the injected coal and consequently a lower conversion degree.

Char, which was collected in the cyclone of the MIRI, was analysed in scope of Task 1.4. Microscopic analysis of char is shown in **Figure 3.14**. Char originating from granular coal mostly showed Inertoid/solid structure. Particles showed porous as well as solid structure. With increasing oxygen content, no significant change in general microstructure appearance was examined. Char from C_{PC} showed a tenuinetwork/network structure. The structure showed a porous particle. This was in accordance with the higher conversion degree.

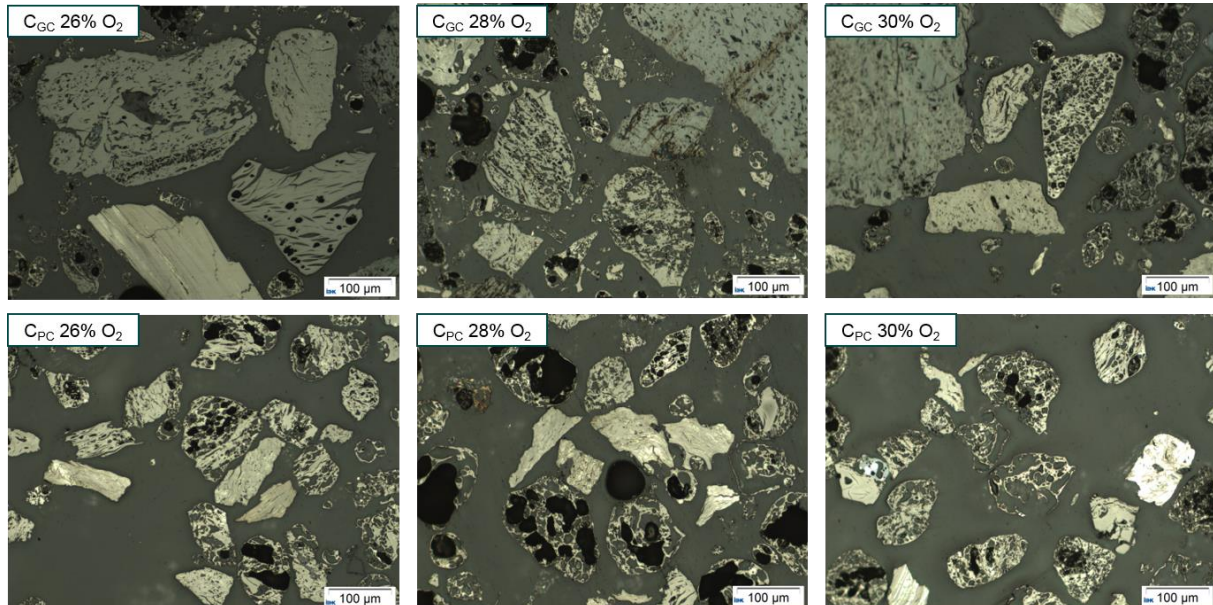


Figure 3.14: Microscopic analysis of char collected in the MIRI

3.2.2.2 EVALUATION OF THE EFFECTIVENESS OF THE DIFFERENT TEST FACILITIES USED BY AMMR

A preliminary test was performed in 2014 using AMMR sinter pot hood as the heating device for the coal sample. It turned out that this facility would not be suitable for the tests. This was due to a too low heating rate of the coal on one hand (33°C/s), and the fact that oxidation took place during the heating procedure, which led to an overestimation of the devolatilisation rate of the coal.

Following this test, the work of AMMR was then focussed on the evaluation of the three other techniques, namely the Gleeble, the plasma torch and the CANMET test facility.

3.2.2.2.1 METHODOLOGY OF THE COMPARATIVE EVALUATION OF THE THREE EXPERIMENTAL TECHNIQUES

All three above mentioned techniques were compared using a fourth coal type, named Coal X, for this purpose. The main characteristics of coal X are given in **Table 3.6**.

The preparation scheme of the coal for the different trials was not exactly the same. It is shown in **Figure 3.15**.

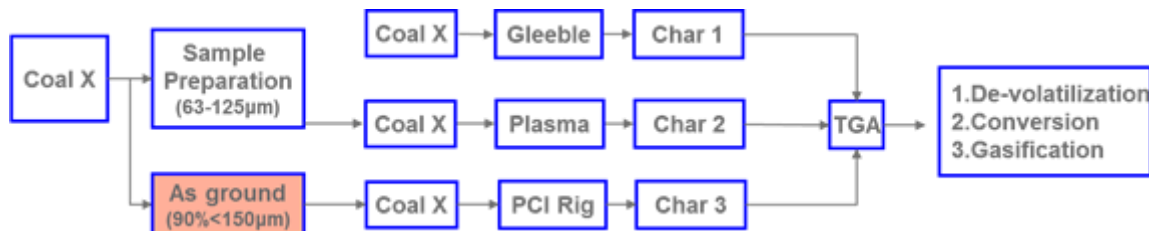


Figure 3.15: Sketch of the testing procedure with coal X for the different techniques

Table 3.6: Characteristics of Coal X used for evaluating the experimental techniques

	Coal A	Coal B	Coal C	Coal X
Coal Types	PC	PC	PC	PC
PC Coal Size, μm	90-125	90-125	90-125	< 150
HGI	35	95	78	42
VM	19.8	17.6	14.1	36.9
Ash	10.3	5.0	10.3	7.4
C	77.9	85.8	75.6	77.9
H	3.9	4.3	3.9	5.2
O	5.6	2.9	3.2	7.0
N	2.1	1.2	1.6	1.7
S	0.3	0.7	0.3	n.a.
LCV (KJ/kg)	31225	29083	31201	30597
SiO_2	46.3	31.8	48.4	53.2
Al_2O_3	22.1	20.2	31.6	27.7
CaO	8.7	10.5	4.5	2.6
MgO	3.5	2.0	1.4	1.0

The main characteristics of the test procedures for the different trials are the following:

- for the Gleeble and plasma trials, only the fraction 63-125 μm of the coal was used, while the complete size distribution of pulverised coal X was used for the tests at the CANMET facility;
- also, the Gleeble and plasma trials were done in inert atmosphere, with then devolatilisation being the only step considered in the test. Contrarily to that, the tests at the CANMET rig were performed under inert atmosphere, but also under 21 %, 23 % and 25 % of oxygen, yielding four different chars at the end;
- for the Gleeble test, the fraction 63-125 μm of Coal A was also tested.

The results of the different experiments are described below.

3.2.2.2.2 RESULTS OF COAL CONVERSION TRIALS

3.2.2.2.2.1 GLEEBLE TESTS RESULTS

A sketch of the sample holder and a picture of the experimental set-up are given in **Figure 3.16**.

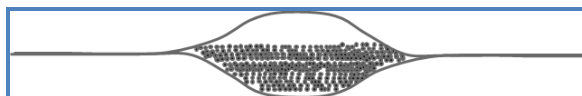




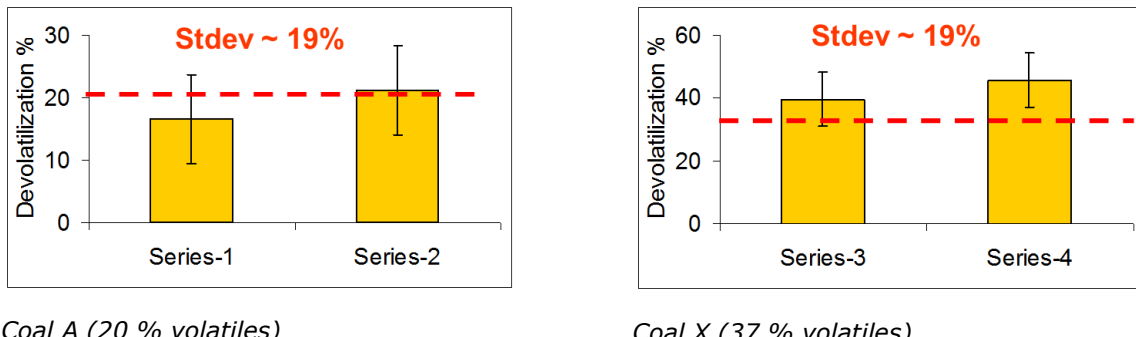
Figure 3.16: Sketch of the sample holder and picture of sample holder in the Gleeble before test

Typical experimental conditions during a Gleeble trial are reminded in **Table 3.7**.

Table 3.7: Typical experimental conditions of Gleeble trials

Heating rate	°C/s	2500
Maximum temperature	°C	1050
Holding time	s	2
Gas atmosphere	-	Inert, Helium
Cooling	-	Forced, Helium

The devolatilisation results obtained on coal A and coal X samples are given in **Figure 3.17**. A similar standard deviation of the devolatilisation rate of $\sim 19\%$ was obtained for both coals, which was rather a poor result.



Coal A (20 % volatiles)

Coal X (37 % volatiles)

Figure 3.17: Results of devolatilisation tests at the Gleeble

3.2.2.2.2.2 PLASMA TORCH TESTS RESULTS

These trials were performed at a facility implemented in École Nationale Supérieure de Céramique Industrielle in Limoges. AMMR had access to this facility by contracting a small company called SILIMELT. A sketch of the test facility is presented in **Figure 3.18**.

The evolution of the temperature during the experiment is given in **Figure 3.19**. It could be seen that while the coal was injected at the tip of the plasma stream, temperature of 600 °C was observed 200 mm below the confinement box. This seemed to indicate that the coal saw an abrupt gradient of temperature just after its injection into the apparatus.

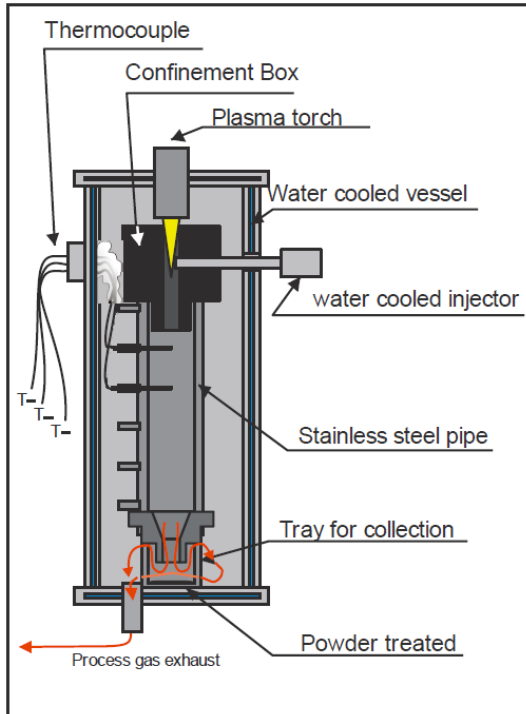


Figure 3.18: Sketch of the SILIMELT test facility in Limoges

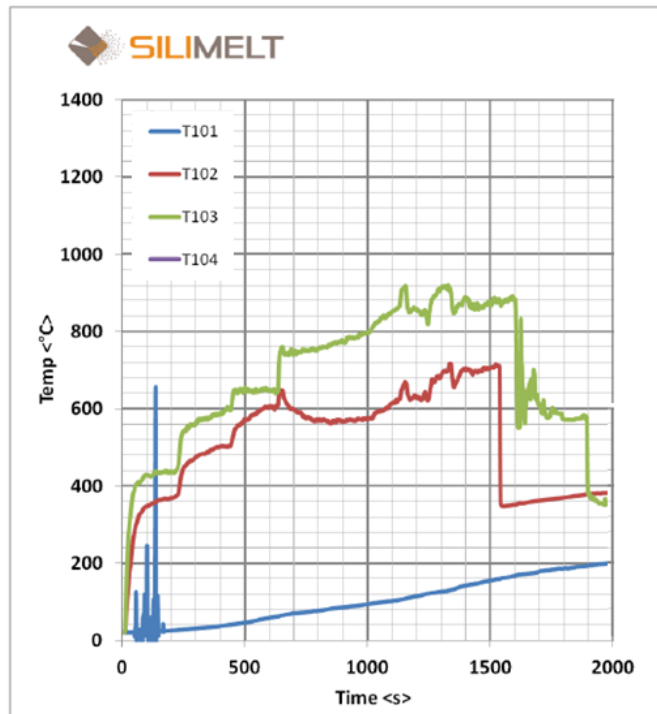


Figure 3.19: Evolution of temperature during the trial 100 mm (T103) and 200 mm (T102) below confinement box

Three char samples were recovered from this trial and the devolatilisation rate was calculated. An important standard deviation was observed (~30 %, **Figure 3.20**).

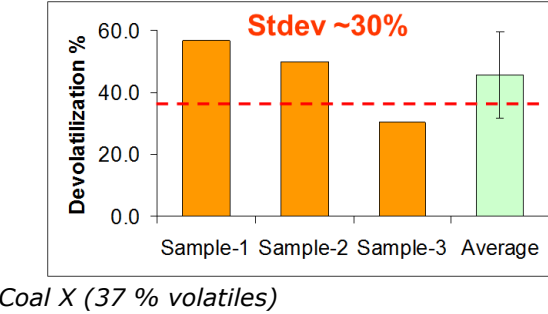


Figure 3.20: Results of devolatilisation tests at the plasma torch

3.2.2.2.2.3 CANMET TEST RIG RESULTS

After the submission of the CharFoCo proposal, AM got access to a specific facility used by our American colleagues for the investigation of coal conversion at the blast furnace.

This existing, (relatively) large scale pilot coal injection facility shown in **Figure 3.21** was implemented at CanmetENERGY (Ottawa, Canada). It could be used to produce char and study devolatilisation, combustion and gasification behaviour of coal. As indicated in **Figure 3.22**, the facility includes air supply, air pre-heater, coal injector, reactor and water quenching system.

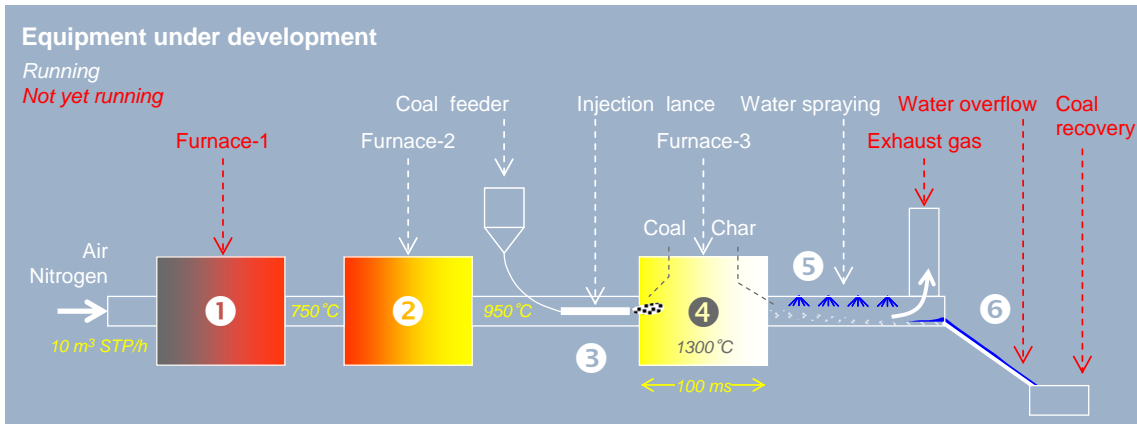


Figure 3.21: Sketch of the experimental set-up of the PCI Test Rig at CANMET

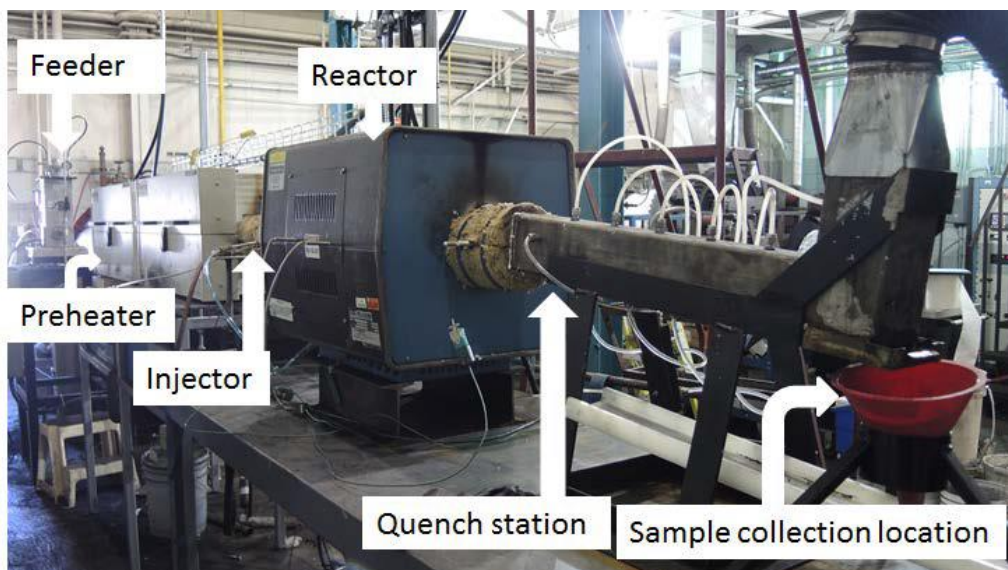


Figure 3.22: Picture of the CANMET test rig facility

As blast furnace tuyere conditions are very difficult to reproduce, the approach considered during building this rig was to be able to achieve reasonably high heating rates and corresponding short particle residence times and to evaluate coals and other solid fuels on a relative basis.

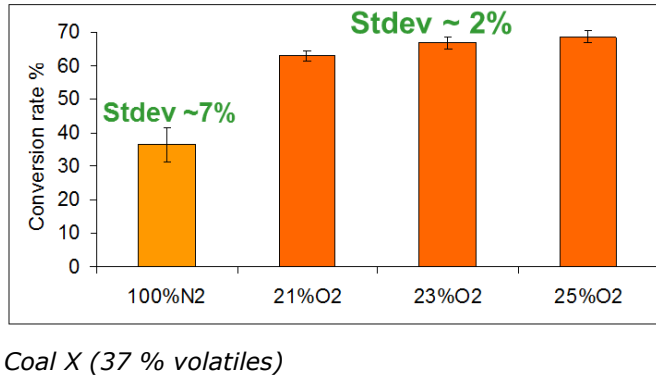
An arrangement was then made for using this rig for the purposes of the CharFoCo project. As a preliminary evaluation, coal X was injected at this rig under 100 % nitrogen and 21 %, 23 % and 25 % oxygen content.

The experimental conditions used during the trials are reminded in **Table 3.8**.

Table 3.8: Experimental conditions during the CANMET test rig trials

Heating rate	°C/s	10000
Maximum temperature	°C	1300
Holding time	ms	130
Gas atmosphere	-	N ₂ , 21-23-25 % O ₂
Cooling	-	Water spraying

The devolatilisation results obtained on coal X samples are given in **Figure 3.23**. Standard deviations for the collected samples correspond to 3 samples of each kind. The consistency of the obtained results was obvious.



Coal X (37 % volatiles)

Figure 3.23: Results of devolatilisation and conversion tests at the CANMET test rig

3.2.2.2.3 COMPARISON OF THE RESULTS – FUTURE PROSPECTS

A synthesis of the results obtained is given in **Table 3.9**.

Table 3.9: Comparison of the results obtained on the different test facilities

	BF condition	Gleeble 3500	Plasma torch	PCI RIG (Canmet)	MIRI	Tammann DTF	COBESI
Objective fulfilment	Dev.	Dev.	Dev.	Dev, Comb. Gasific.	Dev, Comb. Gasific.	Dev, Comb. Gasific.	Dev, Comb. Gasific.
Atmospheric conditions	O ₂ enriched air	inert	inert	Inert, 21; 23; 25 Vol.-% O ₂	26; 28; 30 Vol.-% O ₂	21 O ₂ Vol.-%	21 O ₂ Vol.-%
Heating rate, C/s (approx.)	10 ⁵	3.5 × 10 ³	10 ⁴	10 ⁴	5 × 10 ³	10 ³	2 × 10 ³
Maximum T, C	2000	1250	1000	1350	1300	1300	1500
Char homogeneity	Yes	To be optimized	To be optimized	Yes	Yes	Yes	N/A

The main conclusions from this table are the following:

- the Gleeble technique in its current situation had different drawbacks, among which:
 - o a slightly lower heating rate compared to the other techniques
 - o a relatively high residence time;
 - o the impossibility to produce large amount of char;
- the SILIMELT set-up based on plasma was actually not sufficiently developed to be sure about the conclusions. At the time of the trials, the main problem was linked to the heterogeneity of the produced char.

Moreover, on a practical point of view, a bad news came out at the end of 2015, as this small company was bankrupt. The company was finally taken over by another one, but did not continue the subcontracted research activities they were being done before, in the frame of which our trials were done. So this possibility of making trials had to be given up.

- on the other hand, the CANMET facility seemed to have all advantages regarding our application, with additionally the possibility to operate under oxidising conditions. The only limits concerned the maximum temperature that could be reached (~1350 °C instead of ~2000 °C at the blast furnace), and the heating rate (10⁴ °C/s instead of 10⁵ °C/s at the blast furnace).

Concerning this last point, it has to be pointed out that the heating rate as indicated in the table and generally discussed between specialists was just the result of a calculation, namely the ratio

between the maximum temperature in the reactor and the supposed/calculated residence time in it. It says nothing about the fact that the coal actually has a sufficient residence time to reach the average temperature of the reactor. This should be a point to assess in the future, either by means of direct measurements or by mathematical modelling.

A contract with CANMET was then secured in order to have the possibility to test the three selected coals for the trials (coal B in PC form, coal C in PC and GC form).

3.2.2.3 RESULTS OF AMMR TRIALS AT CANMET

Three tests were ordered by AMMR to CANMET for the evaluation of the conversion degree of the different coals examined in the course of the project. The corresponding results are reported below.

3.2.2.3.1 COAL C IN GRANULAR FORM

3.2.2.3.1.1 TEST METHODOLOGY

Two test runs were done under various gaseous conditions including 100% N₂ to simulate pyrolysis and combustion at different O/C molar ratios. Targeted O/C ratios ranged from 2.4, simulating low PCI injection rate to 1.5, to simulate high PCI injection rate. Two intermediate conditions (O/C ratio) of 1.8 and 2.1 were also investigated.

Parent coal was assessed for Proximate and Ultimate analysis and residues collected from experiments were analysed for Proximate and BET surface area.

The target conditions for the trials are given in **Table 3.10**.

Table 3.10: Standard experimental parameters and conditions at CANMET test rig

Coal particle size	As received (50% +250µm)
Coal injection rate	~1.2 to 1.5 kg/hr
Carrier N2 injection rate	~400 NL/hr
Air flow rate	~10,000 NL/hr
Target O/C ratio in reactor	(1) 2.4 (2) 2.1 (3) 1.8 (4) 1.5
Sampling distance	~0.8 m from injection point
Air temperature	800 ± 20 °C
Reactor Furnace Temperature	~1350 °C
Special condition	100% N2

Combustibility of coal was assessed by degree of burnout. Coal burnout was calculated from ash content of the parent coal and that of collected residues. It is defined as the ratio of mass loss of the total combustibles to the total combustibles present in parent coal and represented by the relation:

$$\text{Burnout (\%)} = \frac{\left(1 - \frac{A_0}{A_1}\right)}{\left(1 - A_0\right)} \cdot 100$$

with

A₀ = mass fraction of ash in parent coal (db)

A₁ = mass fraction of ash in residue (db)

3.2.2.3.1.2 RESULTS OF THE EXPERIMENTS

The chemistry of Coal C, GC form was checked by CANMET before starting the tests. The corresponding results are given in **Table 3.11**.

Table 3.11: Analysis of Coal C, GC form by CANMET

Coal	Proximate (% , dry basis)			Ultimate (% , dry basis)			
	Ash	VM	Fix C	C	H	N	S

Coal C (GC form)	8.99	14.35	76.66	82.6	3.72	1.5	0.26	2.93
------------------	------	-------	-------	------	------	-----	------	------

Regarding the experiments themselves, it was observed with the standard N₂ carrier gas flow rate offset at 400 NL/hr, that it was practically impossible to feed the coal. To overcome this problem, the carrier gas flow rate was increased to ~700 NL/hr and the amount of oxygen mixed in was adjusted to maintain the targeted O/C ratio in the reactor. In spite of this adjustment, unstable feeding rate was encountered.

The main results of the tests are given in **Table 3.12** and **Table 3.13**, respectively for Run 1 and Run 2.

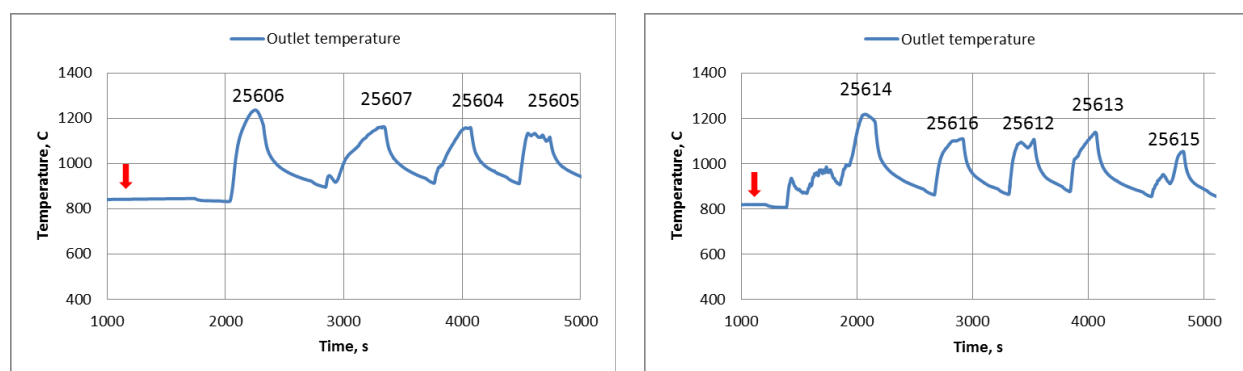
Table 3.12: Main results of Run 1 on Coal C-GC form

Run 1		As received	Test 1	Test 2	Test 3	Test 4	Test 5
Reference number	-	25602	25603	25604	25605	25606	25607
Target O/C	-		100 % N2	1,5	1,8	2,1	2,4
Feed rate	g/mn		24,8	24,1	21,2	29,5	20,4
O2 content in air	%		-	21,0	23,0	21,0	24,0
Actual O/C	-		-	1,65	2,11	1,30	2,31
Maximum outlet temperature	°C		937	1 160	1 135	1 237	1 163
Total burnout	%		0,6	20,3	11,5	12,6	19,0
Ash	%	9,0	9,0	11,0	10,0	10,2	10,9
Volatile matter content	%	14,4	7,9	5,7	3,9	5,1	2,9
BET surface area	m ² /g	1,3	0,6	30,9	28,9	33,6	25,3

Table 3.13: Main results of Run 2 on Coal C-GC form

Run 2		As received	Test 1	Test 2	Test 3	Test 4	Test 5	Test 6
Reference number	-	25602	25611	25612	25613	25614	25615	25616
Target O/C	-		100 % N2	1,5	1,8	2,1	2,1	2,4
Feed rate	g/mn		21,3	27,2	27,2	48,6	18,1	22,7
O2 content in air	%		-	21,0	23,0	21,0	21,0	24,0
Actual O/C	-		-	1,43	1,59	0,69	2,27	2,04
Maximum outlet temperature	°C		891	1 107	1 139	1 218	1 054	1 110
Total burnout	%		9,3	13,7	14,4	10,2	12,8	15,1
Ash	%	9,0	9,8	10,3	10,3	9,9	10,2	10,4
Volatile matter content	%	14,4	9,1	4,7	5,4	5,5	7,4	5,1
BET surface area	m ² /g	1,3	0,5	31,9	30,0	21,8	30,8	38,1

The measured temperature at the outlet of the reactor is given in **Figure 3.24**.



Run 1

Run 2

Figure 3.24: Evolution of temperature at the outlet of the reactor (O/C decreasing from left to right)

The impact of oxygen enrichment on coal conversion is presented in **Figure 3.25**. It seemed that oxygen enrichment did not have much effect on burnout of this coal tested in granular form. The total burnout rate observed was between 10 to 15% with a few outliers. This had to be directly linked to the significant amount of the particles present in the feed that were above 250 µm (~50 %). This amount was significantly different than the conventional pulverized feed (almost 90% <150 µm). With the presence of larger proportion of bigger particles in the coal and short residence time (~160 ms) in the reactor section, the coal particles did not get enough time for proper pre-heating, resulting in low levels of burnout measured. This also explained the insignificant effect of oxygen enrichment on burnout. Apart from that, the fact that Coal C was a

low volatile coal (~ 14%), which generally showed lower burnout values, could have worsened the result. One experimental point (in red circle in **Figure 3.25**) shows a very low calculated O/C ratio. This was the result of unwanted very high average feed rate on one occasion. For that reason, it was not considered as one of the targeted conditions, though reported as an additional condition.

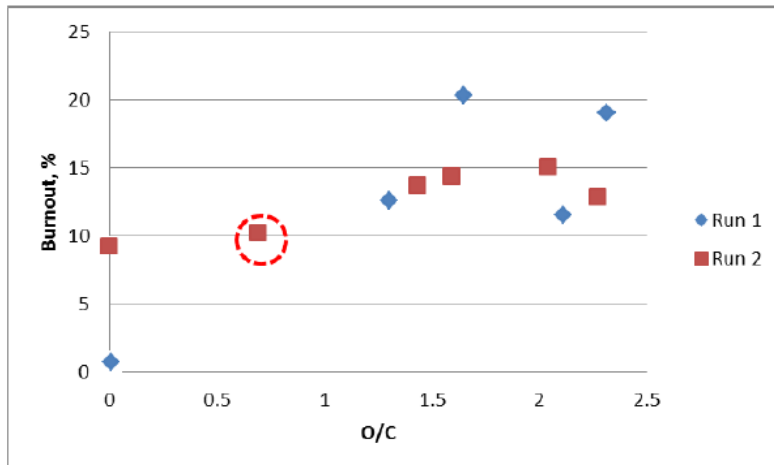


Figure 3.25: Effect of O/C ratio in injection rig on burnout of Coal C GC

Another way to evaluate the burnout rate of the coal was to examine the evolution of the volatile matter before and after the test. The corresponding curve is presented in **Figure 3.26**. It could be seen that the pyrolysis of the coal under nitrogen brought a significant step in volatile matter content, with a limited influence of the O/C ratio afterwards.

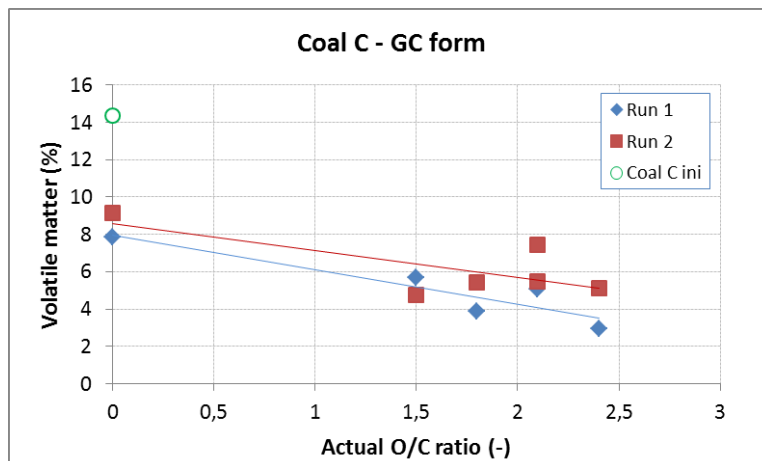


Figure 3.26: Volatile matter content of parent coal C and char as a function of the O/C ratio

Variation of BET surface area for residues at different O/C is shown in **Figure 3.27**.

Apart from few exceptions, no significant variation of BET surface area with oxygen enrichment was observed. This type of observation was expected because bigger size of the particles and short residence time for heating did not allow the particles to acquire representative pore structure.

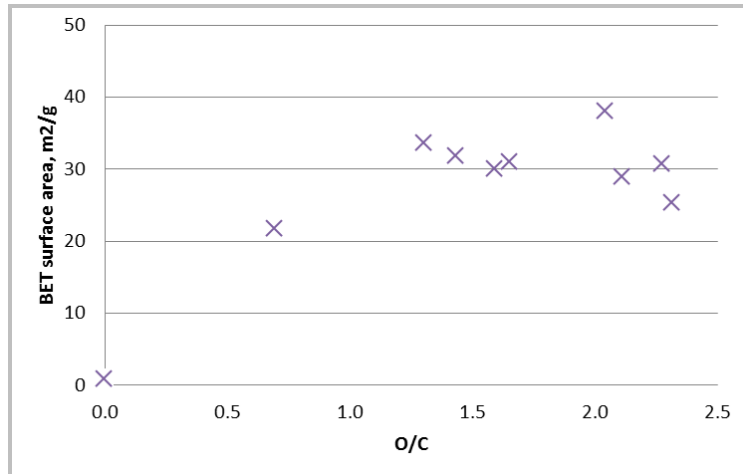


Figure 3.27: BET surface area of initial Coal GC and residue vs O/C ratio in injection rig

3.2.2.3.2 COAL C IN PULVERISED FORM

3.2.2.3.2.1 TEST METHODOLOGY

For coal C, PC form, though originally it was required to run twice, it was run thrice, as Run 1 seemed unsatisfactory. The proximate and ultimate analyses of the coal are given in **Table 3.14**.

Table 3.14: Analysis of Coal C, PC form by CANMET

Coal	Proximate (%, dry basis)			Ultimate (%, dry basis)				O
	Ash	VM	Fix C	C	H	N	S	
Coal C (PC form)	7.93	13.93	78.14	83.4	3.78	1.59	0.31	3.03

Apart from the size of the coal, the conditions targeted for the tests with coals B and C, PC form, were the same as the one mentioned in **Table 3.10**.

3.2.2.3.2.2 TEST RESULTS

The evolution of the temperature measured at the outlet of the test rig during the trials is shown in **Figure 3.28**, **Figure 3.29** and **Figure 3.30** for runs 1, 2 and 3, respectively. The evolution of the burnout rate of Coal C, PC form as a function of the O/C ratio is presented in **Figure 3.31**. The burnout rates of Coal C, PC form and Coal C, GC form are compared in **Figure 3.32**.

The relationship between the O/C ratio and the temperature at the outlet of the rig was not clear even if there was a tendency to get higher temperatures when the O/C ratio was low. This could be linked to the fact that a higher amount of volatiles were burnt in the rig when more coal was injected.

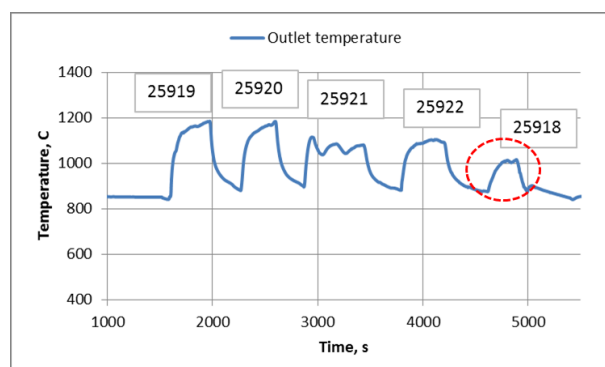


Figure 3.28: Temperature at rig outlet during Coal C, PC form test 1. O/C ratio from left to right: 1.44, 1.85, 2.02, 2.32. 25918: test under 100 % N₂

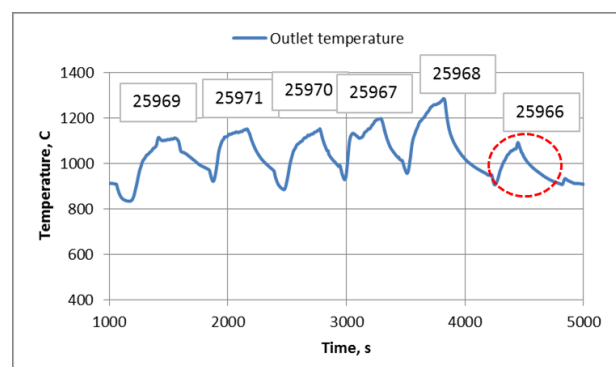


Figure 3.29: Temperature at rig outlet during Coal C, PC form test 2. O/C ratio from left to right: 2.02, 2.13, 2.35, 1.78, 1.72, 25966: test under 100 % N₂

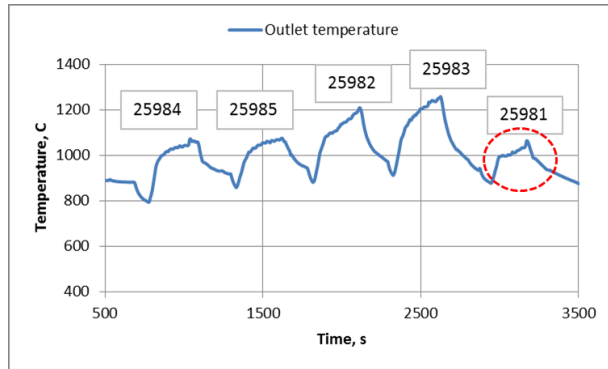


Figure 3.30: Temperature at rig outlet during Coal C, PC form test 3. O/C ratio from left to right: 1.91, 2.35, 1.5, 1.68. 25981: test under 100 % N₂

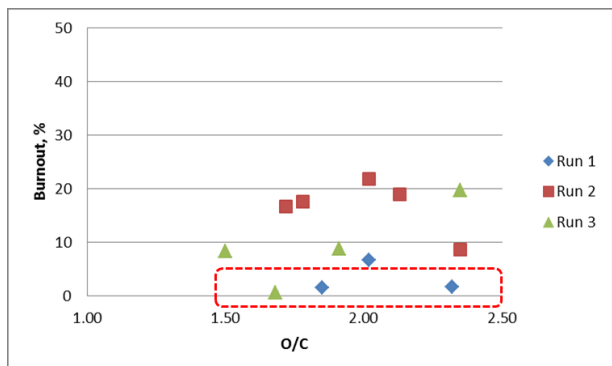


Figure 3.31: Burnout rate of Coal C, PC form as a function of the O/C ratio

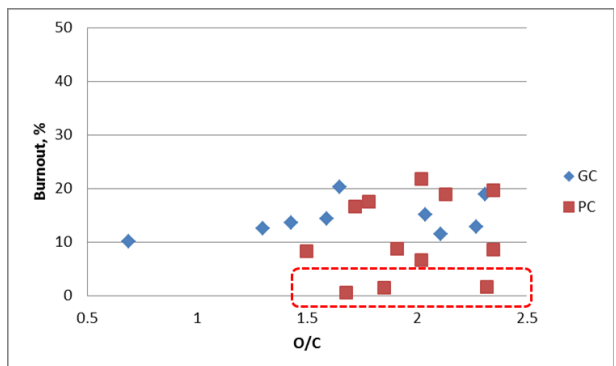


Figure 3.32: Comparison of burnout rates of Coal C PC and GC form

From **Figure 3.31**, it seems that oxygen enrichment does not have much effect on burnout of this coal also in pulverized form. The total burnout observed was between ~7 to ~ 20% with a few outliers indicated by red dotted line. When compared with the burnout values of the same coals in granular form as shown in **Figure 3.32**, both forms showed similar results, probably because the chemistry of coal is controlling the burnout, not only the size of the particles as was thought initially. The level of coal burnout and the effect of oxygen enrichment on burnout could be explained in terms of atomic H/C ratio or aromaticity of the parent coal. Burnout depends on the ignition temperature of the coal and amount of oxygen chemisorbed on coal particles. The ignition temperature increases with decrease in H/C ratio of the coal [1]. In other words, it increases with aromaticity of the coal as aromaticity is inversely related to H/C ratio in the coal [2].

Variation of BET surface area for residues from Coal C, PC form are shown in **Figure 3.33**, whereas the BJH cumulative pore volume are shown in **Figure 3.34**. Though the results of BET measurement were scattered, apart from few exceptions, BJH cumulative pore volume showed similar values at different levels of oxygen enrichment.

3.2.2.3.3 COAL B IN PULVERISED FORM

Though the original plan was to do three tests on Coal B (PC), due to the nature of the coal, it was found practically impossible to carry out all required set of experimental conditions during the runs using the coal B.

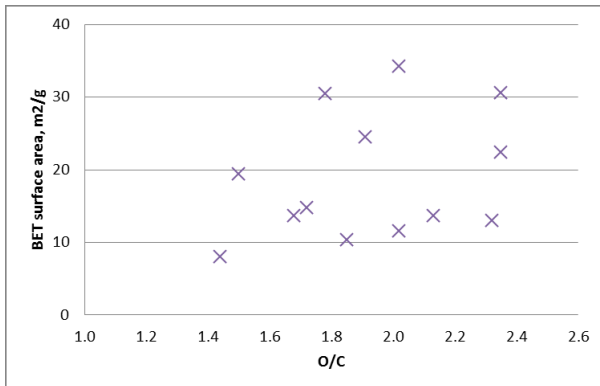


Figure 3.33: BET surface area of residue vs O/C ratio in injection rig for Coal C PC form

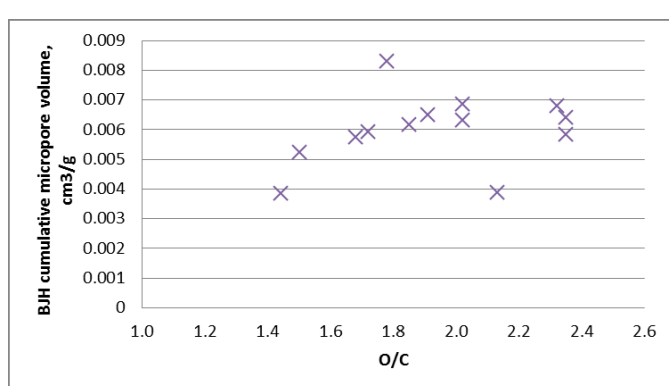


Figure 3.34: BJH cumulative micropore volume of residue vs O/C ratio in injection rig for Coal C PC form

The proximate and ultimate analyses of the coal are given in **Table 3.15**.

Table 3.15: Analysis of Coal B, PC form by CANMET

Coal	Proximate (%, dry basis)			Ultimate (%, dry basis)				
	Ash	VM	Fix C	C	H	N	S	O
Coal B (PC form)	5.60	17.91	76.49	86.1	4.19	1.17	0.88	2.01

Two attempts with Coal B, PC form were made. However for both the cases, the experiment had to be discontinued for blockage in the reactor tube. Suspecting the low fusion point of the coal ash being the cause, fusibility property of the ash was investigated and found to be ~ 1266 °C (ash fluid temperature, **Table 3.16**). This caused some of the ash to stick to the reactor wall (maintained at 1350 °C during PCI tests), during the injection and that build up continued to increase as the injection time progressed. Eventually that blocked the entire internal diameter of the reactor tube (**Figure 3.35**). The ash fluid temperature was compared to the one of other coals classically used for PCI injection. All these other coals did show values higher than 1500 °C.



Stages	Temperature (°C)
Initial	1235
Spherical	1241
Hemispherical	1243
Fluid	1266

Figure 3.35: Blockage of the reactor pipe during experiment with Coal B PC

Table 3.16: Fusibility Properties of Ash under Oxidizing Atmosphere for Coal B (PC) (ASTM D1857)

A combination of high iron and calcium content in the ash could cause low ash melting point in Coal B (PC).

3.2.2.3.4 CONCLUSIONS OF COMBUSTION TESTS AT CANMET AND MIRI PLANT

Finally, the main conclusions of the combustion tests at CANMET and MIRI plant were the following:

- the level of total burnout values for the investigated coal (Coal C) both in granular and pulverised form (GC) was very low, 10-20%. Similar values were obtained for Coal C, PC form (7 to 20 %);

- the effect of oxygen enrichment was not very significant for the tested coal, probably due to its low volatile matter content;

Furthermore analysis of char collected from the combustion tests at CANMET showed no relationship in BET surface area of residues with oxygen enrichment. The same was true for BJH cumulative pore volume. Microstructure analysis correlated with the conversion behaviour and consequently showed less high porous particles.

Injection of coal B in PC form was not possible due to some clogging problems in the reaction chamber/injection lance. Following reasons could be assumed to be responsible for the problematic injection behaviour:

- coal ash composition differed significantly from that of the other coals; higher amounts of calcium oxides were detected
- ash fusion temperature was much lower compared to other coals
- free swelling behaviour of coal B was significantly higher compared to other coals

3.2.3 TASK 1.3 DEVELOPMENT OF METHOD TO PRODUCE BIGGER AMOUNTS OF CHAR AND CHAR PRODUCTION

A Tammann furnace and a muffle furnace lab plants at RWTH were pre-selected as possible facilities to produce char with two different burnout rates. This synthetic char was used in further trials in scope of Task 1.4. After some preliminary trials and the development of different techniques a drop-tube setup of the Tammann furnace was chosen. **Figure 3.36** shows a drawing of the developed Tammann furnace DT-setup. The setup consisted of a feeding unit which transported the coal to a ceramic lance. Compressed air was used to transport coal into the reaction chamber, which was heated to a maximum temperature of 1300 °C. In the reaction chamber, coal reacted with oxygen contained in air. Residues were contained in a water-cooled collector unit.

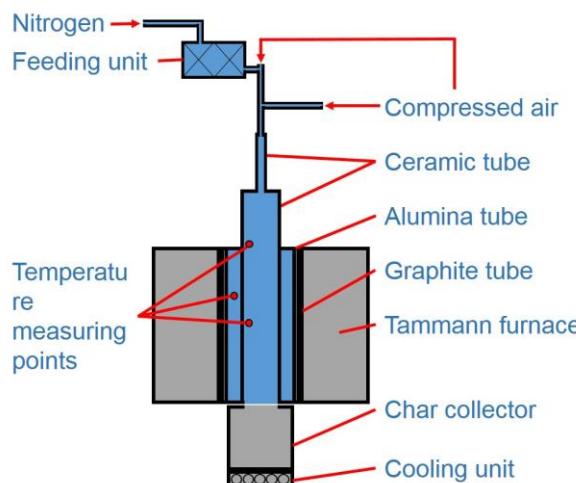


Figure 3.36: Scheme of Tammann furnace-based DT-setup

Two different types of chars were produced. Reaction temperature was varied and two different reaction temperatures were chosen for the production of bigger amounts of char as shown in **Table 3.17**. A total of six chars were generated. 1 kg of each char type was produced and distributed to other partners for further investigation in other task of WP 1.

Table 3.17: Parameters used for production of synthetic char

	B_{PC}		C_{PC}		C_{GC}	
Reaction temperature	900	1300	900	1300	900	1300
Coal injection rate	700 g/h					
Air injection rate	4 l/min					

All synthetic chars were analysed in Task 1.4. The Char produced by the Tammann DT setup was

compared to the char produced in Task 1.1 and 1.4 using the MIRI plant.

Figure 3.37 presents the microscopic images of char originated from Tammann DT setup and MIRI. At a reaction temperature of 900 °C the images show a mixture of reacted as well as unreacted particles. At greater magnification, reacted particles showed a partly porous structure. Particle wall thickness was rather high compared to that of regular tenuisphere/cenosphere structure. At higher temperature (1200 °C) the wall thickness reduces. Next to bigger pores multiple amounts of pores appeared resulting in tenuinetwork/network structures. Char produced by the MIRI rig and Tammann DT setup show comparable structure.

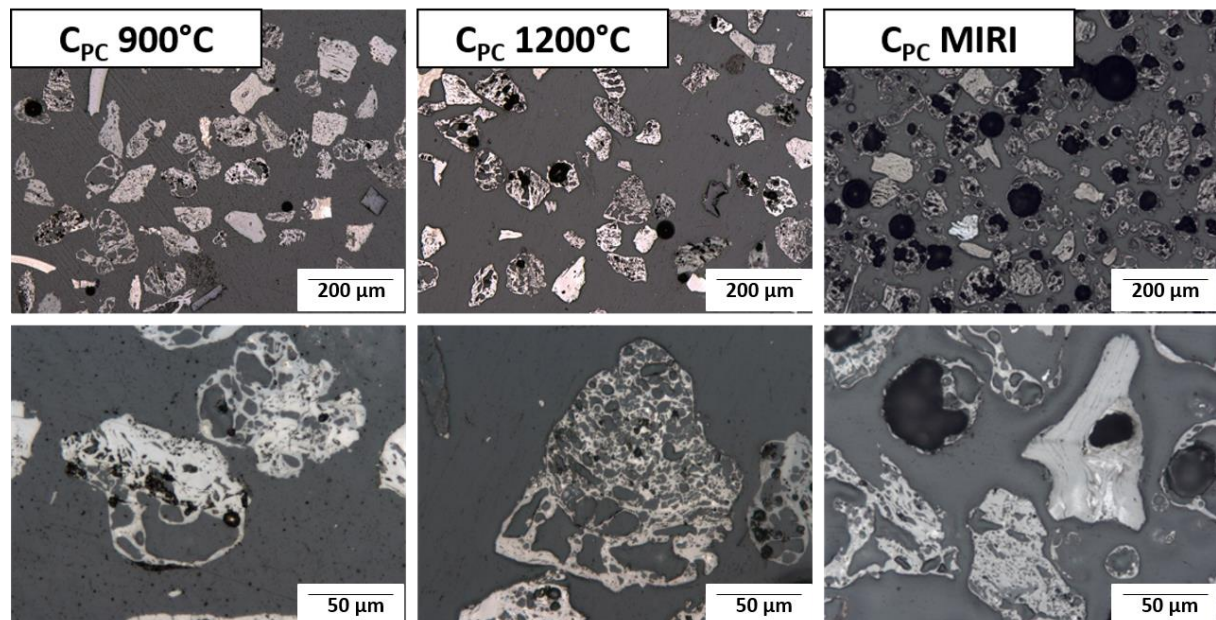


Figure 3.37: Comparison of synthetic char produced by Tammann furnace DT setup and MIRI plant

3.2.3.1 CONCLUSION TO DEVELOPMENT OF METHOD TO PRODUCE BIGGER AMOUNTS OF CHAR AND CHAR PRODUCTION

Various setups were tested to produce char. A Tammann-furnace setup using droptube principle was chosen to produce bigger amounts of char. Two reaction temperatures were chosen to produce different chars. In total 6 chars were produced.

3.2.4 TASK 1.4 CHARACTERISATION AND LABORATORY INVESTIGATIONS OF CHAR

In scope of task 1.4, characterisation and laboratory examination of char was conducted.

Char produced to a limited extent in Task 1.2 using the MIRI, was analysed by various methods. The bigger amounts of char produced in Task 1.3 were investigated more thoroughly.

3.2.4.1 INVESTIGATION OF CHAR PRODUCED IN TASK 1.1

Char which was produced using the MIRI plant accounted up to 50 g depending on conversion degree. The microstructure of char was compared to that of injected coal both in PC and GC forms using LOM analysis as well as SEM analysis. The results for coals were partly presented in Task 1.1. Char structure analysed via LOM was characterised using a classification system introduced by Bailey et al. and Menendez et al. shown in **Table 3.18**.

Table 3.18: Char structure classification based on Bailey et. al and Menendez et al. (3)

Bailey et al. (1990)	Tenuisphere	Crassisphere	Tenuinetwork	Meso-sphere	Inertoid	Solide
Menendez et al. (1993)	Ceno-sphere (Typ 1)	Ceno-sphere (Typ 1)	Netzwerk (Typ 2)	Netzwerk (Typ 2)	Solide (Typ 3)	

LOM images revealed cross-sectional view of the particle. **Figure 3.38** shows LOM images of coal and char in PC size fraction with a magnification of 500x.

Coal particles showed only minor difference in appearance. Coal B however showed a more heterogeneous appearance compared to the other coals. The other coals showed particle with a very strong reflection appearing almost white and particle with some black spots and phases. These resembled different organic components of coals.

Char particles displayed in **Figure 3.38** show major differences compared to its parent coal. All chars with exception for Char B_{PC} consisted of porous as well as dense particles.

Images of Char A_{PC} show particles which can be allocated to a tenuinetwork as well as inertoid morphologies after Bailey et al. While Char B_{PC} presented particles morphologies, which could be assigned to tenuisphere as well as tenuinetwork, particles from Char C_{PC} showed solid particles and crassipheres, which consist of a much thicker particle wall thickness. Char D_{PC} showed mixed porous and inertoid particles.

The particle morphology showed some correlation with conversion degree using the MIRI-plant. Coal B_{PC} which had the highest conversion degree showed the most porous char structure. Coal C_{PC} which was associated with a low coal conversion degree showed less porous particle as well as particles which seemed to have undergone no reaction.

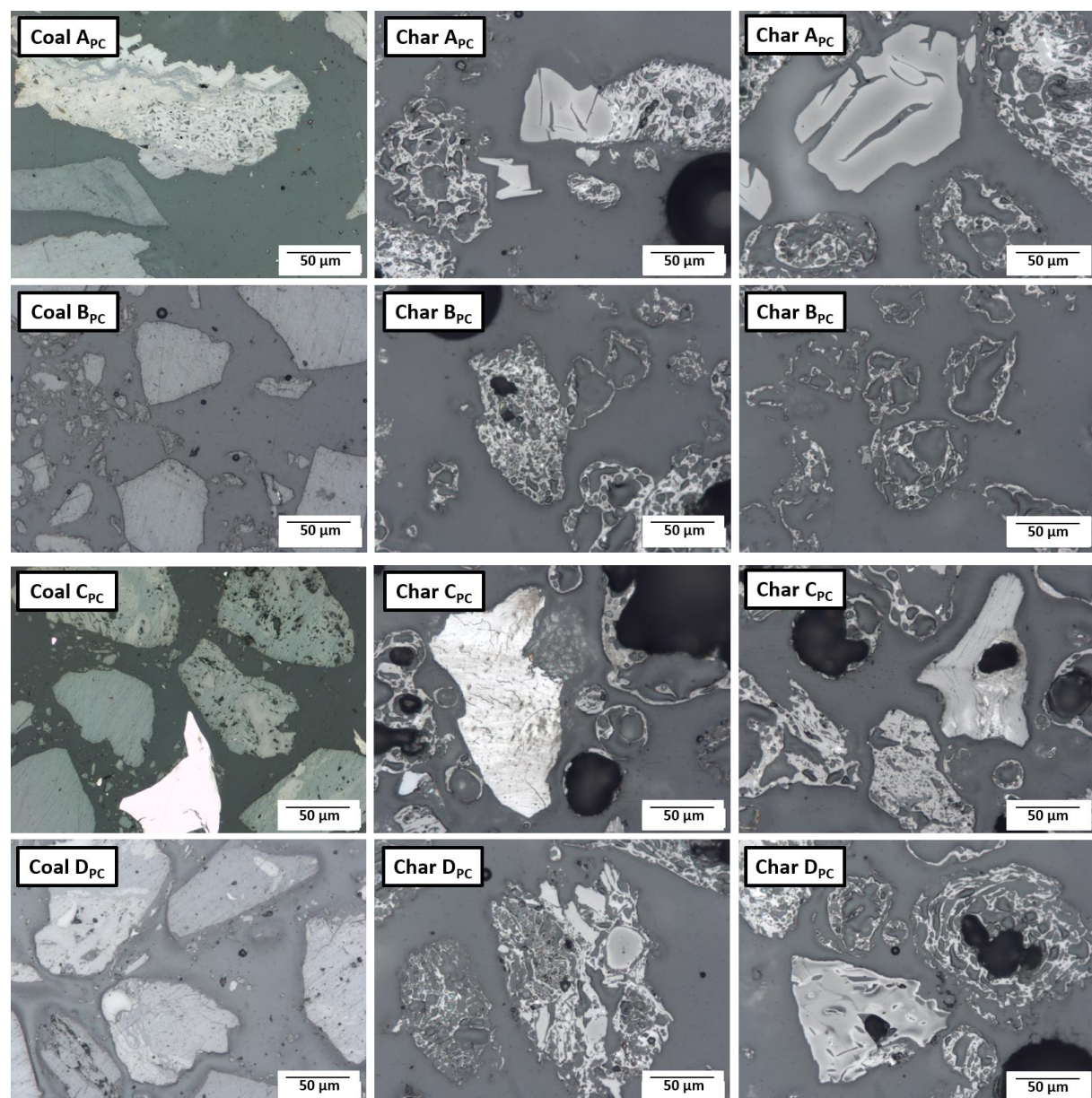


Figure 3.38: Comparison of LOM images of coal and char in PC size fraction (x500)

In addition to the LOM images, SEM analysis of the coal and char were conducted. **Figure 3.39** shows SEM images of coal and char particle in PC form with a magnification of 1000x. SEM-analysis

investigates the surface structure of coal and char particles whereas the LOM analysis examines the cross-section of selected samples.

Coal investigated using SEM method showed only small differences regarding surface structure. However coal A showed a slightly different surface texture. A rather scale like structure could be observed whereas the other coals showed a rather fissured surface.

The surface of char A_{PC} and B_{PC} also showed a porous structure. Char C_{PC} and D_{PC} presented a rather smooth surface. Pores identified in Char A_{PC} were rather small compared to the other coal. However there seemed to be a huge amount of pores which were connected generating a complex pore network. Char B_{PC} presented pores which were much bigger in size. Furthermore the shape of the pores was rather fissured. This indicated a rather fast generation of gas during devolatilisation. Since bigger amount of gas was being generated inside the particle, pressure rose resulting in a forced gas release and therefore fissured pores.

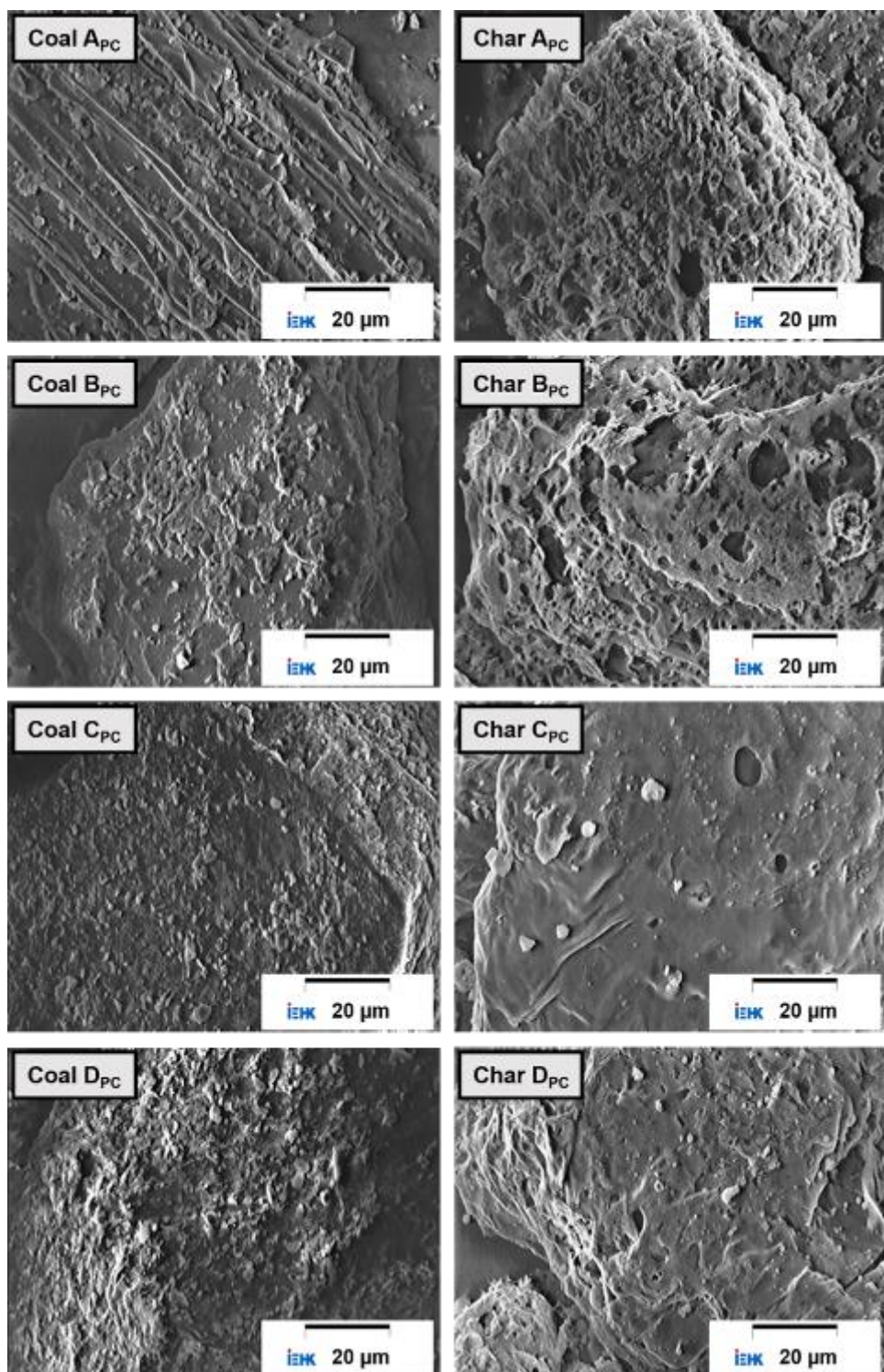


Figure 3.39: Comparison of SEM images of coal and char in PC size fraction (x1000)

Furthermore, the microstructure of char B_{GC} , C_{GC} and D_{GC} was analyzed and compared to the coal particles. The char generated from the GC particles, shown in **Figure 3.40**, due to the wider particle size distribution were much more inhomogeneous compared to char produced with the PC size fraction using the MIRI plant.

As already mentioned, coal B_{GC} had a rather homogenous appearance, whereas coal C_{GC} and D_{GC} consisted of inhomogeneous organic compounds. Greater Char B_{GC} particles showed solid as well as tenuinetwork structures. Smaller Char B_{GC} particles showed a tenuispheric morphology. Char particles from Char C_{GC} showed a unique mesosphere structure. Partly tenuinetworks were identified. Smaller particles mostly consisted of crassispheric and tenuispheric structures. Bigger particles belonging to Char D_{GC} showed a mixed porous as well as mesospheric structure.

Compared to PC_{Char} , GC_{Char} had more complex structure due to its size. However GC_{Char} also presented more unreacted particles.

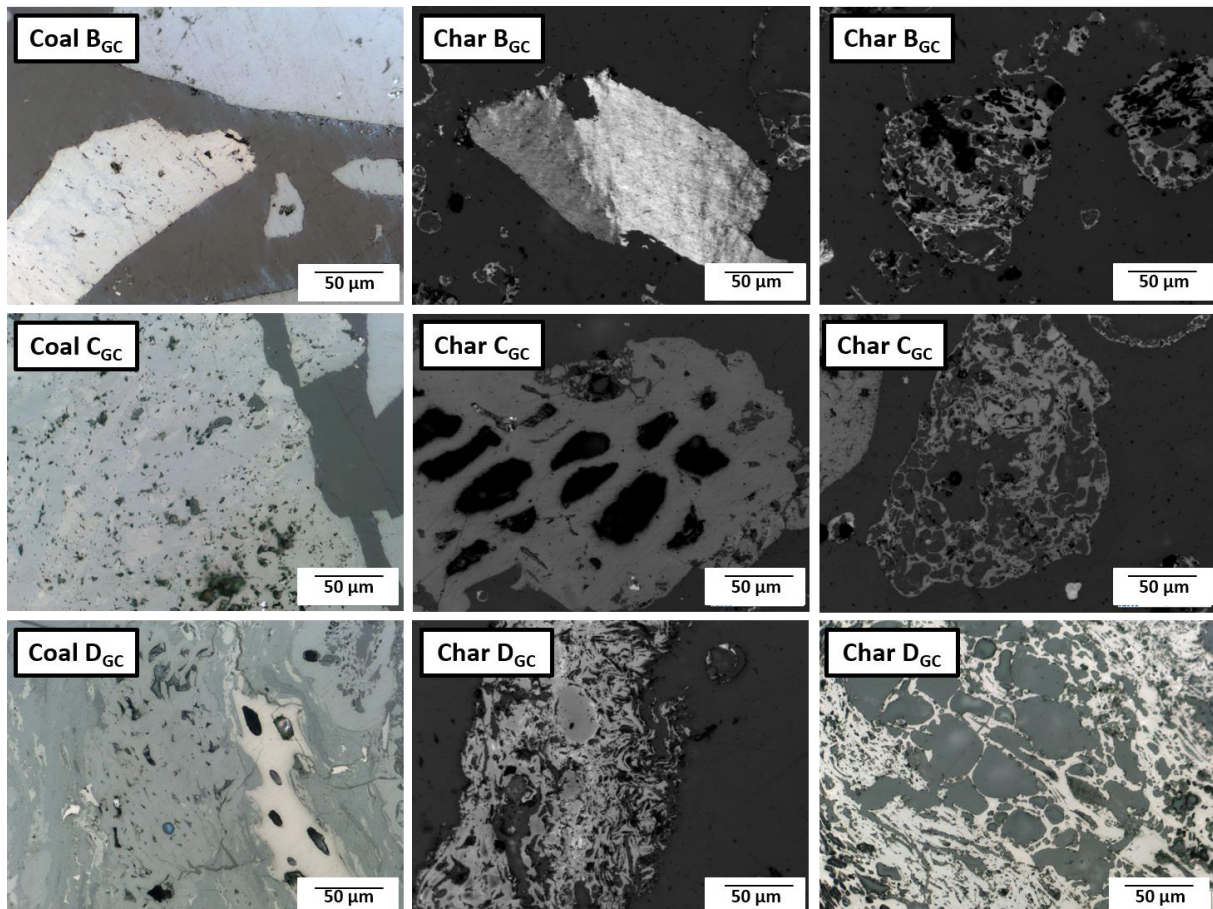


Figure 3.40: Comparison of LOM images of coal and char in GC size fraction (x500)

Regarding the surface, texture char C_{GC} showed a similar smooth surface as in PC form. Char B_{GC} presented a much less porous particle structure as shown in **Figure 3.41**.

The phenomenon of the inhomogeneous char was caused by the wide distribution of the grain size fraction of the granular coal. Based on conversion trials and microstructure analysis of residual char, following conclusion might be taken. Coal in PC form showed a higher conversion degree compared to coal in GC form under the conditions of the oxygen zone of the raceway. PC-char showed a highly porous structure due to high coal conversion degree. GC-char was much more inhomogeneous. Char structure with a porous structure appeared. However a greater amount of unreacted/partly porous particles were identified. These particle usually appeared in a bigger particle size compared to the highly porous particle of GC-char. Smaller particles reacted before bigger particles which led to the appearance of mixed char structures.

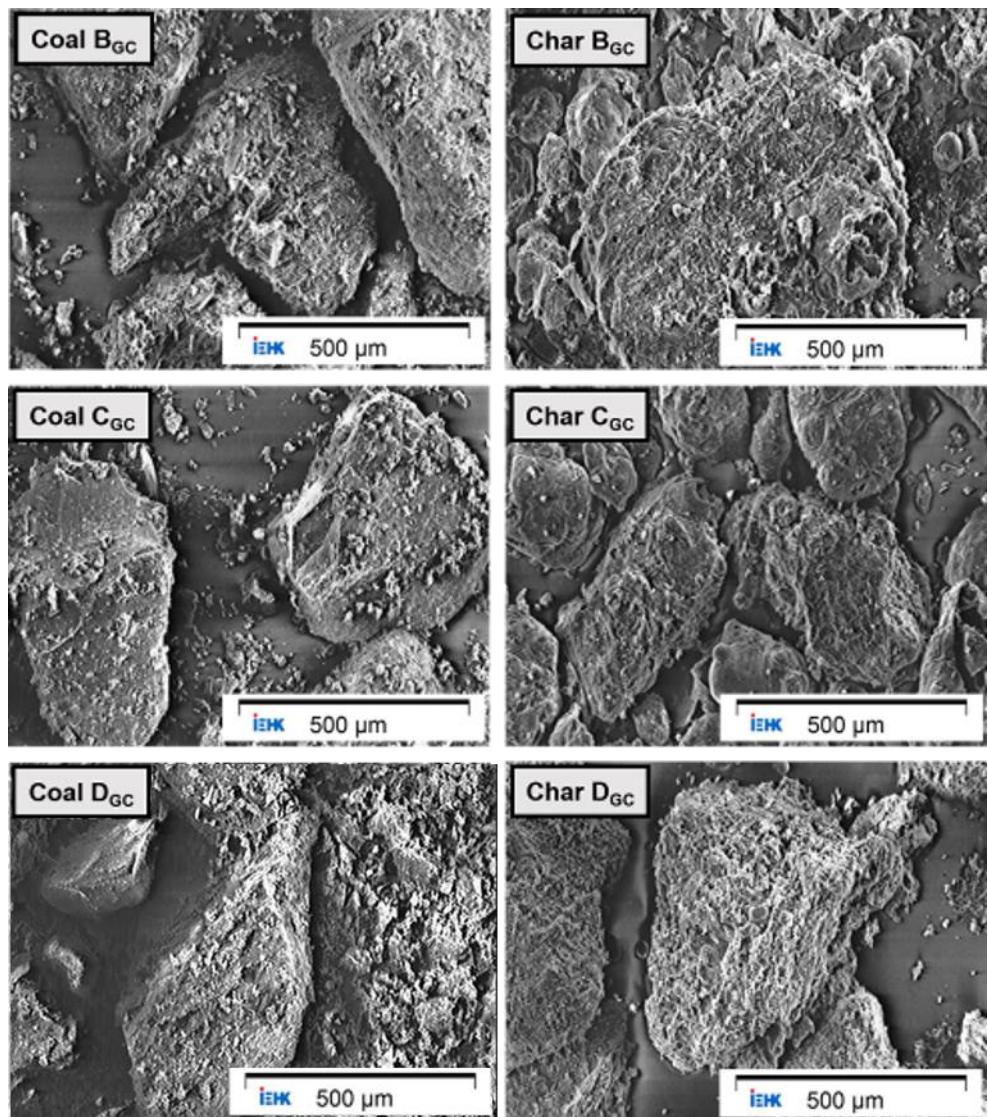


Figure 3.41: Comparison of SEM images of coal and char in GC size fraction (x1000)

3.2.4.2 INVESTIGATION OF CHAR PRODUCED IN TASK 1.2

Char, which was produced at different atmospheric conditions using the MIRI plant, amounted up to 50 g depending on conversion degree.

The microstructure of char was compared to that of coal using LOM-analysis as well as SEM analysis. The results of the analysis were partly presented in Task 1.2.

Different char structures were analysed using LOM-analysis. **Figure 3.42** shows different structure types found in char from Task 1.2. Increased numbers of Inertoid/solid structure were found in GC-char, whereas Tenuisphere/Cenosphere were the dominant char structures in PC-chars. Tenuinetwork/Network as well as Mesosphere/Network could be found in either chars. Thus higher conversion degrees may lead to an accumulation of strong porous structures (Mesosphere/Cenosphere). Larger coal particle showed either Inertoid/solid or Tenuinetwork/Network structures. Due to their large particle size, devolatilisation process was decelerated. Consequently only small parts of volatile matter could be removed leading to these char structures.

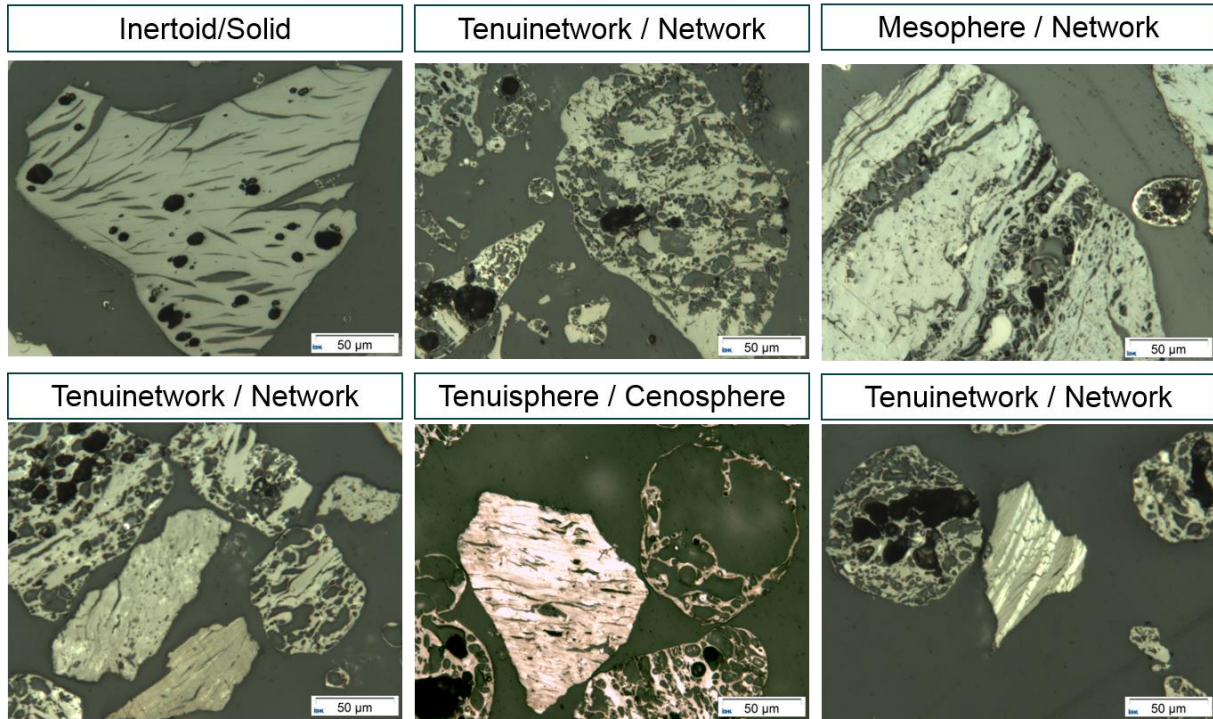


Figure 3.42: Char structure identified from Task 1.2

Using analysis software, the porosity of some chars were determined as shown in **Figure 3.43**. Tenuisphere/Cenosphere structure show an immense porosity (>75 %) whereas Tenuinetwork/Network contain a porosity >35 %. Inertoid/solid char structure varies from their original porosity up to 30 %.

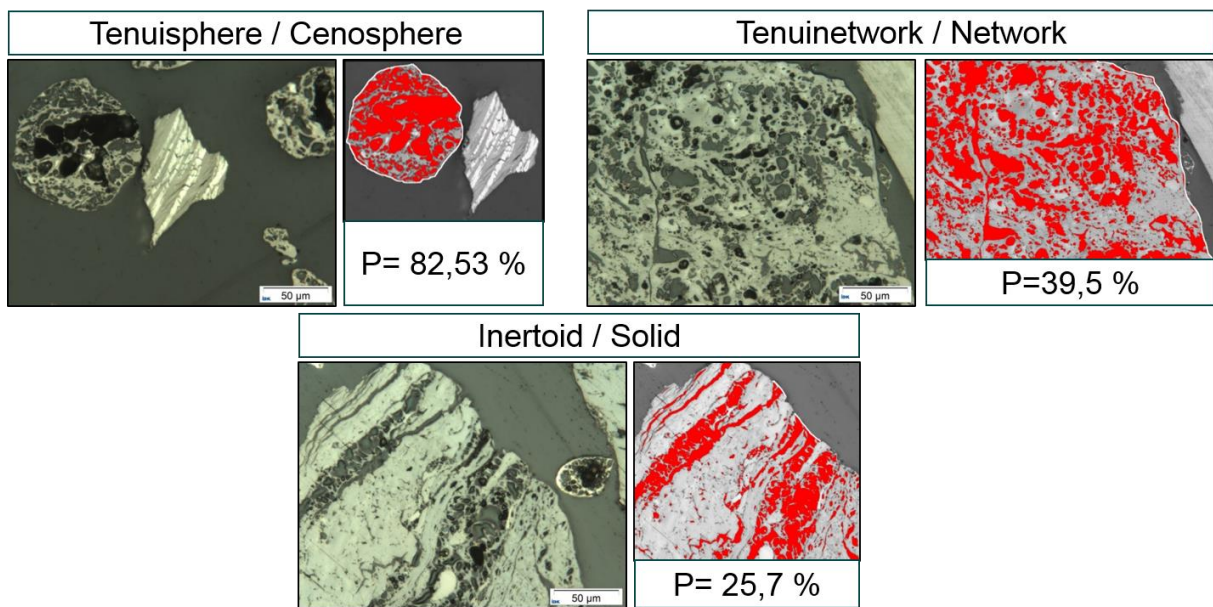


Figure 3.43: Porosity of various char types

3.2.4.3 INVESTIGATION OF CHAR PRODUCED IN TASK 1.3

In the Tammann furnace DT-Setup was produced about 500 g Char per trial. The conditions for the Char production were explained detailed in Task 1.3. Following coals samples were used based on the results of preliminary trials: B_{PC} , C_{PC} , C_{GC} . Different characteristics of the synthetic char were investigated. For each coal type, two synthetic chars were produced resulting in six different chars.

Chemical properties

Chars were chemically analyzed by immediate and elementary analyses. The result of the chemical analysis are presented in **Table 3.19**. The immediate analysis revealed a significant change of

volatile and ash content of char and coals. With increasing reaction temperature, more volatile matter was being removed from the coal. Ash content however changed at a much smaller rate compared to volatile. The change of ash from char_{900} to char_{1300} showed some inconsistency. The lower ash content could be explained based on the char formation using the Tammann furnace. Ash which was bounded inside coals was being released during devolatilisation. Particle size of these ash particles was so small that it could not be contained in the collector. Absolute volatile yield of coal B_{PC} and C_{PC} were very similar. However coal showed a much higher relative volatile yield. Coal C_{GC} showed significant lower removal rate of volatile matter caused by its greater average particle size.

Table 3.19: Chemical analysis of synthetic char produced by Tammann furnace DT setup

	B_{PC}	$B_{\text{PC}900}$	$B_{\text{PC}1300}$	C_{PC}	$C_{\text{PC}900}$	$C_{\text{PC}1300}$	C_{GC}	$C_{\text{GC}900}$	$C_{\text{GC}1300}$
Humidity	0.4	0.0	0.0	1.0	0.0	0.0	1.0	0.0	0.0
V.M.	17.2	11.8	6.6	13.8	8.9	3.2	13.8	9.8	5.8
Ash	4.5	5.4	6.0	7.6	9.8	8.8	7.6	9.9	12.3
C_{fix}	77.9	82.8	87.4	77.6	81.3	88	77.6	80.3	81.9
C	84.6	83.1	84.6	80.2	81.5	84.2	80.2	78.0	74.0
H	4.5	3.3	2.0	4.0	2.1	0.8	4.0	2.7	1.9
N	1.2	1.3	1.2	1.5	1.6	1.6	1.5	1.5	1.5

Elemental analysis of char showed only minimal change regarding nitrogen content. However hydrogen content decreased significantly in correlation with volatile yield. Elementary carbon analysis showed no clear trend.

Physical properties

Particle size distribution of char in comparison with its parent coals is displayed **Figure 3.44**. The particle size distribution from coal differentiated significantly from those of char. Char particle size distribution showed almost identical particle size distribution.

As seen in **Figure 3.44**, the particle size distribution of char clearly differed from that of coal. An increase of particles smaller 125 μm was identified. However also the maximum particle size increased. This phenomenon might be caused by swelling of coal particle during the heating process. Coal and char from B_{PC} showed a similar trend. Char generated from granular coal showed a different size distribution compared to pulvressed coal. Overall small particles fraction decreased. Consequently average particle size increased.

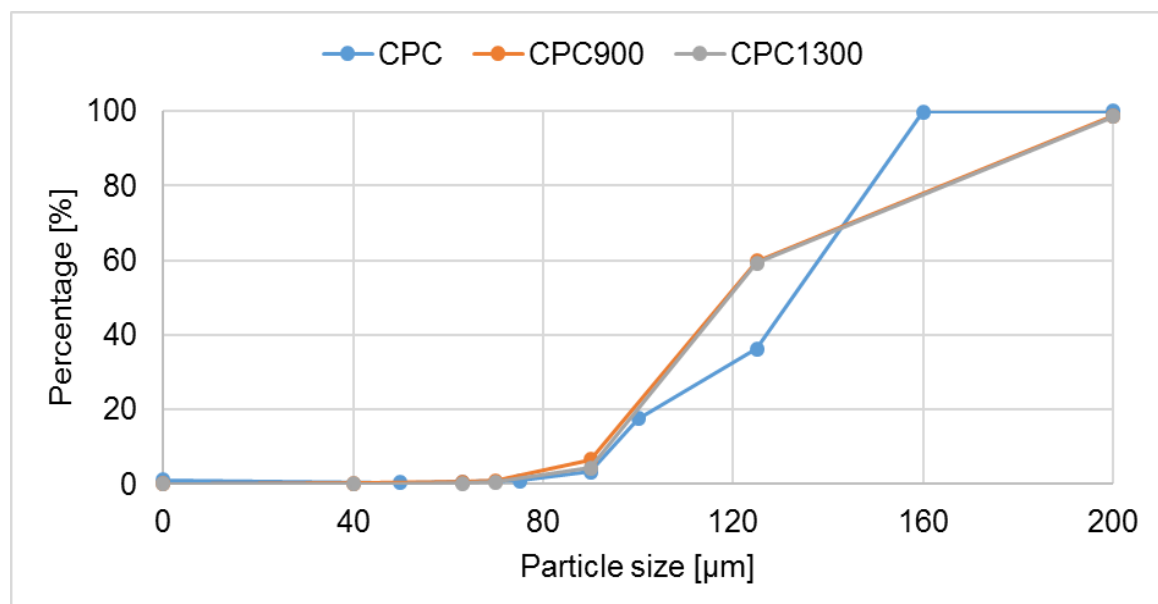


Figure 3.44: Particle size distribution of Char C_{PC} with its parent coal

Further physical properties were analysed. Specific surface area was determined using BET analysis

based on nitrogen absorption. Additionally bulk density of coal and char was compared. Results are shown in **Table 3.20**.

Table 3.20: Results of physical properties of coal and char

Sample	Scenario	Particle size 50 %, d_{50} [μm]	Bulk density [g/cm^3]	Spec. surface area [m^2/g]
Coal B _{PC}	-	139	0.76	2.3
Char B _{PC}	1 (900°C)	124	0.22	24.2
	2 (1300 °C)	122	0.28	28.2
Coal C _{PC}	-	121	0.65	4.2
Char C _{PC}	1 (900°C)	119	0.36	25.6
	2 (1300 °C)	119	0.38	32.3
Coal C _{GC}	-	209	0.73	2.6
Char C _{GC}	1 (900°C)	310	0.53	52.5
	2 (1300 °C)	298	0.44	75.7

Results showed a significant change of physical properties when coal transformed into char. However the synthetic char did not differ from each other significantly. The change of specific surface area changed from coal to char between factors of 5 to 20. Compared to this change, the increase at a reaction temperature from 900 °C to 1300 °C was visible but only minor. This trend was also observed in the bulk density as well as average particle size.

Kinetic properties and char conversion

For determination of kinetic properties of coal and its respective char, a Tammann furnace setup and a thermo-balance was used.

The Tammann furnace AE setup shown in **Figure 3.45** was used to determine the activation energy. In order to calculate the activation energy, the reaction constant was determined at isothermal condition.

Around 1 g of char was added into a crucible. Samples were treated under isothermal condition of 800, 1000 and 1200 °C at atmospheric conditions. The mass loss was recorded over time.

- 1) Gasmixing
- 2) Temperature measurement
- 3) Electric Balance
- 4) Computer
- 5) Transformator
- 6) Graphite pipe
- 7) Crucible
- 8) Alumina pipe
- 9) Alumina plate
- 10)Alumina spheres
- 11)Bottom ceramic

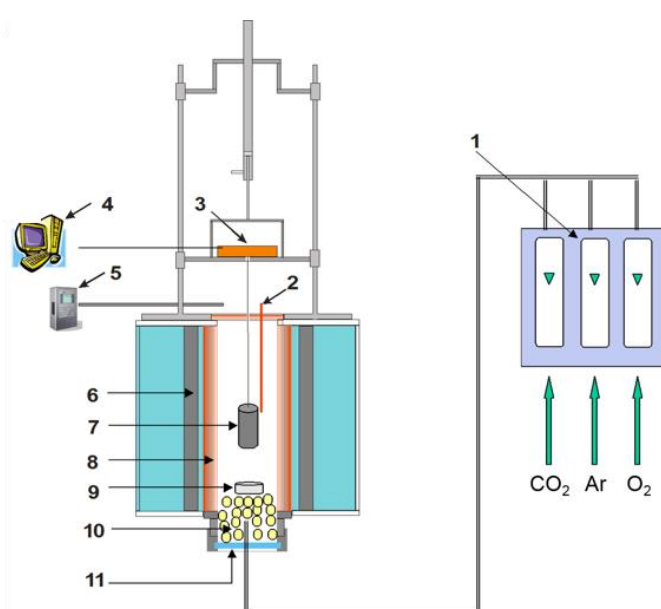


Figure 3.45: Tammann furnace AE setup

Based on Arrhenius equation activation energy could be calculated. Results are displayed in **Table**

3.21. Trials regarding the activation energy were conducted under atmospheric conditions.

All chars showed a lower activation energy compared to their parent coal. This might be caused by the significant increase of specific surface area. This increase of reaction surface area could compensate the absence of volatile matter.

Table 3.21: Kinetic reaction values

	B _{PC}	B _{PC900}	B _{PC1300}	C _{PC}	C _{PC900}	C _{PC1300}	C _{GC}	C _{GC900}	C _{GC1300}
E _A (kj/mol)	36.30	20.51	31.15	43.82	35.67	38.18	50.00	43.93	37.15

However for Char_{PC} a reaction temperature of 900 °C resulted in a lower activation energy compared to a reaction temperature of 1300 °C. However the activation energy of char generated from granular coal decreased with increasing reaction temperature.

Based on obtained results, it was determined that a significant increase of reaction surface can substitute the absence of volatile matter. The decrease in activation energy from coal to Char 900°C could be caused by the immense increase of specific surface area. However when reaction temperature increased to 1300°C, increase of specific surface area cannot substitute the absence of even more volatile matter. Consequently the activation energy increased. For granular coal, the increase of the specific surface area was greater even from 900°C to 1300°C reaction temperature. Furthermore the volatile yield was lower due to the greater particle size.

Consequently a significant influence of volatile matter and specific surface area on the activation energy could be identified, which may be described by following relation:

$$a \cdot x_1 - (-(x_2)^b + (x_2)) + c = P$$

P: activation energy

x₁: volatile matter [Mass.-%]

x₂: specific surface area [m²/g]

a,b,c: constants (with b<1)

In order to determine further kinetic values and char conversion behaviour, thermogravimetric analysis using thermo-balance equipment was conducted. A STA facility from SETSYS evolution was used. **Table 3.22** presents the scenario used in these trials. Under inert atmosphere the sample was heated until the reaction temperature was reached. During the heating process, volatile matter was removed from coal/char. The temperature was held to remove all volatile matter. Then a reaction gas was injected for 90 min. After that the sample was cooled under inert atmospheric condition. Reaction gases used were air, CO₂ and a mixture of CO, CO₂, and N₂.

Table 3.22: TGA-scenario for determining char conversion

Scenario	Duration	Atmosphere	Flow rate
Heating	190 min	Ar	20 ml/min
Homogenize	90 min	Ar	20 ml/min
Conversion	90 min	Air or CO ₂ or CO/CO ₂ /N ₂	20 ml/min
Cooling	90 min	Ar	20 ml/min

Based on the mass loss at the beginning of the injection of the reaction gas, the reactivity of coal and char were calculated.

$$R = \frac{dw}{dt}$$

The results of the TGA trials are presented in **Table 3.23**. All char samples showed a higher reactivity compared to its parent coal. However increase of reactivity differed from coal type. B_{PC} showed an increased reactivity with increasing reaction temperature. C_{PC} and C_{GC} showed a much lower reactivity.

Table 3.23: TGA-results of coal and char under various atmospheric conditions [%min⁻¹]

	B _{PC}	B _{PC900}	B _{PC1300}	C _{PC}	C _{PC900}	C _{PC1300}	C _{GC}	C _{GC900}	C _{GC1300}
Air	2.00	2.30	2.60	2.60	2.50	2.70	2.10	2.40	2.50
CO ₂	1.60	3.49	4.80	1.52	1.98	2.54	1.79	3.23	2.63
CO/CO ₂ /N ₂	0.32	0.71	0.67	0.35	0.54	0.54	0.4	0.58	0.49

The results showed that char consumption by CO₂ was faster than coal. With increasing CO₂ content the char reactivity increases significantly. Consequently gasification of char with CO₂ is possible. On microlevel CO₂ which is generated during reduction could locally be converted to CO and increase gas diffusion.

3.2.4.4 KINETICS OF CHAR GASIFICATION IN TGA

Char samples produced at CANMET were afterwards gasified in AMMR TGA. The objective was to check whether the O/C ratio used for coal conversion had an influence on the subsequent gasification of the char or not.

The conditions used for the TGA tests are presented in **Table 3.24**. A char sample of 20-30 mg was used for the test.

Table 3.24: Conditions of the trials at the Thermo Gravimetric Analyser (TGA)

Step		Initial Temperature (°C)	Final Temperature (°C)	Heating rate (°C/mn)	Duration (mn)	Atmosphere (gaz type)
Drying	1	25	110	5	17	Argon
	2	110	110	0	15	Argon
Pyrolysis	3	110	950	30	28	Argon
	4	950	950	0	40	Argon
Gasification	5	950	950	0	50	CO ₂
	6	950	25	30	31	CO ₂
Cooling	7	25	25	0	60	Argon

A typical gasification curve is presented in **Figure 3.46**. It shows three main steps:

- the departure of the residual moisture of the sample at 110 °C;
- the emission of the residual volatile matter of the coal, starting at ~500 °C during the heating phase under argon atmosphere; this step is almost completed during the plateau period under argon at 950 °C;
- the gasification of the char under CO₂ atmosphere. This phase stops after 150 min of trial, when the temperature is again decreased under argon atmosphere.

As could be noticed, the slope of the curve was quite linear for the gasification part if the start-up and end phase of the gasification were not taken into account. This part of the curve was then used for the calculation of the gasification rate.

The measured gasification rates are presented in **Figure 3.47**. As can be seen, the O/C ratio has little influence, as the gasification rates remain between 0.29 and 0.39 %/min.

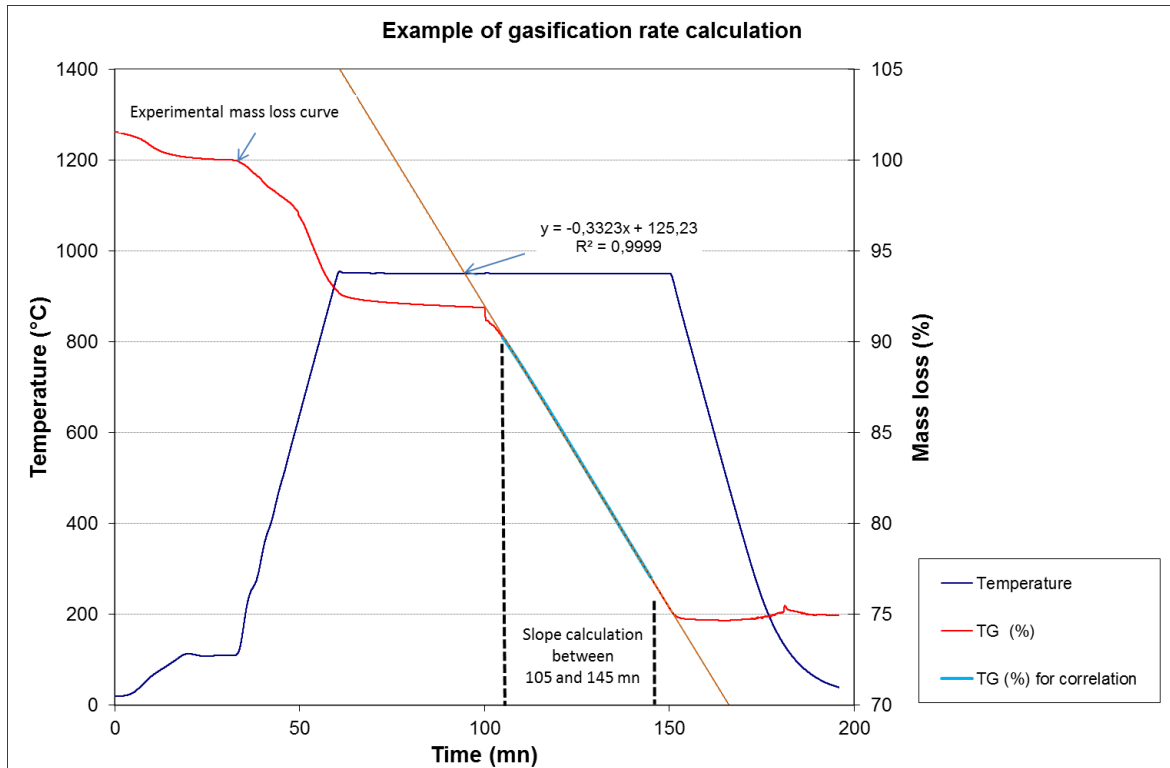


Figure 3.46: Typical TGA gasification curve and gasification rate determination

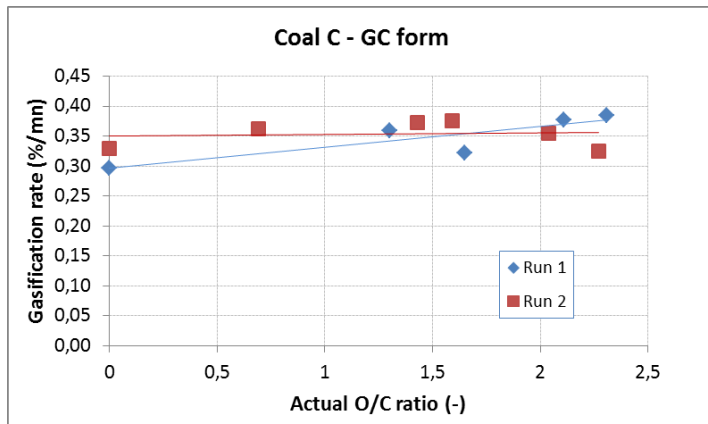


Figure 3.47: Independence of char gasification rate on the O/C ratio

3.2.4.5 CONCLUSIONS OF CHARACTERISATION OF CHAR

Synthetic char produced in task 1.1 - 1.3 was analysed by different means.

Chemical properties had a high correlation with reaction temperature as well as O/C atomic ratio. Volatile matter decreased with increasing reaction temperature (Tammann furnace DT) as well as increasing O/C ratio(CANMET).

It was observed that physical properties changed significantly from coal to char. However the physical properties of char did not differ much by increasing reaction temperature as well as O/C atomic ratios. Furthermore particle size showed only small changes whereas bulk density increased significantly. Consequently it could be assumed that after devolatilisation, a char skeleton was left behind which was highly porous. This could be confirmed by microscopic analysis taken by SEM and LOM.

Investigation of char kinetic properties using the Tammann furnace AE setup to determine the activation energy showed a strong influence of volatile matter and specific surface area on coal/char activation energy. Results showed that an high increase of specific surface area could compensate the absence of volatile matter. TG analyses revealed that char reactivity under various

atmospheric conditions was comparable to coal reactivity and showed only small changes.

Based on results of coal conversion and char characterisation, a rough estimation regarding the char volume entering the raceway was calculated (**Table 3.25**). Based on the results it could be assumed that although coal B had a significantly higher conversion behaviour in the raceway, the same volume of char particle was leaving the raceway. For granular coal, even less volume of char is entering the furnace.

Table 3.25: Calculated char volumes leaving the raceway

	Conversion degree [%]	Char entering the raceway [kg char/100 kg coal]	Bulk density [kg/m ³] [900/1300°C reaction temperature]	Char entering the raceway [m ³] [900/1300°C reaction temperature]
B _{PC}	52.3	47.7	220/280	0.22/0.17
C _{PC}	22.4	77.6	360/380	0.22/0.20
C _{GC}	12.6	87.4	530/440	0.16/0.20

3.2.5 TASK 1.5 CHAR INTERACTION WITH COKE

In order to examine the interaction of char with coke, the Tammann furnace AE setup introduced in Task 1.4 was used (**Figure 3.45**).

Coke cylinder with a diameter of 0.8 cm and 1 cm were produced based on realistic coke samples. These coke samples were covered with char. 10 % of char were added to each coke sample. Coke degradation under atmospheric conditions was analysed at different isothermal conditions.

Table 3.26: Analysis of coke

	Humidity	V.M.	Ash	C _{Fix}	CSR	CRI
Coke	6.92	0.47	10.73	81.88	62.7	26.7

Based on the data the activation energy was determined. Results are displayed in **Table 3.27**. A significant reduction in activation energy was observed. Especially the addition of char C_{PC900} showed an increased reduction in the activation energy.

Table 3.27: Activation energy of coke and coke with char

	Coke	B _{PC900}	B _{PC1300}	C _{PC900}	C _{PC1300}	C _{GC900}	C _{GC1300}
E _A (kJ/mol)	102.986	62.870	51.297	52.334	50.167	60.164	53.128

3.2.5.1 CONCLUSION OF CHAR/COKE INTERACTION

Results showed that activation energy of coke in the presence of char significantly decreased. Thus the starting reaction temperature of coke was shifted to lower temperature. Consequently coke strength might be weakened since the conversion process of coke was shifted to an earlier stage. This especially might influence the shape of the coke windows in the cohesive zone as well the stability of the dead man.

Based on these trials, coke/char could be seen as one component or char and coke reaction has to be observed separately. Further investigation could give more detailed information about what kind of mechanisms influence the reaction.

3.2.6 TASK 1.6 STUDY ON CHAR IMPACT ON THE COKE SURFACE USING THE PILOT PLANT COBESI

Three coal types were investigated using the pilot plant COBESI.

For these trials, the pilot plant was revamped and modified. Since multiple trials with various instrumentation were planned to be conducted, it was decided to renew the lining of the COBESI to minimize external sources of error to the measurement.

The lining of the COBESI was renewed. First the COBESI had to be dismantled. After that, the old refractory material had to be removed. Then, the COBESI was reassembled and lined with new refractory material.

The new lining was finished and an exhaust hood was built. High temperature development due to coal injection made it necessary to install a new exhaust hood. The off gas temperature must not exceed 150°C when entering the exhaust system of the laboratory hall. The diameter of the pipes was expanded. Stainless less pipes as well as a high temperature tube were used. Through this modification, the trial period could be prolonged.

Tata Steel provided RWTH Aachen with approximately 2,000 kg of coke (40 – 60 mm).

The scenarios used for COBESI trials are displayed in **Table 3.28**. After coke was charged, the COBESI was closed and heated up until 200 °C. This temperature was held for 3 hours to remove the moisture. Afterwards the temperature and gas flow rate was increased up to 600 °C and 650 Nm³/h to ignite the coke. When coke ignites, trial parameters were set and coal is injected.

Table 3.28: COBESI trial scenario

Phase	Duration	Blast temperature	Flow rate
Drying	180 min	200 °C	400 nm ³ /h
Heating	Approx. 120 min	600 °C	650 nm ³ /h
Trial		500 °C	400 nm ³ /h
Injection of coal approx. 20 kg/h for 30 min			
Cooling	Approx. 180 min	100 °C	400 nm ³ /h

During this trial, the different measurements were scheduled as described in **Figure 3.48**.

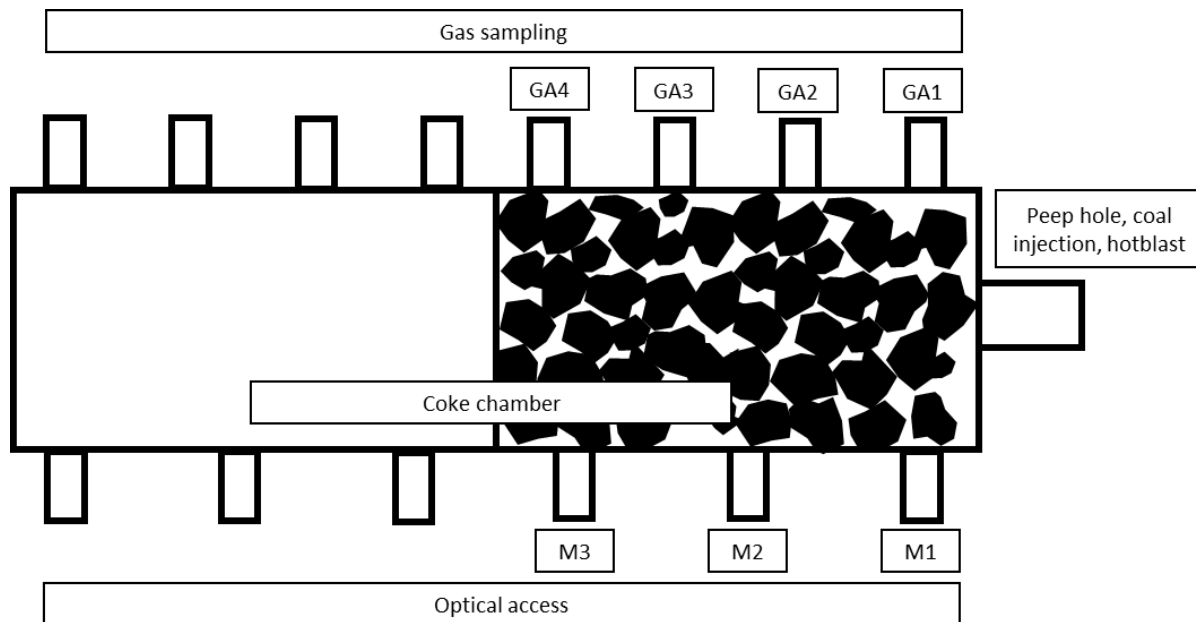


Figure 3.48 : COBESI scheme

Figure 3.49 shows the gas composition and the temperature at different measuring points. At M2

measuring point the maximum temperature was detected. An immediate drop in oxygen content was observed. With increasing distance, the oxygen content decreased. CO₂ increased until GA2 measuring point while CO does not rise until GA3.

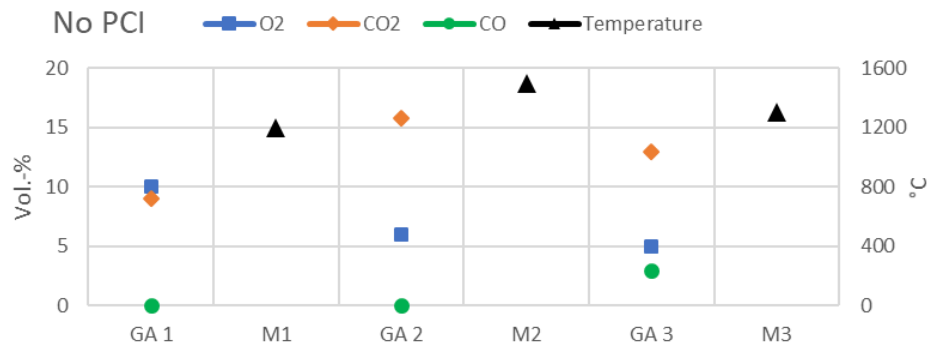


Figure 3.49: Temperature profile and gas composition at different positions during COBESI trial without coal injection

During injection of coal C_{PC} shown in **Figure 3.50** temperature as well as gas composition changed. The maximum temperature decreased. An increase of CO₂ was measured. CO was detected already at the first measuring point and increased steadily. Oxygen content was much lower compared to no coal injection scenario.

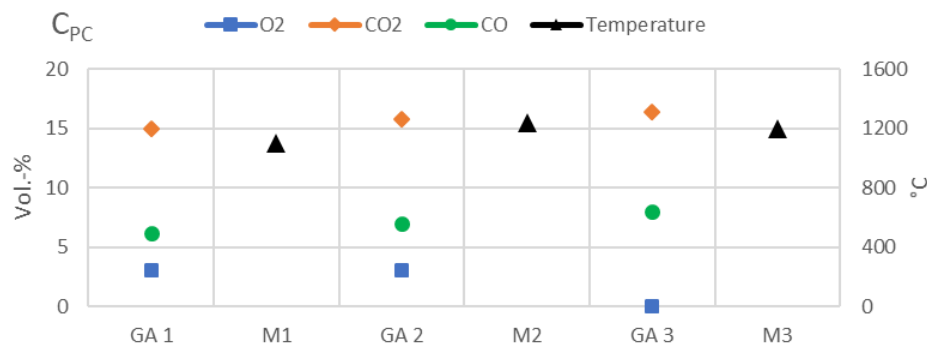


Figure 3.50: Temperature profile and gas composition at different positions during COBESI trial with injection of coal C_{PC}

When injecting coal C in granular form similar behaviour was detected. As displayed in **Figure 3.51**, temperature profile was slightly higher compared to PC-injection. CO₂ content showed no significant change whereas less CO gas was generated. The oxygen content however decreased much quicker.

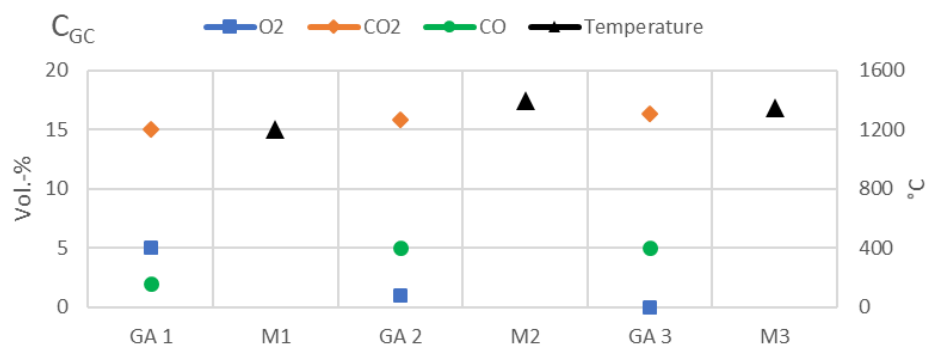


Figure 3.51: Temperature profile and gas composition at different positions during COBESI trial with injection of coal C_{Gc}

Gas composition and temperature measurements by the injection of B_{PC} are shown in **Figure 3.52**. Similar to the injection of C_{Gc} oxygen content depleted quickly. CO content however rose very fast up to 12 %.

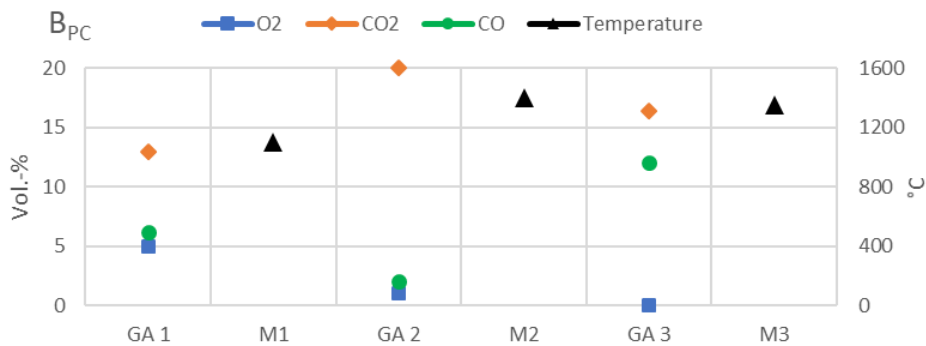


Figure 3.52: Temperature profile and gas composition at different positions during COBESI trial with injection of coal B_{PC}

With the injection of coal, the shift of gas composition was detected. Oxygen levels depleted almost completely at the last measurement point GA3. High increase of CO_2 and CO was observed. The injection of granular coal differs from the injection of pulverised coal. Oxygen content decreased slightly slower with the injection of granular coal compared to pulverised coal. Also lesser amount of CO was generated. This behaviour could be confirmed by the trials conducted with the MIRI plant. However the behaviour of granular coal of COBESI pilot plant did not appear as significant.

Figure 3.53 - Figure 3.55 present the results of the TVC as well as the pyrometer. Temperature development at different regions of interests was measured during injection of coal. However descending coke and its degradation highly influenced the temperature measured by the pyrometer as well as TVC. Only injection of coal C_{PC} showed a significant change of temperature.

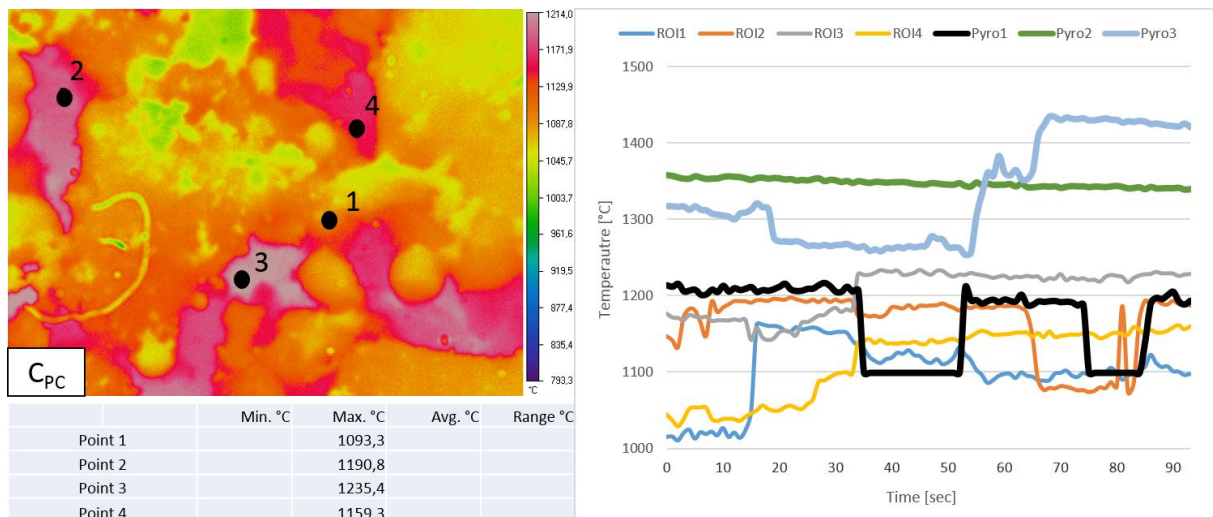


Figure 3.53: TVC image during injection of coal C_{PC}

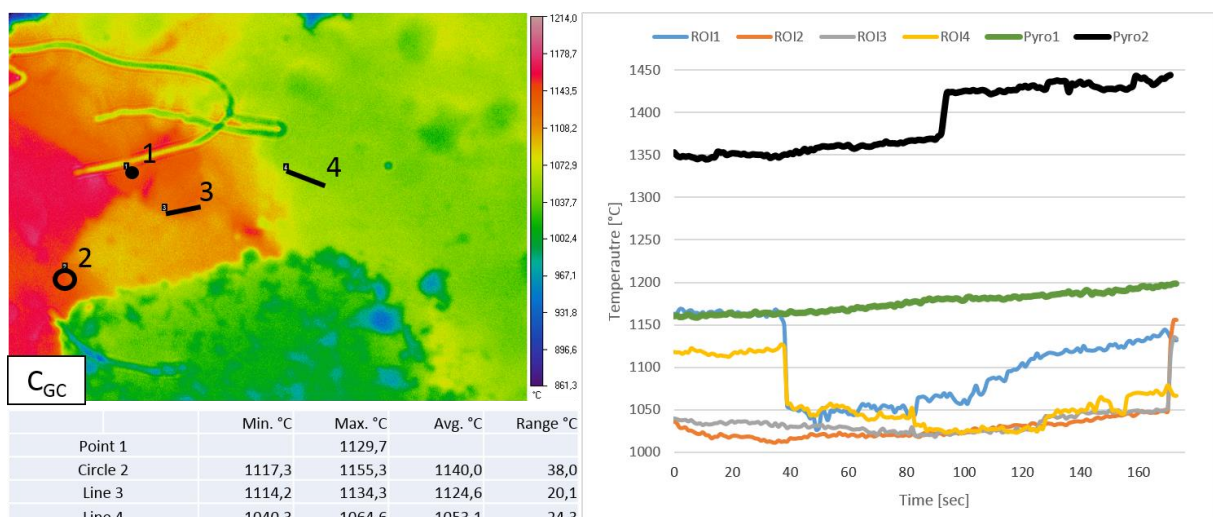


Figure 3.54: TVC image during injection of coal C_{GC}

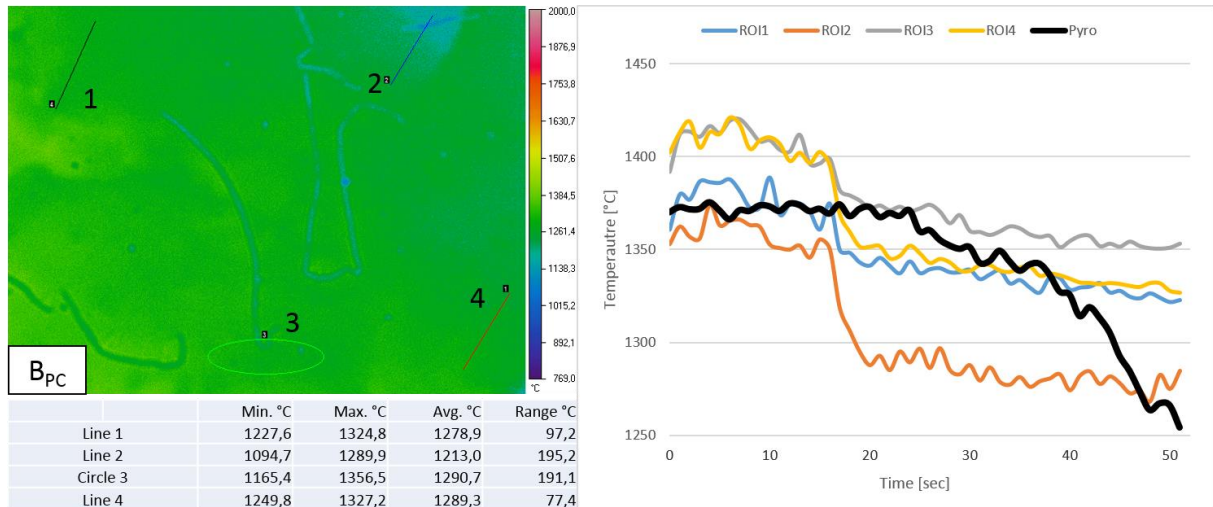


Figure 3.55: TVC image during injection of coal B_{PC}

The coke which remained after cooling the COBESI was collected at different positions and microscopically analysed as shown in **Figure 3.56**. Samples were taken from four positions (Seg 1 – Seg4). Seg1 resembles a sample taken close to the coal injection point whereas Seg4 is taken from a position at the longest distance to the injection point.

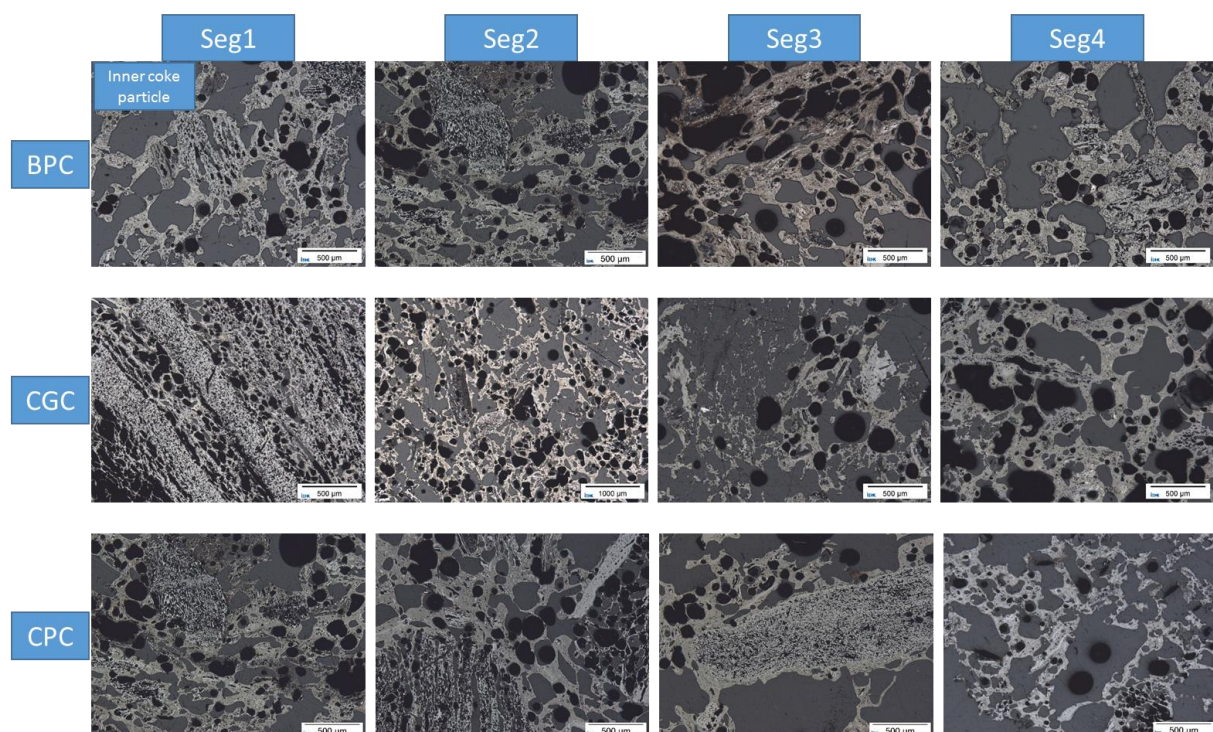


Figure 3.56: LOM images of coke sample sampled after COBESI trials

No significant influence of char on coke surface using LOM could be identified.

3.2.6.1 CONCLUSION OF STUDY ON CHAR IMPACT ON THE COKE SURFACE USING THE PILOT PLANT COBESI

Results show significant influence of coal type and particle size distribution on the coke temperature. Furthermore slight changes in gas composition could be detected. Especially coal B showed higher CO content during trials. However no significant influence of char on the coke surface could be detected using current measurement techniques. Thermal vision camera measurements need higher resolution be able to identify char as well as char/coke interaction. Investigation after the trial showed no clear evidence of char impact on coke surface.

3.2.7 TASK 1.7 CHAR INTERACTION WITH FERROUS BURDEN AND DRAINAGE IN THE DRIPPING ZONE

The influence of char on the reduction behavior of pellets was investigated using the Tammann furnace AE setup. Pellets were covered with char and reduced at a temperature of 1050 °C in the atmosphere 30 Vol.-% CO and 70 vol.-% Ar. 5 l/min was injected into the reaction chamber.

The chemical composition of pellets is displayed in **Table 3.29**. Pellet diameters varied from 1 to 1.5 cm. Its weight varied from 3 to 5 g per pellet. Char varied between 1.0 and 1.5 %.

Table 3.29: Chemical composition of pellets wt.-%

Total Fe	FeO	CaO	MgO	SiO ₂	Al ₂ O ₃	TiO ₂	MnO	P ₂ O ₅	LOI	B ₂	Total slag
65.14	0.57	1.42	0.55	4.22	0.39	0.04	0.17	0.02	0.02	0.34	6.62

For reduction, trials were exposed for 1 h. The reduction degree was calculated based on mass loss. It was assumed that mass loss was caused by removal of oxygen from Fe₂O₃.

$$\eta_{Red} = \frac{100 - m}{m_0}$$

η_{Red} =Reduction degree

m = Mass after reaction

m_0 = Total mass of oxygen in pellet

Table 3.30 shows results of trials regarding the influence of char on the reduction behavior. Significant increase of reduction degree was detected for char covered pellets. Except for char B_{PC900}, all pellets covered with char showed a reduction degree above 80 %.

Table 3.30: Reduction degree of pellets and pellets covered with char

Char type added to pellet	none	B _{PC900}	B _{PC1300}	C _{PC900}	C _{PC1300}	C _{GC900}	C _{GC1300}
Reduction degree [%]	48.0	69.5	81.5	94.0	89.0	83.0	91.5

The increase of reduction degree of pellets with the presence of char may be caused by Boudouard reaction. CO₂ which is produced during reduction of hematite could be transformed to CO due to Boudouard reaction. Since temperature was above 1000 °C ,CO₂ was almost immediately reduced to CO. Consequently reduction of pellets was not limited by transport of CO₂ from the pellet surface.

It could be concluded that char which covers pellet surface might increase reduction significantly under certain conditions. High temperature might accelerate the conversion of char with CO₂ to CO right at the pellet surface and speed up reduction process.

The Tammann furnace special setup was developed to investigate the dripping behavior of hot metal through a coke bed. A scheme of the experimental set up is shown in **Figure 3.57**.

A crucible was produced with holes at the bottom. Pig iron was put together with coke/coke substitute in the crucible. Using a tantalum wire, the crucible was attached to a balance outside the furnace. The furnace was heated till 1350°C with a heating rate of 5 K/min. The temperature was held for 120 min before cooling at 10 K/min. The pig iron melted in the crucible and passed the coke/substitute coke bed. When the hot metal passed the coke/substitute coke bed, it dropped through holes of the crucible and was collected at the bottom of the furnace. The bottom of the furnace was also connected to a balance.

Table 3.31: Scenario for dripping zone trials

Phase	Duration	Temperature	Heating rate
1. Preheating	160	800 °C	5 K/min
	800	800 °C	0 K/min

	110	1350 °C	5 K/min
2. Dripping period	120	1350 °C	0 K/min
3. Cooling	240	200 °C	10 K/min

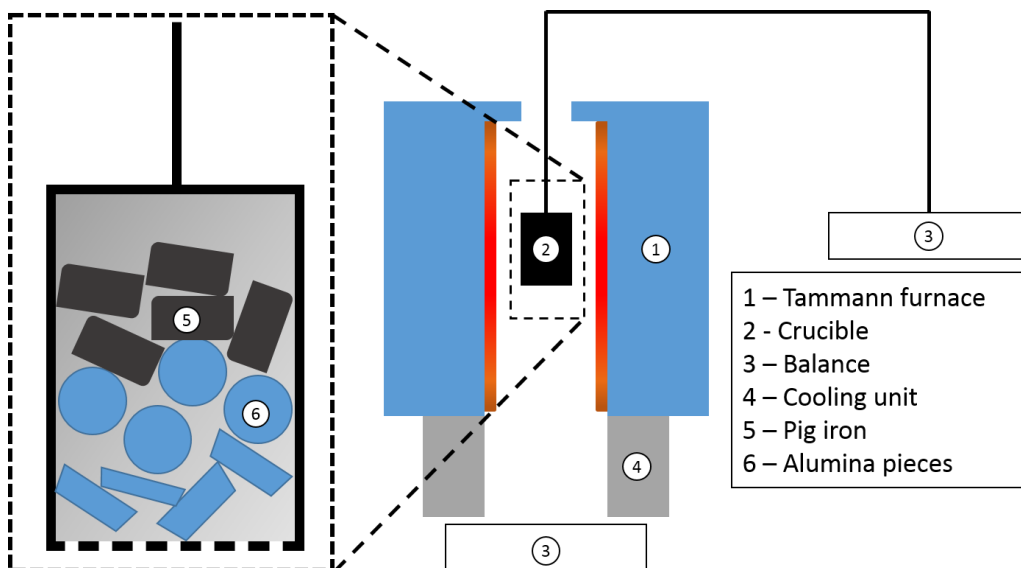


Figure 3.57: Schematic illustration of Tammann furnace DZ setup and magnification of crucible

Preliminary trials showed that coke degradation occurred much faster than melting of pig iron. Consequently, coke was substituted with alumina spheres and pieces.

Results of preliminary trials showed high surface tension. Great amount of crucible and alumina spheres were covered with liquid iron. Liquid iron, which passed through the artificial coke bed, merged together. Consequently no concrete information regarding the droplets could be obtained. Results of the preliminary trials are shown in **Figure 3.58**. The pig iron with a carbon content >3.5 % melted completely. A rather high surface tension could be seen as a layer of liquid iron identified at the crucible inner wall. Liquid metal also covered the dripping holes of the crucible.



Figure 3.58: Collected hot metal passing through the synthetic coke bed

Hot collected metal showed many small droplets which solidified in a spherical form. Furthermore, a greater amount of droplet merged and solidified together into a larger piece.

The results of the trials showed a very slow dripping behavior. Hot metal reaching the bottom of the furnace solidified as small spheres. First trials showed a very low dripping rate.

Trial	Pig iron collected in bottom	Hold up	Dripping rate
1. 80 g Pig Iron	25.1 g	68.6 %	12.55 g/h

2. 120 g Pig Iron	50.4 g	57.8 %	25.2 g/h
-------------------	--------	--------	----------

A testing facility for the simulation of dripping zone was developed and established. Trials regarding the dripping behavior were conducted. Spherical hot metal droplet with high wetting behavior was observed. High surface tension might cause low dripping rate. An increase of input material increased the dripping rate caused by the increase of mass moving through the coke bed. This might increase pressure and consequently dripping rate.

Although the experimental facility was successfully established, a few improvements have to be made to increase reproducibility. The influence of input material on the dripping speed has to be determined. The facility should be modified for adjusting the atmospheric condition in the dripping chamber.

3.2.7.1 CONCLUSION CHAR INTERACTION WITH FERROUS BURDEN AND DRAINAGE IN THE DRIPPING ZONE

Reduction trials with temperatures above 1000 °C show increased reduction behaviour in presence of char. A reason could be an accelerated Boudouard reaction at the surface of the pellet. Since the char is present right at the reaction surface, any CO₂ which is produced will be reduced to CO directly. This way diffusion will be accelerated significantly. A special Tamman furnace setup was developed. First trials were conducted, dripping rates and hold up were calculated.

3.2.7.2 IMPACT OF CHAR ON BURDEN IN THE STACK ZONE AND COHESIVE ZONE

Impact of char on burden in the stack zone and cohesive zone

The impact of char on the reduction and softening behavior of pellets and sinter on the stack zone and the cohesive zone of the blast furnace was studied using the metallurgical lab tests that simulate the blast furnace conditions. As a deviation to the proposed plan of the laboratory investigations, the scheme shown in **Figure 3.59** demonstrates the tests performed. BRASS and ASAM tests were not conducted due to installation maintenance reasons delaying test schedule.

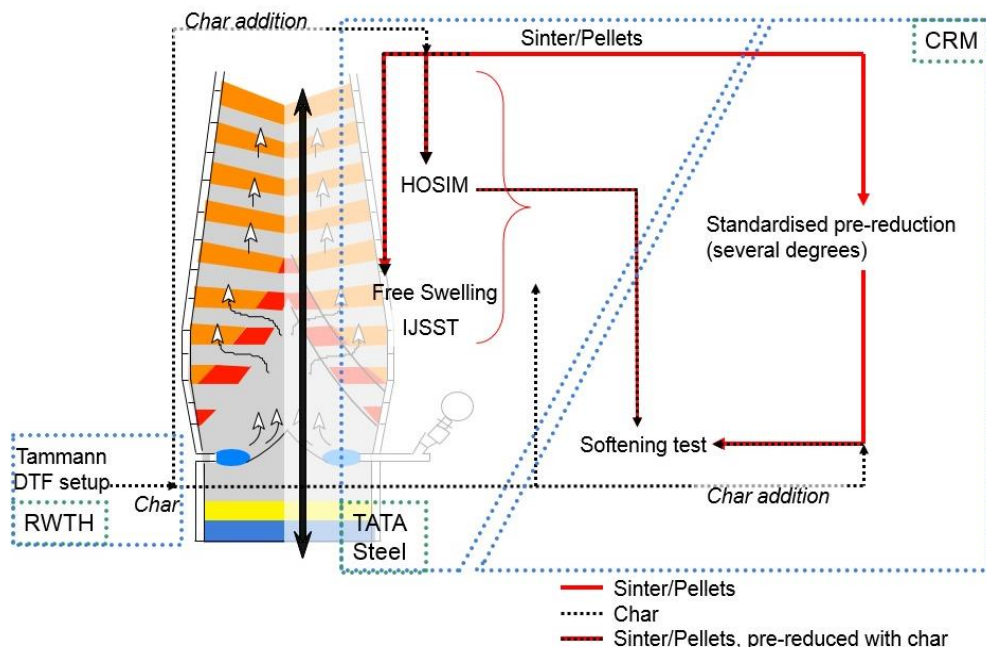


Figure 3.59: Experimental Scheme for laboratory investigations for study of impact of char on burden

The metallurgical tests performed and the conditions involved are presented in **Table 3.32**

Table 3.32: Metallurgical Test conditions and parameters

Test	Material size fraction	Amount used per trial	Temperature	Gas Composition	Other
------	------------------------	-----------------------	-------------	-----------------	-------

HOSIM (full) Q-HOSIM (interrupted)	Sinter (13/10 mm)	500 g	430-910 °C	CO/CO ₂ /H ₂ /N ₂ as per operating line of Blast furnace Flowrate:30 Nl/min	O/Fe end: 0.5 O/Fe end: 1.3
Free Swelling	Pellets (13/12 mm)	10	1050 °C	CO Flowrate: 2 Nl/min	Time: 30 min or 90 min
IJSST IJmuiden Swelling and Softening test	Pellets (13/10 mm)	500 g	Reduction: 950 °C Softening: 950-1200 °C	Reduction: 40% CO/ 60% N ₂ Softening: 100% N ₂ Flowrate:30 Nl/min	O/Fe end: 0.375 Pressure on load: 7.85 N/cm ² Max pressure drop: 1.76 kPa

To study the impact of char on the burden (pellet / sinter), a method to coat the burden material with char was established and used. Coated pellets were prepared using Polyvinyl Alcohol (PVA) as binder. 1% PVA solution by weight was prepared in distilled water at 85-90 °C. A magnetic stirrer was used to obtain a homogenous solution without the formation of lumps. To coat char, approximately 500 g of pellets/ sinter was weighed and sprayed with PVA solution and coated with approximately 1% of char by weight in a tumbling machine for 300 rotations. After tumbling, the coated pellets were dried and sieved at 100 °C in an oven to remove excess coating, moisture and harden the binder.

Hypotheses formed for the study are as follows

1. *Char physically influences the swelling behaviour of pellets*
2. *Char increases the reduction rate and reduction degree of pellets by the effect of carbon*
3. *Char accumulates in the pores of sinter in the stack zone and influences reduction degree and disintegration behaviour*

Influence of char on sinter in the stack zone

The chemical composition of sinter in weight % used in the test is given in **Table 3.33**

Table 3.33: Chemical composition of sinter in weight %

Fe ²⁺	Fe Total	C	S	CaO	SiO ₂	MgO	Al ₂ O ₃	LOI
6.72	57.60	0.023	0.011	9.46	4.16	1.67	2.04	<0.01

The experiments on sinter reducibility in the stack zone were performed in HOSIM. A schematic representation of the test setup is given in **Figure 3.60**.

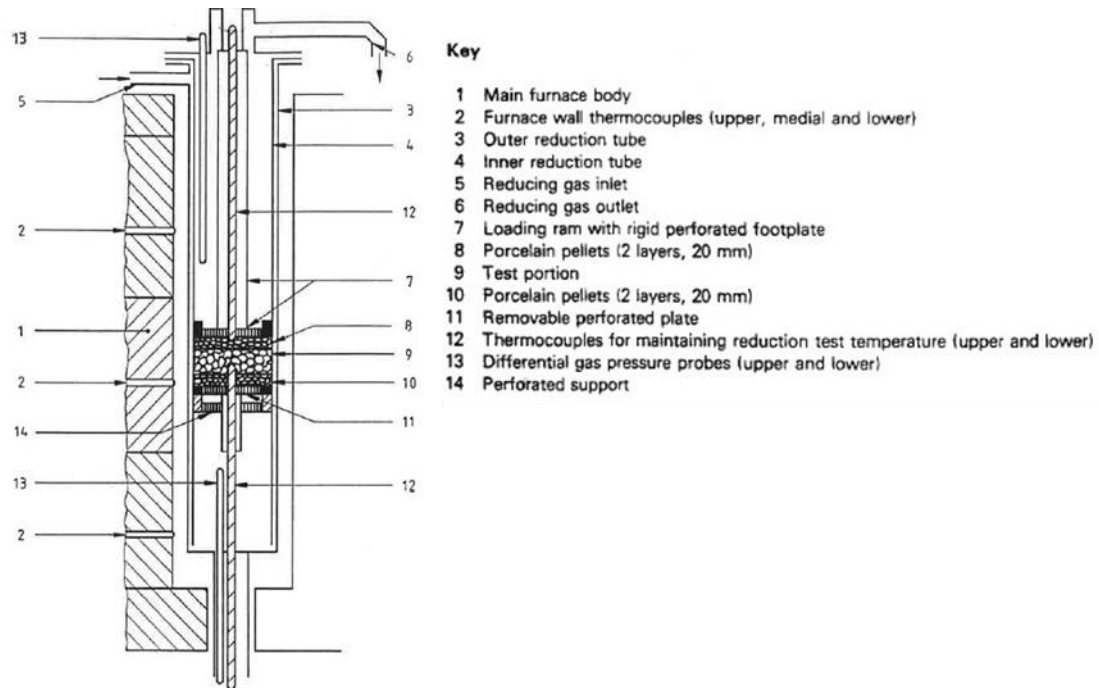


Figure 3.60: Schematic representation of HOSIM experimental test setup

The results pertaining to HOSIM are from an average of 5 trials per test. The reduction time taken to attain the end O/Fe value of 0.5 is shown in **Table 3.34**

Table 3.34: Reduction time in HOSIM to attain end O/Fe of 0.5

Sample	Sinter	Sinter+BPC 900	Sinter+BPC 1300	Sinter+CPC 900	Sinter+CPC 1300	Sinter+CGC 900	Sinter+CGC 1300
Reduction time (min)	185	190	194	195	204	193	194
Standard deviation	2.95	2	2.55	1.53	1.67	2.86	2.51

As a general trend, increase in reduction time in the presence of char was noted. Barring an increase of 10 minutes in reduction time on an average, char CPC1300 stood apart among all the char types showing the longest reduction time. The role of char in the test could be attributed to the physical barrier that it creates in hindering gas flow to the sinter pores. With hampered gas flow distribution to the pores, reduction was slowed.

This is in line with the enhanced role of sinter in filtering dust when compared to pellets in a blast furnace [1].

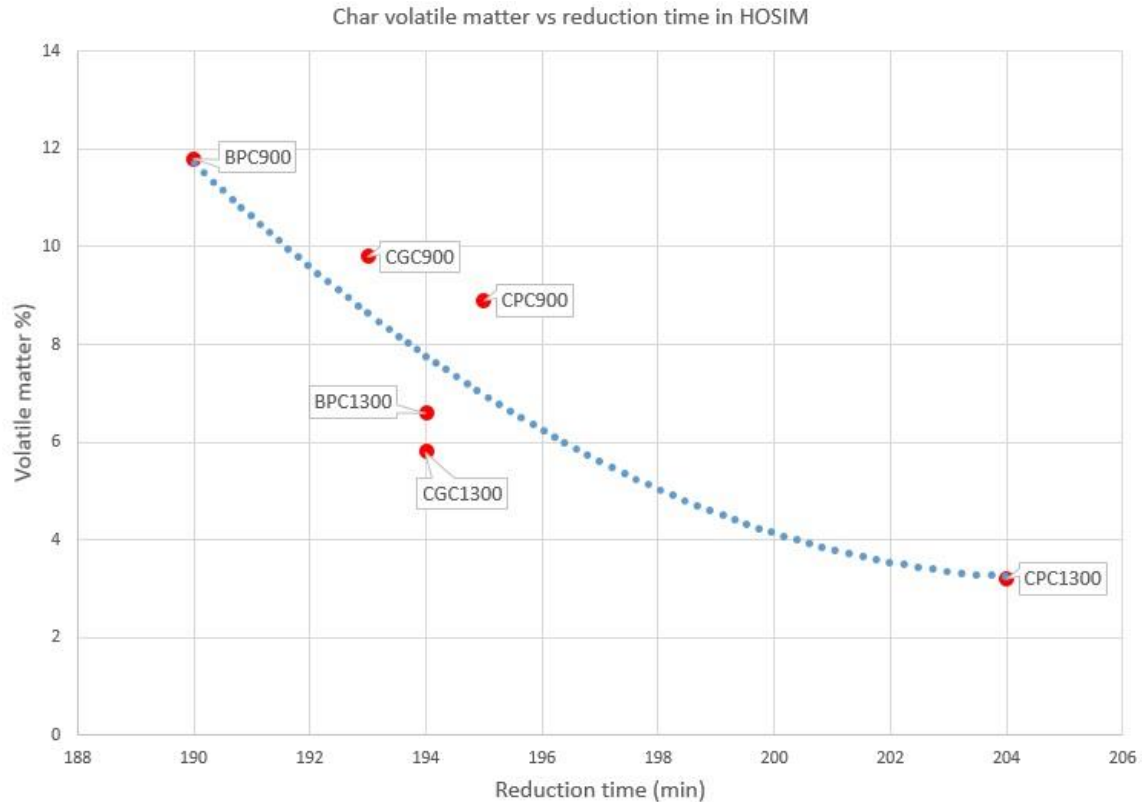


Figure 3.61: Char volatile matter and reduction time in HOSIM

From the comparison of volatile matter present in char (as given in **Table 3.19**) with the reduction time in HOSIM as depicted in **Figure 3.61**, it could be inferred that with higher volatile matter in the char, the reduction was faster. This would be due to the increase in the surface area due to the release of volatiles, allowing the reduction to be quicker.

The decrease in O/Fe ratio over reduction time in the test for sinter and sinter coated with chars is presented in **Figure 3.62**. It was noticed that at later stages of reduction i.e., associated with increase in temperature, the reduction of sinter coated with char was much slower than that for sinter. This deviation in trend from the reference case is owed to the temperature dependant diffusional limitation caused by the char. At higher temperatures, the diffusional limitations were predominant.

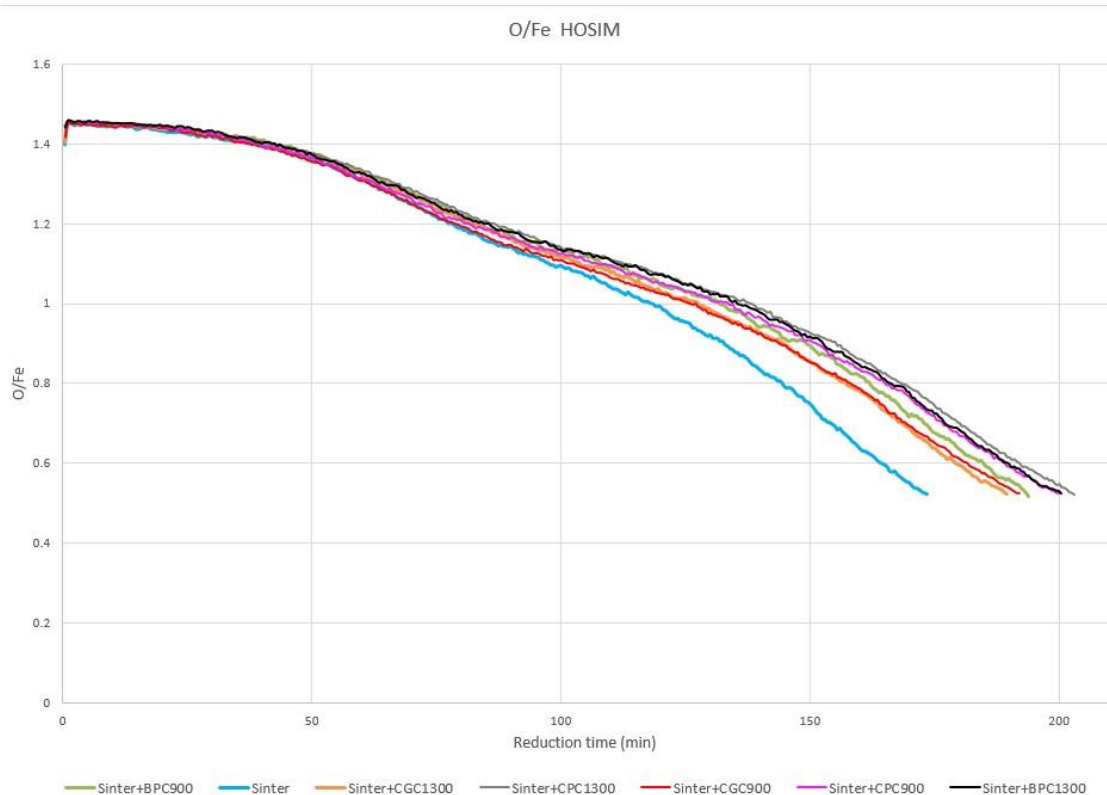


Figure 3.62: O/Fe ratio in HOSIM for tests with sinter and sinter coated with char

The disintegration index of the samples identified as the fraction of material less than 3.15 mm after tumbling for 300 rotations is shown in **Table 3.35**. The values were obtained from an average of 3 trials per test. The values for the samples tested with chars qualitatively indicated that in addition to the reduced sinter fraction, the char that definitely comes under the 3.15 mm fraction also attributed to it.

Table 3.35: Fraction of reduced sinter below 3.15 mm after tumbling

Sample	Sinter	Sinter+BPC 900	Sinter+BPC 1300	Sinter+CPC 900	Sinter+CPC 1300	Sinter+CGC 900	Sinter+CGC 1300
Fraction % <3.15 mm after tumbling	16.42	15.76	18.54	13.38	14.84	15.73	15.67
Standard deviation	1.21	0.98	0.26	0.30	0.74	0.43	0.63

With no marginal differences in the fraction of material <3.15 mm between the sinter and the sinter with chars, there is no concrete interpretation of this value from the influence of char. Although the highest value obtained for the sample with char BPC1300 could be correlated to its least char reactivity from TGA experiments as shown in **Table 3.23**, the speculation of char inducing chemical reactions is dismissed owing to the test temperature conditions being low for char gasification.

Polished sections of samples from the complete HOSIM and Q-HOSIM tests were prepared for the char-free reference case and for the sinter coated with BPC900 case. These were examined with reflected light optical microscopy (LOM) for a qualitative comparison of reduction microstructures and to investigate the fate of the char. The sinter pieces were embedded intact (without crushing) in order to preserve the full spatial context of reduction microstructures. **Figure 3.63** shows the overview images (LOM composite mosaics) of sinter samples after full HOSIM and interrupted Q-HOSIM. Considering the intrinsic heterogeneity of the sinter in general, like-for-like comparison of similar original sinter microstructures, exposed at fragment exteriors, implied that reduction microstructures were qualitatively similar as seen in **Figure 3.64**. The zones marked are (1) unreacted core with original sinter microstructure and phase assemblage, (2) dominated by wustite with little metallic Fe, and (3) dominated by metallic Fe with little wustite (plus larnite, glass and minor C2F (dicalcium ferrite) / brownmillerite).

The only difference noticed was the presence of surviving char predominantly in the rough

topography of the fragment exteriors or in open pores, the region which is highlighted in blue in **Figure 3.64**. A magnified image of the char in the region highlighted in white is shown in **Figure 3.65**. Metallic iron phase and wustite are identified in white and light grey respectively. In addition to char, there was fine sinter dust that was seen adhering to the pores and boundaries, the source of which is interpreted to be the reduction-disintegration product from the test. The settling of dust and char during sample handling to different sinter pieces apart from their in-situ generation and presence have to be taken into consideration in the interpretation. This supports the hypothesis of preferential char accumulation in the sinter pores.

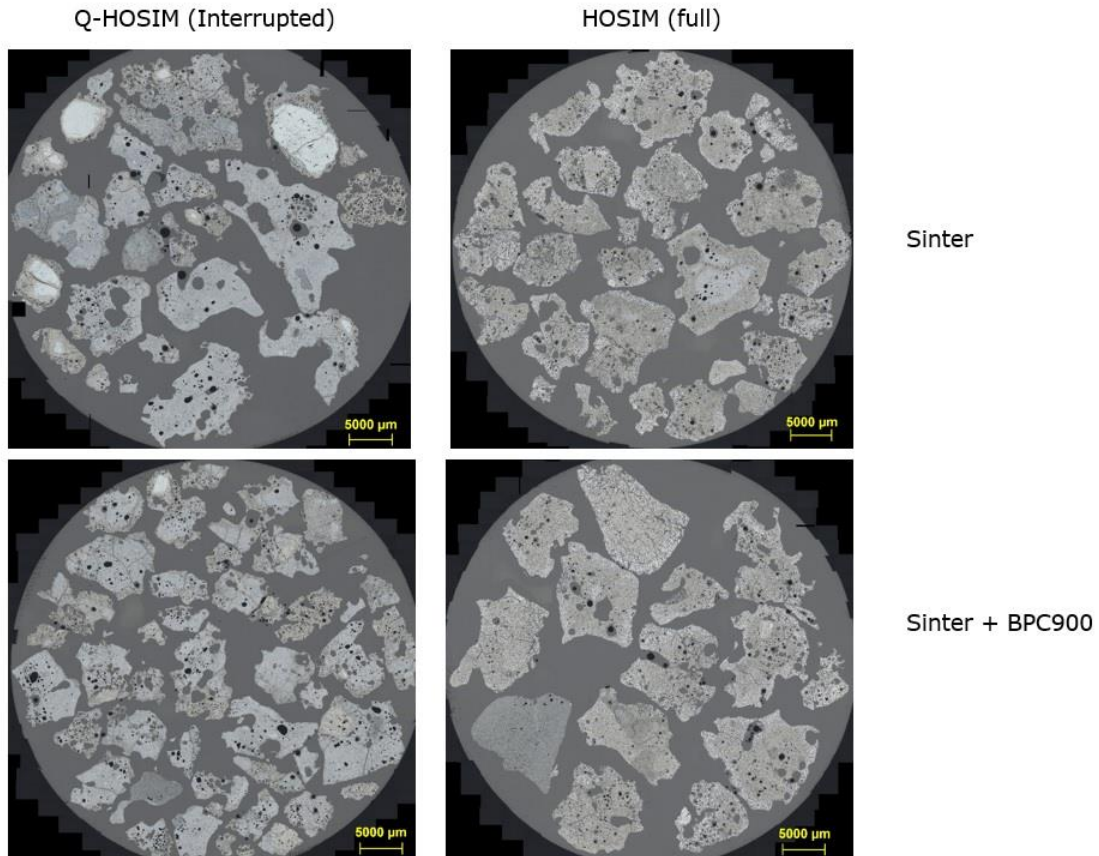


Figure 3.63: Cross sections of sinter and sinter with BPC900 char after reduction from full HOSIM and interrupted Q-HOSIM

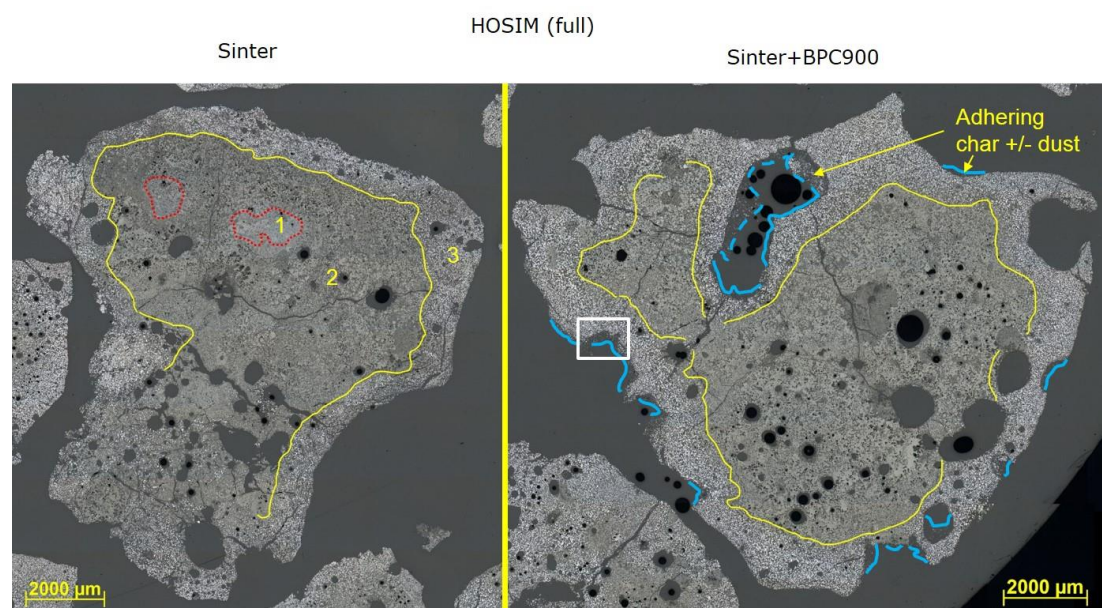


Figure 3.64: Microstructure of sinter and sinter with BPC900 after reduction from full HOSIM

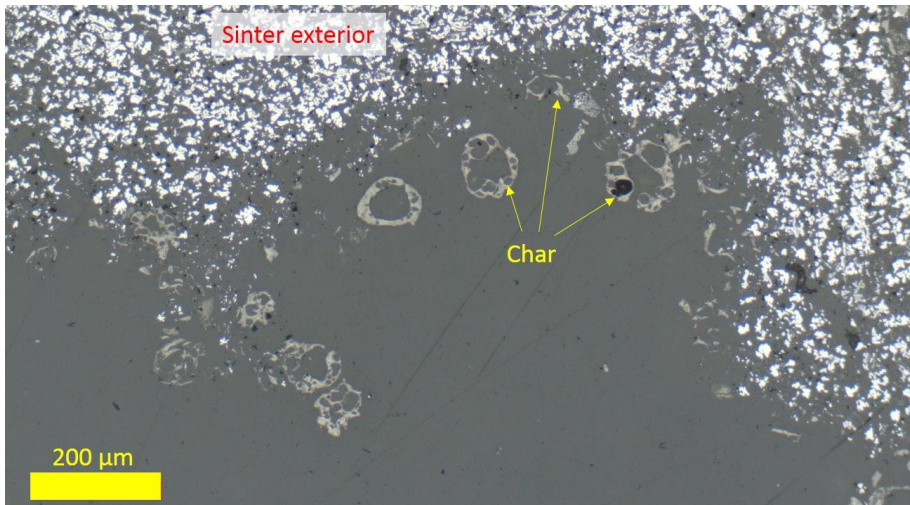


Figure 3.65: Presence of char BPC900 along the sinter pores and boundaries

Bulk chemical and quantitative XRD-Rietveld analysis were performed on full and interrupted HOSIM tests as shown in **Table 3.36** and revealed that actual progression of reduction occurred contrary to the intended degree of reduction (mentioned as O/Fe recorded in the test). In addition to a subtle difference in O/Fe, the two Q-HOSIM samples differed substantially in their bulk mineralogical phase proportions, with the sinter with char BPC900 sample containing substantially more wustite and less magnetite than the reference sample. In the case of the completed HOSIM tests, the char-free sample was slightly more reduced than the other. The factors influencing this discrepancy could be reflected as imprecision in the test procedure (quantification of reduction degree, potential further reaction during cooling), rather than any significant difference in reduction behavior. Based on these four samples, the relationship between bulk mineralogy and reduction degree was consistent i.e., a similar reaction pathway was followed in both cases to arrive at the same net reduction degree as far as can be discerned.

Table 3.36: XRD Analysis on Sinter and Sinter with char BPC900 for interrupted (Q-HOSIM) and full HOSIM

Sample	Q-HOSIM		HOSIM	
	Sinter	Sinter+BPC900	Sinter	Sinter+BPC900
Haematite	0.78	0.72	0.08	0.16
Ca-Magnetite	49.37	44.04	2.01	1.97
Wustite	9.64	19.14	37.47	38.68
Metallic Fe	1.74	0.98	36.10	33.76
*Ca ₄ Fe ₁₄ O ₂₅	1.10	1.25	0.15	0.25
*Ca ₂ Fe ₁₆ O ₂₅	1.86	1.48	1.04	0.58
*Ca ₂ Fe ₂₂ O ₃₃ C2W4F9 /	0.14	0.00	0.17	0.51
CaFe ₂ O ₄ CF	1.44	1.52	0.56	1.04
CaFe ₃ O ₅ CWF	0.92	1.10	0.16	0.00
CaFe ₄ O ₆ CW2F	0.97	0.15	0.53	0.79
Brownmillerite (C2(A,F))	0.22	1.12	1.56	1.40
Kirschsteinite	0.53	0.35	0.00	0.07
Clinopyroxene	2.15	1.15	0.00	0.08
Larnite	7.72	5.52	16.46	13.53
SFCA	21.44	21.49	3.71	7.16
O/Fe	1.32	1.28	0.53	0.56
O/Fe recorded in the test	1.30	1.31	0.52	0.52

(* Note: These were assumed stoichiometries for phases whose reflections were identified, but the actual chemistry of the phases is variable and not analysed directly)

From the results on the performance of sinter in the HOSIM tests, it is inferred that the presence of char influenced the gas flow distribution for reduction progress by physically limiting gas diffusion to the pores, noticed as increase in reduction time. The role of char in chemically influencing the reduction behavior is dismissed after the analysis of microstructure and chemistry, with little or no difference in the reduction end test parameter of O/Fe.

Influence of char on pellet swelling behavior

The physical phenomenon of the transformation of haematite to magnetite is characterized by swelling during reduction as the lattice transition enables anisotropic growth of magnetite. With further reduction, the change accompanying wustite to iron formation is characterized by volume increase, which formed the focus of the free swelling test performed for pellets.

The volume of the pellets was determined before and after the test to understand the change in physical parameters. The pellets coated with char were investigated for swelling by this method.

Isolated experiments of 4 different char weight % up to 1% were carried out for different types of char at 1050 °C for 90 minutes to understand the influence of char amount.

Volume increase %, otherwise called as swelling index is defined as

$$\text{Volume change \%} = \frac{\text{Change in volume after swelling}}{\text{Initial volume before swelling}} \times 100$$

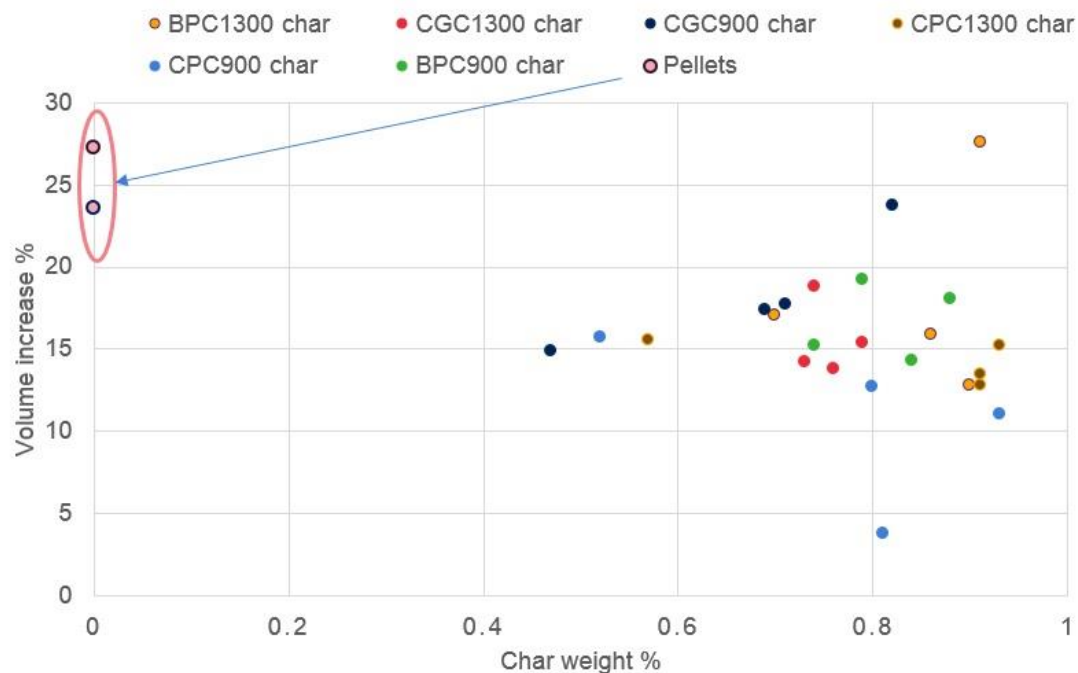


Figure 3.66: Effect of char weight % on the volume increase after free swelling test at 1050 °C for 90 minutes

From **Figure 3.66** it is observed that swelling was not consistent based on the char weight %. Erratic swelling behavior was noticed among the different chars, the reason of which could be attributed to the pellets being inherently different and experiencing different gas atmosphere based on the position in the test crucible with the pellet near the gas inlet witnessing different conditions when compared to the pellet at the gas outlet. On a whole, it could be said that irrespective of varying char weight % and type, the volume increase was lower than that of pellets alone. The volume increase for each pellet in a batch was also not uniform with one or two pellets swelling distinctively resulting in very high swelling index of the batch.

Excessive swelling that was noted in pellets is shown in **Figure 3.67**. The pellet near the gas inlet (adjacent to the letter indicated L) had swollen excessively when compared to other pellets.

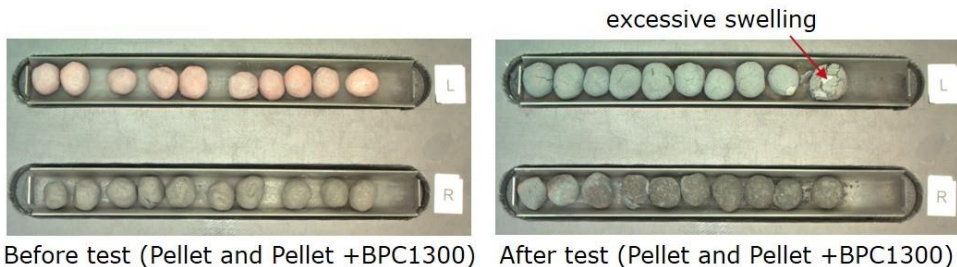


Figure 3.67: Image of pellets (L) and pellets with BPC1300 char (R) before and after swelling at 1050 °C for 90 min

From chemical analysis of the pellets from swelling test at 900 °C and 1050 °C in **Table 3.37**, it was noted that the metallic Fe content was higher for pellet with char BPC900 at 1050 °C than at 900 °C with char speculating the possibility of Boudouard reaction that could have taken place locally at the char surface. In that case, the generation of CO locally is touted to enhance the reduction resulting in higher Fe content. The carbon noted after the test for pellets themselves must be Boudouard carbon, distinct from that of others where the carbon source was char. The trivial amount of carbon noted after the test at 1050 °C and the higher metallic Fe content noted for pellets with chars indicated that the presence of char enhanced the reduction degree of an otherwise identical reduction treatment. However, the difference in reduction degree caused by the type of char was insignificant. Notwithstanding the enhanced reduction degree, swelling index was not higher than that of pure pellets themselves indicating that the char coating also passivated volume increase.

Table 3.37: Chemical analysis of pellets after free swelling test for 90 minutes

Sample	Char weight %	%C in	%C out	%C reacted	Metallic Fe %	FeO %	Fe ₂ O ₃ %
Pellets	0	0	0.15	-	63.5	23.0	4.2
*Pellets+BPC900	0.75	64.95	0.64	64.31	51.7	31.7	7.6
Pellets+BPC900	0.74	64.08	0.05	64.03	75.5	12.9	2.5
Pellets+BPC1300	0.90	82.00	0.11	81.89	77.3	11.2	1.8
Pellets+CGC900	0.82	66.67	0.15	66.52	73.8	12.8	3.6
Pellets+CGC1300	0.76	58.75	0.03	58.72	75.7	14.2	4.3
Pellets+CPC900	0.81	66.83	0.06	66.77	75.1	13.0	2.4
Pellets+CPC1300	0.91	77.35	0.04	77.31	75.7	13.0	1.8

(*Note : Test performed at 900 °C for 90 minutes)

To understand any homogeneous effect of char on the swelling behavior, coating of approximately 1 % by weight was used in swelling tests for 30 minutes. The shortened time for swelling was selected to identify the presence of char on the pellet after the test. For this purpose, a char bed amounting to approximately 2.5 g in the test crucible was used to embed the char coated pellets. From an average of 20 pellets tested, it was observed as in **Figure 3.68** that the swelling indices were still lower than that of pellets, with no visible cracks on the surface.

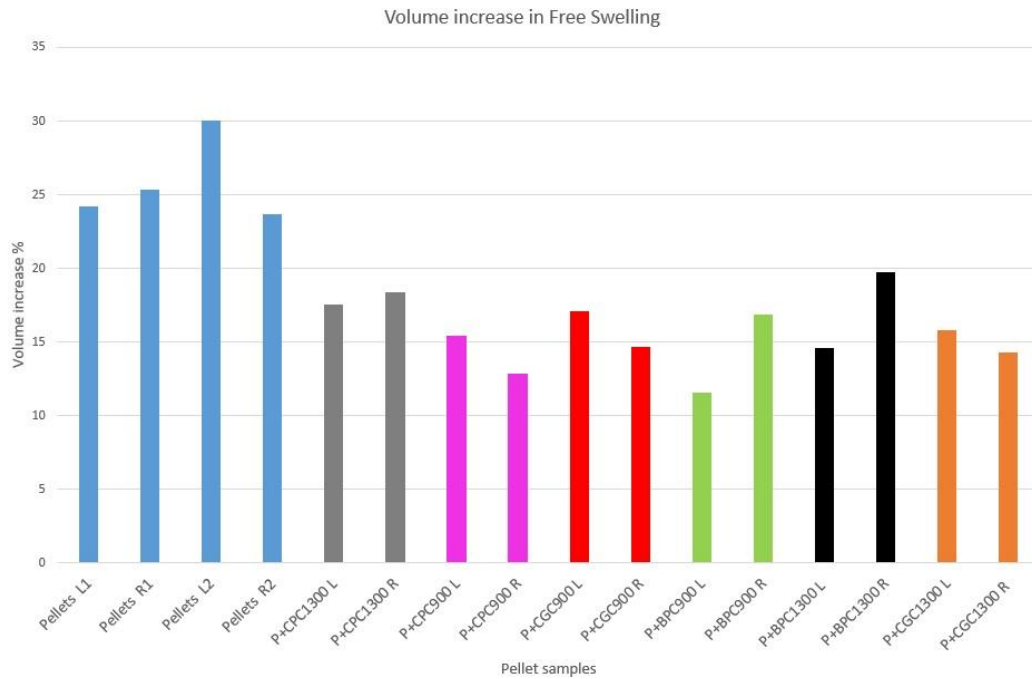


Figure 3.68: Comparison of volume increase for pellets and char coated pellets in char layer in crucible after swelling at 1050 °C and 30 min

As a modification to the test of char coated pellets, swelling tests of pure pellets in a bed of selected chars were performed. Char BPC1300 and Char CPC900 were selected based on maximum and minimum volume increase exhibited in test for 90 minutes in **Figure 3.68**. To show the change in the side of pellets exposed to the char layer after the swelling test, the pellets were turned as in **Figure 3.69**. The side exposed to the char layer was visibly different in light grey color. This could be because of the pellet side exposed to the char not being subjected to the same reduction atmosphere as the side above. However, this cannot be attributed with certainty to the presence of char alone. To understand from a qualitative point of view, microstructure analysis was done on these pellets which were not subjected to probable surface modification that would occur during the measurement of volume change.

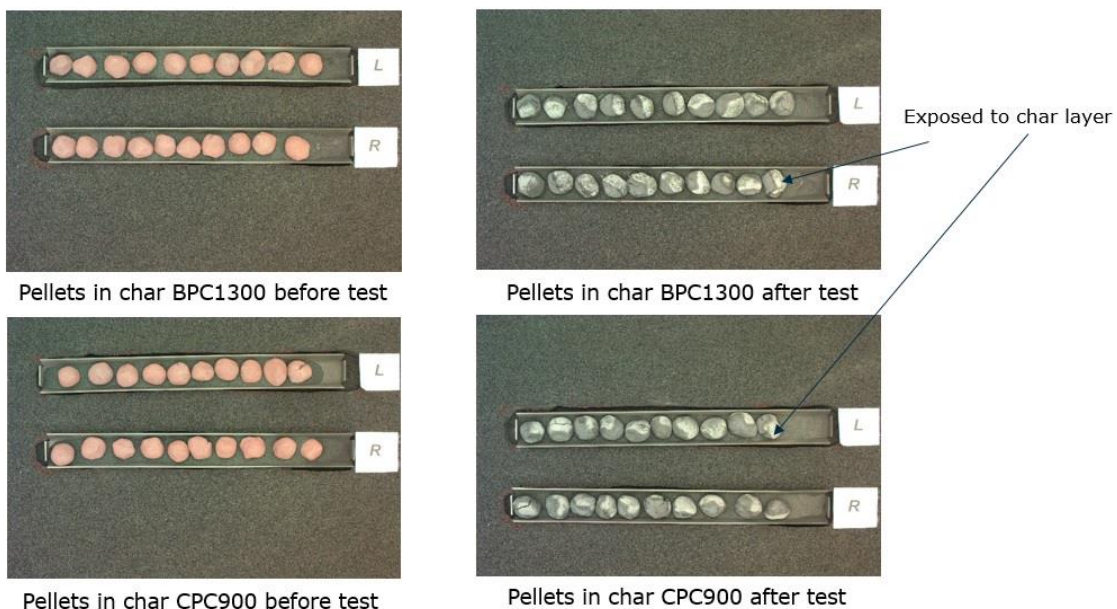


Figure 3.69: Pellets in a layer of char BPC1300 and char CPC900 before and after swelling at 1050 °C for 30 min

Observation of the microstructures of the pellets after tests in **Figure 3.70** revealed a difference in the reduction degree and texture on the upper gas-exposed surface versus the bottom of the pellets. The pellet side predominantly exposed to CO atmosphere (top side) in the test showed higher overall reduction degree and a reduction texture dominated by thin concentric metallic Fe layer growth around individual wustite cores. In the case of the under-side of the pellet (in contact

with the char), the overall reduction degree was lower and identified with sparsely dispersed iron in the form of coarser flakes. It can be inferred that the presence of char layer in addition to the inherent difference in gas atmosphere in the crucible resulted in difference in reduction texture and progress. There was no iron whisker formation noted in both the cases.

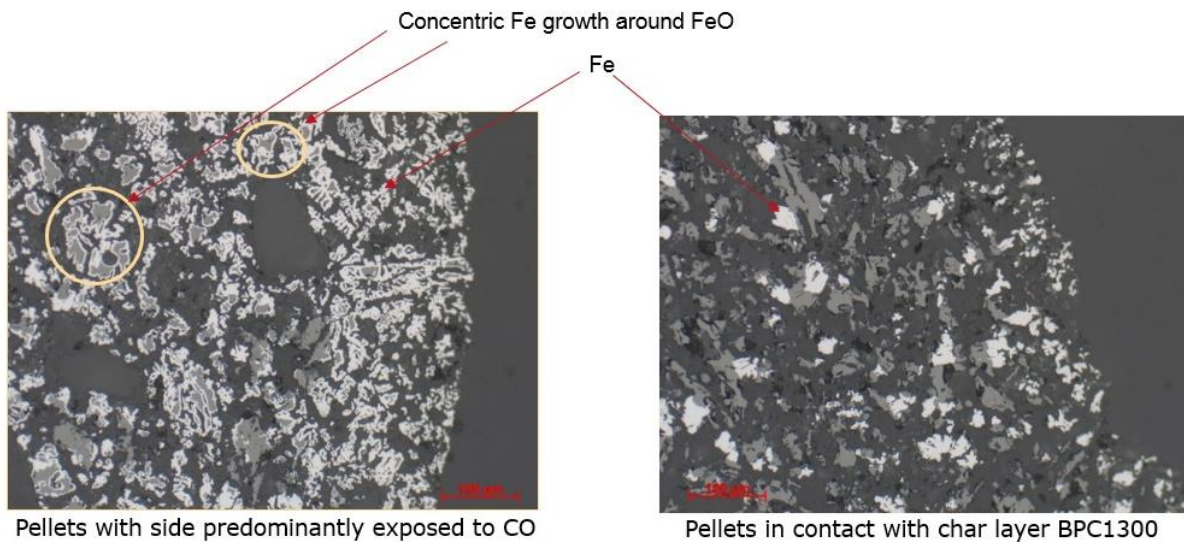


Figure 3.70: Microscopic analysis of pellet in BPC1300 char exposed predominantly to CO and char

From the free swelling tests, it is reasoned that the presence of char alone did not passivate swelling. With previous knowledge from camera testing on the behaviour of well fired pellets undergoing a transformation of volume change during swelling and subsequent shrinking as the reduction progresses, it could be inferred that maximum swelling would have occurred during the progression of the test itself. Given the higher overall degree of metallization of the pellets in the experiments with char addition, and presence of the typical metallization textures associated with shrinkage at advanced reduction degrees, it cannot be ruled out that the pellets have experienced some degree of shrinkage from their maximum volume during the course of the reduction. This shrinkage might be further advanced than the less strongly-reduced pellets without char addition.

Influence of char on pellets in the softening zone

The evolution of ferrous burden shrinkage after swelling and reduction was studied to understand the impact of char on softening of the pellets. The important results from this swelling and softening test are the reduction time, height change, weight loss and pressure drop. A schematic representation of the IJSST setup is shown in **Figure 3.71**

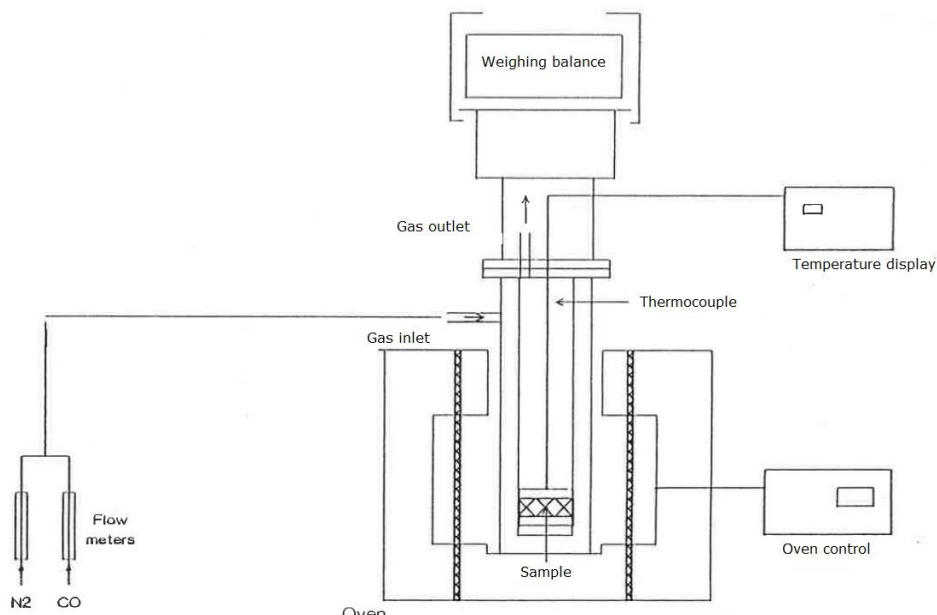


Figure 3.71: Schematic representation of IJSST experimental setup

It has to be noted that owing to time constraints in the scheduling of experiments, only one test for each sample was performed. Contrary to the intended char coating of approximately 1% by weight, lower coating levels were attained in certain experiments, the results of which are explained with microscopic analysis.

Comparing the reduction time as shown in **Table 3.38**, it was seen that the pellets with char reduced faster than the pellets themselves, which was in line with the hypothesis. The isothermal reduction atmosphere at 950 °C possibly facilitating reaction in the presence of carbon in the char with the evolved CO₂ to generate more CO locally would explain the low reduction times. To maintain homogeneity in the comparison of results from IJSST, only those tests with 1% char by weight are presented.

Table 3.38: Reduction time in IJSST

Sample	Pellet	Pellet+BPC900	Pellet+BPC1300	Pellet+CPC900	Pellet+CPC1300	Pellet+CGC900	Pellet+CGC1300
Reduction time (min)	141	98	104	136	121	130	124

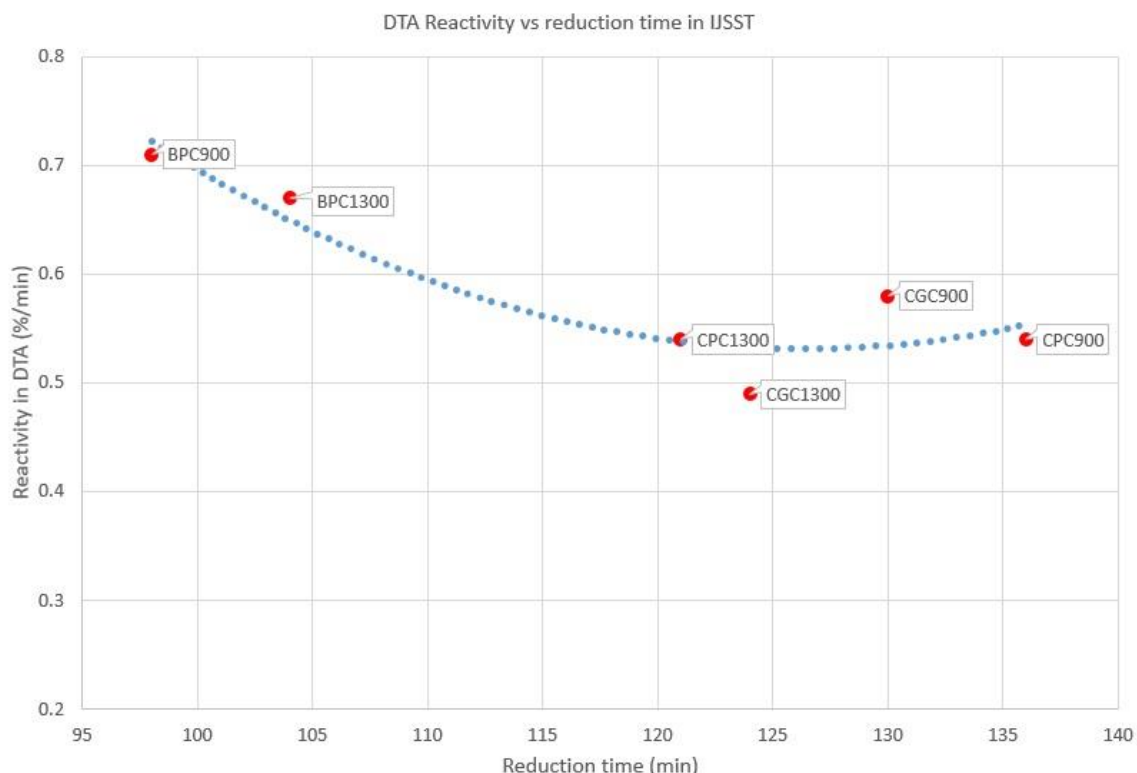


Figure 3.72: Reactivity of char in DTA and reduction time in IJSST

From **Figure 3.72**, it could be seen that the reactivity of char in gas mixture of CO/CO₂ and N₂ measured from DTA (Table 3.23) as part of task 1.4 relates well with the reduction identified in IJSST. The chars produced from coal B reduced faster than the chars from coal C owing to their higher reactivity.

Another parameter that could be related to the reduction time is the porosity of char measured from microscopic images presented in Task 1.4. As shown in **Figure 3.73** With the exception of char BPC900, it was observed that higher the porosity, lower was the time taken for reduction.

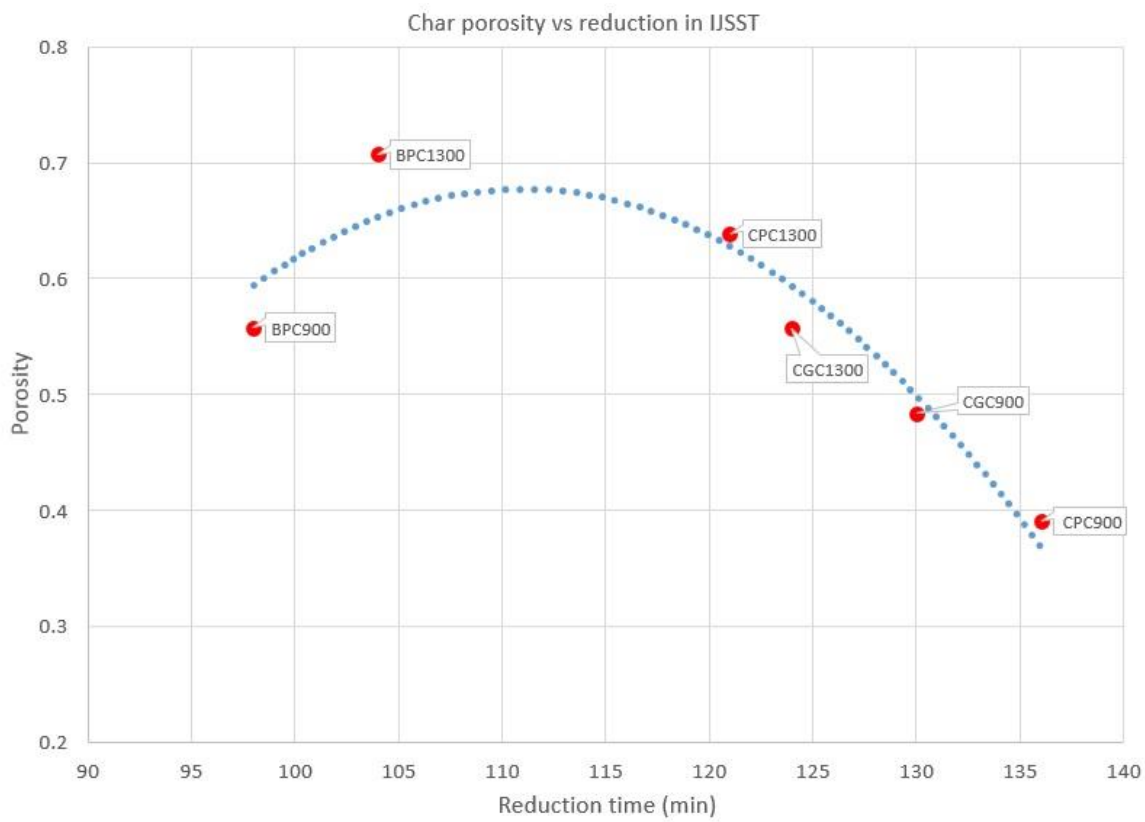


Figure 3.73: Char porosity in relation to reduction time in IJSST

The weight loss measured in the test is presented in Figure 3.74as follows

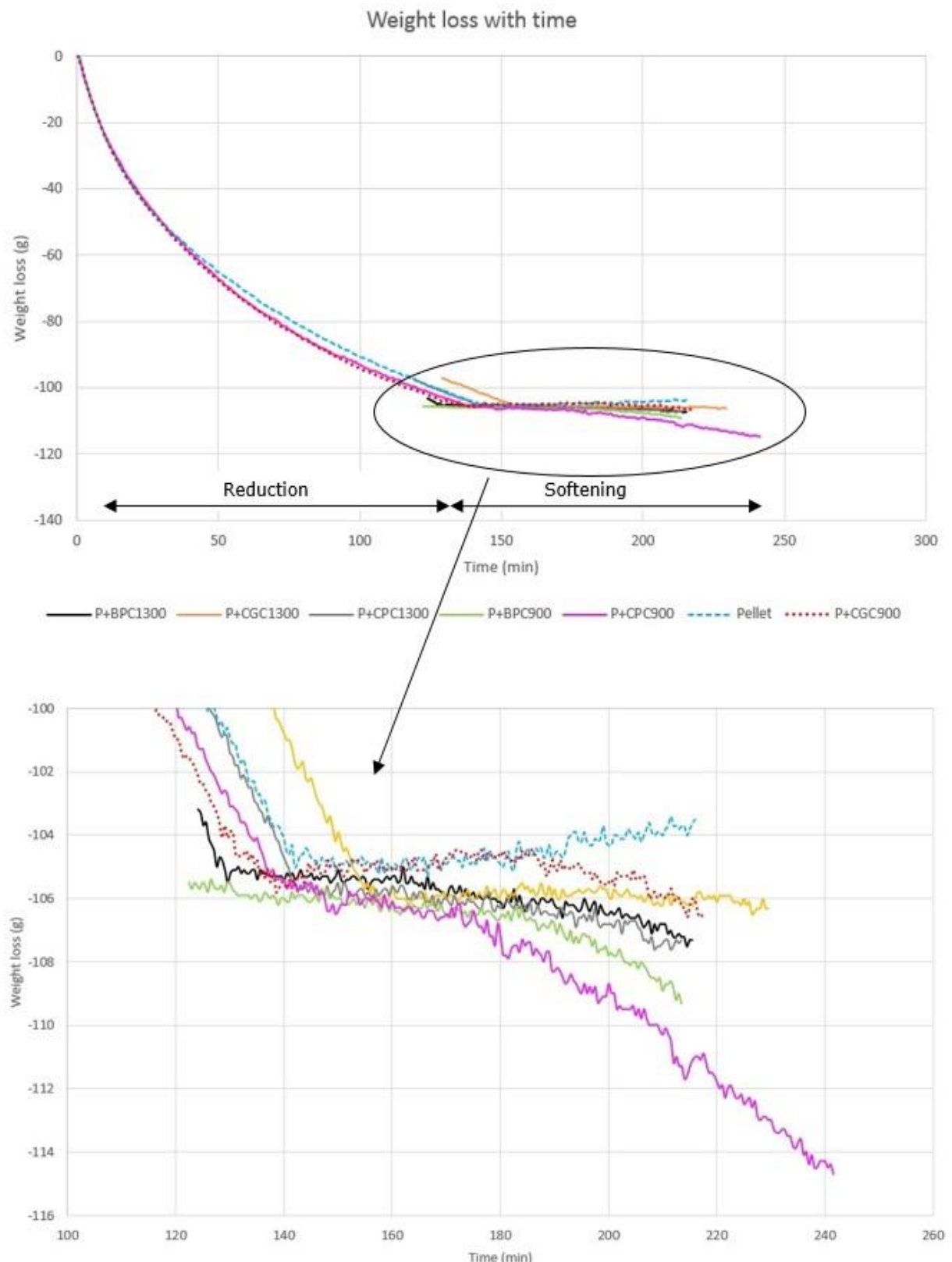


Figure 3.74 Weight loss with time in IJSST

For pellets covered with char, weight loss was observed even during the softening stage, implying that reduction continued further, with the sample of char CPC900 showing maximum weight loss

thereby confirming its high reactivity (as observed in char reactivity test in TGA in **Table 3.23**)

In **Figure 3.75**, the influence on pressure drop with increase in the bed temperature is shown. As softening proceeded along temperature, decrease in gas permeability led to increase in pressure drop. The rise in pressure drop for pellets coated with char occurred at higher temperatures when compared to the reference pellets, implying higher gas permeability. In **Figure 3.76**, it could be seen that when compared to pellets, pellets coated with chars exhibited slower pressure drop increase over the corresponding bed contraction.

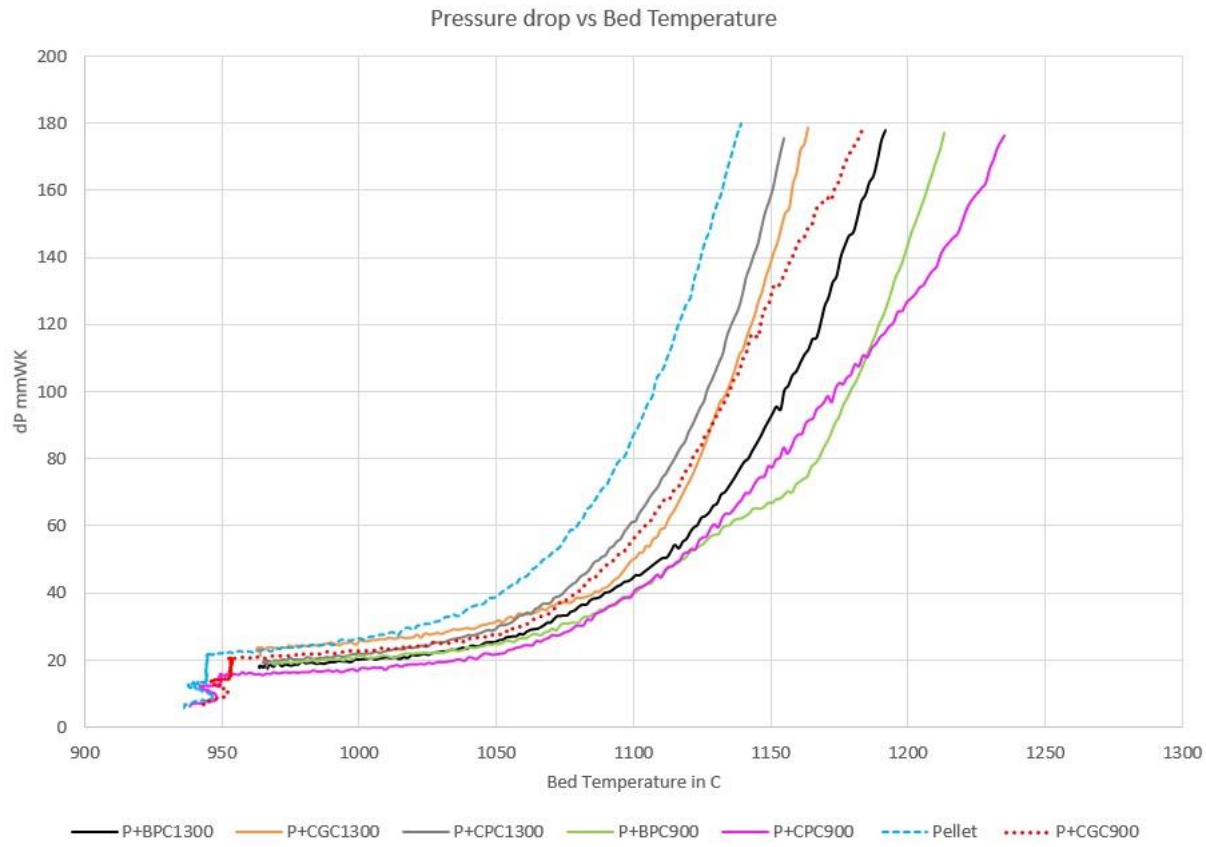


Figure 3.75: Pressure drop increase with temperature in IJSST

Bed shrinkage, as a measuring parameter is associated with constant pressure exerted by cylinder during the test whereas the pressure drop can vary according to the nature of the pellet to fill the reduced volume during softening which is unique based on the pellet structure, plasticity and bed packing.

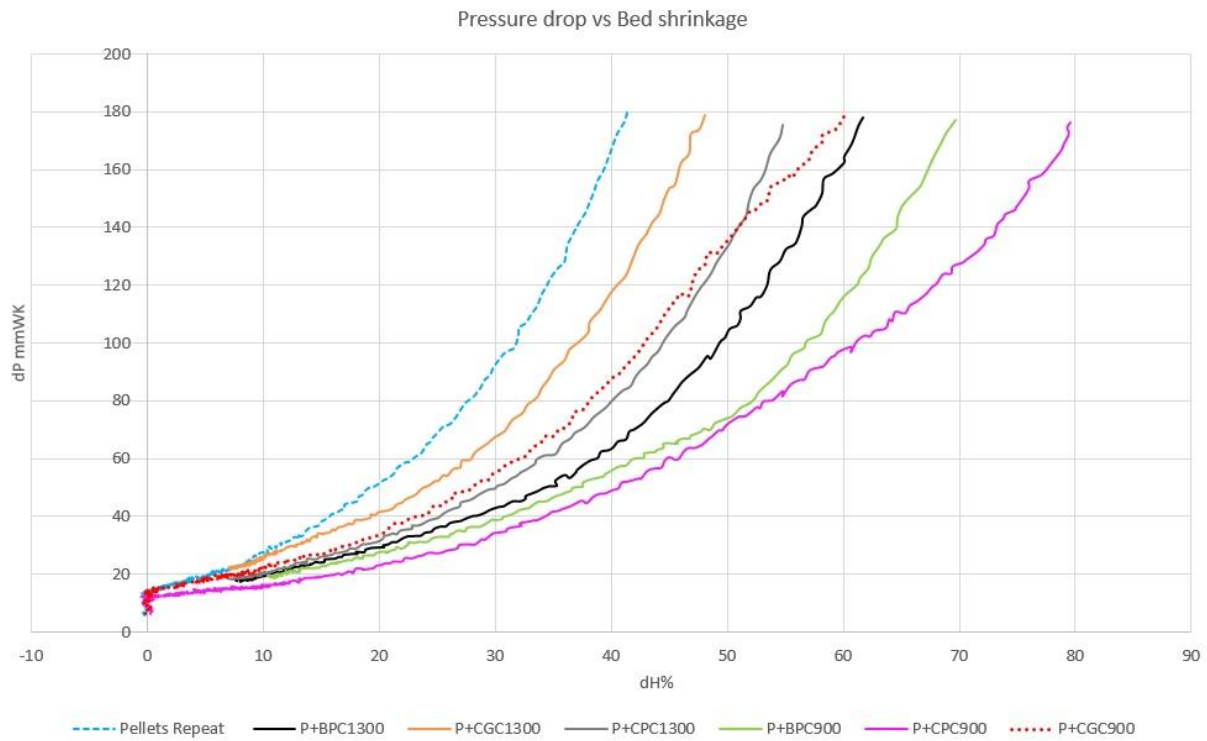


Figure 3.76: Comparison of pressure drop increase with bed shrinkage

The onset of the cohesive zone is given by the difference in the temperatures at which bed attained contraction of 10% and 25% of height. From **Table 3.39**, it could be seen that there was no distinguishable difference caused by the presence of char, with the thermocouple device measurement error amounting to 10 °C. The influence on the onset of cohesive zone, which would subsequently affect the dripping zone, could not be established from the tests. These experimental result were used in MOGADOR modelling to correlate parameters.

Table 3.39 Comparison of temperatures for the onset of cohesive zone

Sample	Pellet	Pellet+BPC 900	Pellet+BPC 1300	Pellet+CPC 900	Pellet+CPC 1300	Pellet+CGC 900	Pellet+CGC 1300
T at dH=10%	1060	1062	1060	1053	1053	1060	1079
T at dH=25%	1106	1107	1101	1095	1094	1103	1120

The observation of delayed pressure drop increase for pellets with char and thereby the role of char are explained here with microscopic analysis. A comparison of the degree of bed shrinkage obtained for increasing char weight % is presented in **Figure 3.77** with larger extent of bed shrinkage noticed for pellets with char of 1% by weight.

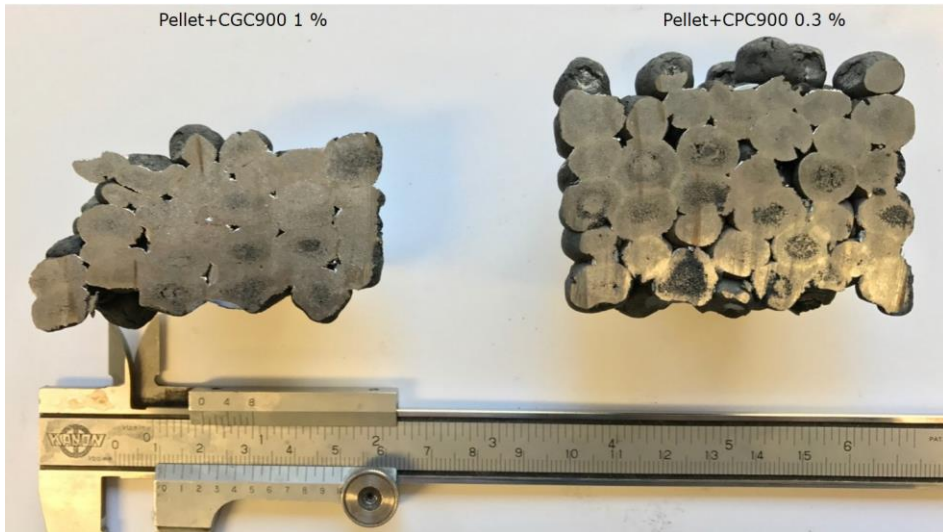


Figure 3.77: Comparison of the magnitude of bed shrinkage

Cross sections of pellets, pellets with 0.3 % and pellets with 1% char by weight are shown in **Figure 3.78**. Clear differences were seen in the amount of deformation of the individual pellets, loss of original inter-pellet void, sintering of adjacent pellets, and reduction microstructures.

A key difference between the samples with 1 % char versus the char-free reference case was the degree of coalescence/ sintering of adjacent pellets. With no char addition as shown in **Figure 3.79** (magnified yellow zone on the right), adjacent pellets were coalesced, with a lenticular zone of apparently higher (bulk) density of metallic Fe marking the overlap of two original pellet boundaries. The fact that these coalesced zones were strongly metallized leads to the inference that this happened only during the softening phase of the experiment after earlier metallization of the rims during the isothermal pre-reduction phase.

For the pellets coated with char of 1% weight as in **Figure 3.80** (magnified yellow zone on the right) and **Figure 3.81**, this intergrowth or coalesced pellet boundary was not seen because of the adherence of char between the boundaries forming a physical boundary layer separating the pellets.

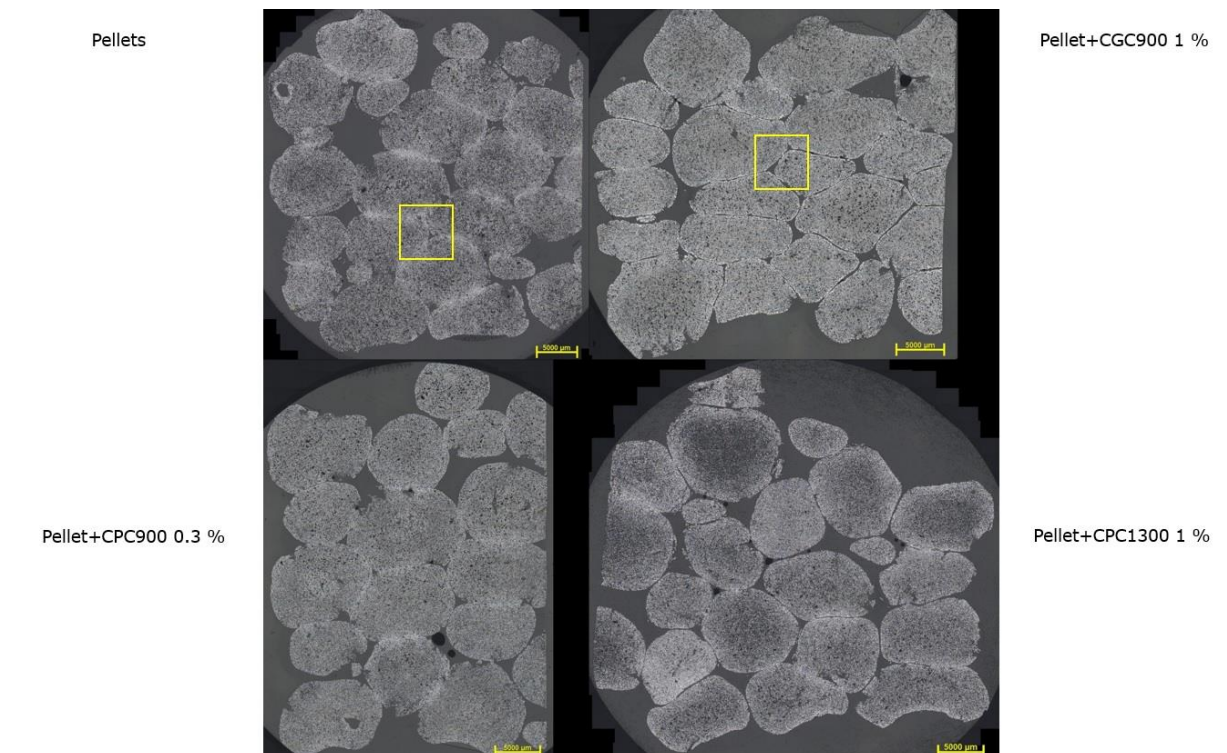
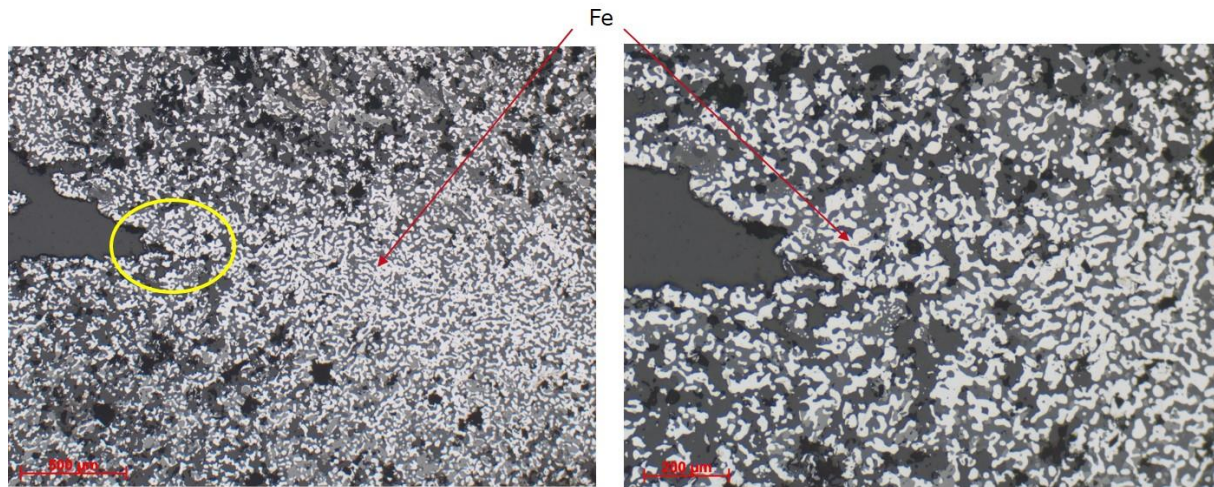
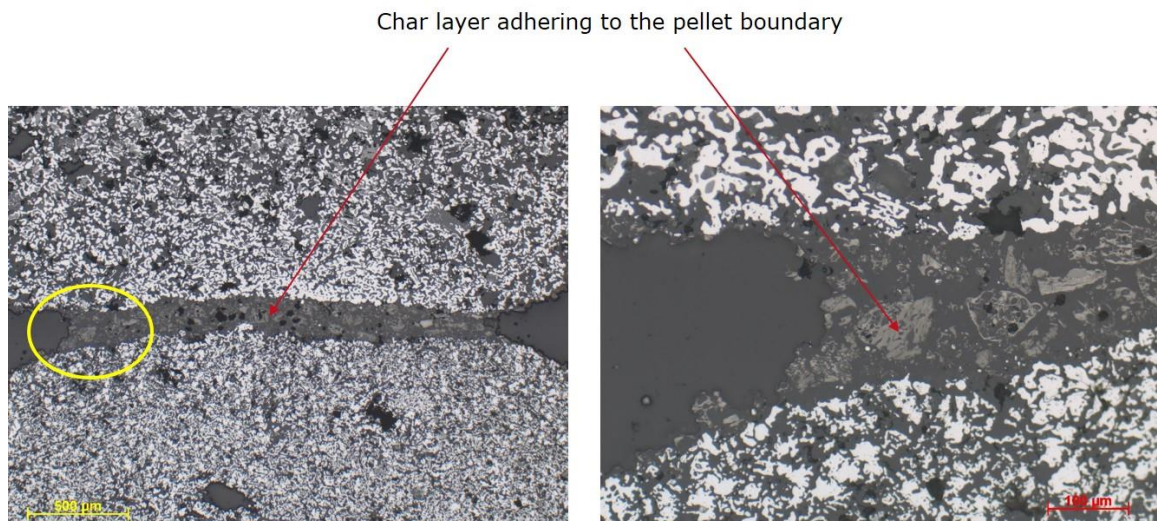


Figure 3.78: Full mosaic cross sections of softened pellets and pellets coated with varying char % by weight



Dense metallic iron formation - blended region of softened pellet from IJSST

Figure 3.79: Pellet boundary after softening



Char adhered between pellet boundary for pellet with CPC1300 char from IJSST

Figure 3.80: Pellet boundary after softening in the presence of char CPC1300

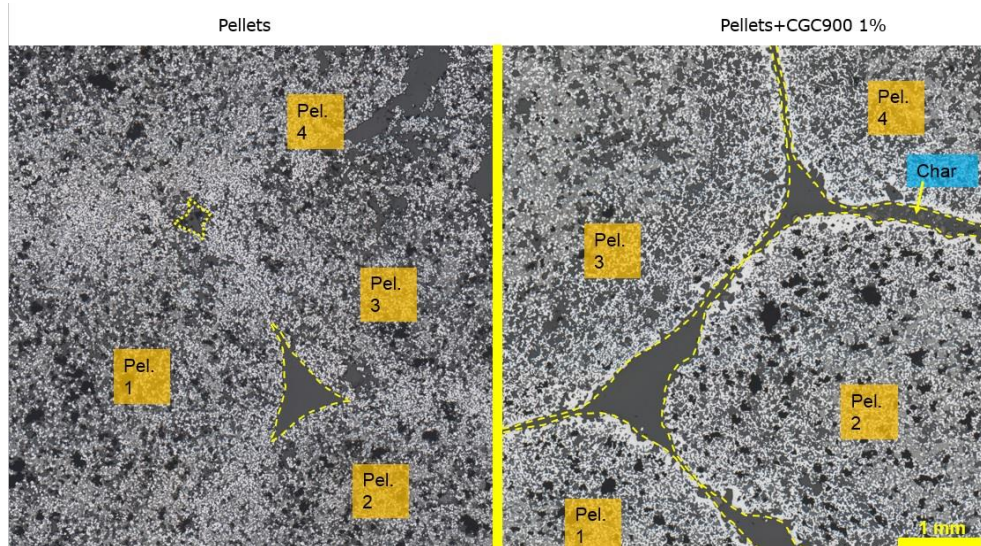


Figure 3.81: Pellet boundary after softening in the presence of char CGC900 with separate boundaries

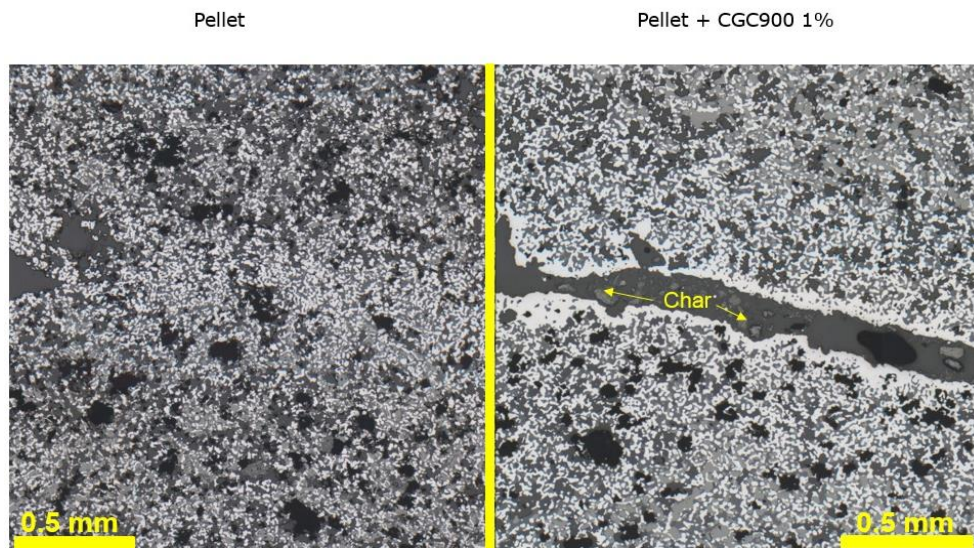


Figure 3.82: Pellet boundary after softening indicating the presence of char after softening

The presence of char as a layer separating adjacent pellets, and preventing coalescence in **Figure 3.82** would create thin channels for gas to flow, delaying the buildup of pressure drop. Irrespective of the degree of overall compaction and deformation of individual pellets being clearly higher at the point of test interruption, the pellets remained physically separate. Maintaining these thin channels along the boundaries between heavily deformed pellets mitigates the loss of the majority of initial inter-pellet void up to higher temperature. In the absence of char, pellets become coalesced at an earlier stage of deformation, rendering the generally higher total void fraction largely closed to gas flow.

3.2.7.3 SOFTENING TRIALS AT CRM

Aim of the test and link with cohesive zone in the BF

Softening test is a part of the blast furnace ferrous burden characterisation (**Figure 3.83** and **Figure 3.84**). These materials don't have an accurate melting point but a mushy melting area called the cohesive zone. In the CRM test (developed in 1959), the cohesive zone is characterised by a temperature domain inside which the studied sample is subjected, thanks to a mechanical load, to a height reduction. "Start of softening temperature" (T-3) and "Start of melting temperature" (T-25) have been conventionally defined as corresponding to a reduction of respectively 3% and 25% compared to the initial height. Values of T-3 and T-25 give an idea of the cohesive zone position and the difference $[(T-25)-(T-3)]$ depicts the extent of this zone for a given BF thermal profile. This relates to the position and thickness of the so-called "cohesive zone" inside the BF.

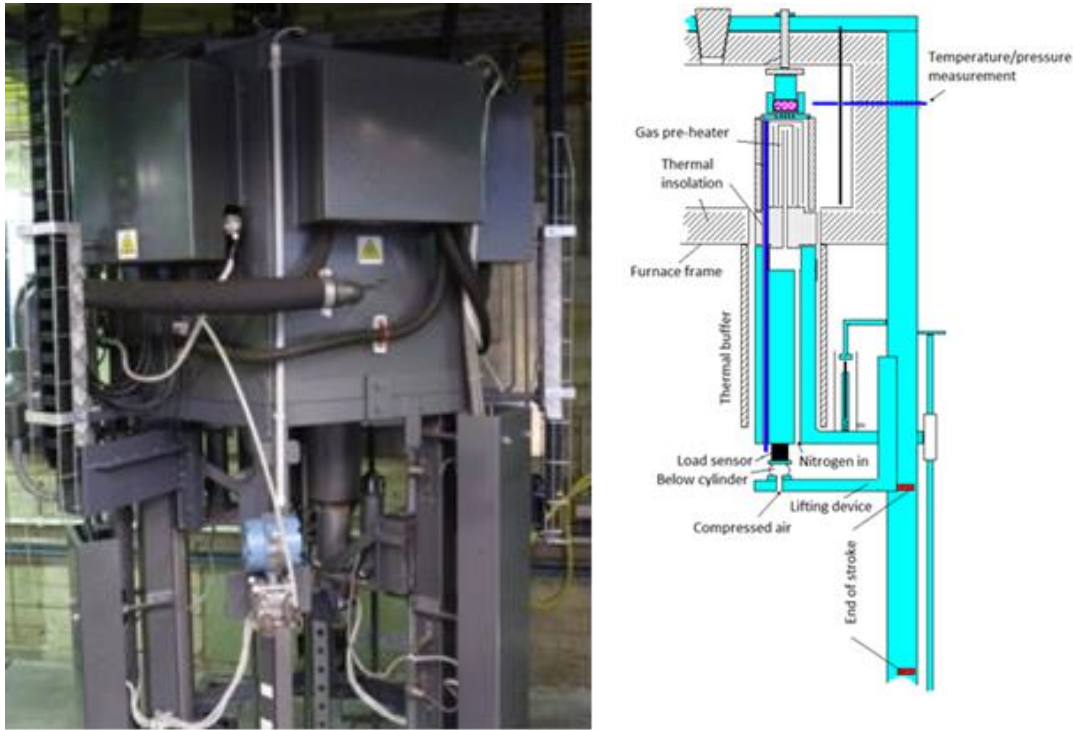


Figure 3.83: CRM Softening test apparatus (l); Simplified sketch of CRM softening (r)

It must be noted that the two upper-defined temperatures vary for a given material with its reduction rate depending on its movement in the BF shaft. This is why the softening test is done, for the same material, on several samples pre-reduced at different rates. Material is then characterised by two curves: T-3 in function of pre-reduction and T-25 in function of pre-reduction. For the rest of this report and to ease the reading, "start of softening" will be more simply referred as "softening" and "start of melting" as "melting".

In addition to temperature and shrinkage measurement, the apparatus also records the sample permeability during softening. This measurement is of high interest as permeability of ferrous burden in the cohesive zone is directly related to the BF productivity.

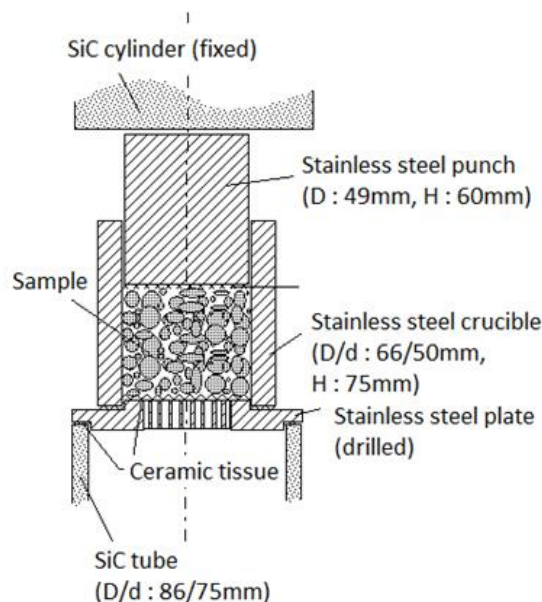


Figure 3.84: Sample in the crucible and punch

The core of the device is a 1500°C electrical furnace allowing treating three samples simultaneously. Operating diagram is shown on **Figure 3.85** (for clarity, only one sample is presented).

Figure 3.85 explains the interpretation of the softening trials results. The softening and melting lines (blue and red) are dependant of the burden material. On the same graph of temperature vs reduction degree, one could draw the specific descent paths depending of the blast furnace. The combination of these curves give an idea of the position and the extent of the cohesive zone inside the furnace.

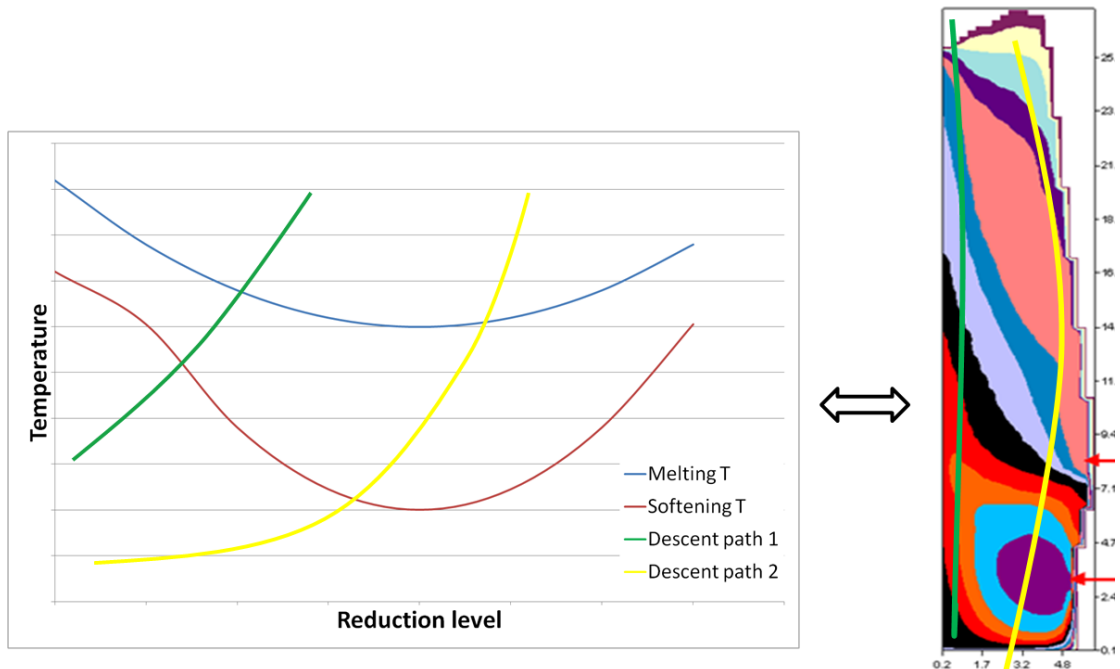


Figure 3.85: Interpretation of softening curves

Softening trials procedure for the CharFoCo trials

- Step 1: material preparation (for sinter)
 - Sieving ([10-12.5 mm] fraction)
 - Crushing of bigger fractions if necessary and sieving
- Step 2 : Reduction (2 x 500g of material)
 - In reducibility furnace
 - Several reduction times to obtain several reduction degrees
 - Gas mix : 40% CO, 60% N₂
- Step 3 : material preparation
 - Crushing + sieving to get [3-5mm] grain size distribution
 - Optionally : mixing with char (CPC900)
- Step 4 : softening test
 - two trials per reduction degrees of the same material for repeatability check
 - Individual shrinkage under load (1 kg/cm²) & permeability measurements.

Pre-reduction step

As previously stated, before performing softening trial, the ferrous burden had to be reduced in separated furnace (the one used for reducibility/RDI trials). Several reduction times, and therefore several reduction degree were used for these trials: from 20 to 100 (for sinter) or 140 (for pellets) minutes. The reduction conditions were the same for reducibility tests:

- Temperature: 1000°C (+/-1%)
- Reducing gas: 60% N₂, 40% CO (+/-1%)

The reduction degree attained for the different reducing times are given in **Figure 3.86**. The reduction time for pellets was augmented compared to sinter in order to reach the same final reduction degree of 74%.

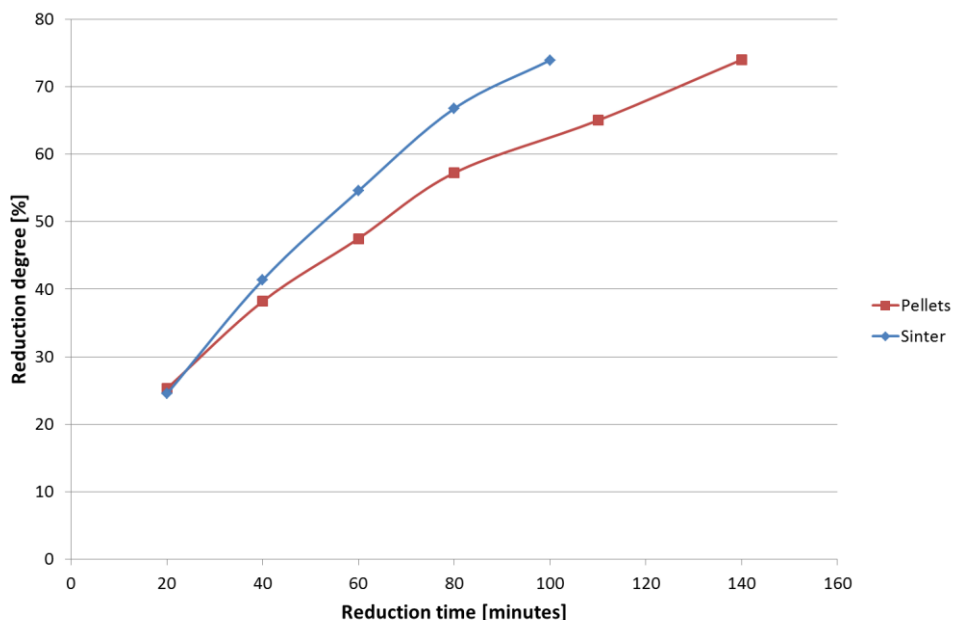


Figure 3.86: Port Talbot ferrous burden reduction degree in function of reduction time

Mixing of char with ferrous burden

The mixing of char with sinter or pellet was performed in a planetary mixer with water as a binder

3.2.7.4 REFERENCE SOFTENING TRIALS

The pre-reduced ferrous burden materials were then tested in the softening trial apparatus. The test was duplicated for reproducibility purpose.

Sinter

Port Talbot sinter was pre-reduced during different times (20, 30, 40, 60, 80 and 100 minutes). The results of the softening trials after pre-reduction are given in **Figure 3.87**. The tests appeared

to be highly repeatable. It could be noticed that the trial with a pre-reduction step of 30 minutes was not duplicated; a single test was added at the end of the project to confirm the impact of char on burden softening.

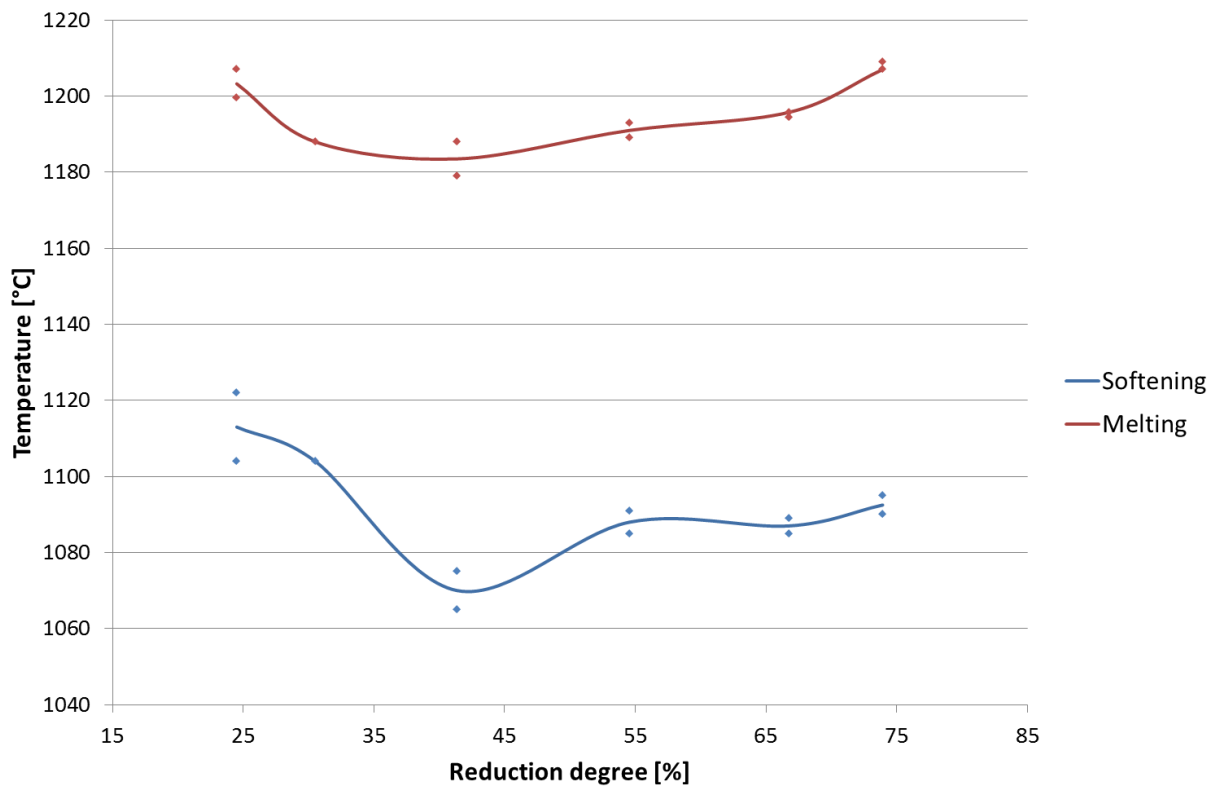


Figure 3.87: Reference softening trials results for Port Talbot sinter

During the trials, the pressure drop across the burden was also monitored. The final pressure drop measured at the end of the trials (when the sample height reached 75% of its initial value) are given in **Figure 3.88**.

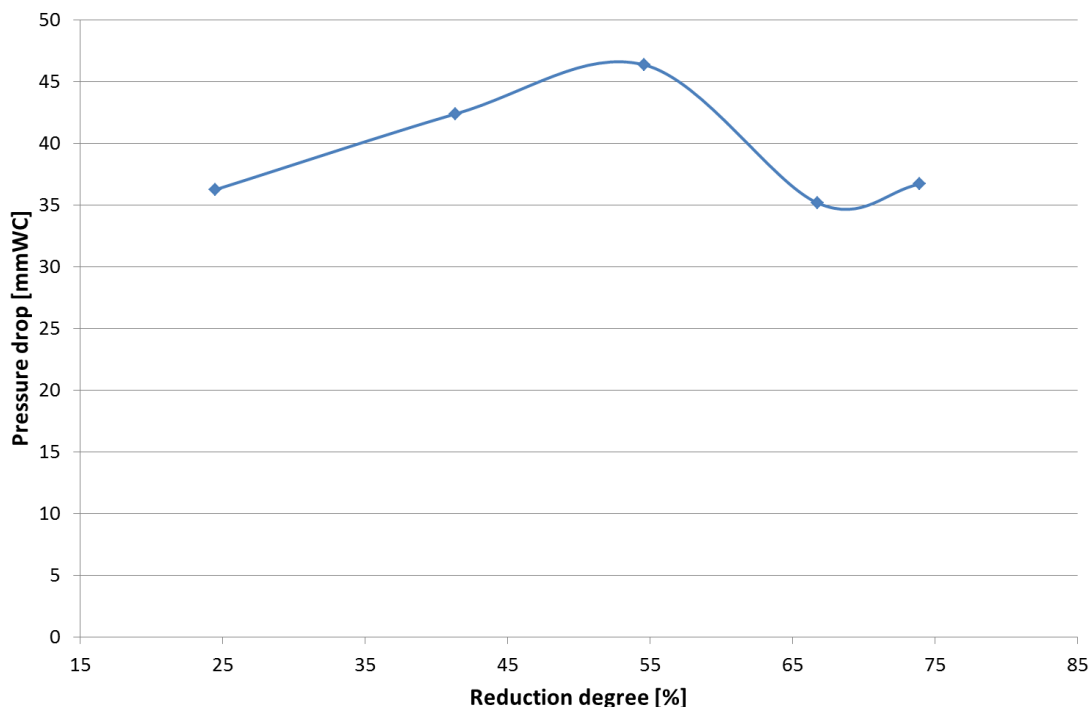


Figure 3.88: Pressure drop of reference trials for Port Talbot sinter

Pellets

Port Talbot pellets were pre-reduced for different times (20, 40 60, 80, 110 and 140 minutes). The results of the softening trials after pre-reduction are given in **Figure 3.89**. As for the pellets, the test results were clearly very well repeatable.

Opposite to the sinter case, the softening/melting temperatures were continuously decreasing with reduction degree. This could be explained by the fact that, for crushed pellets, liquid slag or wustite could flow out of the particles when sinter tends to retain this liquid phase, avoiding to hollow the particles and therefore keeping an higher strength [2].

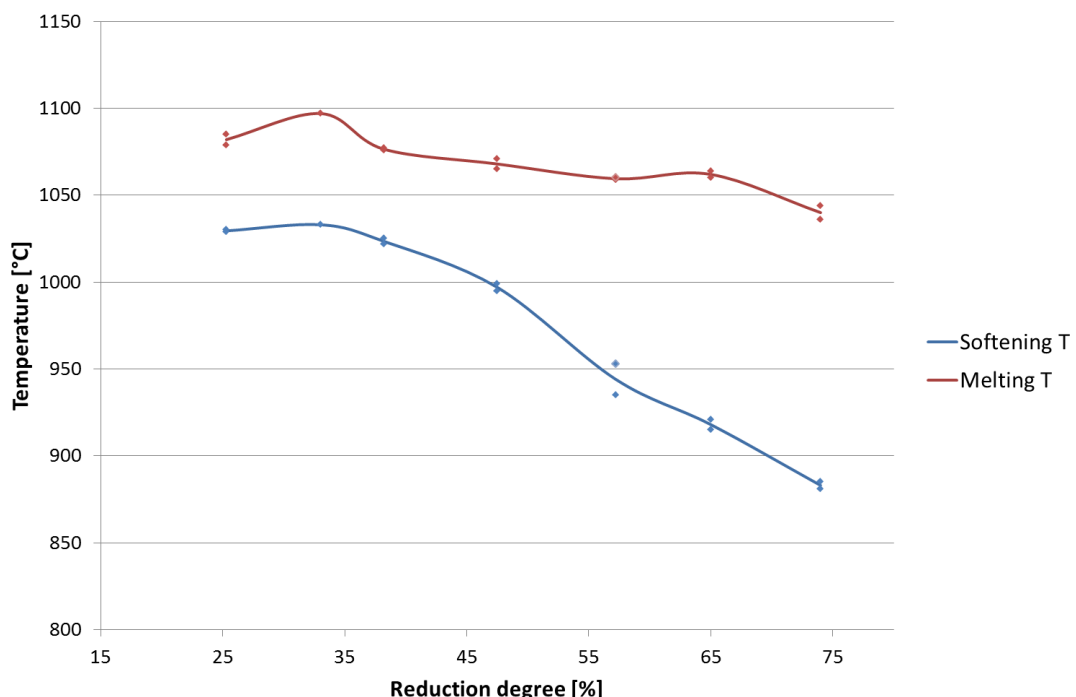


Figure 3.89: Reference softening curves for Tata Steel Port Talbot pellets

3.2.7.5 SOFTENING TRIALS WITH ADDITION OF CHAR

In order to estimate the impact of char hang up inside the blast furnace during its descent into the shaft, several softening trials were performed with char mixed with the burden following the procedure explained before. For these trials, 3 g of char was added to 125 g of ferrous material (sinter or pellets), so the char mass fraction is 2.4%.

Softening of sinter with addition of char

Figure 3.90 is similar to **Figure 3.87** but with addition of orange and green points corresponding respectively to softening and melting temperature for the mixes sinter-char (char being added after reduction step), it seemed that the addition of char had impacted the softening/melting temperature in a quite large extend but not always in the same direction. Sometimes, the temperature increased and sometimes it decreased. In addition, the change was more important for the lowly reduced material than at the end of the curves.

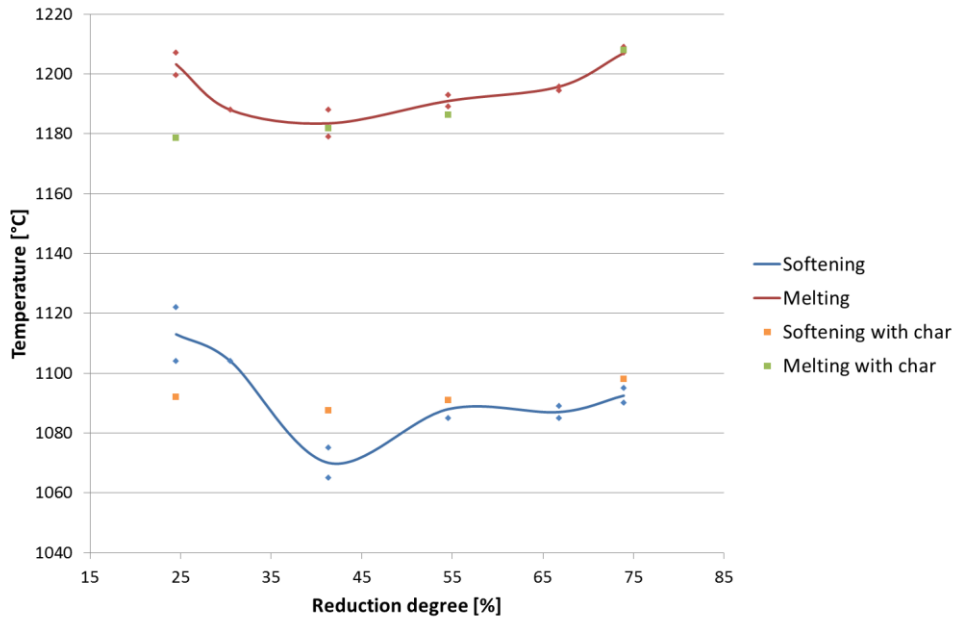


Figure 3.90: Softening results for sinter mixed with char

An explanation to this behaviour could be that the contact between char and sinter during the high temperature softening trial induced a complimentary reduction of the ferrous material even in the nitrogen inert atmosphere. In order to check this hypothesis, the material was recovered after the trials and re-analysed, in particular for what concerned the iron states. Results showed a clear increase of the reduction degree for all the tested material and lower the initial reduction degree, higher was the increase of reduction during the softening trial. These results are given on **Table 3.40**. The increase of reduction degree varied from 7.5% (for the lowest pre-reduced material) to 3% (for the highest pre-reduced one).

Table 3.40: Evolution of sinter reduction degree during softening trials

Reduction time [minutes]	Initial reduction degree [%]	Final reduction degree [%]	Reduction increase [%]
20	24.5	32.0	7.5
40	41.5	48.0	6.5
60	54.5	60.0	5.5
100	74.0	77.0	3

Therefore, the orange and green points of **Figure 3.90** could be moved in order to take into account the increase of reduction due to the char during the trial. This modification is depicted in **Figure 3.91**. In this case it could be observed that the points seemed to be quite well aligned with the ones of the reference curves. Nevertheless the behaviour was not exactly the same as, for the reference trials, the reduction degree of the sinter was constant during the whole trial when it was increased from initial pre-reduction degree to the final one for the tests with the char.

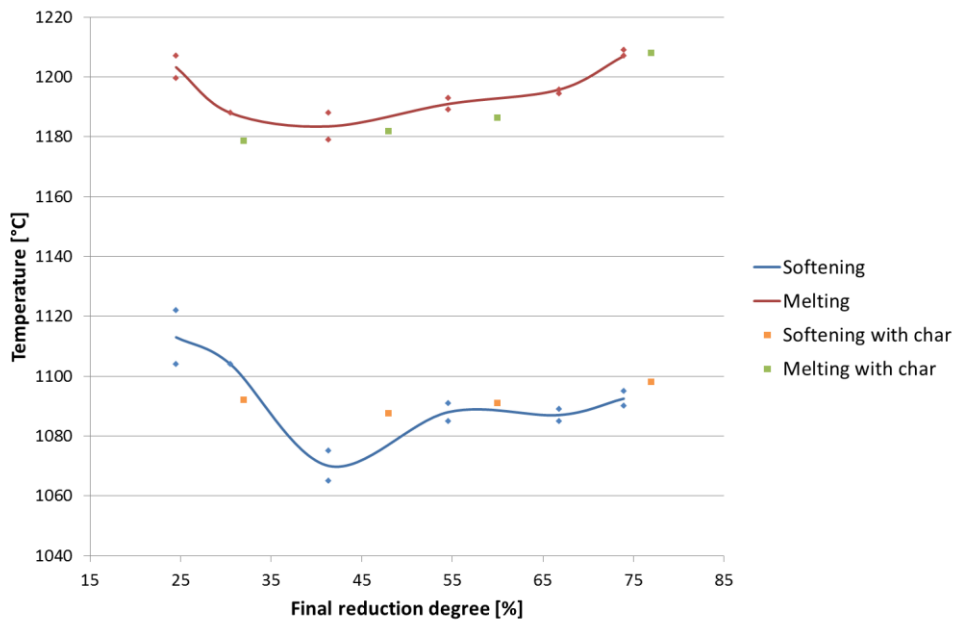


Figure 3.91: Softening results for sinter mixed with char taking into account complimentary reduction due to char

Finally, the average values of softening and melting temperature for all the final reduction degree were reordered as a single set of data and a polynomial trend line drawn for all of them in **Figure 3.92**.

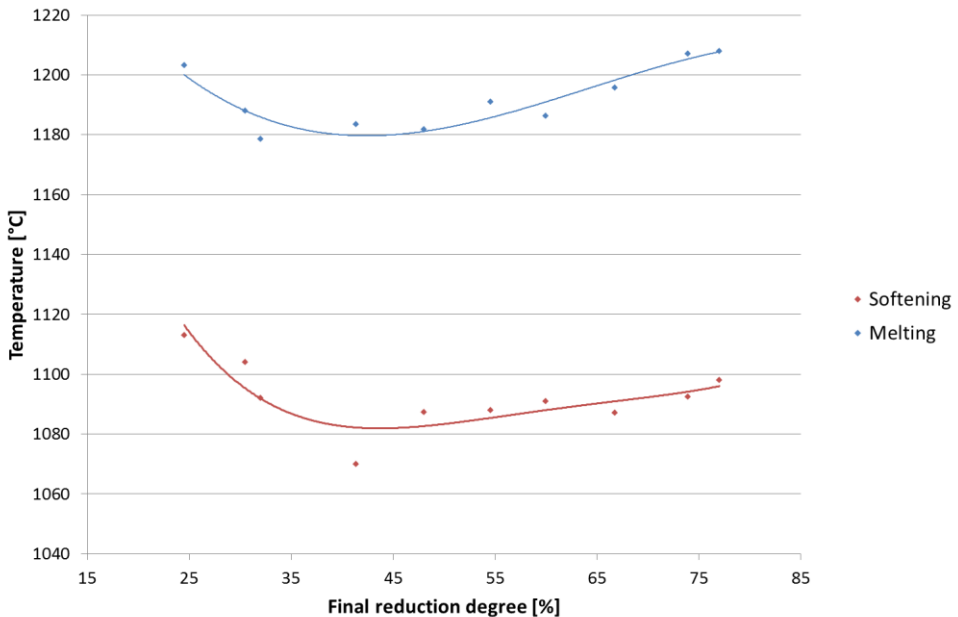


Figure 3.92: Softening results for sinter-char mixes and trend line

Micrographs of sinter samples after softening trials

In order to better understand the impact of the char on the behaviour of the ferrous burden during softening, several samples were analysed with microscope after softening trial. As could be seen in **Figure 3.93**, in the absence of char, an interpenetration of particles could arise, increasing the strength of the bed.

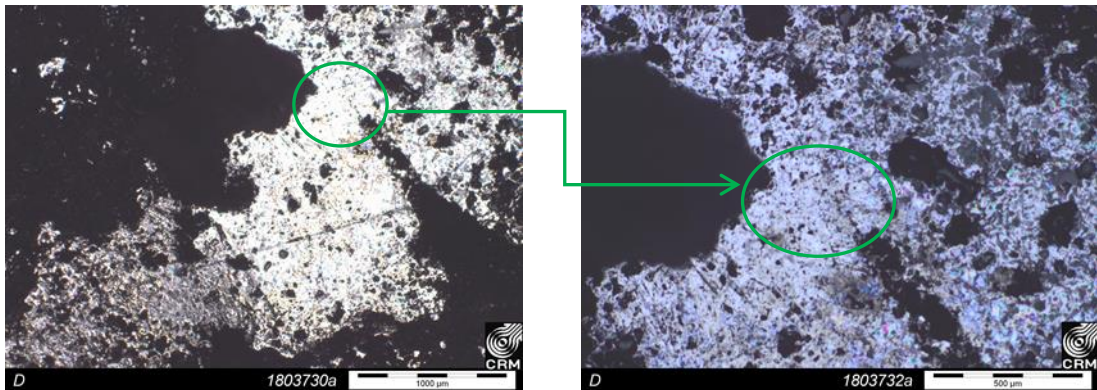


Figure 3.93: Sinter particles after softening trial without char addition

On the contrary, when char was added and covered the ferrous material as in **Figure 3.94**, it prevented the interlocking of the particles and favoured the slipping among them. Nevertheless, due to the very irregular shape of the particles, the overall mechanical impact was limited and locking still occurred.

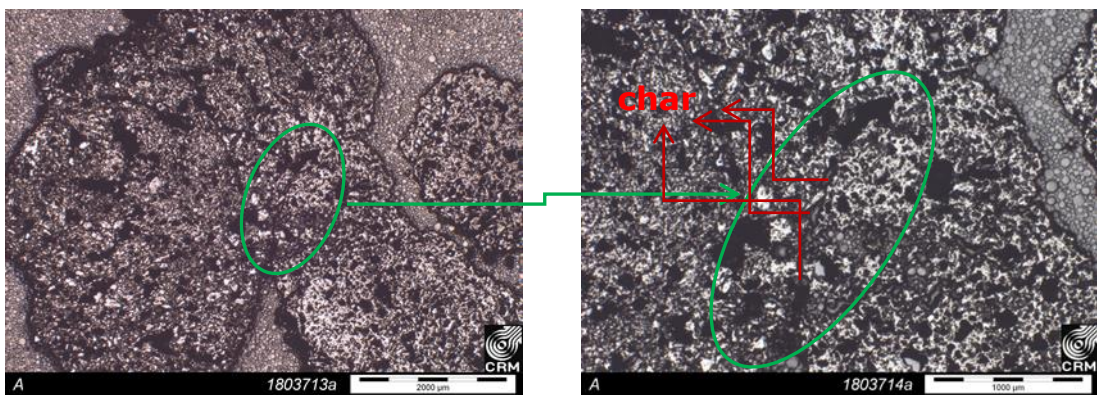


Figure 3.94: Sinter particles after softening trial with addition of char

Softening of sinter after HOSIM reduction

Selected sinter samples had been processed at Tata Steel IJmuiden with the HOSIM apparatus. For these trials, the sinter samples were covered with char before the HOSIM trial and several kinds of char were used. Results are given in **Figure 3.95**. It appeared clearly that the addition of char during the HOSIM reduction process increased the softening and melting temperatures but the impact could be more or less important depending on the char, CGC900 having the higher effect and CPC1300 the lowest one.

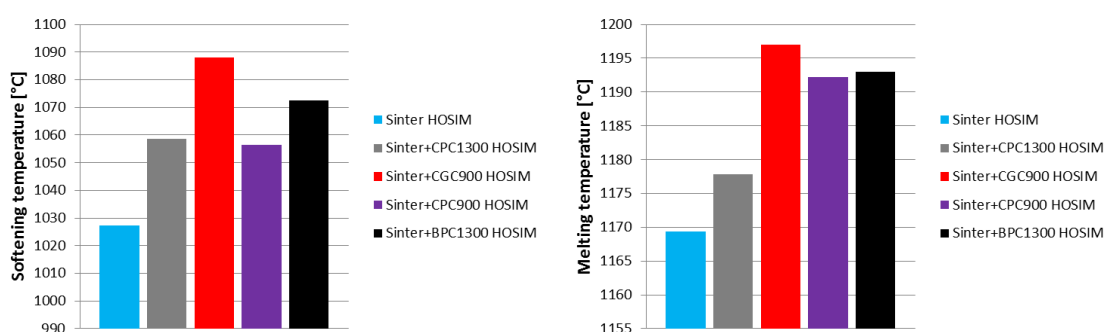


Figure 3.95: Softening (left) and melting (right) temperature of samples processed in HOSIM

Softening of pellets with addition of char

Similarly for what was done for sinter in **Figure 3.90**, **Figure 3.96** gives the softening results obtained with 125 g of crushed pellets mixed with 3 g of char considering the initial pre-reduction degree. Here, the impact of char seemed to be lower and even negligible except for very lowly pre-reduced material (~25%). Here again, it was observed that the reduction degree increased during

the high temperature softening trial due to contact between the carbon of the char and the ferrous oxides. The initial and final reduction degree obtained for the pellets are given in **Table 3.41** where it could be seen that the complimentary reduction was lower for the pellet than for the sinter, ranging from 5 to almost 0%.

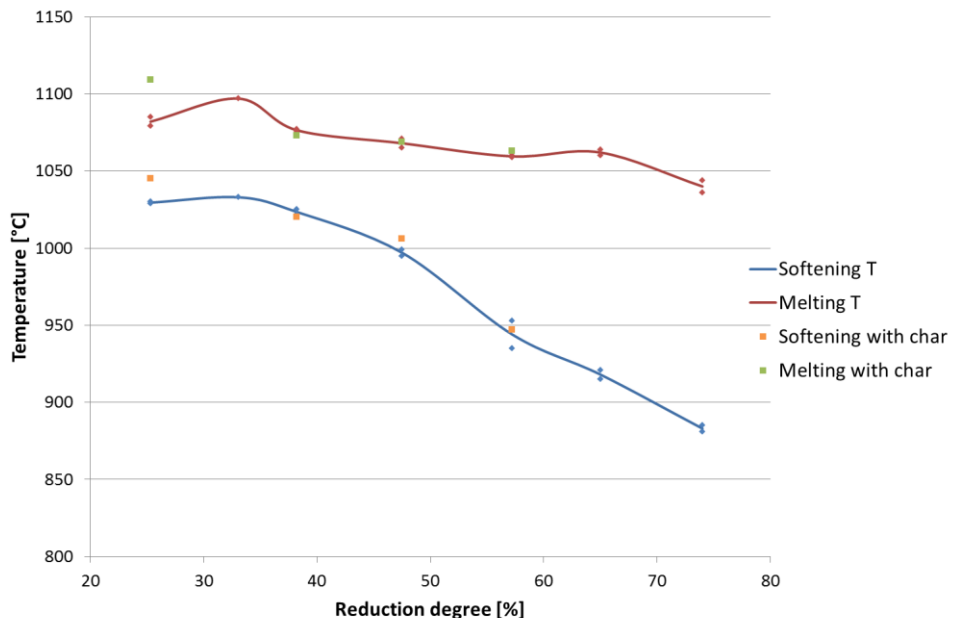


Figure 3.96: Softening results for pellets mixed with char

In **Figure 3.97**, the experimental points corresponding to trials with char addition (green and orange) were shifted to take into account the complimentary reduction due to char.

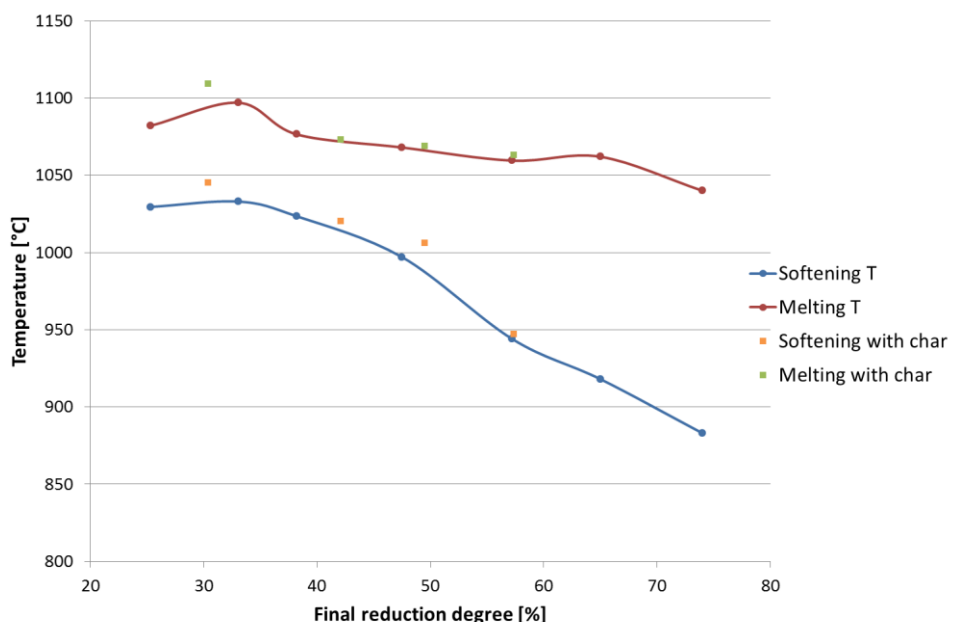


Figure 3.97: Softening results for pellets mixed with char taking into account complementary reduction due to char

Table 3.41: Evolution of pellets reduction degree during softening trials

Reduction time [minutes]	Initial reduction degree [%]	Final reduction degree [%]	Reduction increase [%]
20	25.5	30.5	5
40	38.0	42.0	4
60	47.5	49.5	2
80	57.0	57.5	0.5

As done for sinter, the average values of softening and melting temperature for all the final reduction degree were reordered as a single set of data and a polynomial trend line drawn for all of them in **Figure 3.98**.

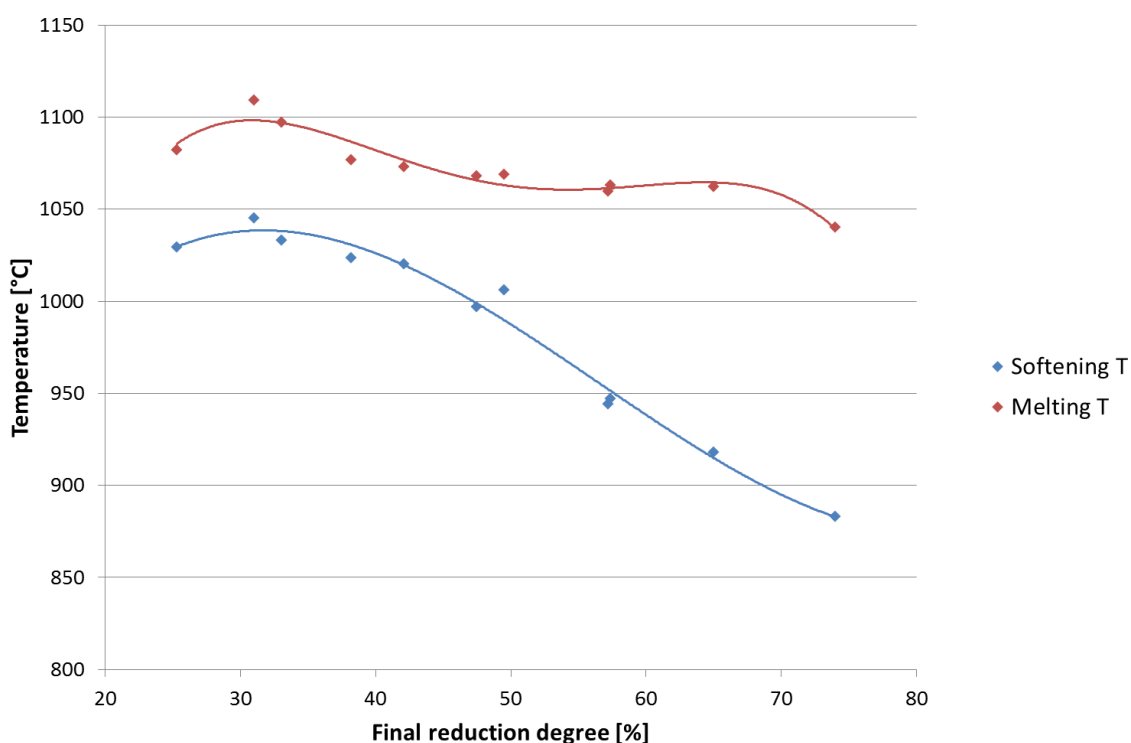


Figure 3.98: Softening results for pellets-char mixes and trend line

Micrographs of pellets samples after softening trials

Similarly to what was done for the sinter, pellets samples were analysed with microscope after softening trials. The conclusions were similar: without addition of char, sintering occurred among particles and created solid binds (**Figure 3.99**) when, with char addition, particles were kept isolated one from the other, thanks to the “coating” of char (**Figure 3.100**) but without massive impact on the global bed strength.

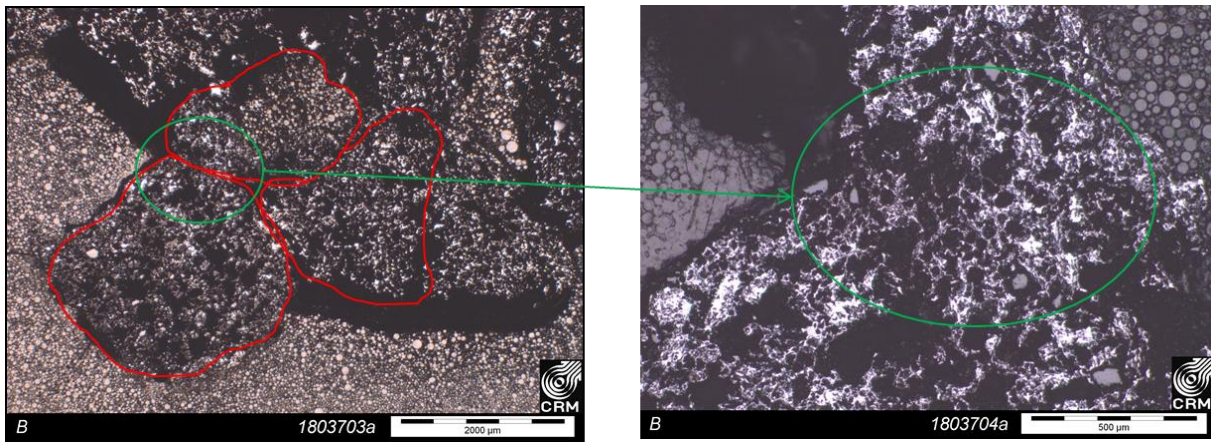


Figure 3.99: Crushed pellet particles after softening trial without char addition

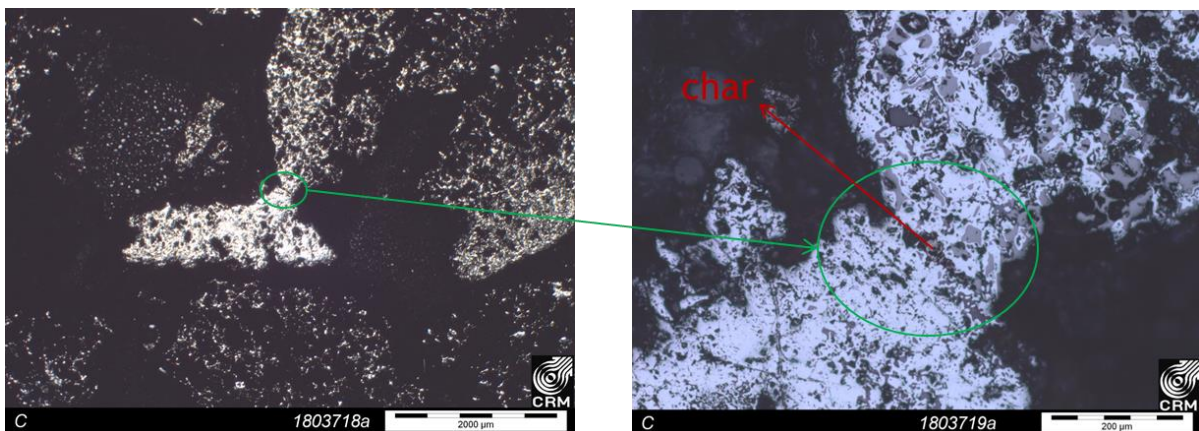


Figure 3.100: Crushed pellet particles after softening trial with addition of char

Softening of Pellets after IJSST reduction

Reduction trials had also been performed by Tata Steel using the IJSST tool. In **Figure 3.101**, the softening and melting temperature are given for pellets alone reduced in the CRM furnace and by the IJSST and for pellets mixed with char and reduced by IJSST. The reduction degree was 74% in every case. It appeared that the results were very similar for pellets alone whatever the reduction tool, but that the addition of char during the reduction step increased the softening and melting temperature.

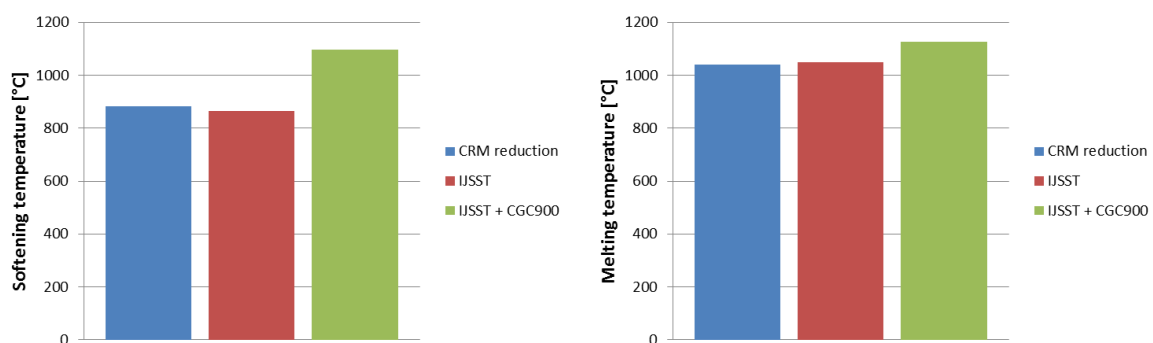


Figure 3.101: Softening (left) and melting (right) temperature of samples processed in IJSST

3.2.7.6 CONCLUSIONS

The objective of this set of softening trials was to study the impact of char hang-up inside the ferrous burden during its descent in the blast furnace shaft. It appeared that this char induced a complimentary reduction due to the contact of carbon with the ferrous oxides. This additional reduction was sensibly higher for sinter than for pellets due to the higher macro porosity of sinter.

The modification of the ferrous burden reduction degree could result in a displacement of the cohesive zone in the BF but this was quite hard to estimate as the trials procedure (reduction in a separate device and softening under nitrogen) was far from the actual BF behaviour.

3.3 Work package 2: Development of advanced measurement techniques for raceway monitoring

3.3.1 TASK 2.1 DEVELOPMENT OF TUYERE INSTRUMENTATION

The objective of this WP is the definition and optimisation of instrumentation arrangement and design of the tuyere instrumentation, based on the existing combustion models in FLUENT (minimised impact of the instrumentation on the gas flow and temperature maps compared to the other tuyeres). CRM measurements concern raceway atmosphere composition, raceway dimensions and coal movement. For a better understanding of the raceway conditions, adapted measuring techniques have to be developed in order to improve knowledge about these 4 topics:

- Movement of the char
- Raceway depth
- Gas chemical analysis
- Temperature of the raceway

Adapted techniques have to be implemented in harsh environment: hot gas (200 m/s, ~1050 °C) and hot raceway (2100-2300 °C).

3.3.1.1 GEOMETRICAL EVALUATION OF ACCESS POSSIBILITIES

A visit and a meeting were organised at Port Talbot blast furnaces. With the help of their drawings and some additional pictures, a CAD design was performed to assess the feasibility of the different accesses.

These accesses are the following ones:

- A) Through the cooling chamber of the tuyere. For this, the length of the endoscope is short (~1.5 m) but the diameter is very limited (about 15 mm) and a curved access is probably needed.
- B) Through a tube attached to the coal lance. The length of the endoscope is short (~1.5 m) and the diameter can reach ~3 cm or maybe more.
- C) Through a tube opposite (symmetry in a vertical plane) to the coal lance. The length of the endoscope is short (~1.5 m) and the diameter can reach ~3 cm or maybe more.
- D) Through the peep sight. The length of the endoscope is long (~3 m) and the diameter can probably reach ~4cm or maybe more for one part.
- E) Endoscope in 2 straight perpendicular parts (optically connected with mirror/prism):

The total length of the endoscope is long (1.5 m) and the diameter can reach ~3 cm.

Some contacts were taken with a supplier of industrial endoscope to evaluate what commercial solution could be investigated. Option A was preferred in terms of flexibility and size of field of view. Options B, C were preferred in terms of simplicity of mechanics and also because the critical part of the tuyere was not to be changed. Option D would have probably led to the least image quality because of the big length of the needed endoscope. Option E was probably the most difficult optically. Finally, option C was chosen and the endoscope was purchased by Tata Steel.

Geometrical evaluation of access points for the endoscope were additionally performed using ANSYS.

Addition option A: Through the tuyere cooling

This option had a big advantage: The probe or camera could be cooled with the tuyere cooling and the probe or camera would be able to detect the conditions close to the raceway. However a minimum diameter of the probe of 40 mm would still be required to cool down the tip sufficiently.

In order to explore this option, the cooling was first modelled. The results (**Figure 3.111**) show

that the water flows freely in circles around the cooler (**Figure 3.102**), before it exits the cooler.

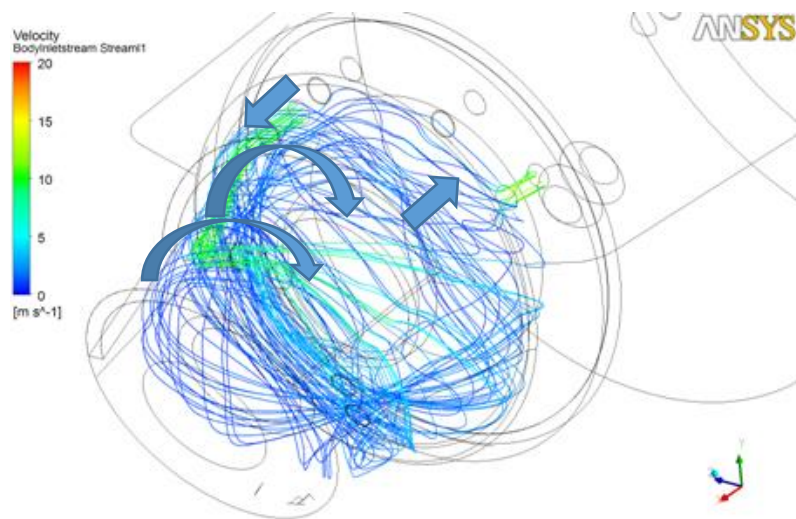


Figure 3.102: Circulation in the body of the cooler

The largest heat load was expected at the top of the cooler, so the best position for a probe would have been to penetrate the cooler at the bottom. But a cross section revealed that the copper was relatively thin compared to the thickness of the probe. This solution resulted in a reduced cooling water channel which would increase the resistance for the water to circulate around in the cooling, and result in hot spots on the cooling.

It became clear that either the nose tube was in the way, or the body water chamber became very small. As this option was not feasible, the probe needed to be placed on the outside of the cooling, also preventing a penetration of the nose cooling. But this would result in higher temperatures of the probe, as less cooling was available. The probe could withstand temperatures up to 1800°C, gases from the raceway would have a temperature of 2100°C or higher, so this position would be critical. This option would require a new tuyere cooling to be manufactured, as the additional copper needed to be added.

Addition Option B: Through a tube attached to the coal lance

This option would bring you directly at the correct position. But it would increase the diameter of the coal lance significantly. As the combustion depended on the mixing rate of the coal with the hot blast, this option would seriously influence the combustion of the coal. Because of the thickness of the new coal lance with probe, a turbulence would be created behind the new lance, increasing the mixing time of the coal with the hot blast. The refractory around the tuyere would also need to be adapted in order to facilitate the thick lance.

Addition option C: Through an additional lance

Contrary to the option of the peep sight, the probe or camera would only be exposed to the harsh conditions across a small distance. At the same time the coal lance would limit the view of the camera or probe and the probe will not be able to pass the coal lance, unless angle and position were changed (new design, new set up).

In an attempt to see what was possible, a geometric model was set up with the view angles of the camera (**Figure 3.103**) The grey surface is the outer boundary of what is seen by the camera.

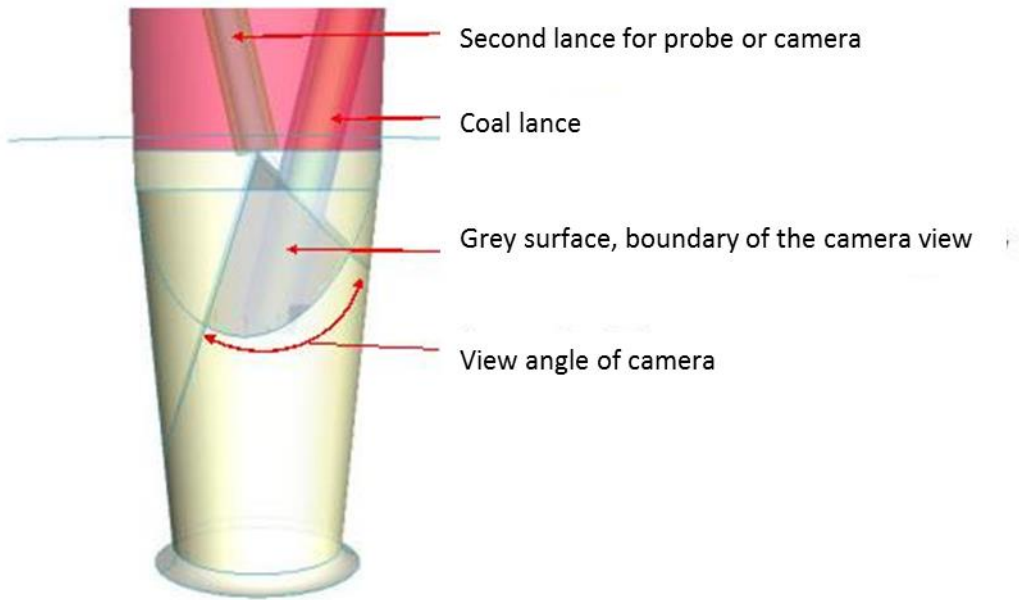


Figure 3.103: Camera views from the additional lance

The view angle of the camera was sufficient to show what happened close to the coal lance and further on. For optimisation, the position of the second lance could be changed, although the installation limits needed to be kept in mind.

Option D Through the peep sight

When a probe was inserted through the peep sight, the attached light sensor would be partially blocked. The probe would also need to be of a large length, in order to measure significant gases and temperatures. Limitation corresponding to the position with respect to that of the coal lance was also identified.

The angle of the peep sight tube also limited the view of the camera (**Figure 3.104**). (In blue is the outline of the peep sight and the orange circle is the exit of the tuyere.)

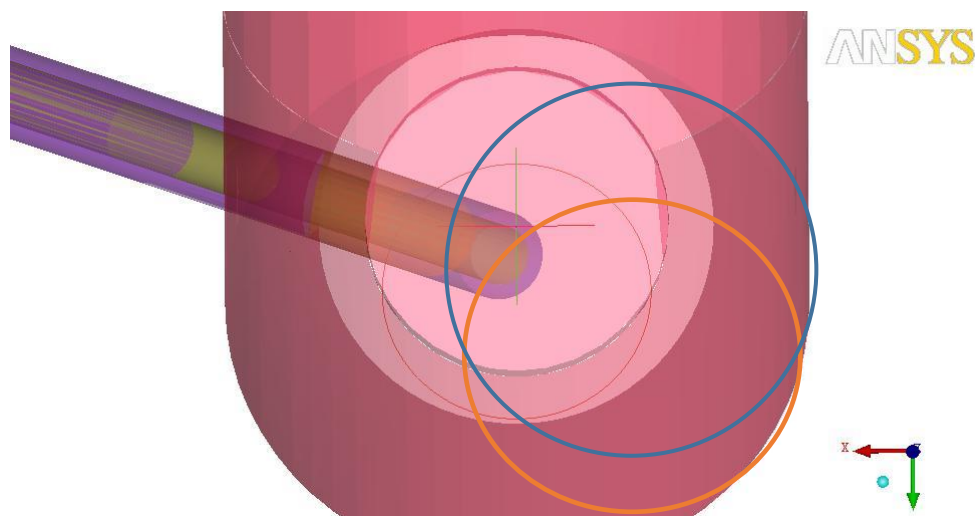


Figure 3.104: View from the peep sight (blue circle), orange circle is the exit of the tuyere

The above picture was created from straight in front of the peep sight. The picture shows that the bottom of the exit of the tuyere, cannot be seen with the camera.

The option of entering the blast furnace through the peep hole was therefore excluded.

According to the dimensions, an endoscope was purchased at the company MParts. A cooling unit was manufactured which was able to supply the necessary water supply and filtered pressurised

air/nitrogen to cool the tip.

It was planned to manufacture the according pipe work in the frame of the project to insert the probe on the opposite side of the coal injection pipe. However, due to time constraints for engineering a safe and operable system, the endoscope could not be used in CharFoCo.

3.3.1.2 MOVEMENT OF THE CHAR

This topic deals with the monitoring of the unburned coal, called char. Two aspects are important: the change in size and the direction of flow of particles.

A market study was performed. Different manufacturers were identified: Optronis, IDT, AOS Technologies, Photron, Allied Vision Technology, Dalsa, Vision Research, Jai, Vieworks, HSVision, SeeFastTechnologies, MegaSpeed Corp., PCO. Identified models were compared in terms of performance, speed, resolution, sensitivity and price.

The final choice fell on IDT NX8-S2. The specifications of this fast camera can be found in **Table 3.42**. This camera was tested in laboratory.

Table 3.42: Camera specifications

Manufacturer	IDT
Model	NX8-S2
Sensor	CMOS
Pixel size ($\mu\text{m} \times \mu\text{m}$)	8.7x8.7
Framerate / second (fps) (maximum)	4000
Max pixels number (H x V)	1600 x 1200
Min exposure time (μs)	1
Recording frames	5099

Figure 3.105 illustrates the relation between the Field of View (FOV) and the maximum particle speed that can be monitored with this camera. The particle is supposed to be detectable if its imaged size (PSz) is at least the size of one pixel. The FOV has to be adjusted to reach the resolution CR = FOV / PSz. The particle speed (PSp) is supposed to be detectable if the time necessary to grab the image is less than the time for the particle to travel a distance corresponding to half of the Field of View, i.e. time= 1/CS = IID / PSp with IID=1/2 FOV. CS is the camera speed (i.e. acquisition rate in frames per second).

In other words, when the particle size that has to be monitored increases, the FOV can be increased for the same camera resolution allowing an increased movement of particles ,and so a higher particle speed can be monitored. To fix the idea, with this camera, for a particle size of 0.1 mm, the FOV can be 160 mm and the maximum detectable speed particle is theoretically 300 m/s.

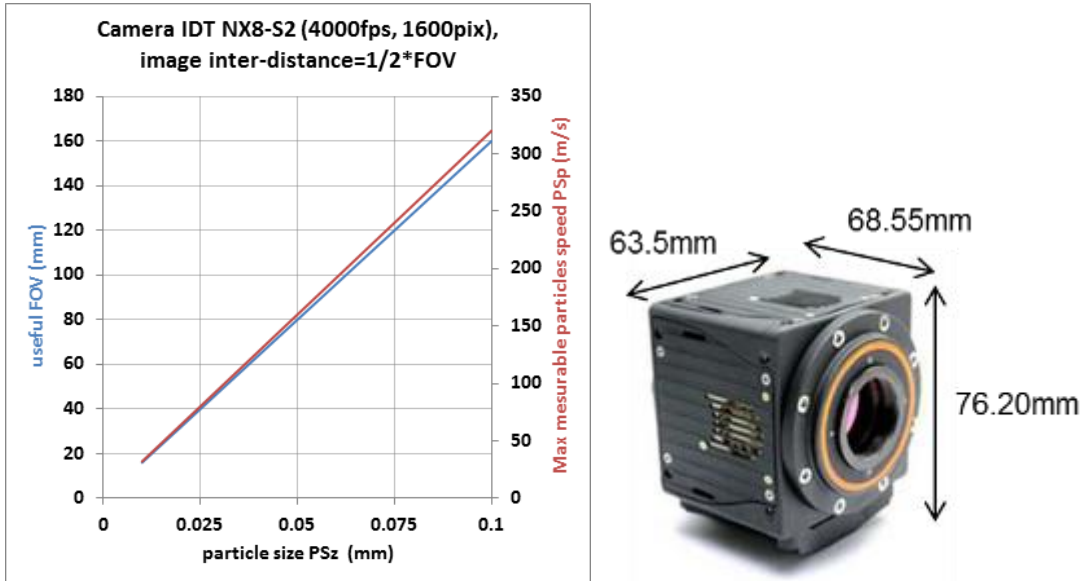


Figure 3.105: Relation between particle size, field of view and maximum particle speed for selected camera (illustrated on the right)

Test at Laboratory

The selected fast camera was tested during a trial on one of the CRM melting furnaces (**Figure 3.106**). A few recorded images are represented on **Figure 3.107**. Coke dust was injected to see the possibilities of this camera (in terms of speed and sensitivity) to visualize small particles and particle heaps displacements in a high temperature environment. The coke dust moving near the operator rod can be seen (top left and middle). Flame and fume could be observed without being disturbed by the surrounding intensive thermal radiation. A lot of sparks moving at very different directions and speeds were also present (top right). Their lifetimes were very different and less than 0.3ms for some of them. The speed of one particle, with a long lifetime was measured at 0.7m/s (bottom).

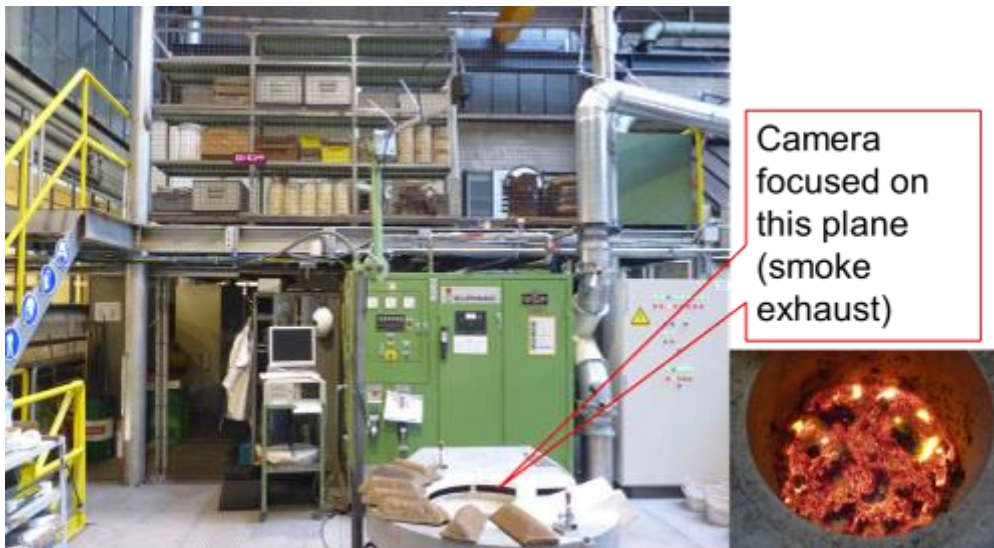


Figure 3.106: Fast camera installed on the CRM melting furnace

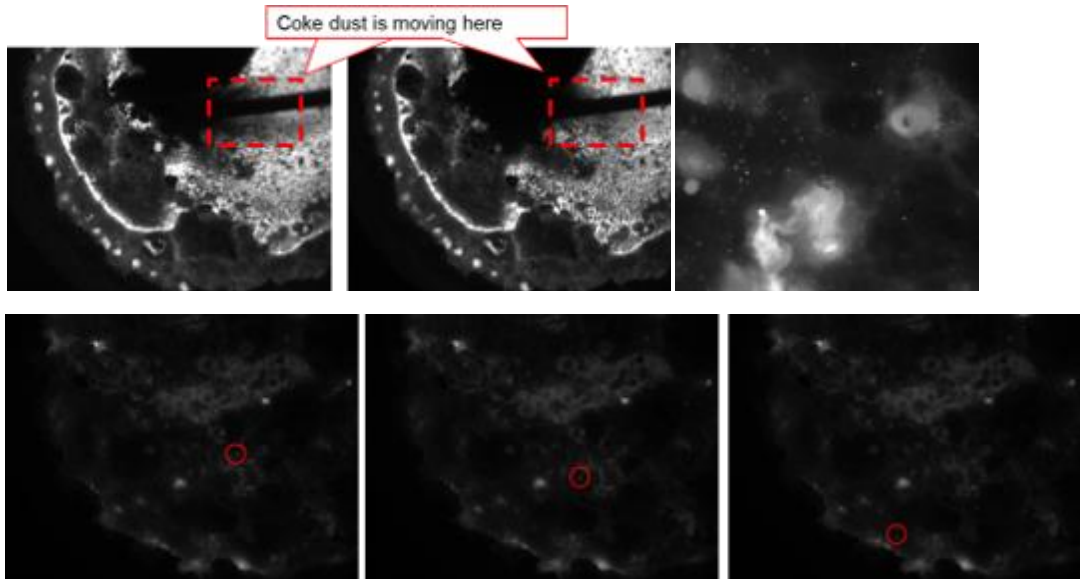


Figure 3.107: Images acquired on the CRM melting furnace with the selected camera: moving coke dust (top left and middle); flame, fume and sparks (top right); particle moving at 0.7m/s (bottom)

Software was developed to communicate and capture the pictures with the High speed camera and save them into a computer. This software enabled to change the settings of the camera (exposure time, width, height, number of saved pictures, and rate of data acquisition).

3.3.1.3 RACEWAY DEPTH

Laser distance measurements

A method, already tested for monitoring the liquid level on the blast furnace runner was re-used here for a longer distance measurement and a higher temperature environment (**Figure 3.108**).

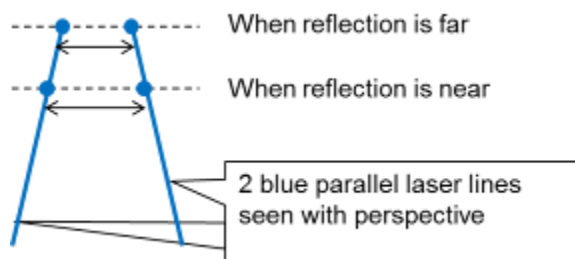


Figure 3.108: Method used to measure the depth of the raceway

This method consists in aiming the target point with two spaced laser lines. Depending of the distance at which the reflection (or diffusion) occurs, the apparent distance between the two spots will vary because of the perspective on the condition that the objective is not telecentric. This distance will be measured using a camera and automatic image processing.

The measurement system is composed by one camera, one blue laser ($\lambda = 465$ nm), one prism and one beam splitter/mirror (**Figure 3.109**). The laser beam is split into two parallel beams by the prism and targets the raceway wall.

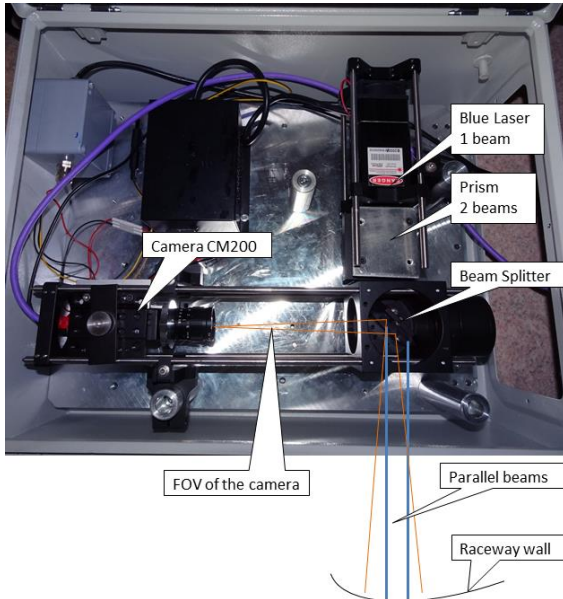


Figure 3.109 : Schematic of the raceway depth measurement

The depth of the raceway is known to vary between 1 and 1.5 m. The length of the path including the tuyere and the blow pipe is about 2.5m. So the total distance to measure will vary between 3.5 and 5m if this system is installed on the peep hole.

To verify this measurement, a theoretical law was calculated:

$\tan(\theta/2) = (\text{width} / 2) / \text{depth}$	$X = 1236 (0.02) / \text{width}$
$\text{depth} = 24.72 / \tan(\theta/2) X$	

X is the apparent distance, the depth is the distance between the camera and the raceway wall, 1236 is the number of pixels according to camera width, θ is the angular field of view, and 0.02 is the distance between the 2 parallel beams.

A comparison between the theoretical apparent distance and the apparent distance obtained by image processing showed an average difference of 7 pixels. A calibration table would be used to convert the apparent distance into raceway depth.

This measurement system was tested in laboratory. Software was developed to communicate with the camera and to save the images at 1 Hz, an automatic processing was created to calculate the raceway depth from the picture.

Radar distance measurements

In 2017, two radar sensors Vegapuls 64 were purchased by Tata Steel. These radar sensors use a lens to bundle the radar stream which is a novel technology. Radars with an opening angle of 14° and 7° were purchased and tested at a cold rig, built at Tata Steel,. Commissioning trials with the radar were performed at the cold rig

3.3.1.4 GAS ANALYSIS

Classical NDIR optical gas chemical analysis is performed with an absorption measurement inside a chamber filled with a gas. A laser emitter is installed at one side and a spectrometer at the other side to analyse the transmitted light.

Here, this method was not usable because only one side of the chamber (the raceway) was accessible. So, an emission measurement had to be performed.

Emission bands were identified at around 1.18 μm for the CO, around 1.43 μm for the CO₂ and around 0.76 μm for O₂. Sensitivity had to be checked considering that the intense thermal radiation will affect the dynamics of the spectrometer. Overlapping emission bands from other gases had to be also checked.

This measurement system comprises two fibres and two spectrometers, the range of the spectrometers are 300 nm to 1100 nm and 900 nm to 2100 nm.

After analysis, an overlapping with other chemical contents prevented any CO/CO₂/O₂ detection at those wavelengths (300 nm-2100nm). In this range, the measurement system detected alkali contents (Na, Li and K).

Based on Hitran data, the peak intensity for CO₂ is equal to 5.86×10^{-23} at 1.43 μm and is equal to 3.54×10^{-18} at ≈ 4 μm.

The peak intensity for CO is equal to 1.56×10^{-23} at 1.18 μm and is equal to 4.54×10^{-19} at ≈ 4 μm. In order to detect CO and CO₂ contents, a new measurement method was developed; this method would be sensitive at higher wavelengths (≈ 4 μm) as the peak intensity is higher at ≈ 4 μm.

An automatic processing was developed to calculate the element variation and ratio. The ratio is the intensity of the peak (Counts/ms) divided by the first intensity of the peak for a measurement, ratio is dimensionless. The critical part of this measurement was the calibration. It could only be done at high temperature to get an emission and currently no method is implemented at BF to determine CO₂ and CO.

The processing takes into consideration the limits of the measurements. The first limit is the saturation which is the maximum intensity of each wavelength (Counts), the maximum is around 65000 counts for each wavelength of each spectrometer. Second limit is sensitivity of the spectrometer; this limit is taken into account by a restriction of the average. A too small average meant that the spectrometer is not sensitive enough and the ratio Signal/Noise is too small.

3.3.1.5 TEMPERATURE

This temperature measurement is combined with the spectrometric gas analysis. The raceway will be considered as a black-body. So the Planck's law (**Figure 3.110**), giving its spectroscopic thermal radiation, can be directly fitted on the measurement. This will be used to calculate the local temperature of the raceway. Nevertheless, the raceway is known to present large temperature gradients and temperature variations. So, the location and stability of the aimed target point can have a big influence on the results. The interpretation of the measurements has to take this into account.

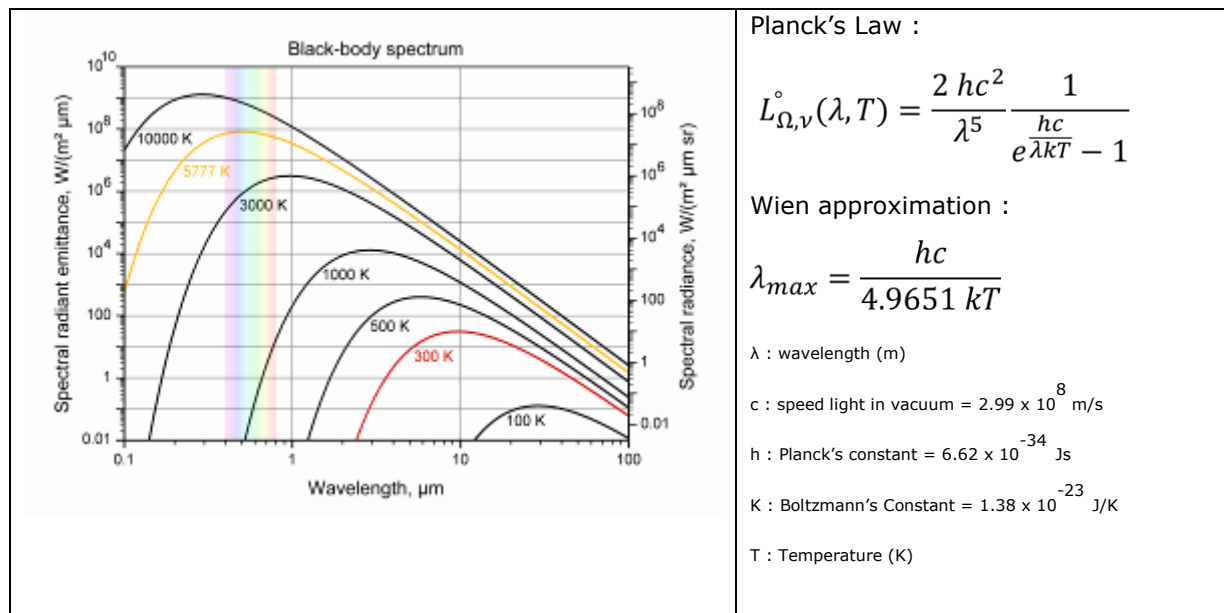


Figure 3.110: Thermal radiation emitted from a black-body

A calibration was done in CRM to transform the spectrum into the Planck's law. Once the Planck's Law is known due to the Wien approximation, the maximum is linked with the temperature.

3.3.2 TASK 2.2 CFD CALCULATIONS FOR EVALUATING THE CONDITIONS AT THE INSTRUMENTED TUYERE

The CFD calculation that AMMR was supposed to do in this task for supporting the design of the instrumented tuyere was finally taken over by Tata Steel for confidentiality reasons.

CFD calculations based on ANSYS CFX are a classical tool at Tata Steel and can be used for different purposes, among which are the evaluation of flows and thermal conditions in different devices. For this project, two types of simulations were performed.

First calculations were used to predict the temperature contours of the tuyere cooling. The aim was to see whether it was possible to put a probe through the cooling.

The second set of simulations involved the tuyere and combustion. The aim was to verify the simulations using the measured pressures and the raceway depth, so that later, a prediction could be made of how much coal burned and how much char was left.

3.3.2.1 METHODS

The drawing of the tuyere and cooling would be reconstructed in Ansys Designmodeler as far as possible, based on 2D Autocad drawings provided by the constructor of the tuyere.

Boundary conditions for the simulations of the cooling were estimated, as little information was available and the conditions being harsh.

For the second set of simulations, boundary conditions were taken from a period in which radar measurements were performed. From the data available, 5 significant cases were simulated and a trend was determined from these results.

Simulations on the tuyere cooling

Several designs of the tuyere cooling are found in literature. The design for Port Talbot involves a large body chamber and an additional nose cooling. The body chamber is used to cool the top of the cooler, which receives the highest heat load (**Figure 3.111**).

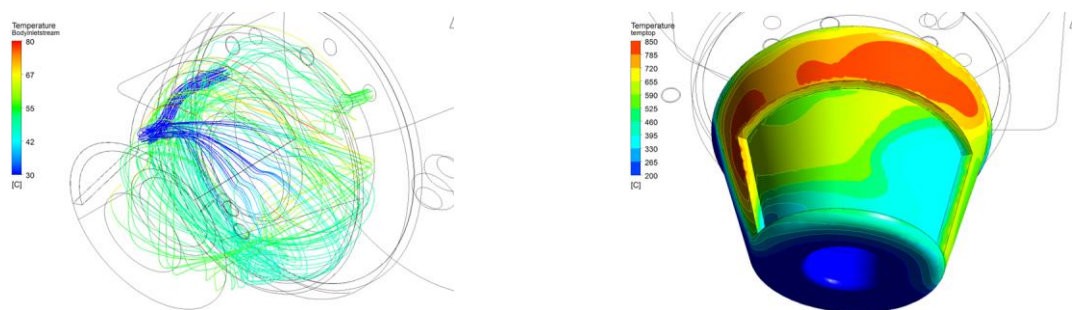


Figure 3.111: Cooling water streamlines and copper temperatures of tuyere cooler

Several variations of the boundary conditions showed that the highest temperature was always on the top. Lowest temperatures could be found on the bottom of the tuyere, which led to the conclusion that the probe must be placed at the lower side of the cooling. From the streamlines it became clear that the top could only be cooled sufficiently, when the body chamber was intact. Free flow is essential for the cooling.

3.3.3 TASK 2.3 TESTS WITH INSTRUMENTATION AT COBESI FOR THE TUYERE INSTRUMENTATION

Two meetings and a visit were organised at the COBESI (**Figure 3.113**) to discuss the details of a trial. The objectives of this trial were:

- To demonstrate that the laser spots can be reflected enough towards the camera and that the apparent space can be used to calculate the raceway depth
- To demonstrate that some absorption/emission peaks in the Near infrared can be used to estimate CO or CO₂ content
- To realise optical measurement of gas at flanges T1, T2, T3, T4, T5, T6.
- To demonstrate that some particle movement or mass flow can be observed with the fast camera

A trial was organised with standard COBESI configuration (the second chamber (with T1, T2, and

T3) is empty) and the first chamber (with T4, T5, and T6) is filled with coke) as in **Figure 3.112**, where the following prototypes were tested:

- Raceway depth (reduced) through the axial flange (peep sight),
- Gas analysis through side flanges T1, T2, T3, T4, T5, T6,
- Movement of particles through side flange T3, T4, T5 and T6.

During this trial, the different measurements were realized as described in **Table 3.43**.

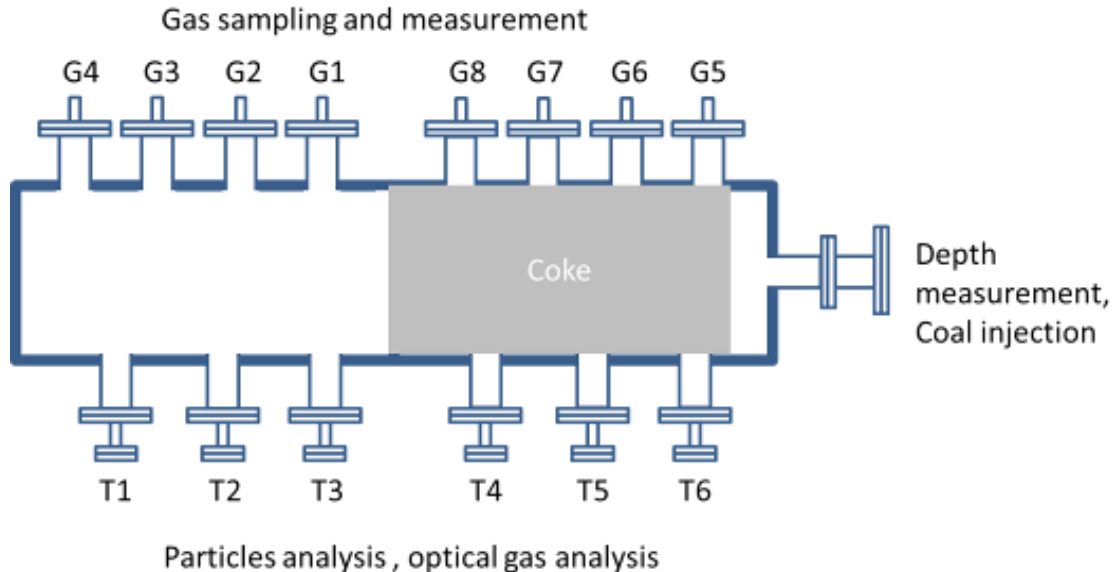


Figure 3.112: COBESI instrumentation

Table 3.43: Time scheduling of the trial at COBESI

Heating period		30 min of trial with stabilised conditions						Cooling period	
		5 min	5 min	5 min	5 min	5 min	5 min		
NO injection	Coal	Coal injection						NO Coal injection	
Depth measurement (peep sight)		gas analysis (T1)		gas analysis (T2)	gas analysis (T3)	gas analysis (T4)	gas analysis (T5)	gas analysis (T6)	
particle analysis (T6)				particle analysis (T5)	analysis (T4)	particle analysis (T4)	analysis (T3)		

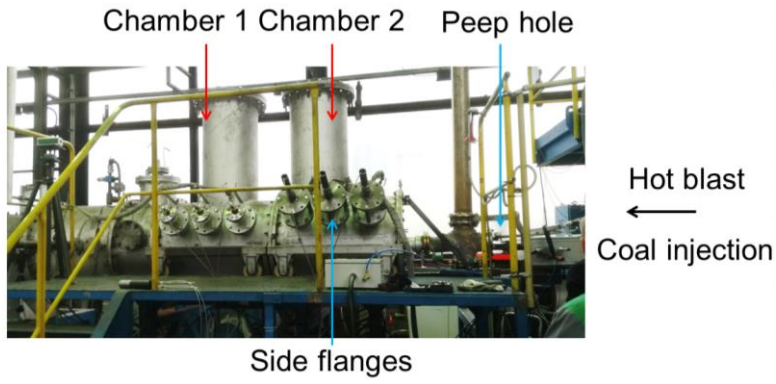
Results at COBESI

A trial was performed in RWTH in Aachen on the 4th April 2017 to verify the measurement method and to make a first acquisition in harsh environment. Dedicated mechanical adaptations were built for this trial.

The fast camera was used for the COBESI trial through the side flanges (**Figure 3.113**). During the trial, several high frequency measurements were realised. Those measurements showed the movement of some bright and dark particles (**Figure 3.114** & **Figure 3.115**). The high frequency was 11507 Hz and the low frequency was 5 Hz. The movement of the particles was not noticeable with the low frequency.

The time between two pictures is 8.69×10^{-5} s for the high frequency and 0.2 s for the low frequency. With the high frequency, the same particle was seen on several pictures. The calculation of the velocity was based on those several pictures, **Table 3.44**.

Along the width, 1472 pixels characterize 2.5×10^{-2} m and along the height, 400 pixels characterize 6.8×10^{-3} m.



Chamber 1 : empty Heating :3-4 hours
 Chamber 2 : full of coke Stabilised conditions :30 min

Figure 3.113: COBESI Description

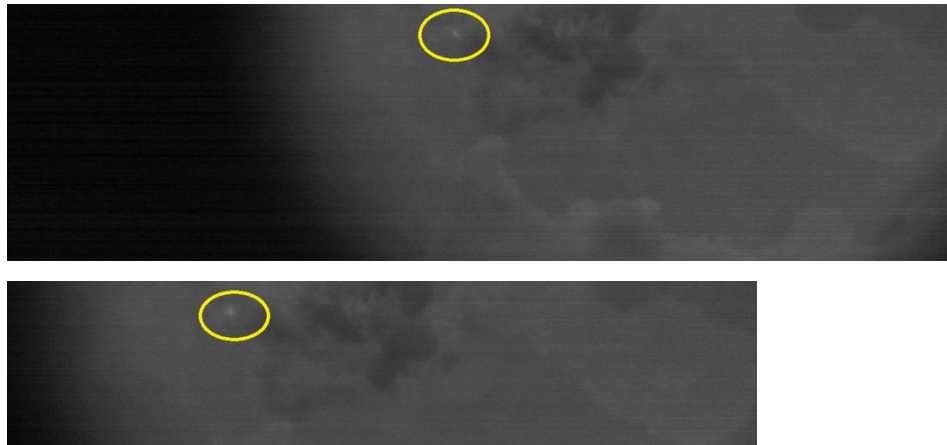


Figure 3.114: Bright Particle



Figure 3.115: Dark Particle

Table 3.44: Properties of the particles

	Bright particle	Dark particle
Height (pixels)	10	6
Height (m)	170×10^{-6}	102×10^{-6}
Width (pixels)	10	7
Width (m)	170×10^{-6}	119×10^{-6}
Speed along the height (m/s)	0.391	0.78
Speed along the width (m/s)	2.93	2.15

The raceway depth measurement was placed through the peep hole along the blast axis and injection direction (**Figure 3.116**).

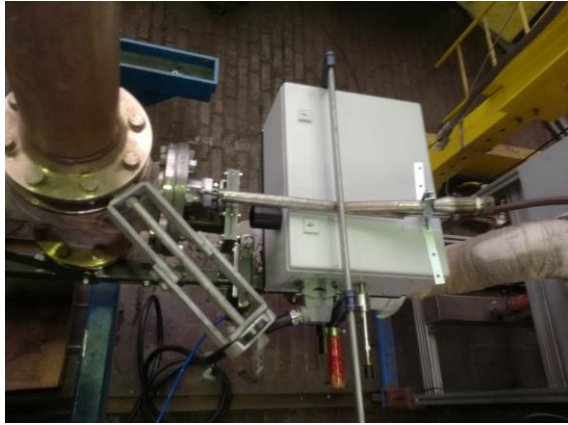


Figure 3.116: Raceway Depth measurement system at COBESI

The results of this trial are shown in the chart below (**Figure 3.117**):

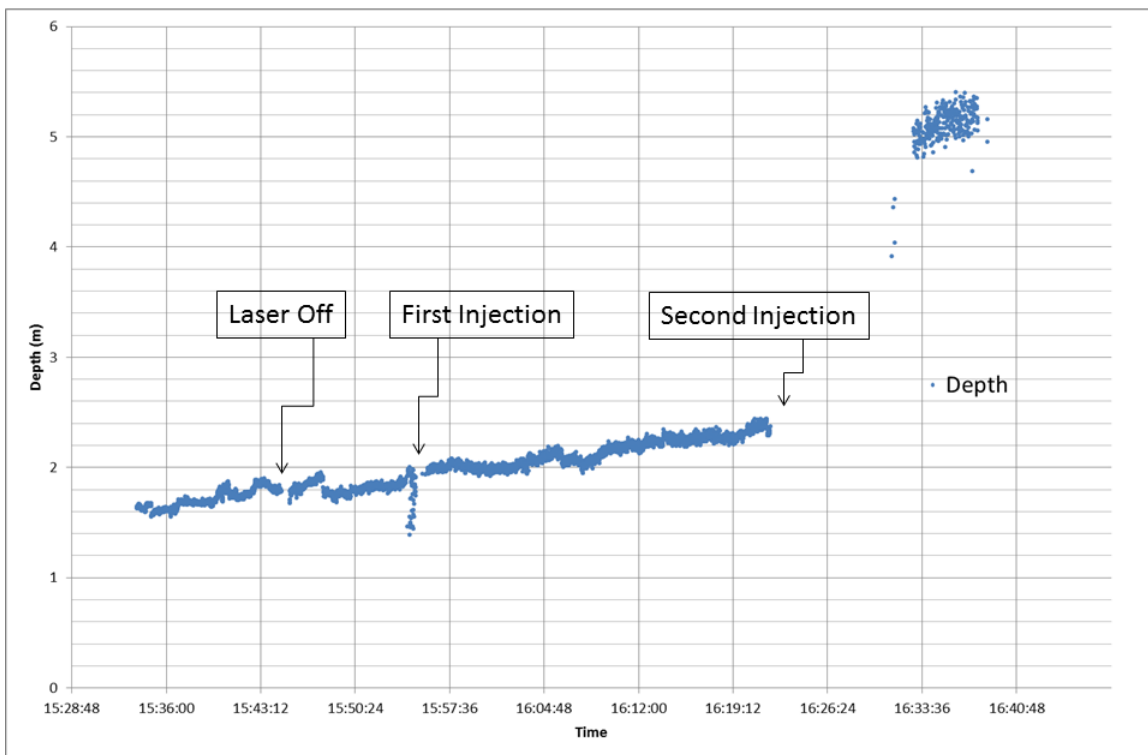


Figure 3.117: Depth evolution during COBESI Trial

As a reminder, the two parallel beams are targeting the coke wall inside the chamber 2 (**Figure 3.113**), the depth is the distance between the camera and the target (coke wall). The distance of 1.6 m was consistent with preliminary measurements. The depth increased which meant that the coke was consuming along the blast direction. Some gaps/blanks are visible in the chart. For several pictures, the contrast between the dots and the background was not sufficiently high and the automatic processing could not calculate the depth (**Figure 3.118**). During the injection, the intensity of the two dots was weaker than without injection due to the diffusion effect. After the second injection (16:30), a (probably partial) collapse of the coke bed was observed and the measured distance corresponded very well to the depth of the furnace. The fluctuations in the measured depth at this stage were due to the image processing limitations combined with the low intensity of the laser dots at such a long distance.

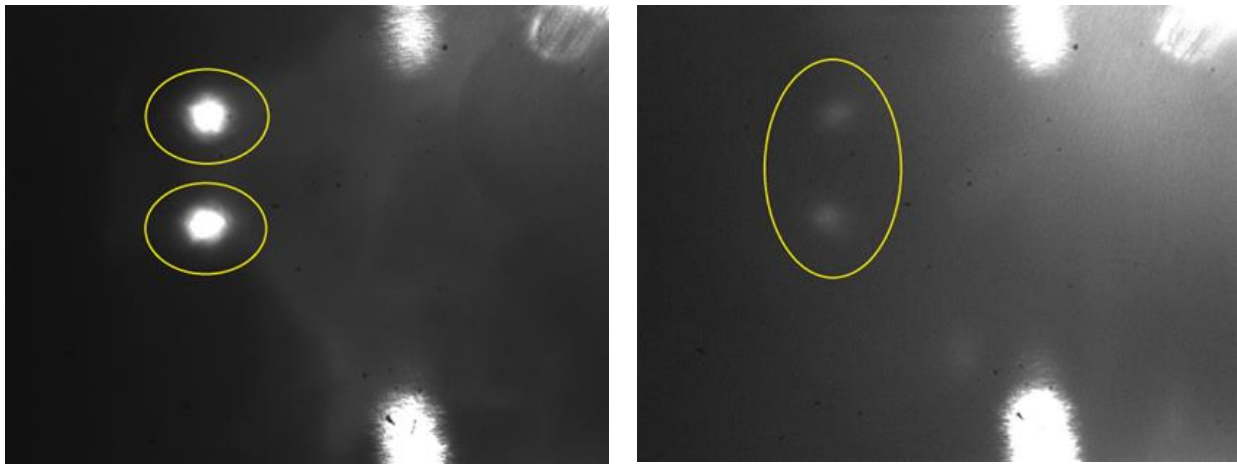


Figure 3.118: Laser Dots

On the left, the dots were clearly defined. On the right the noise was higher and the dots were more difficult to distinguish.

The fibres were placed through the side flanges (**Figure 3.113**). Three areas with emission peaks were detected (**Figure 3.119**). The last area comprises a double peak which is characteristic of potassium.

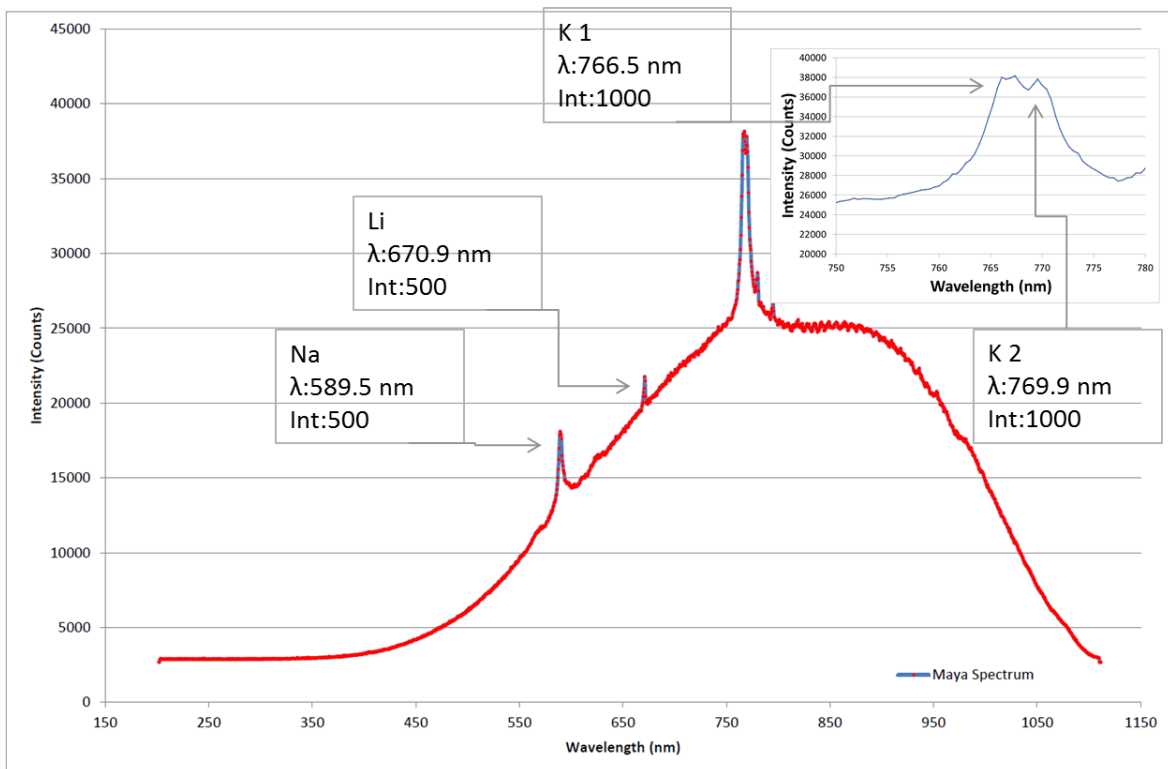


Figure 3.119: Alkalies emission peaks

The goal of the processing is to calculate the intensity of each peak during the trial. This intensity depends on the quantity of the element, the intensity of the spectral band and the sensitivity of the spectrometer.

Several measurement were performed, the results before the first coal injection is shown below (**Figure 3.120**).

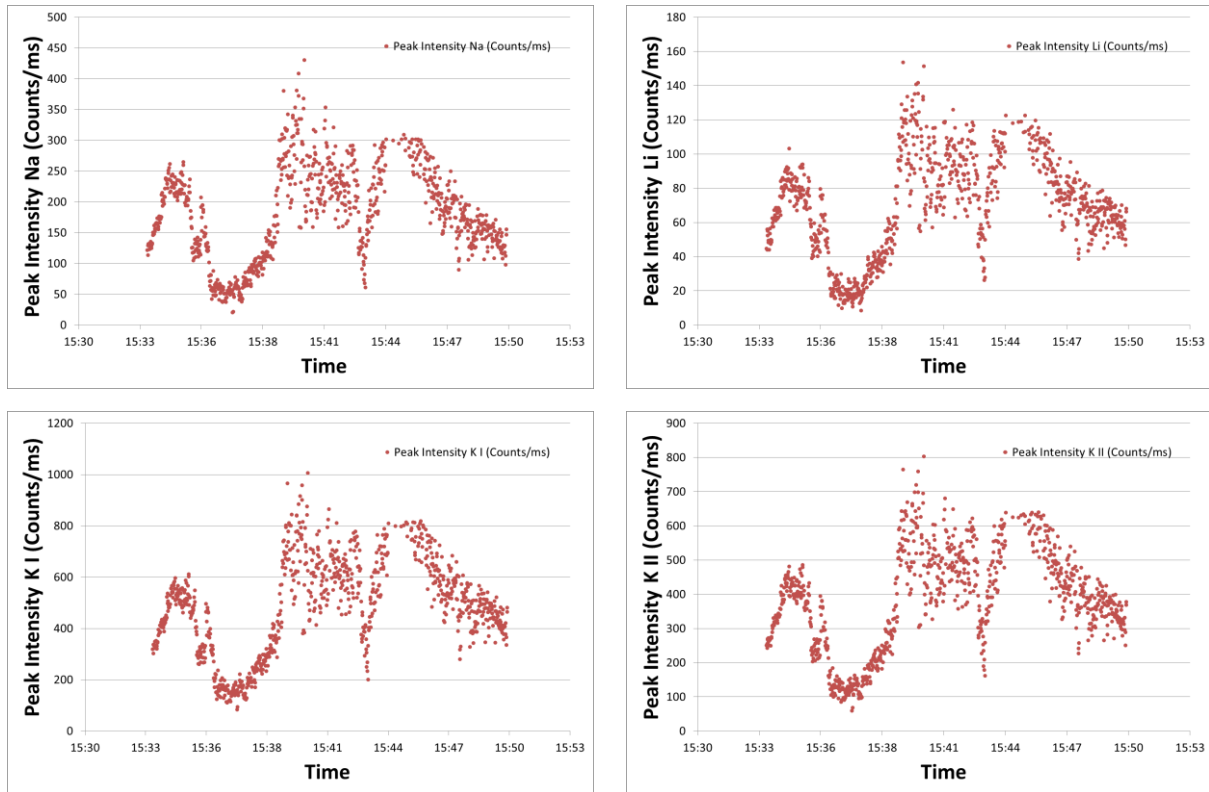


Figure 3.120: Alkalis intensity before first injection during COBESI trial

During this period (14:32 to 14:49), the alkalis varied in the same way. The first peak of potassium (K1) was higher than the second (K2), the sensitivity was higher for this peak. The intensity of the Na peak was two times smaller than the K2 peak due to the fact that the intensity band for Na (500) is two times smaller than the intensity band for K (1000). This was also linked with the quantity of Na and the sensitivity of the spectrometer. The intensity of the Li peak was low, the quantity of Li and the sensitivity could explain this.

The results after the first injection are displayed in **Figure 3.121**.

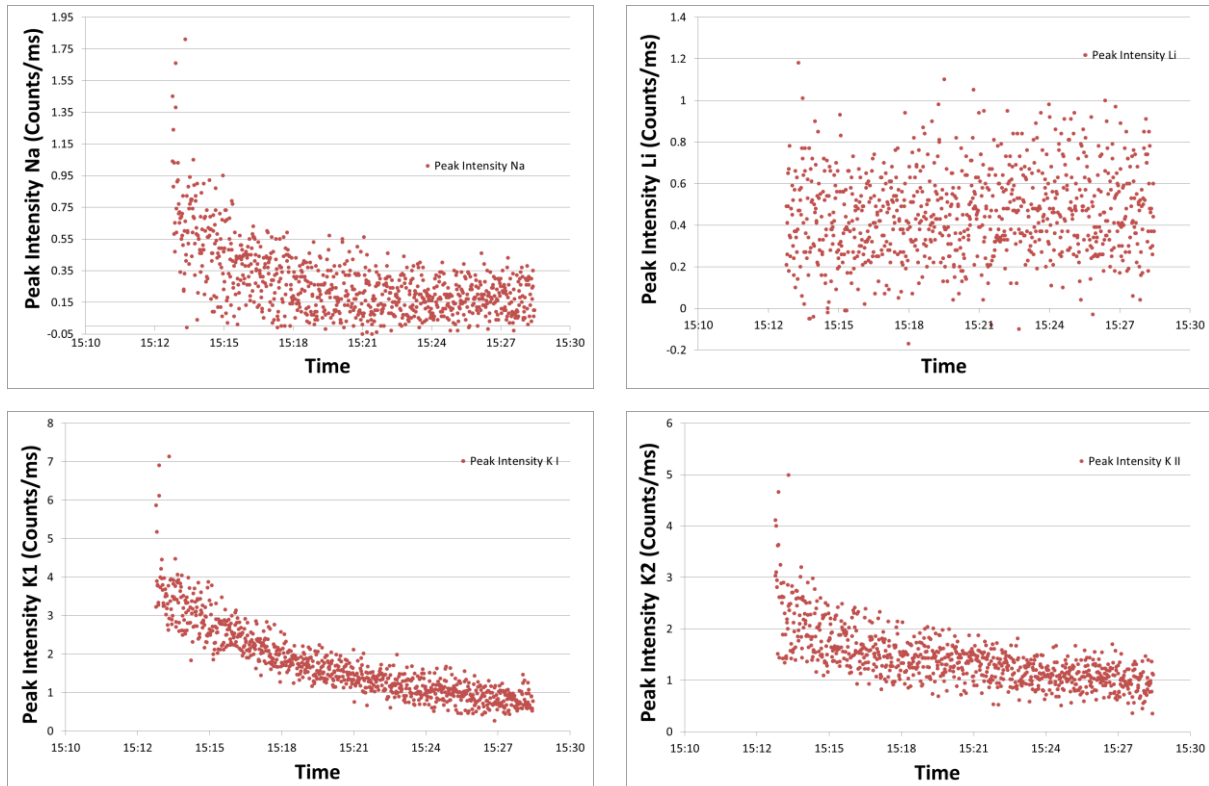


Figure 3.121: Alkalis intensity after first injection during COBESI trial

For all alkalis, the intensity was too small to consider any presence. This low intensity signified that

during injection the alkalis were consumed and no peaks were detected.

Temperature variation before the first injection is presented in **Figure 3.122**

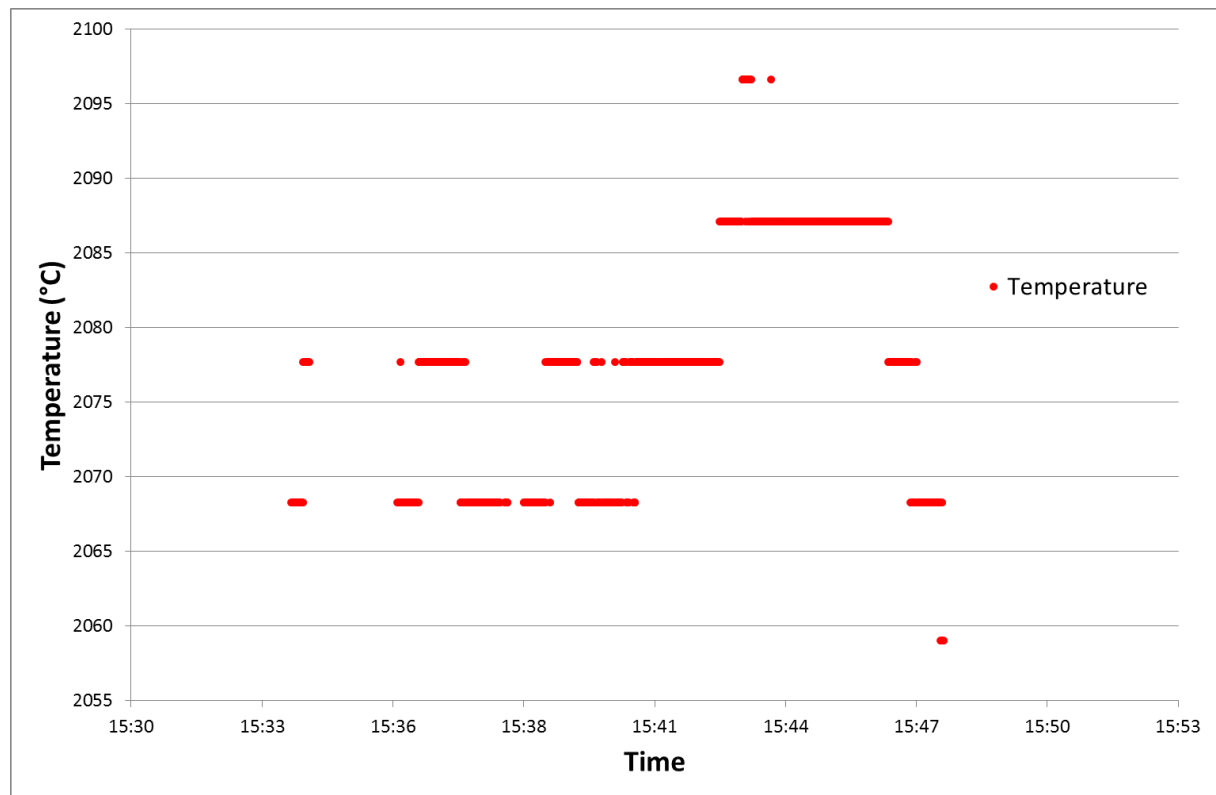


Figure 3.122: Temperature variation before injection during COBESI trial

The temperature was around 2075°C which was realistic and only 256 temperatures were possible with this measurement as the spectrometer had only 256 pixels.

The temperature after the injection could not be determined because the integration time of the spectrometer was too high and the noise at this integration time was also too high.

3.3.4 TASK 2.4 COMMISSIONING OF TUYERE

The different methods were adapted to proceed to the industrial tests. New mechanical adaptations (supports, positioning systems,..), electrical command and electrical design were developed to support the harsh environment of the Blast Furnace.

3.4 Work package 3: Blast furnace tests

The general objectives of WP3 are:

- to investigate raceway conditions at high coal injection rates;
- to evaluate the extent of char transfer within the blast furnace shaft;
- to understand the limiting factors regarding coal injection and consumption and propose solutions to overcome them.

More in detail, specific aims of this Work Package are:

- to analyse raceway conditions, coal behaviour and relate them to plant data to improve BF data usage;
- to investigate raceway conditions with focus on conversion of coal particles in the raceway, char evolution and interactions with coke;
- to generate input data for laboratory injection tests and the comprehensive blast furnace model (MOGADOR);
- to measure the thermo-chemical conditions in the shaft of a blast furnace with high PCI-rate;
- to develop a technology for dust sampling over the radius and the height of the blast furnace to investigate how high char rises in the BF shaft;
- to investigate bottlenecks for coal injection rate increase to work around those;
- to perform tuyere coke core boring and tuyere coke racking samplings.

3.4.1 TASK 3.1 BLAST FURNACE TESTS WITH INSTRUMENTED TUYERE

3.4.1.1 OBJECTIVES

The main objective of Task 3.1 is the application of measuring techniques developed in WP2 at a blast furnace in order to gain new information on coal conversion in the raceway and raceway conditions and phenomena

3.4.1.2 METHODS

The industrial blast furnace trials at different coal injection rates should be supported by tuyère measurements using a thermo-vision camera (TVC). This camera is also used at pilot trials at the COBESI plant in Task 2.3. The camera is suitable to measure the surface temperature in range of 800 – 3000°C at pilot and industrial facilities; the frequency makes up 60 Hz (60 images/sec). The software is used to calculate the temperature field distribution.

The TVC was used during a 2-day BF trial conducted at Port Talbot BF 4. Different BF conditions were applied. On the first day, different coal injection rates with high oxygen enrichment were applied. After the measurements, oxygen enrichment was decreased until the next day to ensure more stable conditions.

Coal ignition and conversion in the raceway and particle movement were used by CRM to investigate, which way char particles leave the raceway. The radar sensor and the laser – distance measurement were used to determine the raceway size during two measuring campaigns at Tata Steel Port Talbot.

Process calculations and comparisons with laboratory tests were carried out.

3.4.1.3 CONDUCTED WORK

Two measurement campaigns were performed at BF 4 in Port Talbot. The first on 4./5.12.2017; the second on 05./06.03.2018. During the first campaign, RWTH performed thermo vision camera measurements; CRM performed spectrometer and laser measurements and Tata Steel performed radar measurements. The second trial was performed with the radar raceway size measurement for clarifications of open questions from the first trial.

3.4.1.4 RESULTS

Thermal vision camera results

Thermal vision camera recorded the change of temperature profile with changing coal injection rates. Process parameters are shown in **Table 3.45**.

Table 3.45: Scenarios for TVC at Port Talbot

Tuyere	Changed condition	PCI at tuyere	Calculated rate/ tHM	Oxygen enrichment	Blast temperature, °C
9	Change of coal injection rate	25 kg/min	200	8	960
		12.5 kg/min	100		
		0	0		
		12.5 kg/min	100		
		25 kg/min	200		
		0 kg/min	0		
		25 kg/min	200		

Figure 3.123 shows temperature distribution at different injection rates during scenario 1. By decreasing the injection rate, a decrease in coal plume size could be recognized. Furthermore, the cold part of the coal plume decreased significantly in size. The background should mainly consist of raceway coke. Its radiation intensity increased when injection rate decreased. When coal injection was turned off, a higher background temperature radiating from the coke could be observed. After turning the coal injection back on, the background temperature initially stayed high and subsequently decreased to its original state.

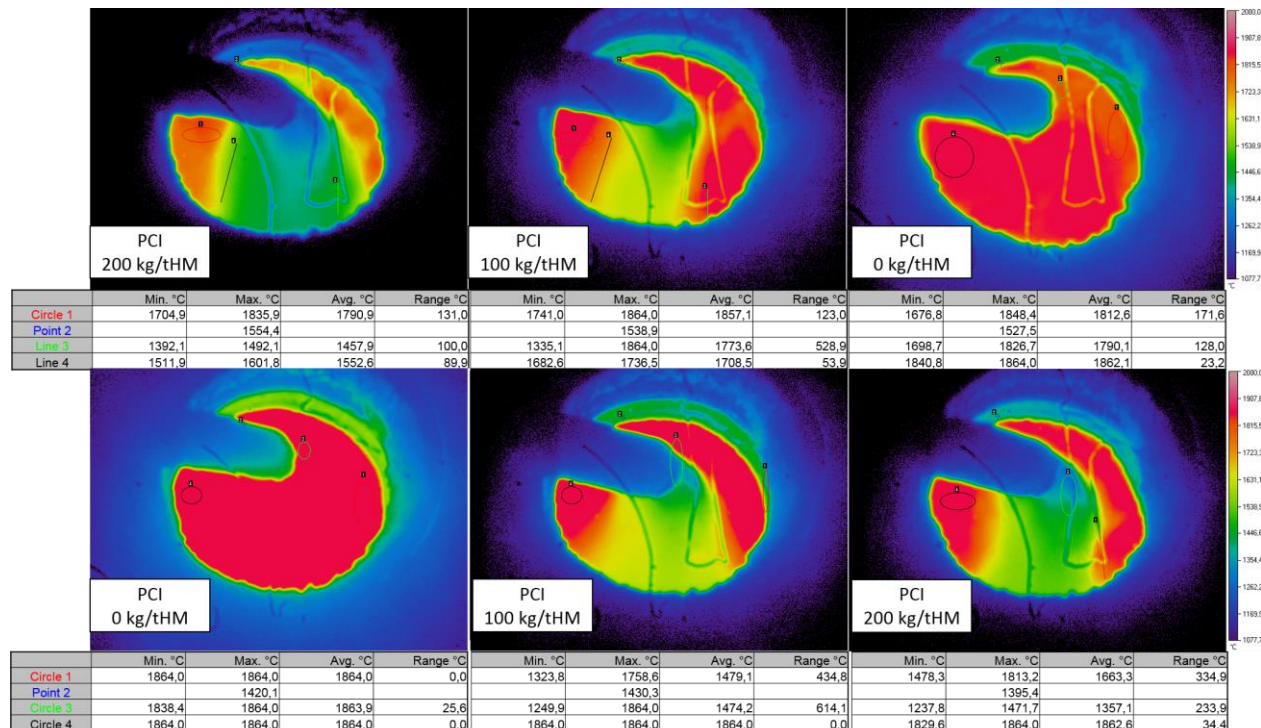


Figure 3.123: Images of TVC at different coal injection rates (scenario 1)

Figure 3.124 shows the specific regions of interest (ROI), used for data quantification and comparison. **Table 3.46** shows the ROI and its purpose for this measurement.

Table 3.46: ROI for TVC and its purpose

ROI number	Area description	Purpose
1	Injection lance	
2	Coal plume free area	Influence of coal injection rate on coke background radiation
3		
4	Coal plume centre	Change of coal plume centre
5	Coal plume periphery	
6		Influence of different parameters on coal plume shape and stability
7		
8		
9	Area around plume	
10	Area of tuyère without injection lance	overview
11	Area of tuyère with injection lance and tuyère tip	Change over overall tuyère temperature

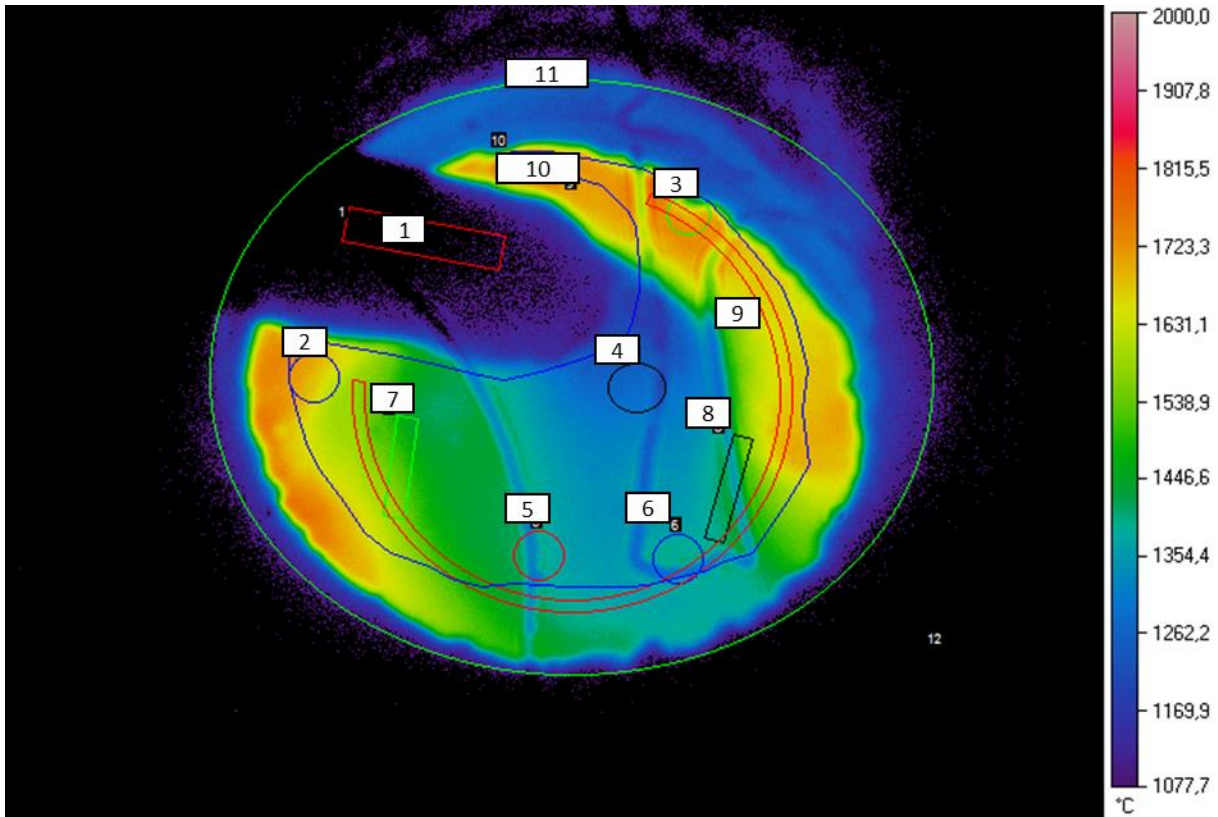


Figure 3.124: Overview of regions of interest for temperature measurement at a Port Talbot BF tuyère

Figure 3.125 shows a clear increase in temperature when decreasing injection rate from 200 kg/t HM to 100 kg/t_{HM}. When decreasing coal injection rate to 100 kg/t_{HM}, an increase of around 130°C was detected. When stopping coal injection, temperature increased by approximately 450°C.

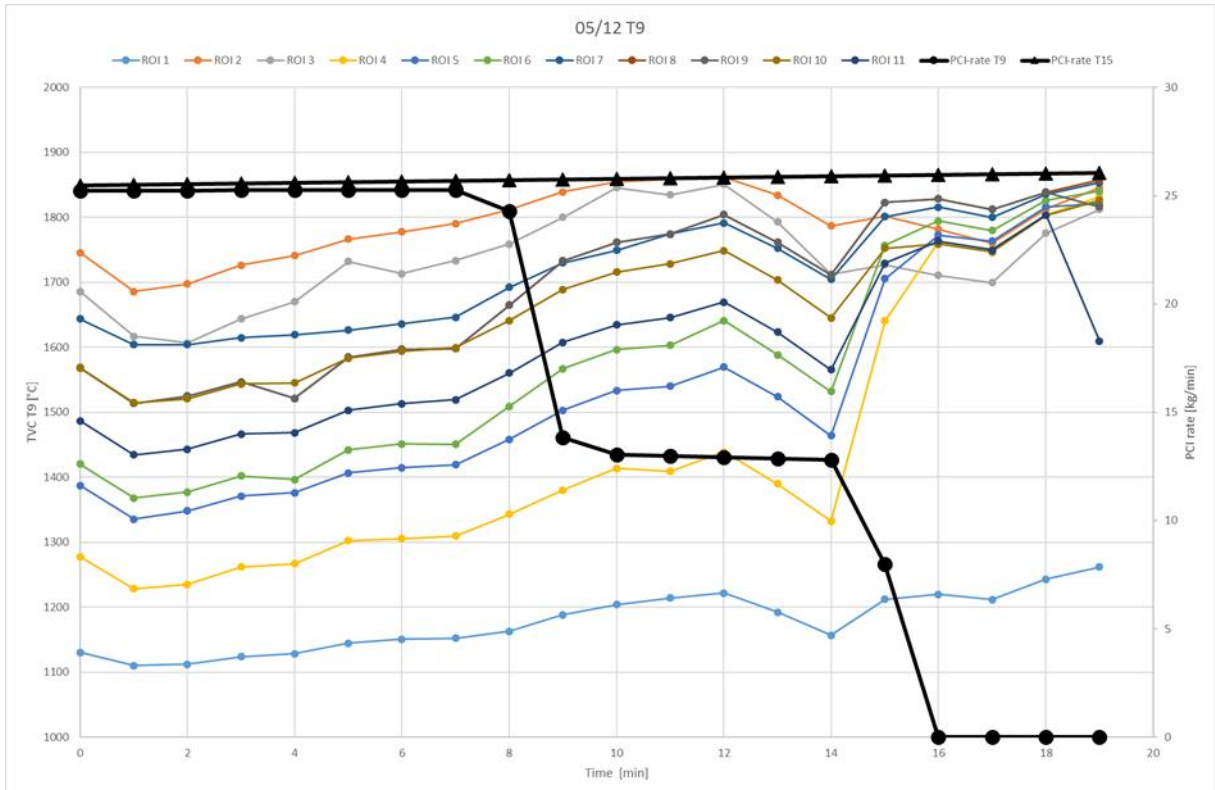


Figure 3.125: Temperature development at tuyère 9 with change of injection rate at tuyère 9

Right before stopping the coal injection, a small temperature decrease was detected. This change could be explained by the increase of hot blast rate right before the temperature drop, shown in **Figure 3.126**. This temperature drop exceeded 80 °C.

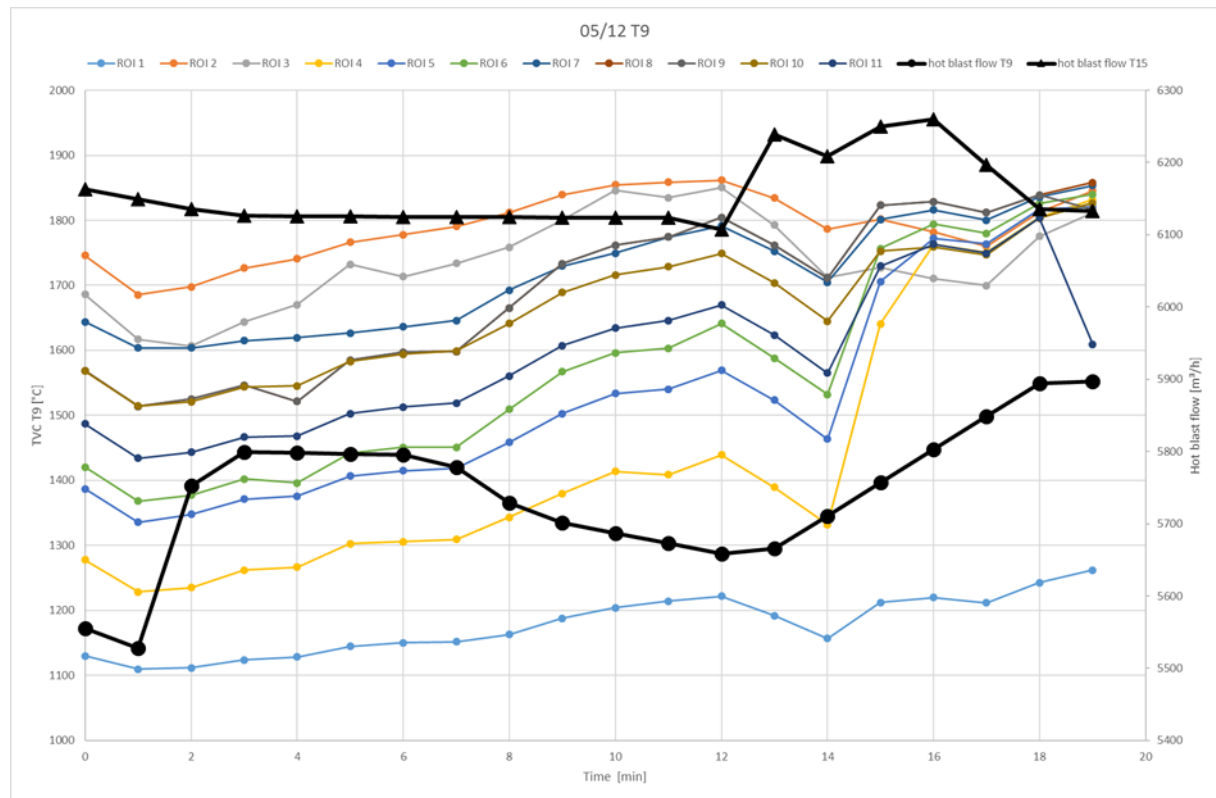


Figure 3.126: Temperature development at tuyère 9 with increasing hot blast rate at tuyère 9 and 15

Results of TVC measurements indicate the significant impact of even minor changes of BF process parameters such as hot blast volume on coal injection behaviour.

Temperature & Alkali contents

The fibres for the spectrometric measurements were placed in front of the peep holes. Measurements were performed at different tuyeres, as well as process conditions. (**Figure 3.127**)



Figure 3.127: Fibres at Port Talbot

The spectra are collected every second, process parameters are given per minute. A minute average is therefore used for data comparison. The chart (**Figure 3.128**) illustrates the original temperature (second values).

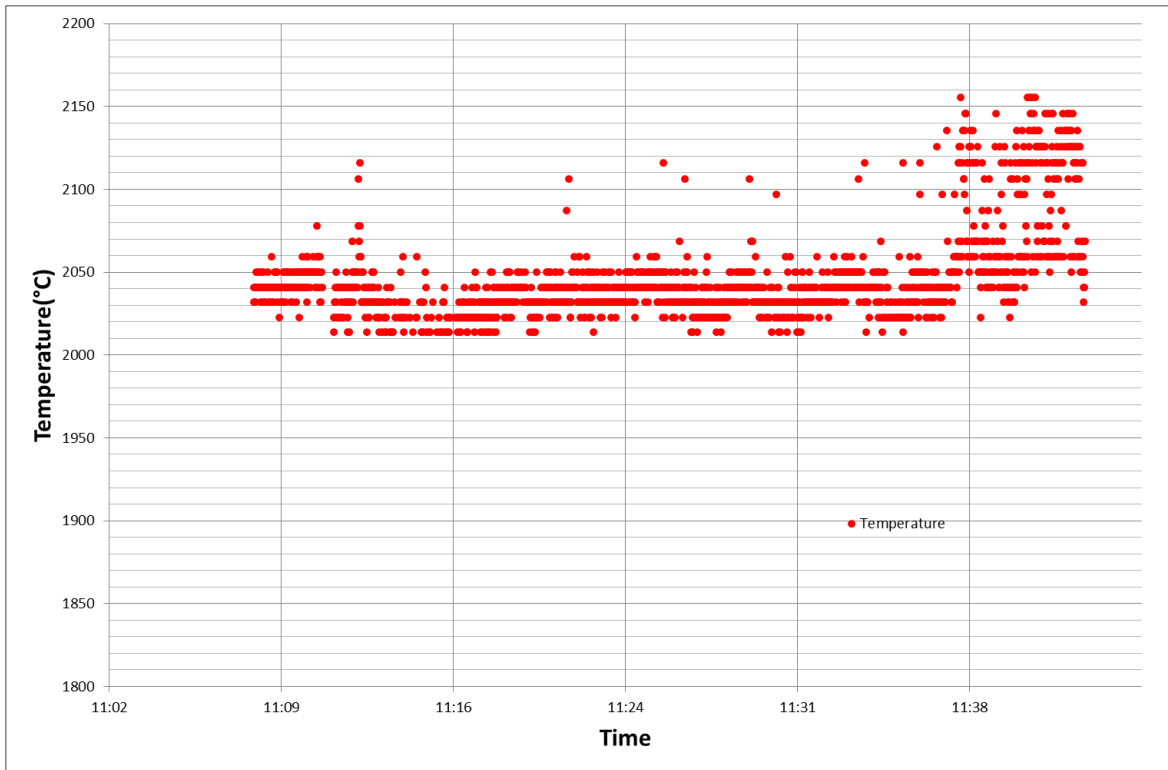


Figure 3.128: Temperature evolution at tuyere 12 in BF4 PT

This specific measurement was performed between 11:08 and 11:43 on 5th December 2017. The average temperature of 2045°C is a realistic value, indicating the proof of concept of the technique. During the whole measurement, the temperature was stable, as no major process changes were found. The comparison between the temperature and coal injection rate is shown in **Figure 3.129**.

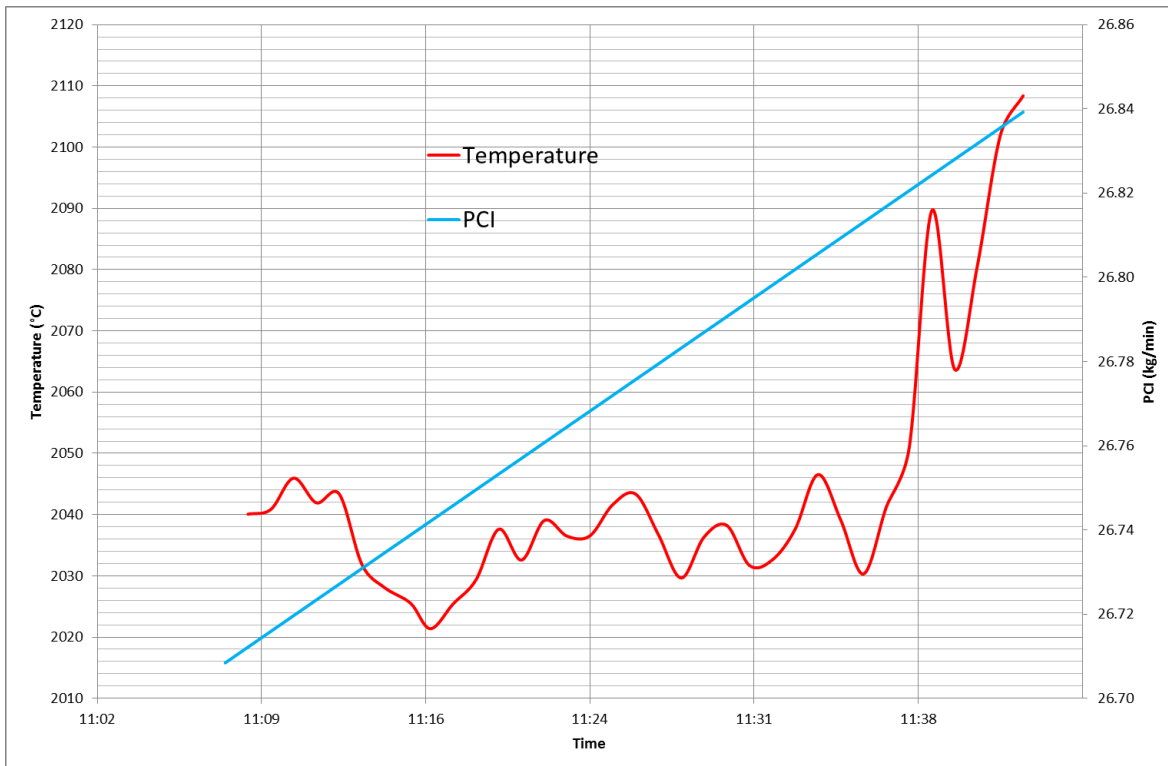


Figure 3.129: Comparison between Temperature & PCI T12 BF4

The coal injection rate was constant during the measurement period. Another measurement at tuyere 12 was performed 12:06 - 15:35. During this measurement coal injection was varied

between ≈ 20 kg/min to ≈ 10 kg/min to ≈ 0 kg/min.

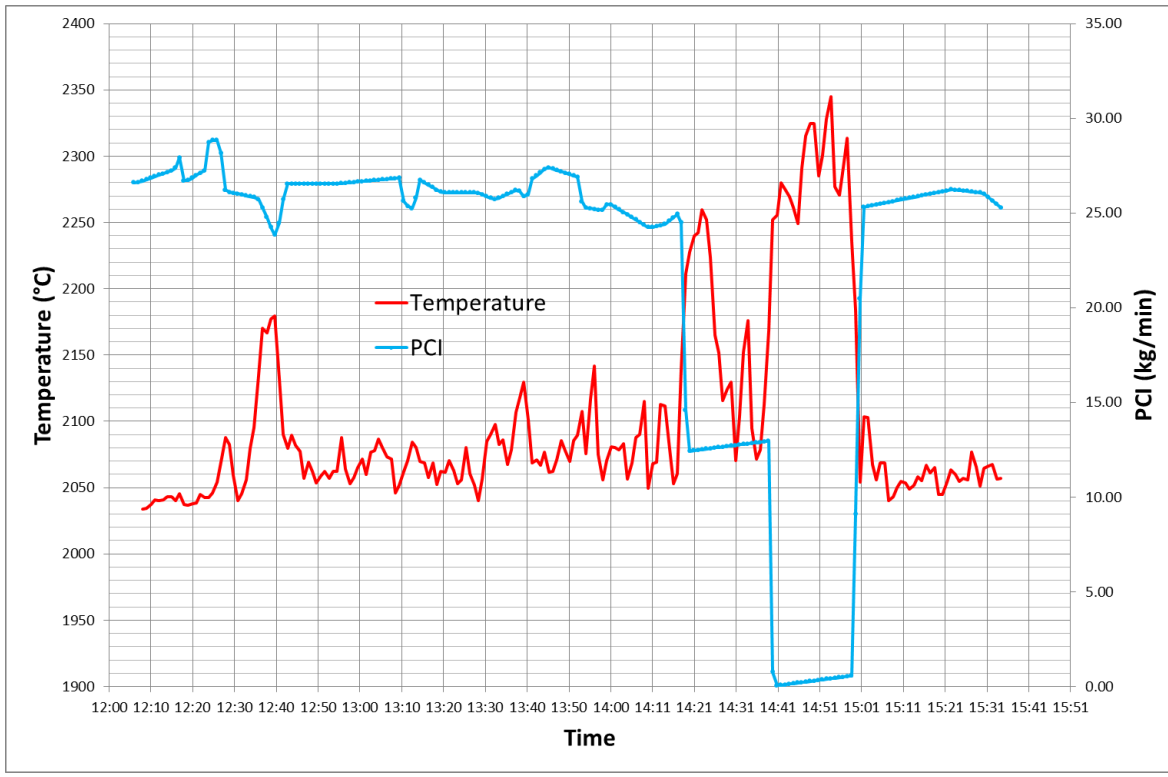
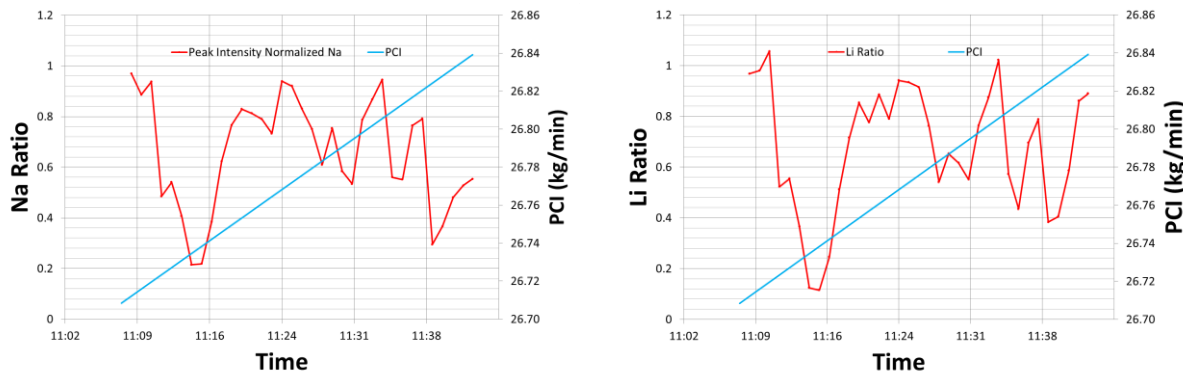


Figure 3.130: Comparison between Temperature & PCI T12 BF4; Second measurement from 12:06 to 15:35

The measured temperature was consistent; the maximum value appeared at the minimum injection rate. After decreasing to 12 kg/min, a temperature increase to 2250 °C was detected in approximately 5 min, followed by a temperature decrease to 2100 °C. Without injection, the temperature exceeded 2300 °C. At 15:00, the coal injection was increased to 25 kg/min and the temperature reached its previous level around 2075 °C. (**Figure 3.130**) The common assumption for a temperature decrease for coal injection rate increase was confirmed.

The intensity of the alkaline spectra during those measurements are shown below (**Figure 3.131**):



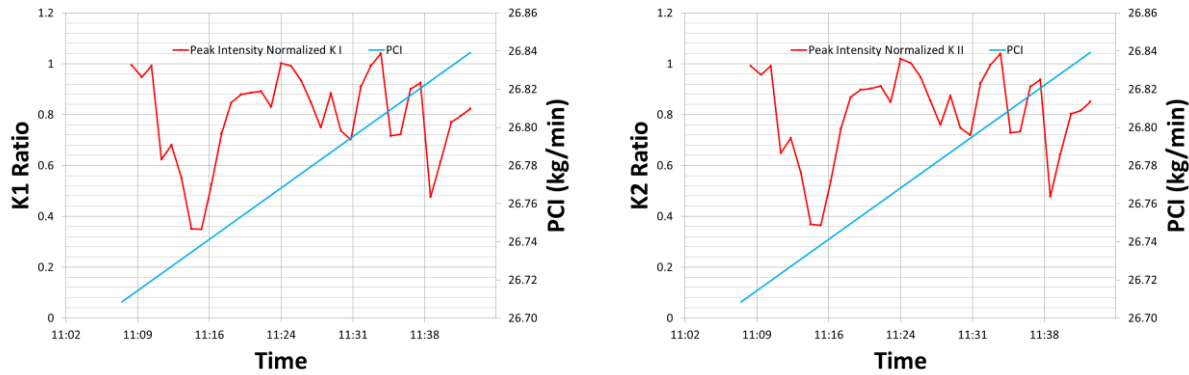


Figure 3.131: Alkali contents at T12 BF4

The average intensity was 67, 34, 159 and 160 Counts/ms for respectively Sodium, Lithium, Potassium 1 and Potassium 2. To recall, the ratio is dimensionless: it corresponds to the peak intensity (Counts/ms) divided by the initial intensity for the specific measurement. Ratio K2 and K1 had a comparable evolution (**Figure 3.132**). The Ratio K1/Ratio K2 varied from 0.98 to 1.05 indicating, both are potassium-peaks. Also, the evolution of the sodium potassium peaks are comparable: the Ratio/Ratio varied from 1 to 1.5. However, the correlation with the Lithium peak is low. Process conditions were not varied during this phase.

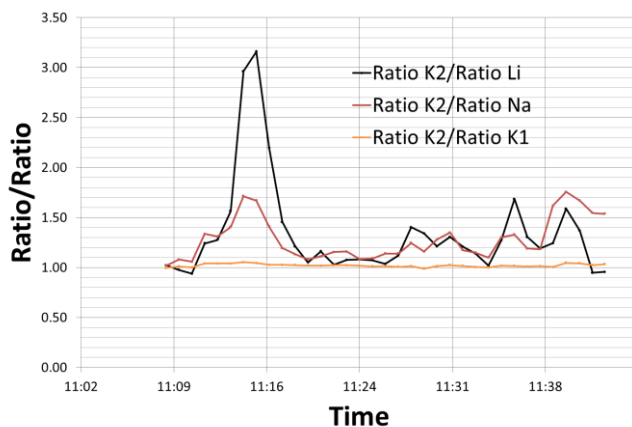


Figure 3.132: Ratio/Ratio

The previous conclusions were validated by the measurement, below.

A correlation between coal injection rate and Li - Ratio is shown in **Figure 3.133**.

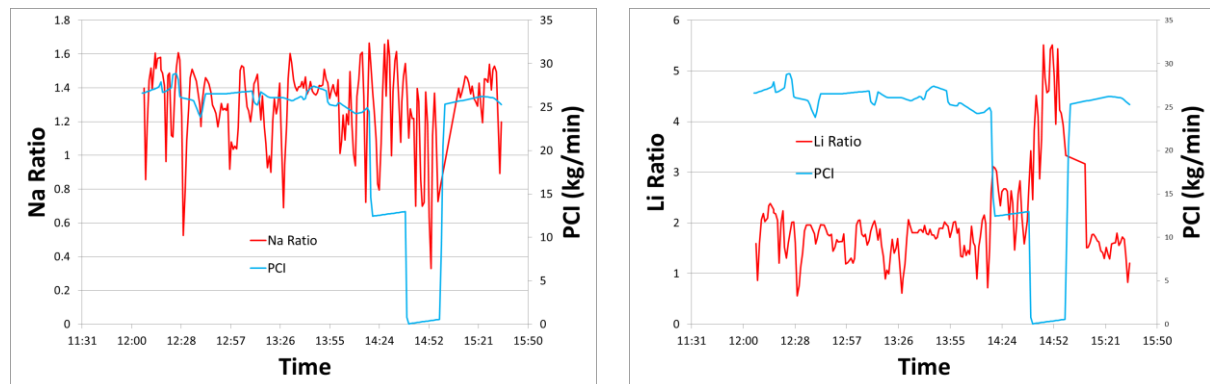


Figure 3.133: Comparison between Ratios & Process coal injection rates

The intensity of the Li peak increased when coal injection rate was reduced. The peak intensity depends on the quantity of the element, intensity of the energy of spectral band and of the sensibility of the spectrometer. Only the quantity of the element changed. A conclusion for other alkali elements was difficult to draw.

The alkaline peaks can be correlated to the boiling points of the specific elements, **Table 3.47**.

Table 3.47: Alkaline boiling points

Element	Na	K	Li
Boiling point	883 °C	759 °C	1130°C

Compared to Li, the foot of the Na and Li cycles in the BF shaft can be assumed to be further up the shaft, as boiling temperatures are lower. More intense coke combustion might then just introduce more Li to the raceway and leave Na and K spectra unchanged.

Raceway Depth

Laser distance measurement

The laser was placed in front of the peep hole of several tuyère at Port Talbot BF4 (**Figure 3.134**).

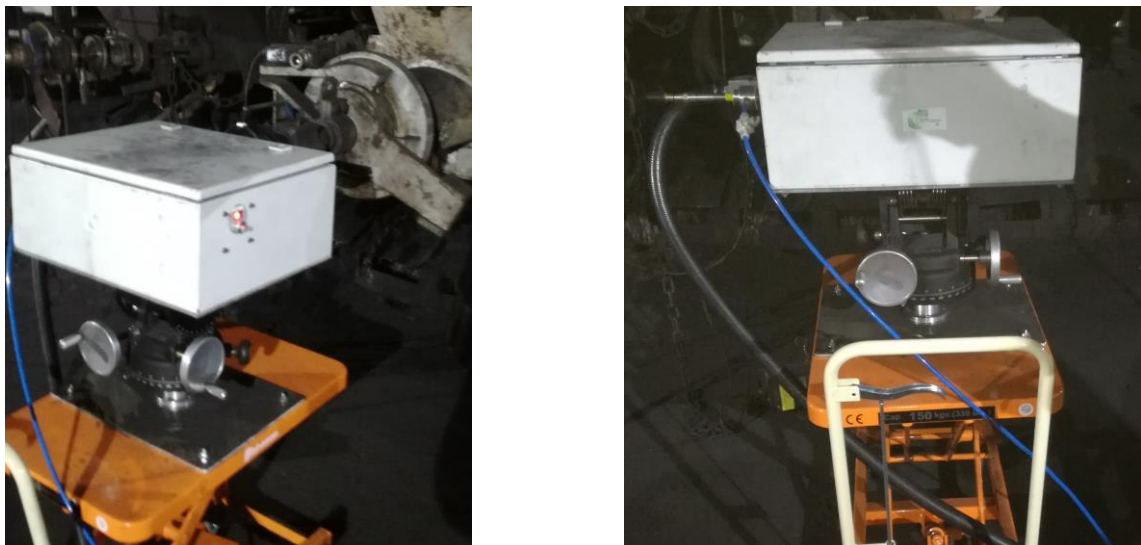


Figure 3.134: Raceway depth measurement system at Port Talbot

Automatic processing of the image analysis was developed: The method included processing to a threshold, resizing of the two dots, determining the centre of the dots and recalculate the apparent distance and according raceway depth. The critical part was to determine the right threshold value in every case.

The background of the picture changed during the measurement due to the changes in coal injection. Some pictures for periods without injection are shown in Figure 3.135. The coal lance is noticeable.



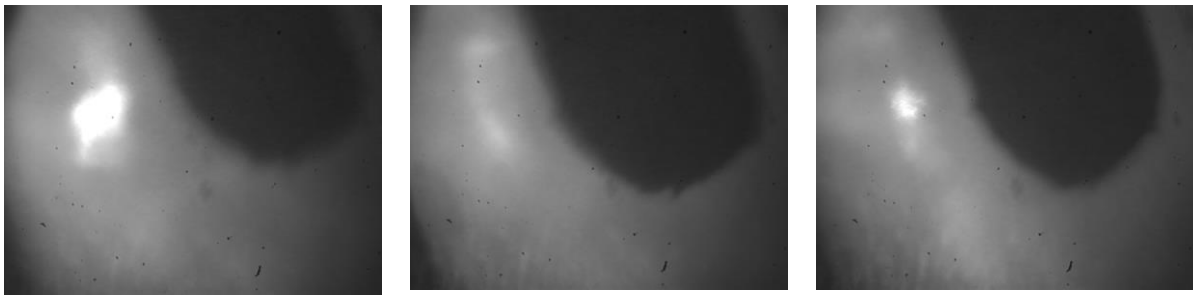


Figure 3.135: Two dots without PCI injection

Frequent raceway size changes occur during periods of constant coal injection rates. The coal plume absorbs raceway radiation, including those of the two laser dots, leading to a lower contrast and difficulties with image analyses, compared to periods without coal injection.

Also, could the coal plume may interfere with and diffuse the beams. Coke pieces circulating in the raceway may also be targeted.

Therefore, the position of the two dots fluctuates during the measurement.

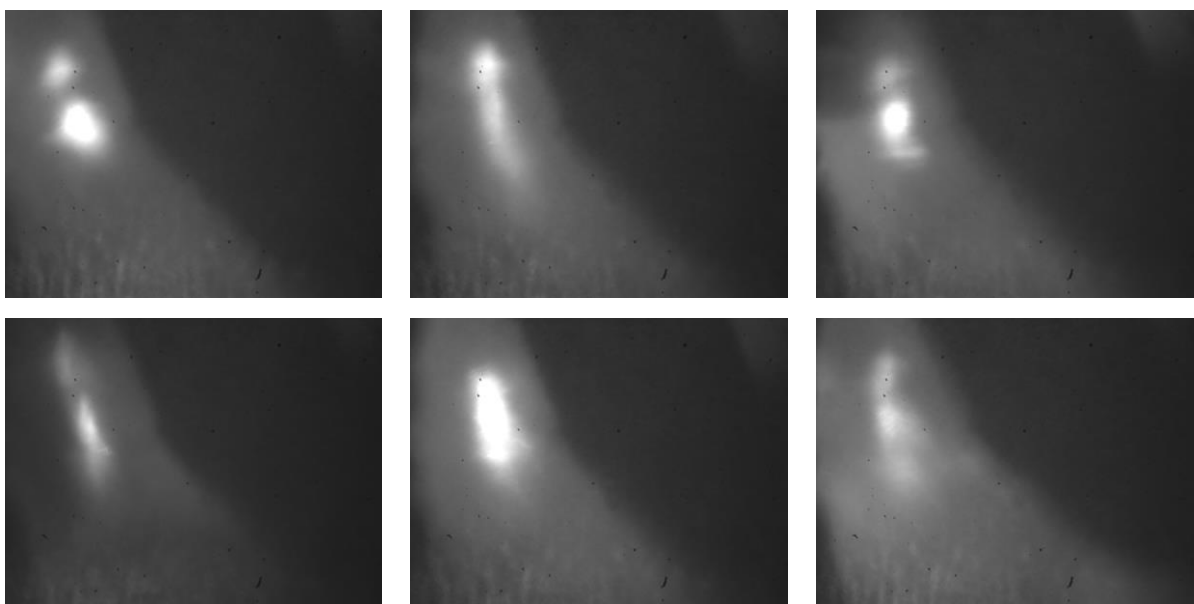


Figure 3.136: Pictures with coal injection

In **Figure 3.136**, the tip of lance was not noticeable. For some pictures, only one or more than two dots were detected.

All of this increased the level of complexity for the processing. A certain amount of the pictures were not well contrasting and the two dots were not clearly identifiable.

Nevertheless, results were obtained. Results for 19 minutes are shown below (**Figure 3.137**), those 19 points stem from 1140 pictures (19 x60 seconds).

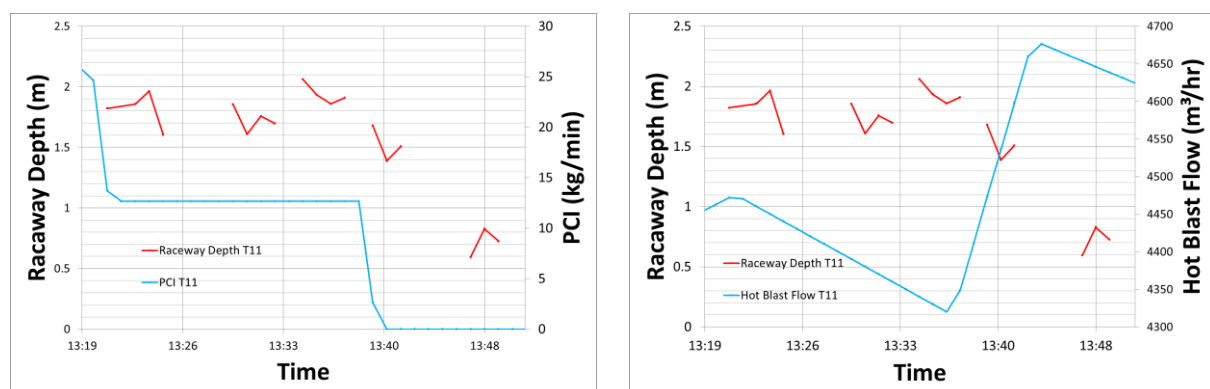


Figure 3.137: Comparison between Raceway depth and PCI/Hot Blast Flow

The depth decreased when the coal injection rate was decreased (Figure 3.137, Left) (Figure 3.137, right). However, to correlate this with coal injection, a longer trial is required.

To improve this measurement, the laser has to be used at its highest power and the camera has to be set to the lowest gain and exposure time; this combination would give the best contrast. Some optical adaptations and/or a measurement with laser modulation could increase the accuracy and reduce the error rate.

Radar distance measurement

The first test at Port Talbot BF 4 was conducted to prove feasibility of the measurement and develop a way for data analyses and quantification.



Figure 3.138: Radar placed behind a peep-hole at BF 4, Port Talbot

A typical result of a distance measurement is shown in Figure 3.139 (l). The according distribution of measured data points at the different sizes is shown in Figure 3.139 (r).

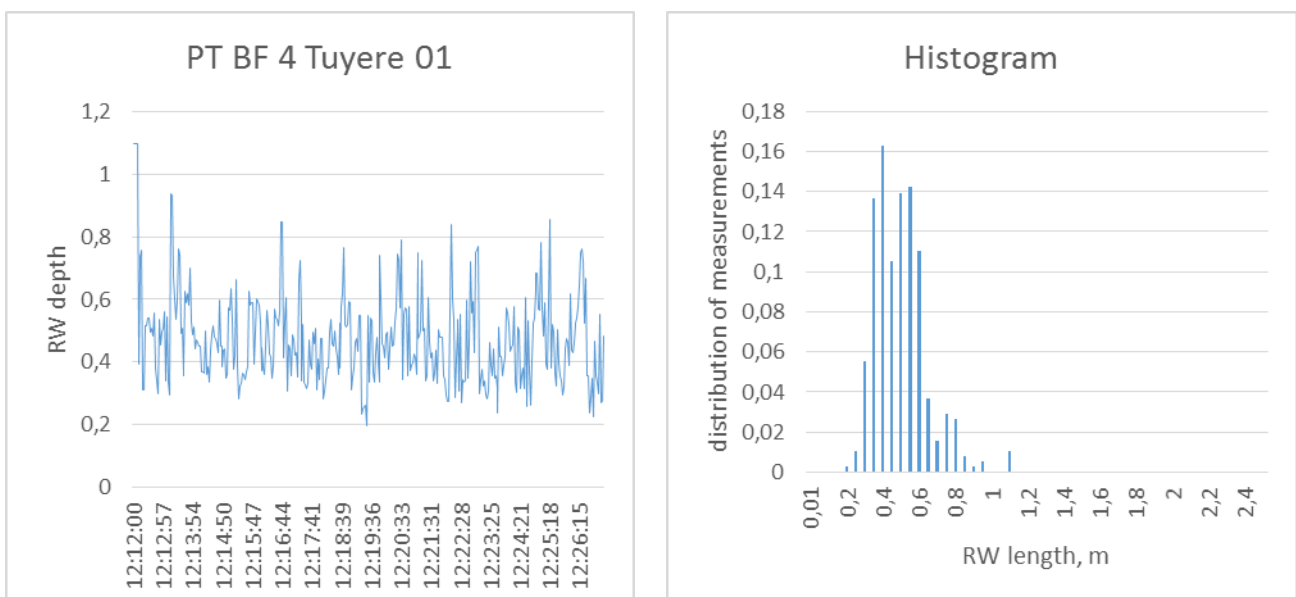


Figure 3.139: Radar raceway size data (l); histogram of measured data points for the according period (r)

The sizes varied considerably. For quantification purposes, the data was further processed by construction of an additive graph, **Figure 3.140**.

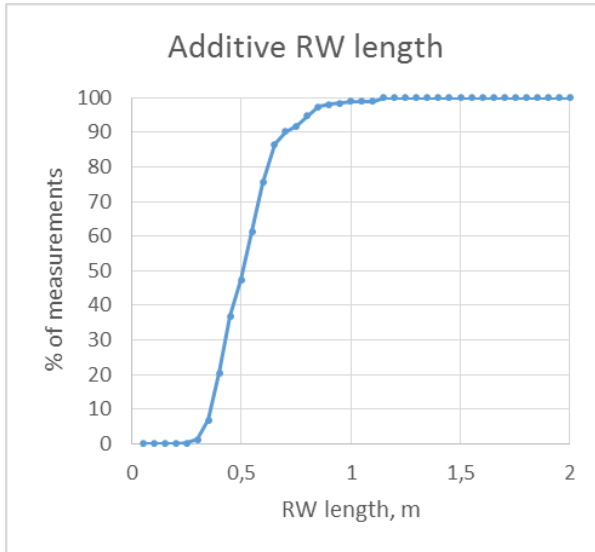


Figure 3.140: Additive raceway length

The following diagram shows the data, as measured during the first campaign at BF 4 in Port Talbot.

For tuyere 9, the raceway size increased with increasing GCI rate. At the second campaign day, tuyere 15 was measured. The results showed that when going from 200 to 0 kg/ t_{HM} and back to 200 kg/ t_{HM} GCI, the curve moved back to the initial position. However, the differences in size were smaller, at this tuyere.

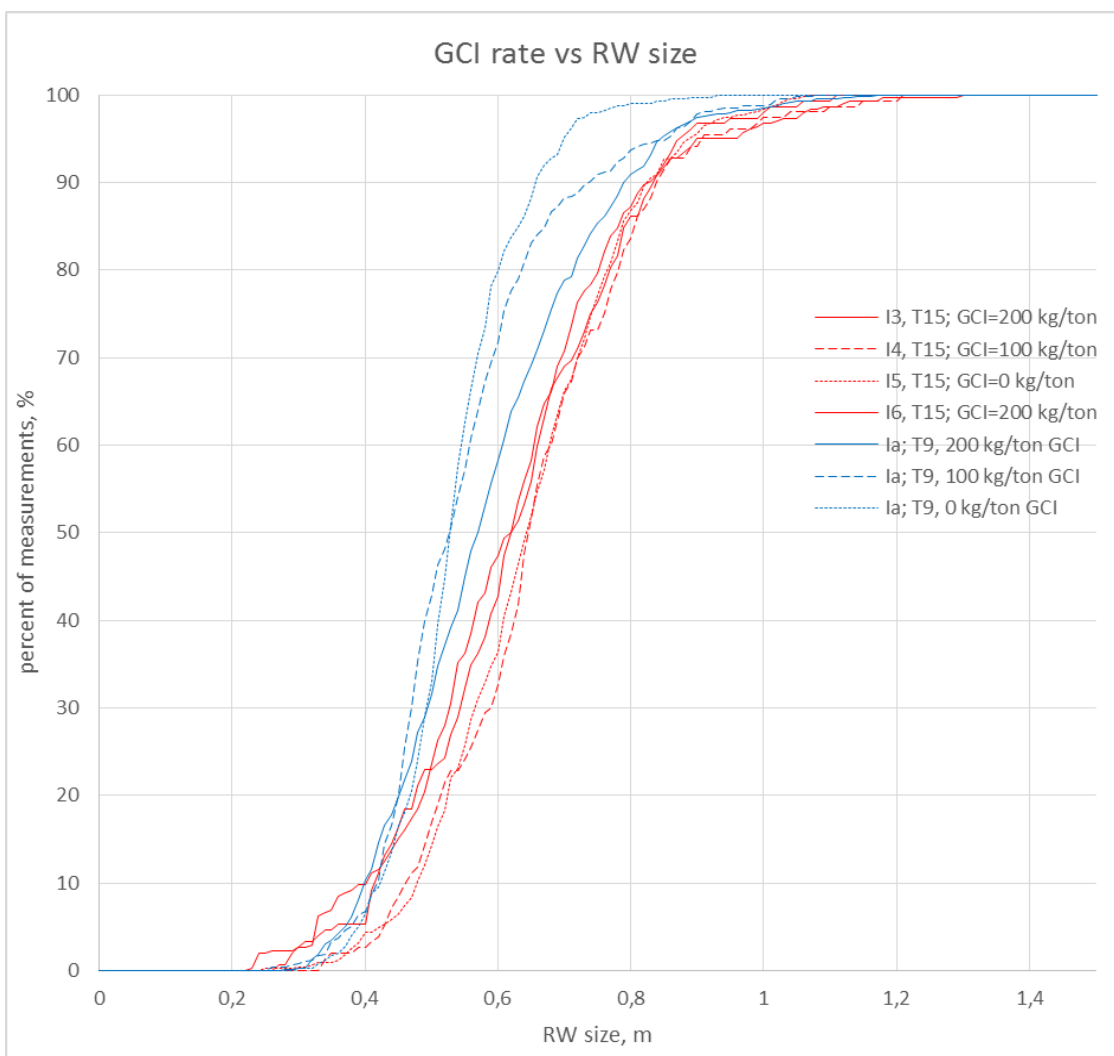


Figure 3.141: Comparison of raceway data for two tuyère at 0, 100 and 200 kg/ t_{HM} GC injection rate.

For easier quantification purposes, the value at which the raceway length exceeds 80 % of measured

data points was defined as raceway size.

Due to the beforementioned significant differences in the measured raceway size, a second radar trial was performed on 07.03.2018 – 08.03.2018. During this trial, all tuyeres of PT BF 4 were measured.

Two distinct raceway size levels could be identified, **Figure 3.142**. Some of the tuyeres showed a fluctuation between both levels; others showed a more stable raceway with only the lower or higher level.

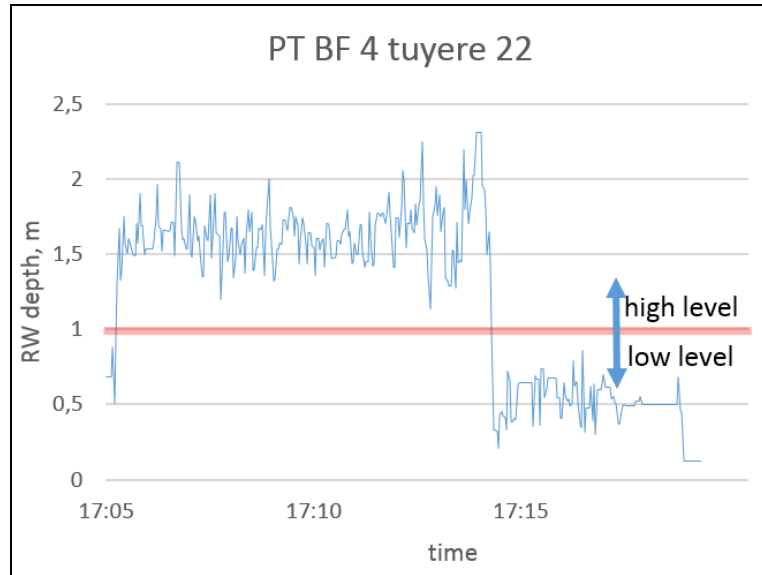


Figure 3.142: Raceway size BF 4 in Port Talbot; measured with radar sensor

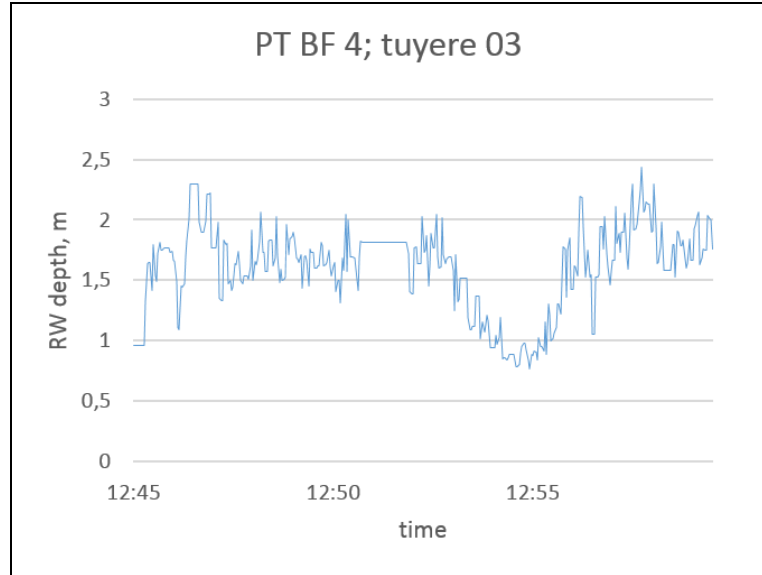


Figure 3.143: Raceway size BF 4 in Port Talbot; measured with radar sensor

The two different levels were further analysed as two different raceway states with different raceway sizes, **Figure 3.143**. Additionally, maximum and average values of the periods were calculated.

The diagrams in **Figure 3.144** show the average raceway sizes (\bar{l}) and the two distinct size levels (r ; low: blue, high: orange) of PT BF 4, dependant on the tuyere position. The axis length represents the BF diameter at RW level to illustrate proportions of raceway to BF.

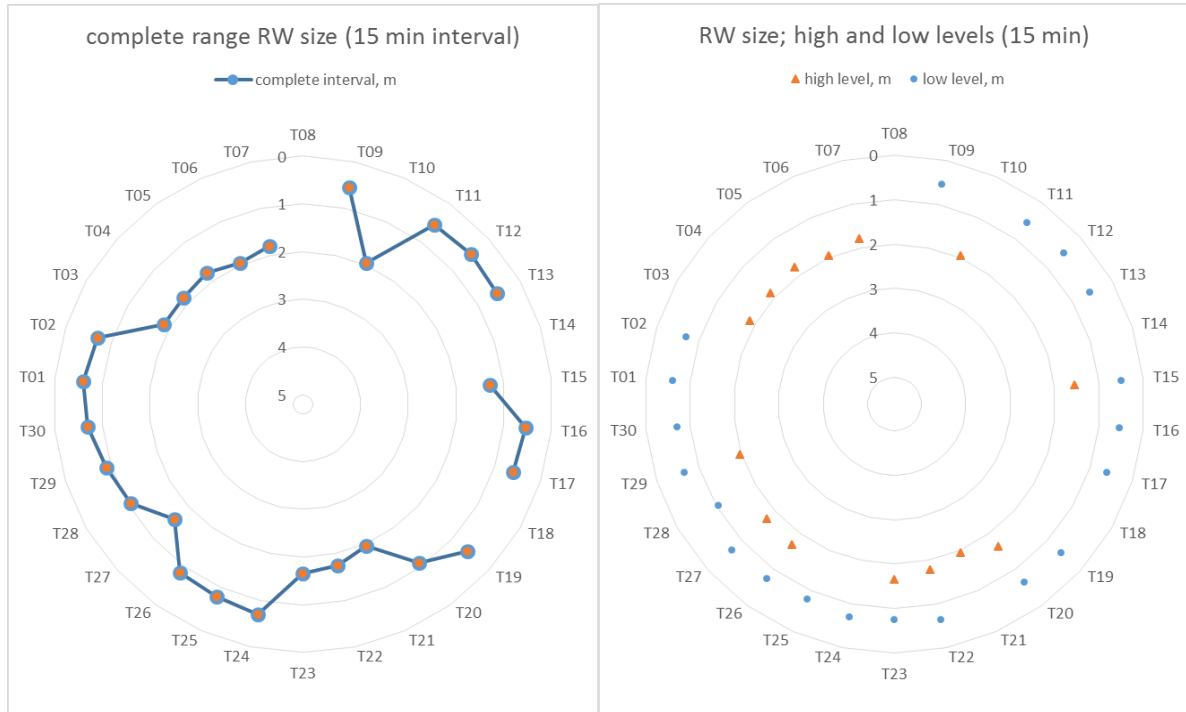


Figure 3.144: Raceway size PT BF 4 based on complete time interval (I); Raceway size based on two distinct levels (larger 1 m: high level; smaller 1 m: low level)

The high raceway levels are plotted in the below diagram. The grey area might indicate the position of active coke zone and dead man position, **Figure 3.145**.

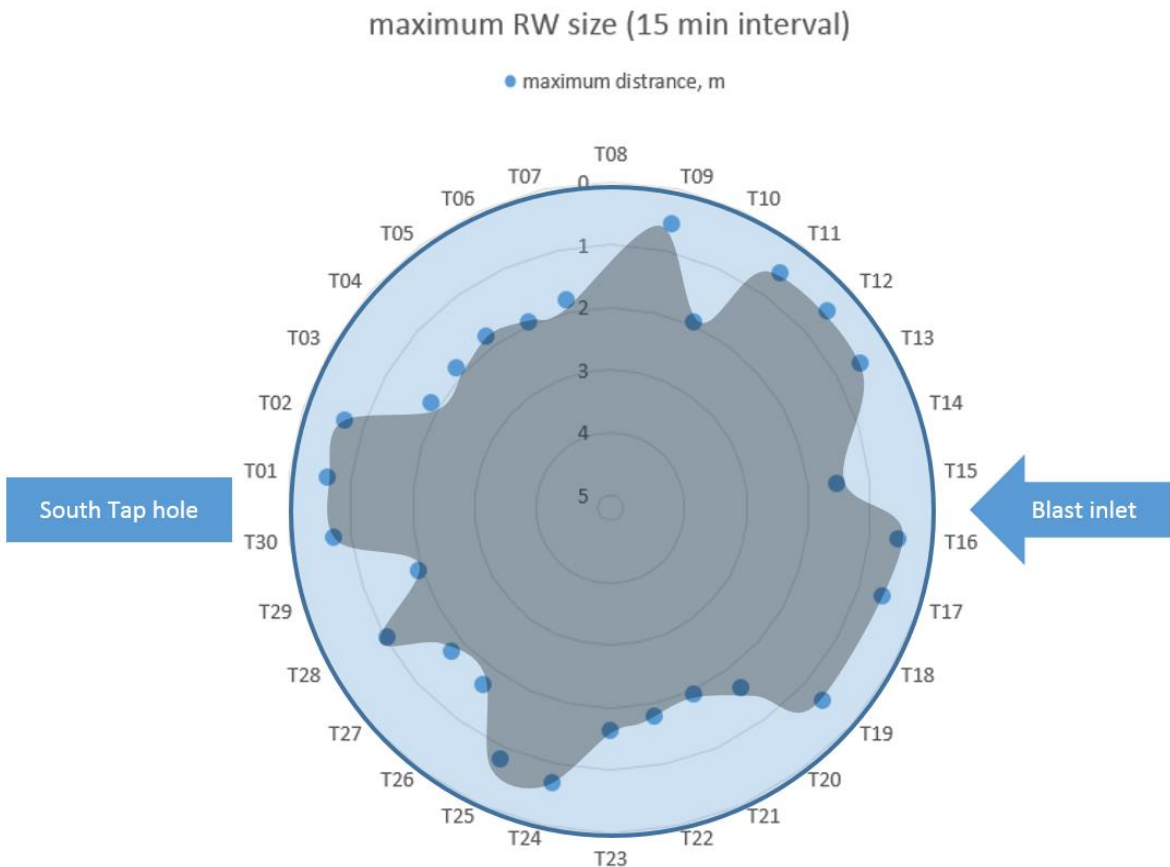


Figure 3.145: Raceway size PT BF 4 based on high levels

The blast enters the bustle pipe between tuyère 15 and 16. During the trial, just one tap-hole located between T1 and T30 was used. Differences in raceway size seem to depend on the position with regards to blast inlet and tap hole position, **Figure 3.146**. However, low-level RW's were not detected for tuyeres 3 to 7.

RW sizes of tuyeres PT BF 4

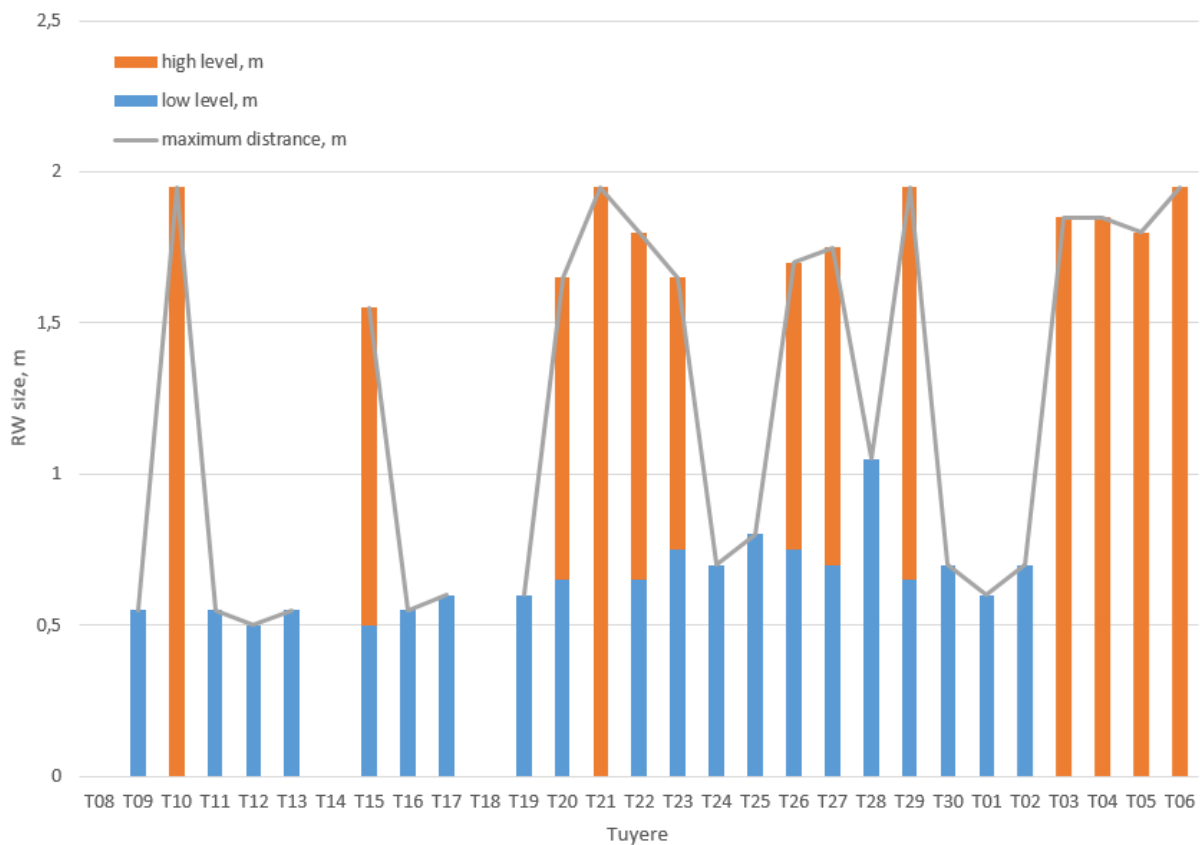


Figure 3.146: High (orange) and low (blue) raceway level at tuyère 1-30; PT BF 4

Besides the impact of circumferential position, the tuyère diameter is supposed to affect the established raceway size. **Figure 3.147** shows the different calculated RW sizes for the two tuyère diameters 115 and 125 mm.

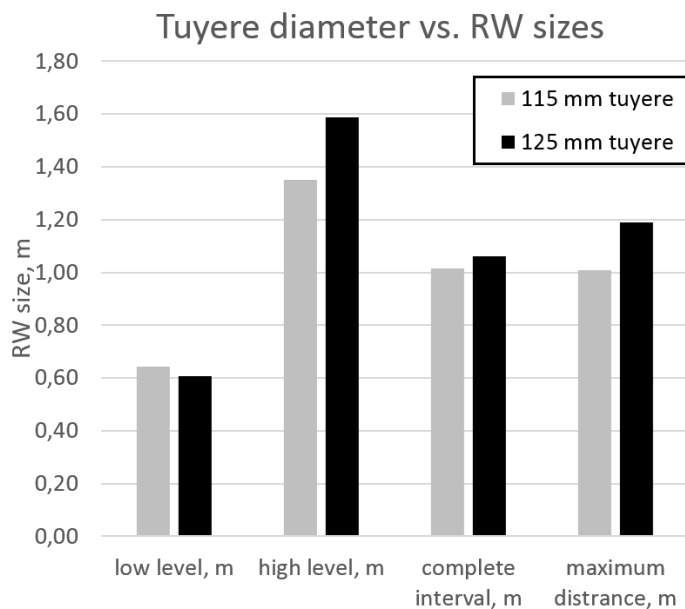


Figure 3.147: Raceway sizes for different tuyère diameters

When in a low-level state, both tuyère sizes show a similar raceway size. However, the high-level raceways are larger for larger tuyère diameters.

Table 3.48: Average of raceway sizes of tuyères, dependant on diameter

	115 mm tuyère	125 mm tuyère
low level, m	0.64	0.61
high level, m	1.35	1.59
complete interval, m	1.02	1.06
maximum distance, m	1.01	1.19

Size measurement by radar was successfully used in the frame of CharFoCo.

The impact of the tuyère diameter on raceway size could be shown. For tuyere 9, a higher coal injection rate resulted in a larger raceway. At T 15, the impact was smaller.

The raceway size profile over the circumference showed a significant influence of the tuyère position with regards to blast inlet and tap hole position on the raceway size.. This shows it is essential to take into account: 1. Various tuyeres over the BF diameter and 2. Measure a long time interval, as the times at which the raceway stays in the two modes will be important for the path of the char through the blast furance. The change between the two distinct raceway states might be explained by raceway collapses: The coke between the raceways is consumed until the structure collapses due to loss of mechanical stability.

The two distinct raceway sizes between which the raceway changes could be shown for laser-raceway size, as well as radar measurement.

3.4.1.5 RESULTS

The different techniques show interesting results. A first correlation to blast furnace parameters could be shown.

In particular:

- The global temperature inside the raceway increases when the coal injection decreases.
- The Li ratio increases when the coal injection decreases. Sodium and Potassium show similar evolution.
- The raceway depth measurement shows promising results and more tests are needed in link with identified improvements.

Simulations to determine the raceway depth and to compare with the radar measurements

For further explanation of the raceway size phenomena, mathematical simulations were performed:

It is assumed that the raceway depth is determined by the amount of kinetic energy that leaves the tuyère. This kinetic energy is influenced by combustion and the amount of gasses that are injected through the tuyère.

As the raceway depth was not known in advance, simulations were performed without a definition of a raceway. Then, the kinetic energy was determined from the simulations and the raceway was approximated with an empirical equation from the literature. In order to compare with the measurements, several different cases were simulated, mainly differing in the amount of hot blast.

First results showed little combustion. As the porous bed and reactions with the bed were not regarded, it was difficult to estimate how much combustion was achieved in the end.

An example of the velocity field found in the simulation is seen in **Figure 3.148**.

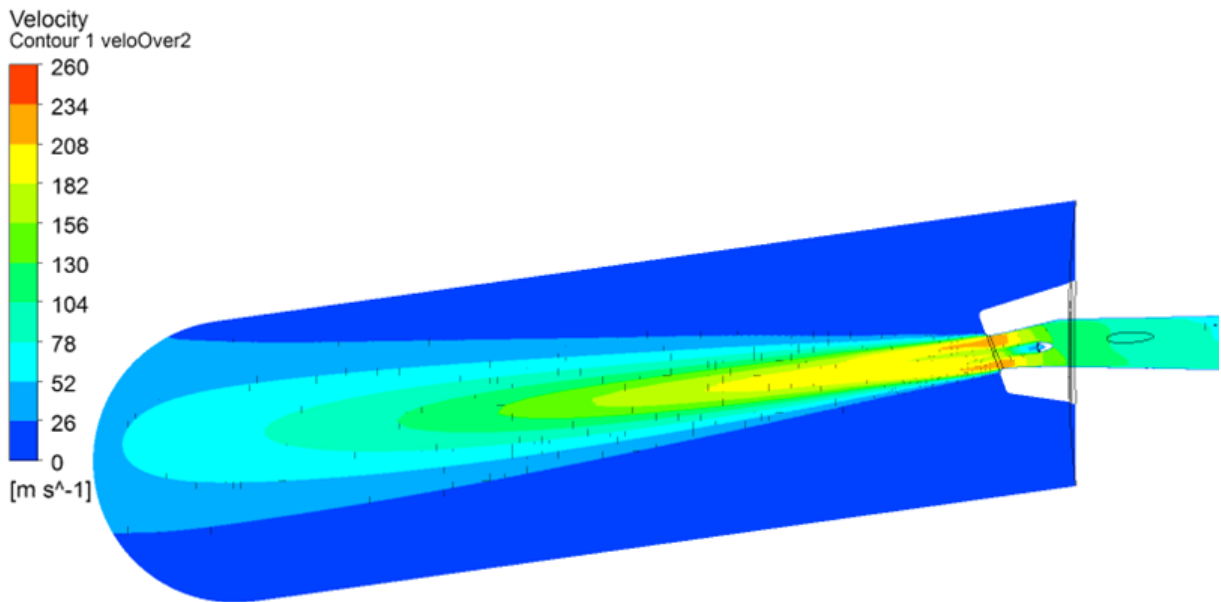


Figure 3.148: Gas velocity field in the assumed raceway

For each tuyère, the hot blast varied between 4000 and 8000 Nm³/hr. Steady state simulations were performed for hot blast amounts of 4500 and 6500 Nm³/hr. Other parameters (such as oxygen levels, coal amount and hot blast temperature) were also varied, but resulted in less difference of the kinetic energy. All simulations were performed for one tuyère diameter.

As the pressure difference over the tuyère determines the velocity and therefore the kinetic energy, this was considered a proper initial verification of the model. The amount of hot blast per tuyère varied between 4000 and 8000 Nm³/hr. Dividing it by the cross section of the inlet gave the inlet velocity and, considering the density at the inlet, initial pressures were found between 0.18 and 0.74 bar. Performing the same calculations for the outlet of the tuyère (assuming a uniform velocity across the outlet), the pressure drop across the tuyère varied between 0.2 and 0.85 bar, depending on the amount of hot blast. The simulations showed pressure drops in the same range, also varying with hot blast amount, **Table 3.49**

Table 3.49: Pressure drop across the tuyère simulations

Case	p-min bar	p-max bar	delta P bar
1	-0.194	0.281	0.475
2	-0.230	0.341	0.572
3	-0.108	0.153	0.261
4	-0.144	0.211	0.355
5	-0.200	0.291	0.491

Simulations were performed where just one parameter (coal, hot blast temperature or hot blast amount) is varied (**Figure 3.149**).

Coal	Force/m³	Deviation
	Overall Total	%
100%	786	-
49%	772	-2
24%	766	-3

Hot blast temperature C	Force/m³	
	Overall Total	Deviation
1150C	786	-
1180C	802	2
1210C	818	4

Hot blast volume	Force/m³	%
	Overall Total	Deviation
100%	786	-
82%	533	-32
105%	858	9

Figure 3.149: Results of simulation; comparison of different cases

It became clear that the hot blast had a significant effect on the force at the tuyère exit and therefore, on the kinetic energy, created.

The kinetic energy was plotted against the amount of hot blast. This would show whether the assumption that the kinetic energy was mainly determined by the hot blast is justified. Five different relevant cases from practice were taken and simulated (therefore different from the previous cases). The cases differed in hot blast amount and temperature, oxygen and amount of coal.

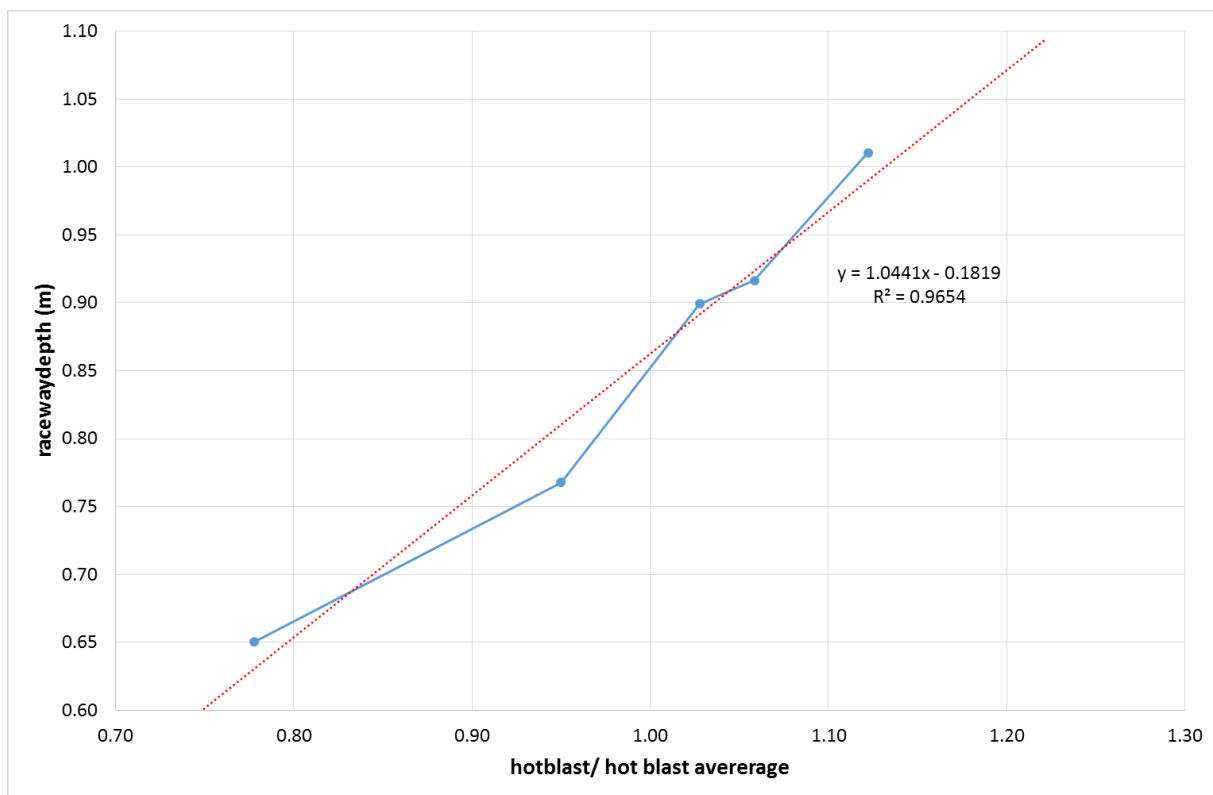


Figure 3.150: Relation hot blast amount and raceway depth

Although the relationship was not fully linear, the hot blast did have the most significant influence on the kinetic energy.

In order to make a comparison with the measurements, the equation from article was used [3] to calculate the raceway depth (**Figure 3.152**).

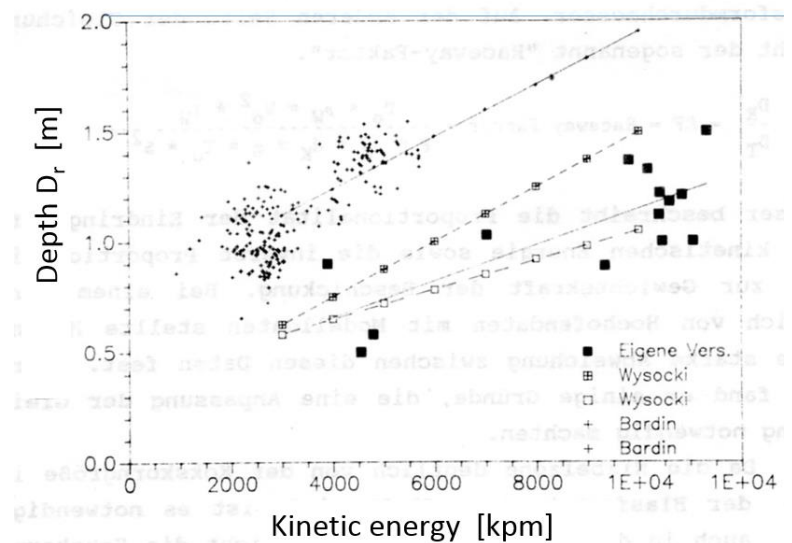


Figure 3.151: Correlation between kinetic energy and insertion length of raceway measurement [3]

The equation used was empirical and based on 80% of the data that the writer collected.

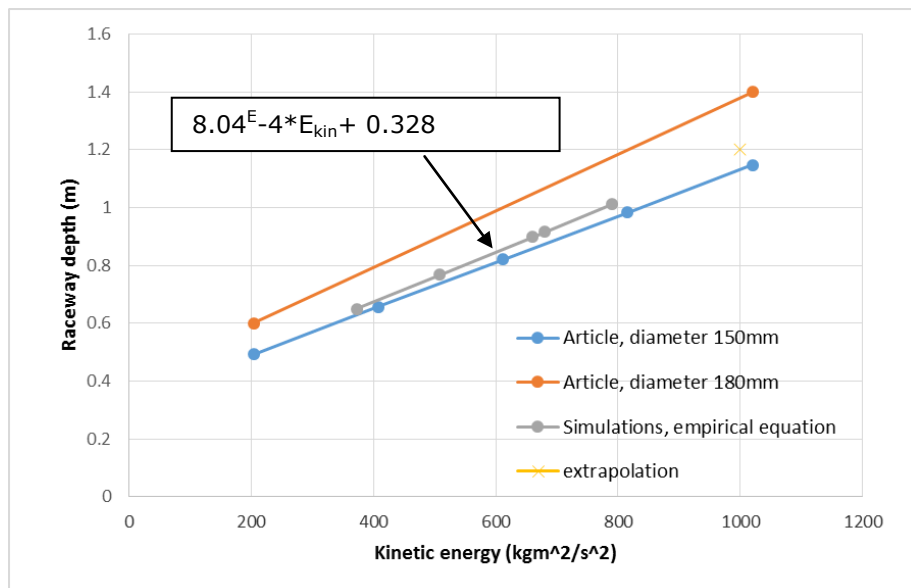


Figure 3.152: Calculated relationship between the kinetic energy and the raceway depth.

From **Figure 3.152**, it seemed that the raceway depth varied between 0.6 and 1.2 m, depending on how much hot blast was administered to the tuyère. The case of 1000 kg m²/s² was not simulated, but the kinetic energy was derived from **Figure 3.150** and then plotted (yellow cross in the graph). A larger or smaller exit diameter of the tuyère could influence the result.

Figure 3.153 shows the raceway depth from the simulations compared to the measured raceway depth.

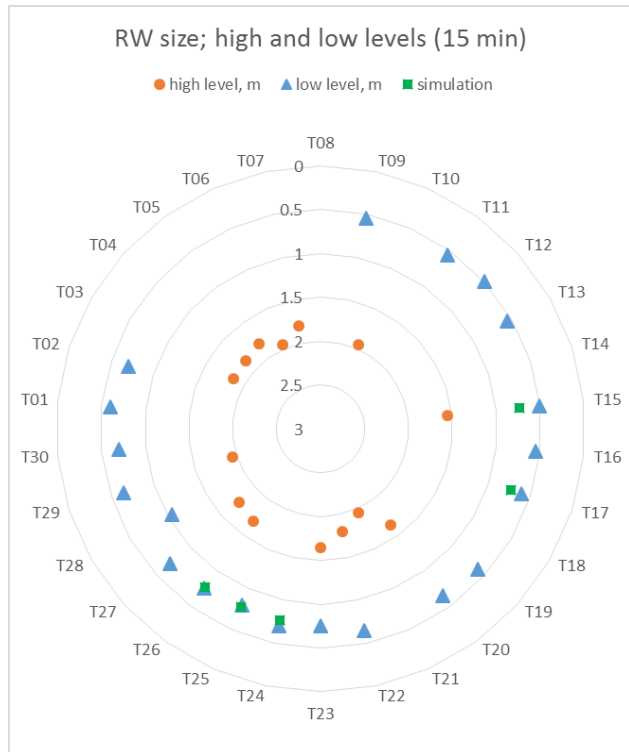


Figure 3.153: Raceway depth simulations compared with the radar measurements

The calculated raceway from the simulations seemed to match well with the minimum raceway depth that was measured. Note that the simulations are steady state, so variations in hot blast are not taken into account. To check for variation in the hot blast per tuyère, the minimum and maximum values of the two day of the measuring of the hot blast are plotted (Figure 3.152).

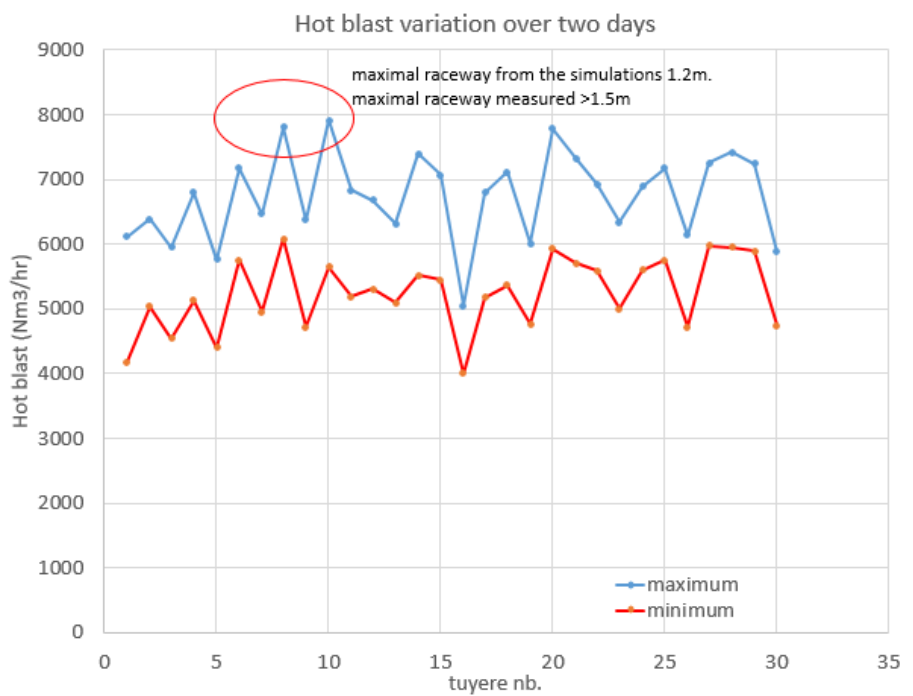


Figure 3.154: Hot blast per tuyère, minimum and maximum values

Some tuyère did obtain more hot blast than the sampled tuyère, but when calculating back, (Figure 3.152 and Figure 3.150) the maximum calculated raceway would be about 1.2 m. This is significantly lower than the measured 1.8 m. As the relationship between the hot blast and kinetic energy seemed linear (Figure 3.150), another explanation would be needed to explain the larger raceway depth. One explanation could be the relevance of the equation under today's injection rates: The formula was derived in 1979. Nowadays, more coal is injected and this might significantly contribute to changes in raceway size. The measurements with the thermographic camera (Figure 3.128) shows that the temperature on the exit of the tuyère will decrease as coal is

injected. This was also found in the simulations (**Figure 3.155**).

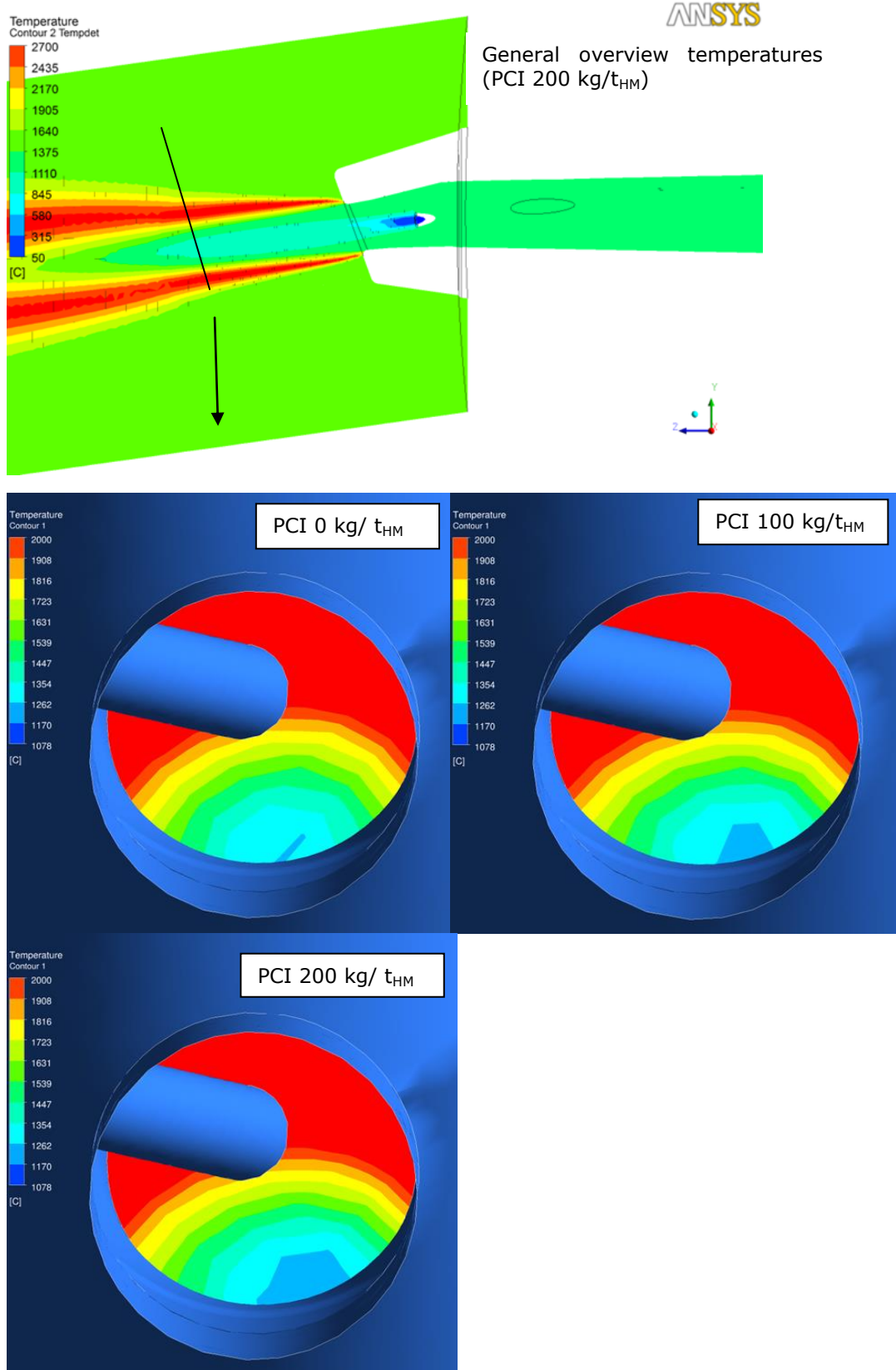


Figure 3.155: Temperature at 0.7 m from the tuyère, seen from the peep sight

The area with a low temperature increased in size, as more coal was injected. As the injected coal is relatively cold and it takes time to mix with the hot blast, a cold wake is formed behind the lance. Note that the CFD simulations do not show the background temperature of the radiation of the bed.

3.4.2 TASK 3.2 BLAST FURNACE TRIALS

Several blast furnaces of the industrial partners of the project are currently operating at coal injection rates of 200 kg/t_{hm} and more. At the same time, different techniques are available for investigating the inner state and the characteristics of the materials in the furnace:

- the multi-point vertical probing technique was developed at industrial scale [4] and is now a very reliable technique for the thermo-chemical mapping of the shaft. It was used at pilot scale at the EBF for R&D purpose during the ULCOS project;
- coke core boring experiments were already performed in the past [5, 6] and can still be used to evaluate coke characteristics at high PCI rate;
- char particles in the flue dust were investigated [7] but not from the inside of the furnace.

3.4.2.1 EVALUATION OF HIGH PCI OPERATION AT AM BREMEN BF2

Two trial campaigns were performed at AM Bremen BF2 during the project to evaluate the inner conditions of the furnace at high PCI rate.

The first campaign was performed in April, May and June 2016. It included the following trials:

- a Flexible Vertical Probing (FVP) trial for testing dust sampling at different levels over the height of the shaft of the blast furnace (14/04/2016);
- a coke core boring exercise on 31/05/2016, followed by coke scrapping at the same tuyère to characterise the bosh coke size and its degradation between the upper and lower furnace;
- a Multi-Point Vertical Probing (MPVP) on 14/06/2016 aiming at characterising the thermo-chemical conditions in the shaft of the furnace.

The second trial was performed in June 2017. It included:

- a coke core boring exercise on 20/06/2017, followed by coke scrapping at the same tuyère to characterise the bosh coke size and its degradation between the upper and lower furnace;
- a Multi-Point Vertical Probing (MPVP) on 29/06/2017 aiming at characterising the thermo-chemical conditions in the shaft of the furnace.

It was impossible to make a new attempt of dust sampling over the shaft height, at that time. The analysis, done after the first test showed that an improvement of the technology used for the sampling over the shaft was necessary to get reliable results. Modifications of the probe were designed and some equipment ordered. But the late arrival of the material on the one hand, and the stoppage of the furnace for a partial relining in the last semester of 2017 made it impossible to organise a new campaign before the end of the project.

3.4.2.1.1 DUST SAMPLING OVER THE SHAFT HEIGHT BY MEANS OF FVP TRIAL

For dust sampling, the classical Flexible Vertical Probing (FVP) technique used at AMMR had to be adapted, especially regarding the head of the probe. The gas sampling opening had to be specifically designed for the collection of char particles, which is supposed to be lower than 1 mm in size. Also the gas flow rate had to be significantly increased compared to the usual practice to avoid the settling of the sampled particles in the pipe itself, before reaching the filters with which the dust is collected. The sampling conditions retained for the first test to be done in Bremen were the following:

- in order to avoid settling of the dust particles in the gas sampling pipe, it was estimated that the gas speed in the line should be in the order of 25 to 30 m/s. Assuming a pressure of 2 bar(g), and ambient temperature, it means that the sampled gas flow rate should be in the range of 4 m³/h. This is a significant increase compared to the usual gas sampling rate during FVP trials (500 l/h);
- instead of the circular holes usually used for gas sampling, three 1 mm large slits were made at the bullet surface for the sake of carrying over only material with a smaller dimension, and in particular char in suspension in the sampled gas. A sketch of the

bullet is given in **Figure 3.156**.

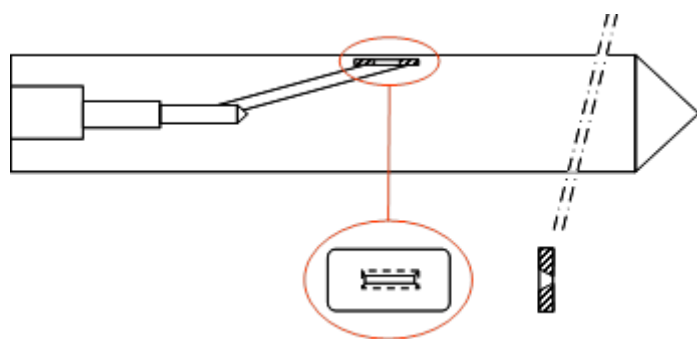


Figure 3.156: Sketch of the FVP bullet used for sampling dust in the shaft of the furnace

The configuration of the trials is presented in **Figure 3.157**.

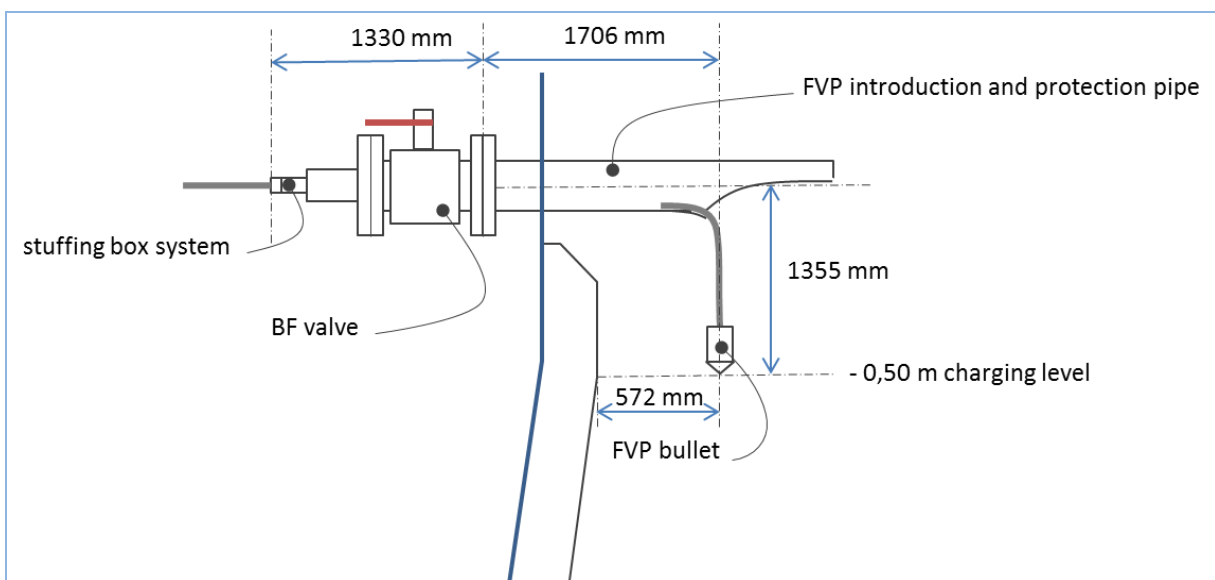


Figure 3.157: Sketch of the introduction system of the Flexible Vertical Probe

Regarding the innovative part consisting in sampling dust over the shaft height, the arrangement used for dust collection is presented in **Figure 3.158**.



Figure 3.158: Schematic of the dust sampling system used during the FVP trial

It includes:

- a specific connection on the gas line to transport the gas to the filter;
- the filter itself;
- a gas meter to check the actual gas flow rate and its evolution with time until the clogging of the filter occurs.

The fact that this FVP trial was dedicated to test dust sampling, temperature and gas analysis measurements were slightly impacted. As a matter of fact, the gas analysis was somewhat disturbed at the time the dust was sampled. The corresponding characteristics of the probing are given in **Figure 3.159**. From these measurements, this FVP trial looks relatively typical.

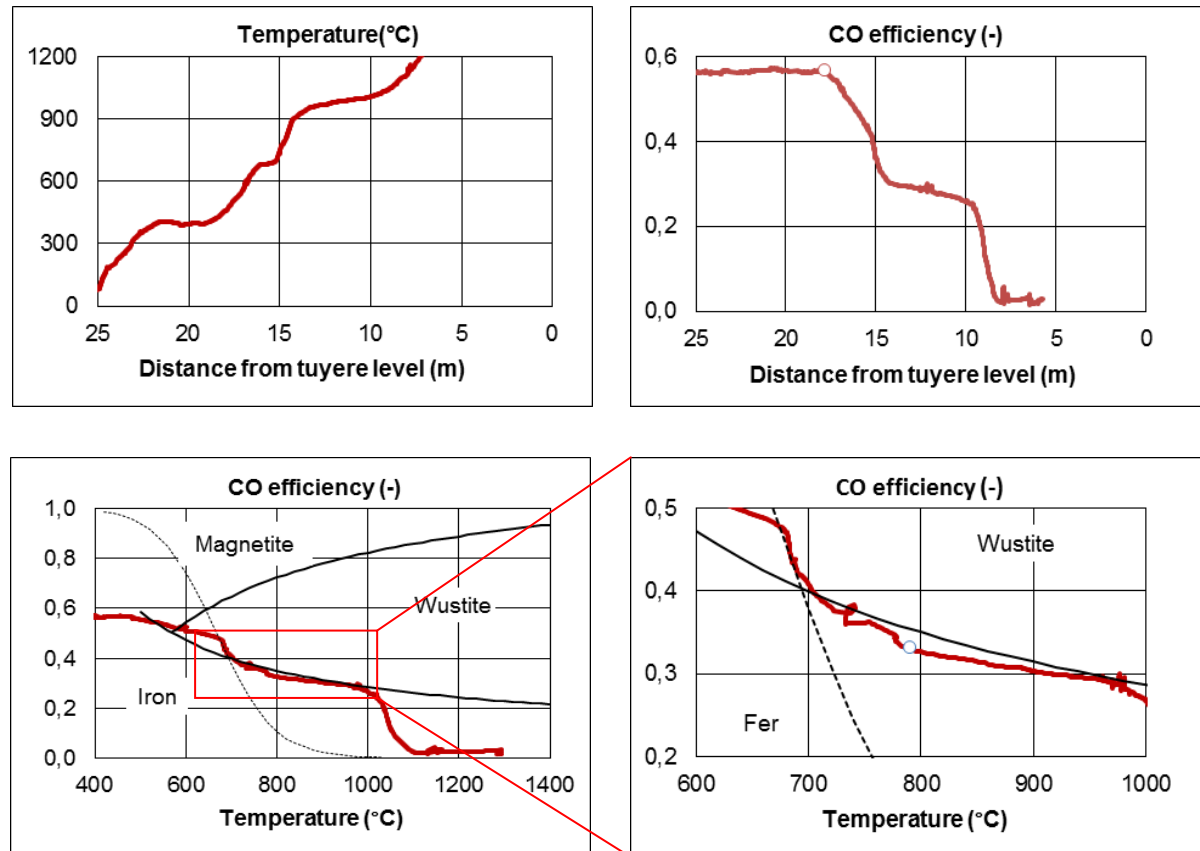


Figure 3.159: Characteristics of the FVP trial of 14/04/2016 at BF2.

Temperature and CO efficiency profiles (top left and right, respectively) and Chaudron's diagram (bottom). The dot in the bottom right figure indicates the point selected for specific consumption calculation (μ) for the formation of the first metallic iron.

Regarding dust sampling, a filter with a small mesh size was used in the very beginning, which resulted in a very fast clogging. Consequently, the filter was changed to a larger mesh that enabled sampling durations up to 10 minutes afterwards. The picture of the different samplings done along the trial is given in **Figure 3.160**.



Figure 3.160: Different filters taken during the FVP trial

As can be seen, the filters colour turned to black during the sampling, and it was then expected that some carbon dust, either from coke or char, would be found on the filter during SEM observations. This was actually not the case. The only component that could be identified was KCl

crystals **Figure 3.161**. The black colour was then most likely coming from very fine soot.

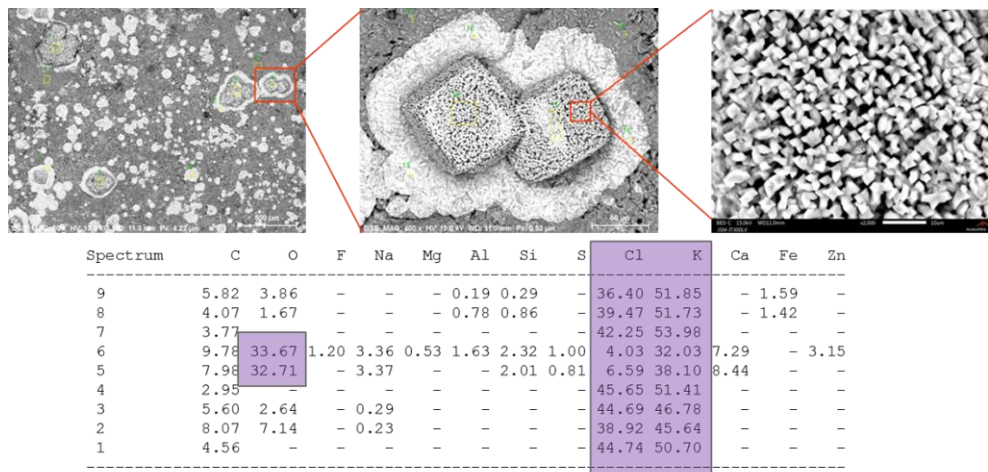


Figure 3.161: KCl crystals observed by SEM on the filter corresponding to sample 8

KCl compounds are actually formed inside the furnace and leave it with the gas. The sampled gas also initially carries moisture from the burden reduction. This moisture can condense in the outer part of the FVP pipe so that the KCl compounds may dissolve in the water. Part of this "salted" water is most likely carried away with the gas during the sampling, which explains that the filters were initially wet when they were recovered. It is then suspected that the KCl crystals formed afterwards during the drying of the filter. If condensed water stagnates at the bottom of the pipe rolled on the FVP drum, then particles carried out with the gas might also be trapped there during the trial. We then decided to inspect the part of the FVP pipe remaining on the drum. By introducing compressed air in it and using the same filtering system as during the trial, it was possible to recover some dust that initially deposited in the pipe when the gas crossed the condensed water. This dust was further examined with the SEM, to investigate its different constituents and evaluate whether a clear distinction between species could be made.

Figure 3.162 presents the general aspect of this dust and two morphologies of the carbon that could be detected. Whether this carbon could come from both, coal and coke or only from coke was not determinable from this image alone. The chemical composition of the particles was then checked to see if some differences could emerge. Unfortunately, maybe partly due to the pollution by "salted" water, it was not possible to detect any tracer enabling to differentiate between coal particles and coke particles (**Figure 3.163**).

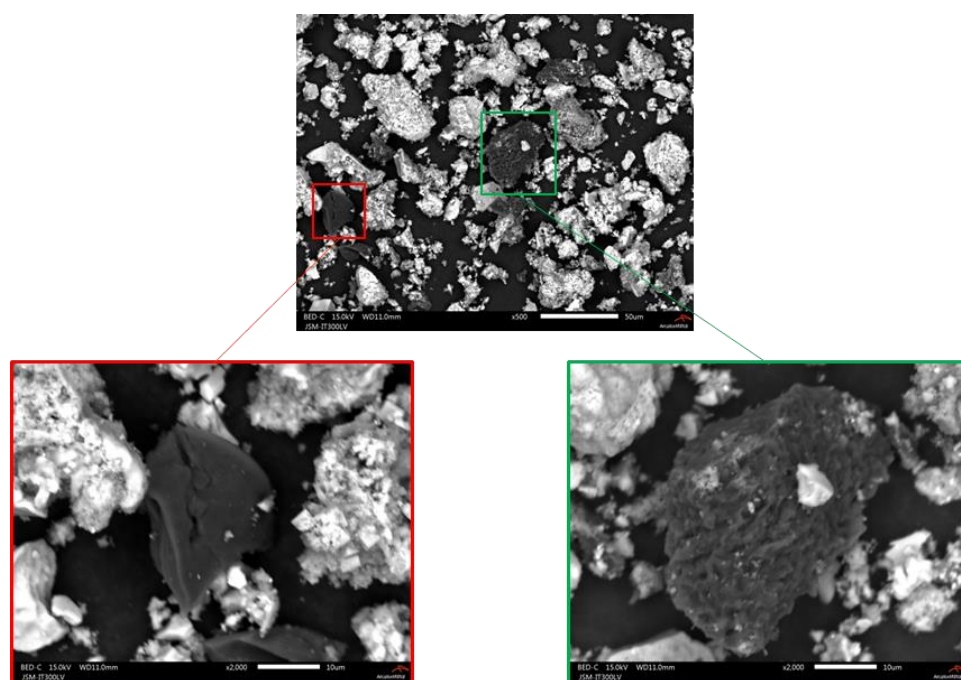
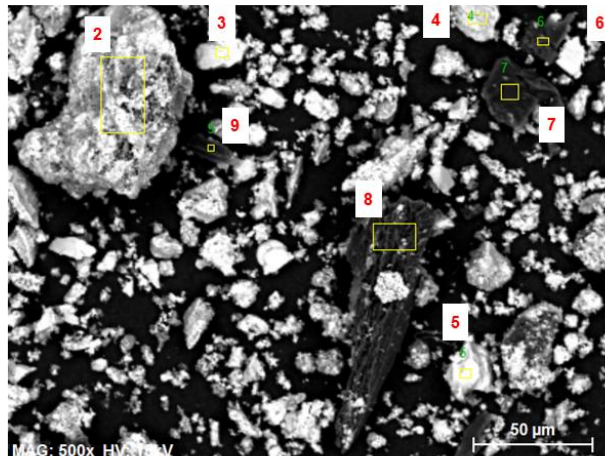


Figure 3.162: General aspect of the dust collected in the FVP pipe. Details of carbon particles morphologies



Spectrum	C	N	O	Na	Mg	Al	Si	S	Cl	K	Ca	Cr	Fe	Ni	Zn
9	93.86	2.02	2.53	—	—	—	—	0.48	0.28	0.22	—	—	—	—	0.61
8	89.98	—	4.24	—	0.02	0.05	0.54	0.77	0.36	0.54	0.21	0.34	0.71	—	2.23
7	90.92	2.72	4.21	—	—	0.20	0.34	0.57	—	0.12	—	—	—	—	0.92
6	85.82	1.87	6.34	—	0.30	1.32	1.72	0.61	—	0.22	—	—	0.86	—	0.95
5	5.97	—	21.14	0.38	0.17	0.24	0.34	1.00	11.87	1.23	0.20	5.63	4.28	47.55	—
4	17.44	—	20.65	—	0.58	0.48	0.85	1.02	4.31	6.56	1.17	12.47	23.46	7.58	3.43
3	6.59	—	14.96	1.38	—	—	—	1.44	15.06	4.52	—	3.14	8.57	44.34	—
2	34.60	—	17.87	0.88	0.51	3.00	3.16	0.62	9.68	15.14	2.10	—	6.60	—	5.84

Figure 3.163: Analysis of some of the dust particles collected in the FVP pipe

As a conclusion, this first attempt to sample dust in the shaft was disturbed by steam condensation in the pipe rolled over the FVP drum. The only way to improve things will be to warm-up this drum in order to keep the pipe at a temperature above ~ 70 °C. If successful, the second tricky part will be to find out some means for quantifying the respective proportions of coke and char in the sampled dust.

An improved design of the probe was then investigated. It was essentially based on the utilization of heating wire for the probe itself, and also for the different parts on the way of the probe to the furnace (notably the BF valve and the unrolled length of the pipe between the drum and the BF valve). The basic design of the new probe is presented in **Figure 3.164**. It still has to be tested at the blast furnace.

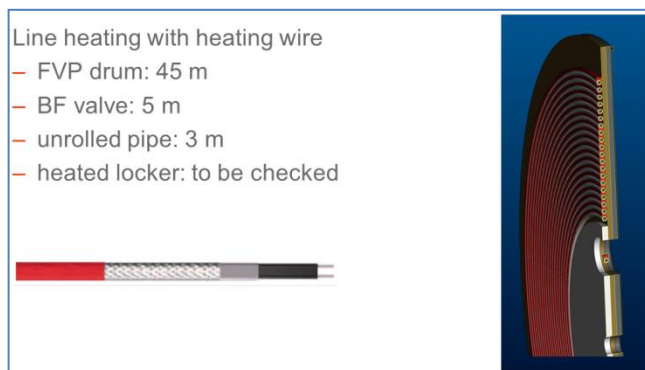


Figure 3.164: Design of the heated probe based on heating wire

3.4.2.1.2 COKE CORE BORING AND COKE SCRAPPING EXERCISE

In order to check the influence of high reducing agent injection on the evolution of the inner situation of the hearth and on the evolution of the coke size distribution between the top and bosh of the furnace, coke core boring and coke scrapping exercises were done on 31/05/2016 and 20/06/2017. A few pictures of these tests are presented in **Figure 3.165**.

The first step after visual observation of the core was to organise the sampled materials in different lots according to their characteristics. For the 2016 trials, 7 lots were identified, while for the test done on 20/06/2017, only 4 lots could be collected, one of them corresponding to the clay used for clogging the tuyère during the stoppage. This was most likely due to the fact that the core boring could take place not before 3 hours after the stop of the furnace, which was a relatively long delay for this type of trial.

The second stage was to position them along the radius taking into account the information from the ultrasonic displacement sensor implanted in the probe. **Figure 3.166** gives the structure of the probe as well as the positions of the different lots along the radius. Each lot is afterwards treated according to the scheme given in **Figure 3.167**. Note that in the present case, the chemistry of iron, slag and others on the > 10 mm fraction was not determined.

After treatment, the raceway depth free of liquids was estimated to be 0.93 m long. The bird nest had a length of 0.52 m. Coke could be sampled inside the dead man over a depth of 0.93 m.

The different characteristics of the 2016 core are presented in **Figure 3.168**. In Graph 1, the bird nest limit is shown by the increase in iron content. Graph 2 and 3 show the coke characteristics. Coke finer than 10 mm represent ~45 % of the dead man coke. Also, the d₅₀ of the coke in the raceway was ~30 mm in average, and was constantly decreasing from the tuyère tip towards the dead man. One could also notice the huge amount of overall fines <10 mm in the dead man (~55 % in Graph 4), with an almost 50/50 share between coke and liquids (Graph 5 and 6).

The characteristics of the 2017 core are presented in **Figure 3.169**. The determination of the positioning of the raceway was in this case not possible based on the figure. From the probe penetration depth point of view, it should be located at ~1.0 m from the tuyère nose. However, it could be seen that the distribution of fines and liquids were totally different from the ones of the 2016 trial (Graph 6 for example).

Additionally, after the first trial, fines from Lot 1 (deepest inside the dead man) and Lot 4 (birds nest) were taken for examination at the SEM. The objective was to check whether some clear differences in the carbon structure could be observed so that char and coke particles could be identified. Fractions < 125 µm and 125-250 µm were examined. It came out that if both types of particles exist inside the samples, it is impossible to easily distinguish them with the SEM. This is illustrated in **Figure 3.170** (< 125 µm) and **Figure 3.171** (125-250 µm).



Coke core boring exercise

Coke scrapping exercise

Figure 3.165: Pictures of coke sampling at tuyère level

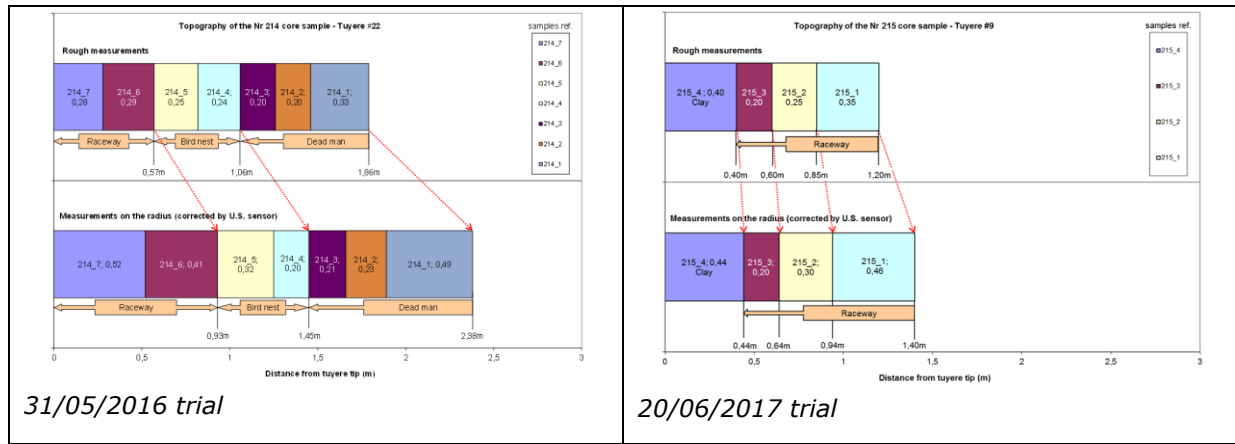


Figure 3.166: Determination of the actual positioning of the different lots over the radius

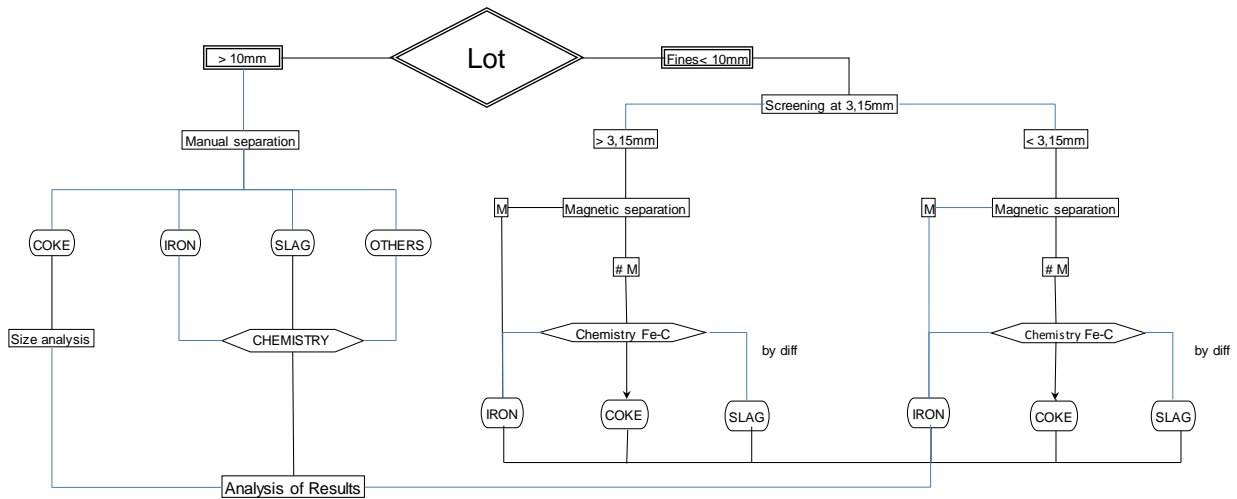


Figure 3.167: Characterisation procedure of each lot of the core

3.4.2.1.3 ADDITIONAL OBSERVATIONS

The coke core boring experiment was performed at BF2 on 20/06/2017 (1 week before the MPVP trial). During this trial, iron pellets were recovered within the core. As this is somewhat surprising, these pellets were taken for observation at the Scanning Electron Microscope. The main point of investigation was the reduction degree of the pellets.

Figure 3.172 presents the pellets prepared for observation. Referring to their size, it looked like they were of two different types. The smallest ones were referred as Pi, and Gi for the biggest ones.

A chemical map of the section of pellet G1 was done close to its surface. It clearly indicated that oxygen and iron were present at the same time, with some additional calcium close to the surface (**Figure 3.173**).

Analyses of a large portion of the surface gave the composition of the pellet. Obviously, this pellet had not undergone any reduction, as indicated in **Figure 3.174**. It still contained ~95 % of haematite!!

The same approach was done for all pellets, with the same outcome: none of these pellets had been reduced, the iron in them being in the haematite form. This could be of importance for explaining the position of the cohesive zone, as would be discussed later.

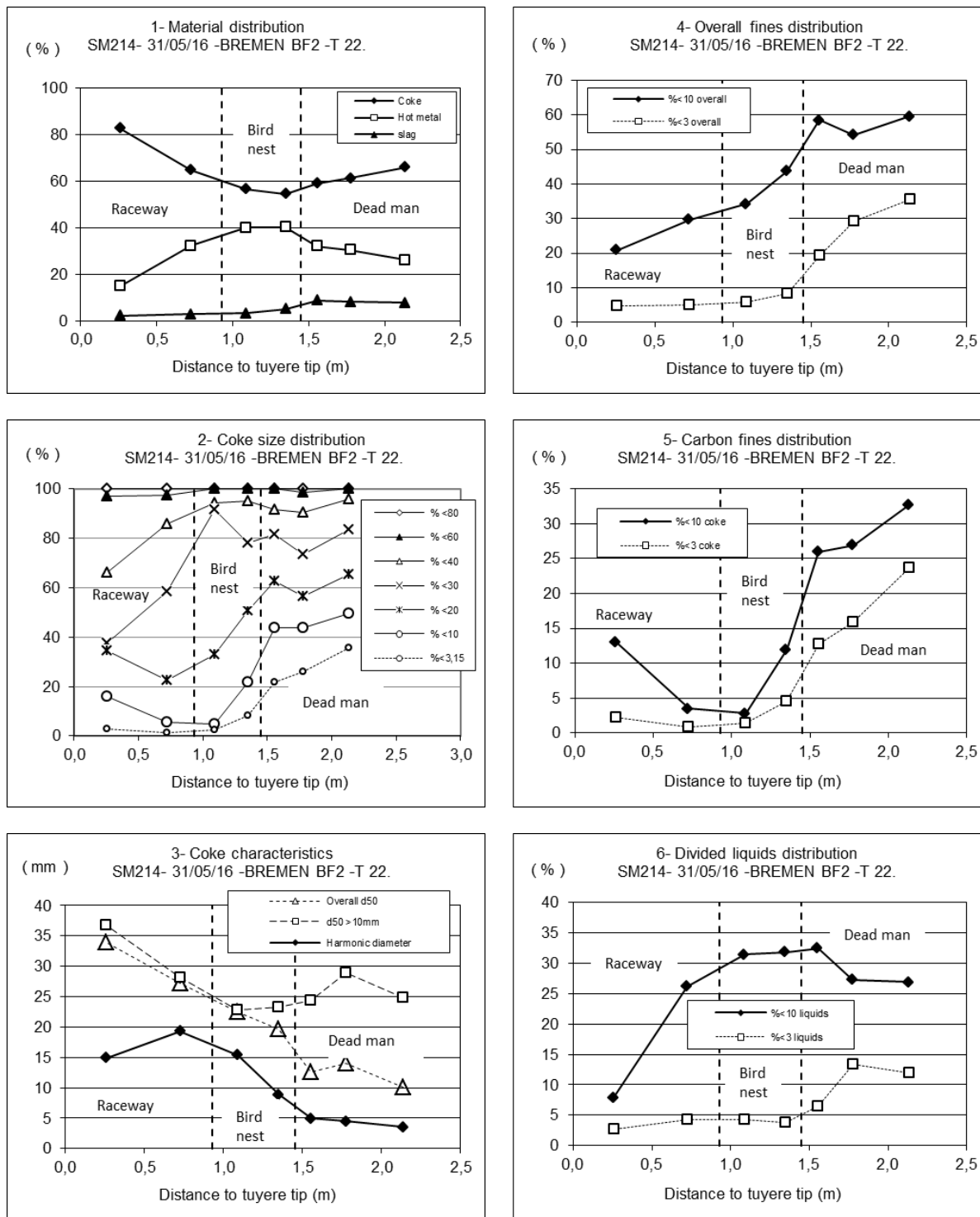


Figure 3.168: Characteristics of the core sampled at AM Bremen BF2 on 31/05/2016

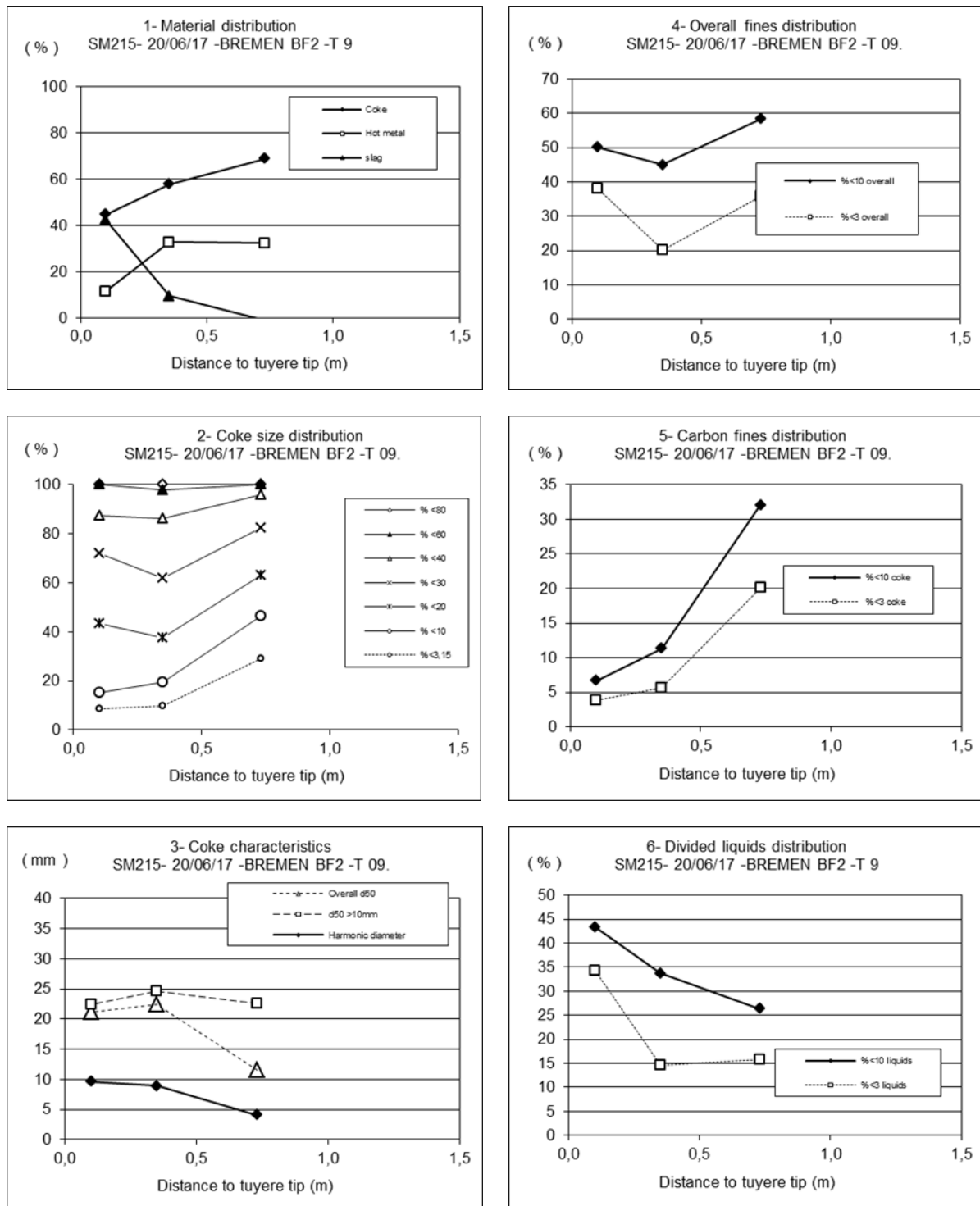


Figure 3.169: Characteristics of the core sampled at AM Bremen BF2 on 20/06/2017

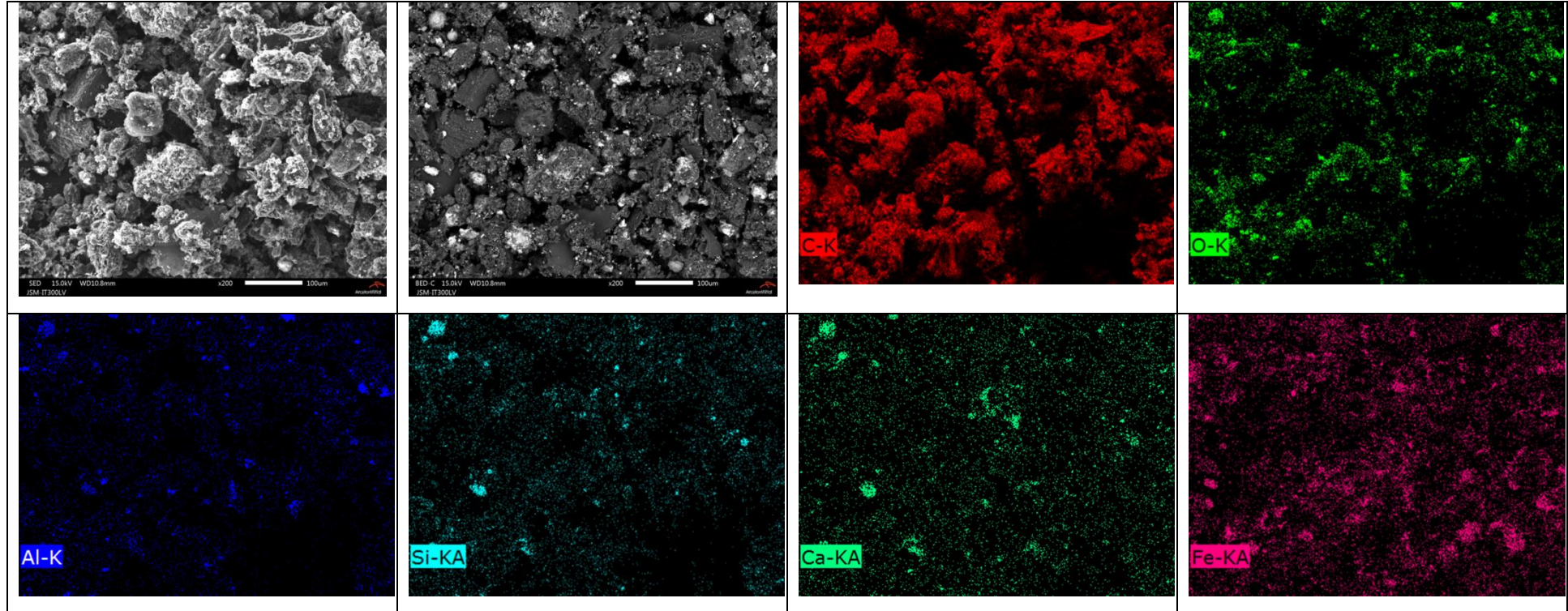


Figure 3.170: SEM observation of fines < 125 µm of Lot 1 – Top left 1st picture: structural aspect; 2nd picture: chemical contrast

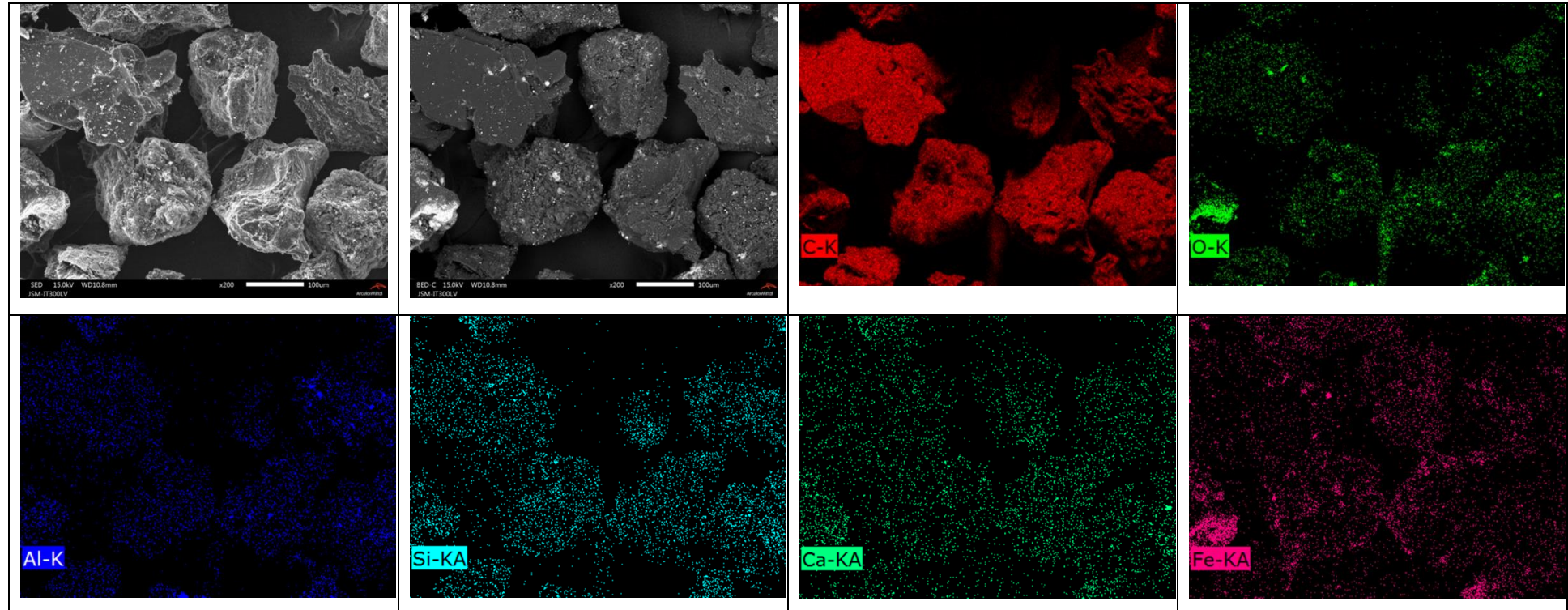


Figure 3.171: SEM observation of fines 125-250 μm of Lot 1 – Top left 1st picture: structural aspect; 2nd picture: chemical contrast

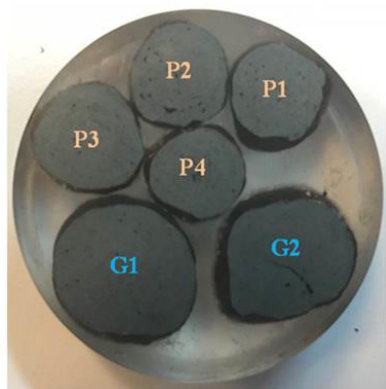


Figure 3.172: Pellets as prepared for SEM analysis

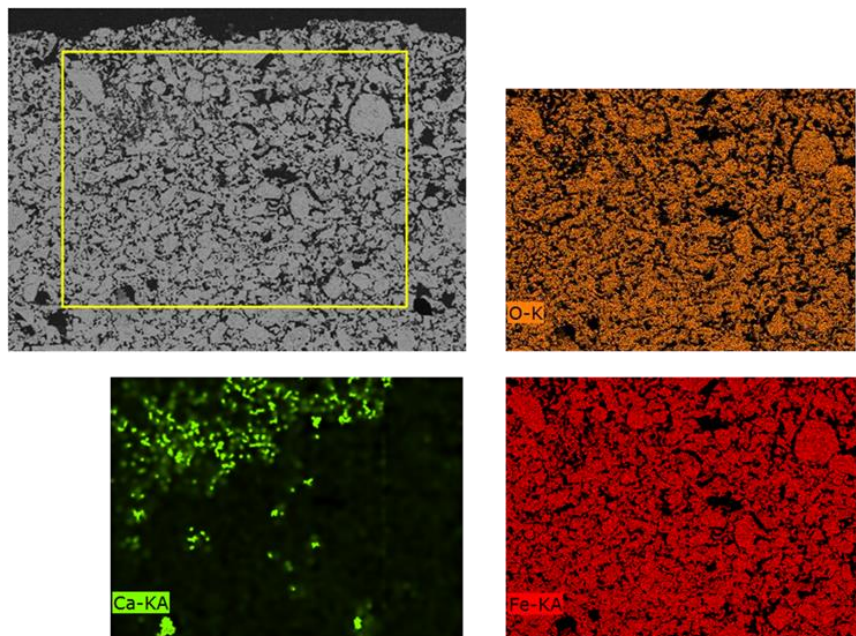


Figure 3.173: Chemical map of pellet G1 close to its surface obtained by SEM analysis

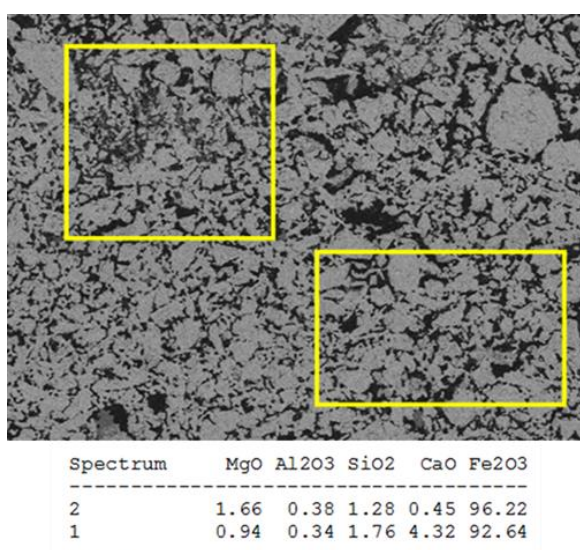


Figure 3.174: Chemical composition of the sample showing that it still contains ~95 % of hematite

3.4.2.1.4 MULTI-POINT VERTICAL PROBING

The technology of the MPVP is now well known and is reminded in **Figure 3.175**. In the case of Bremen BF2, the profilometer bench was used for the introduction of the probe. Two trials were performed, one on 14/06/2016, the other one on 29/06/2017. Similar conditions were used during the second trial in order to confirm the results of the first campaign that looked rather specific compared to other MPVP trials performed in the AM Group.

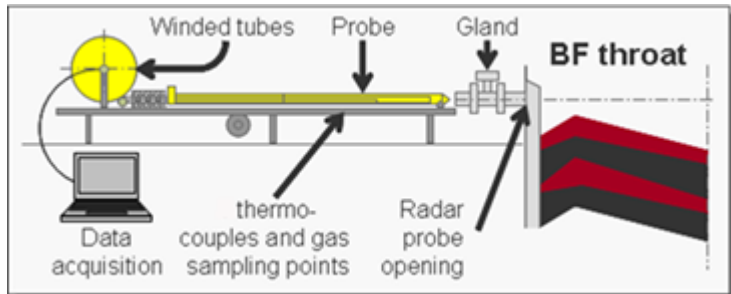


Figure 3.175: Sketch of the Multi-Point Vertical Probe system

3.4.2.1.4.1 MULTI-POINT VERTICAL PROBING ON 14/06/2016

3.4.2.1.4.1.1 DIRECT MEASUREMENTS AND THEIR PRELIMINARY INTERPRETATION

The information from the displacement sensor and the inclinometer, the thermocouples, and the gas analyses are given in **Figure 3.176**, **Figure 3.177** and **Figure 3.178**, respectively.

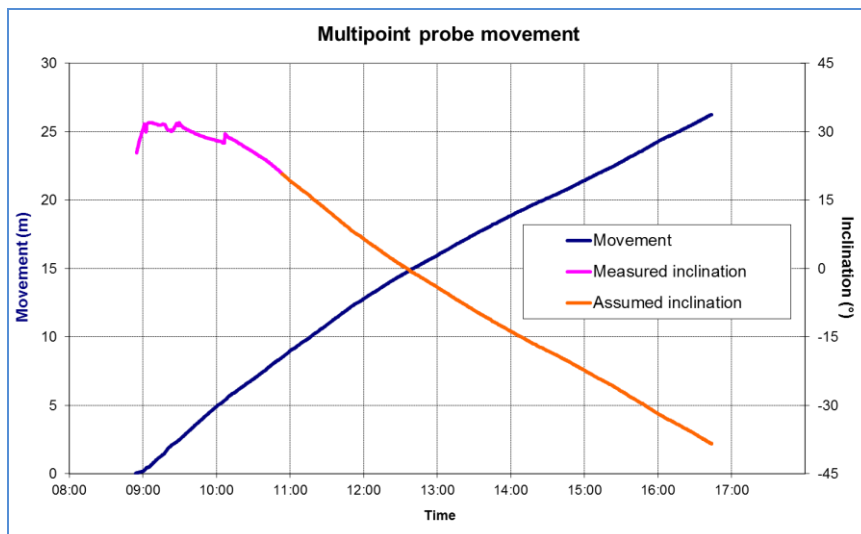


Figure 3.176: Displacement and measured and estimated inclination of the MPVP probe during the trial

The main comments that can be made are the following:

- the inclinometer was kept for 2 hours and finally broke at a temperature of ~ 230 °C;
- regarding the temperature profiles:
 - o ①: the extension of the drying zone is of the order of ~ 5 m, which corresponds to a high but still classical value. There is then no issue with the drying of the burden
 - o ② and ②': a particular shape is observed in the heating profiles at Points 2, 3 and 4, with either a peak or a hole between 17.5 and 25 m above tuyère level (TL)
 - o ③: the intermediate plateau corresponding to the reduction of hematite into magnetite is observed only for Point 1, and it is quite narrow
 - o ④: a classical thermal reserve zone is observed between 900 °C and 1000 °C at all points except in the centre where it looks more like a transition between low and high temperatures

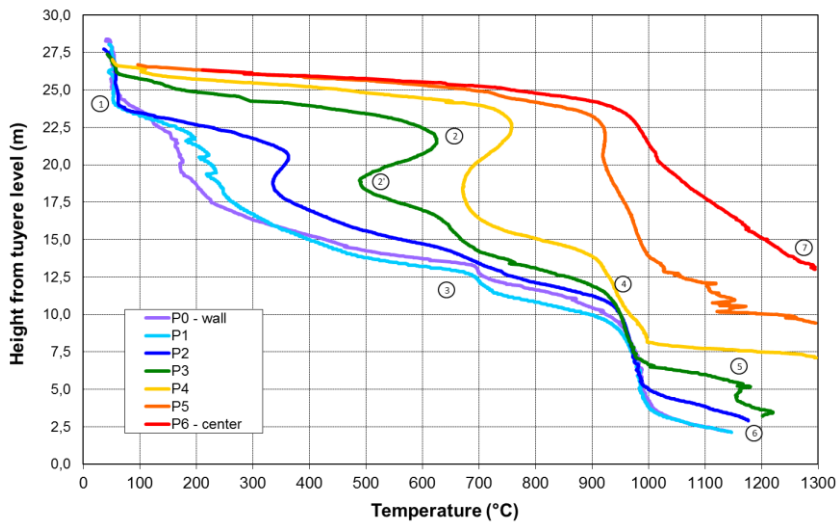


Figure 3.177: Temperature profiles measured during the MPVP trial of 14/06/2016 at AM Bremen BF2

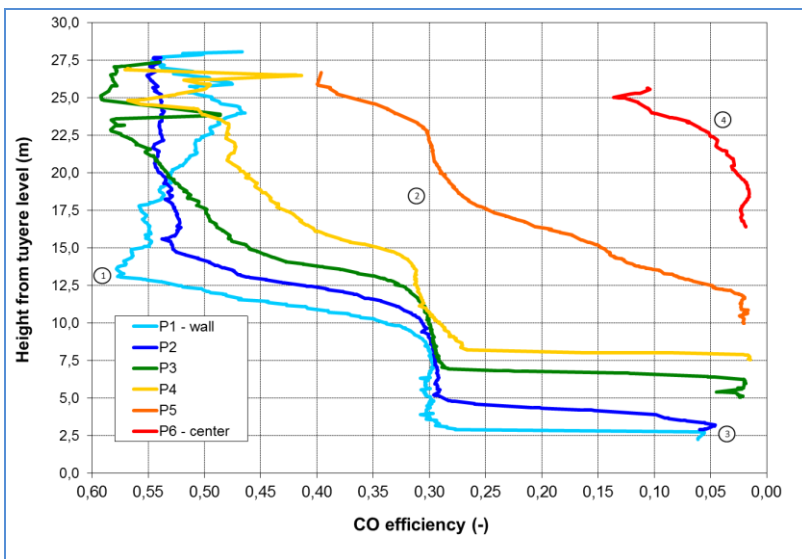


Figure 3.178: CO efficiency profiles measured during the MPVP trial of 14/06/2016 at AM Bremen BF2

- ⑤: a small thermal reserve zone is observed at ~ 1170 °C at Point 3; this happens sometime and could have to do with the recirculation of tramp elements
- ⑥: a low position of the root of the cohesive zone is observed, lower than 2,5 m above TL. This might be put in relation with tuyere tilting problems sometime observed at BF2
- ⑦: the cohesive zone in the centre of the furnace is rather high. A classical inverted V shape of the cohesive zone is then expected
- regarding the CO efficiency profiles:
 - ①: the reduction of the burden is significantly delayed at the wall of the furnace. 15 m are lost before it starts
 - ②: a chemical reserve zone is observed at all points except in the centre of the furnace
 - ③: the low position of the root of the cohesive zone is confirmed by the chemistry
 - ④: the CO efficiency in the furnace centre is always below 15 %, which is consistent with the high C/(C+O) ratio at this position, Figure 3.187.

3.4.2.1.4.1.2 TEMPERATURE, CO EFFICIENCY AND PRESSURE MAPS

This preliminary information is confirmed by the temperature and CO efficiency maps (**Figure 3.179**).

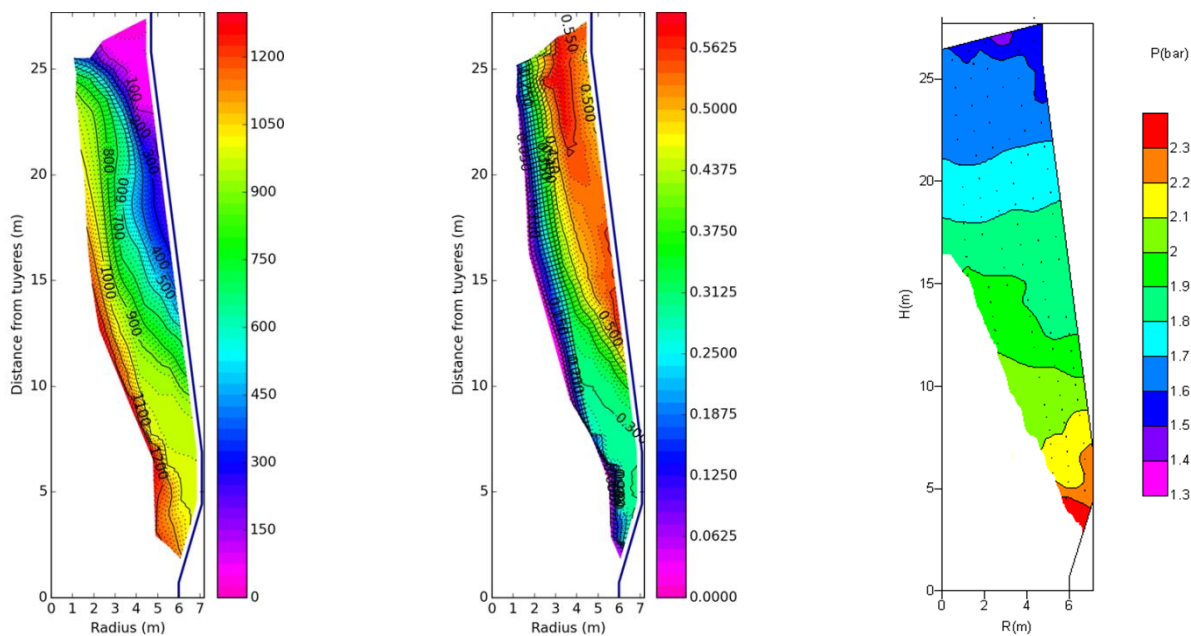


Figure 3.179: Thermal and CO efficiency maps, and pressure map resulting from the MPVP trial at BF2 on 14/06/2016

These maps make the following facts even more evident:

- a marked inverted V shape cohesive zone develops in the furnace;
- the periphery of the furnace (~70 % close to the top) is not concerned by the reduction of the ferrous burden. At the wall, the reduction starts only 12 m above TL. This is something exceptional that has rarely been observed during MPVP trials;
- another special feature of this trial is the particular shape of the [400-700 °C] temperature range, which is almost vertical, and covers a significant height of the shaft. As a matter of fact, this zone develops at mid-radius (~1.5 m away from the wall) over a height of ~8 m (between 24 m and 16 m above TL) and has a width of ~1 m or more.

This temperature range is known for being the range in which the ferrous burden is sensitive to the degradation during reduction due to the transformation of haematite into magnetite. It could be that such degradation actually occurs at BF2. If this is actually the case, some kind of low permeability wall would build-up at mid-radius, then contributing to the deviation of the gas towards the centre of the furnace. Higher in the furnace, when the central (hot) gas would encounter material not yet affected by the degradation under reducing conditions, it would have the possibility to move in the direction of the furnace wall, then explaining the higher temperatures found at Points 2, 3 and 4 between 20 and 22.5 m above TL (**Figure 3.177**). This could also explain the fact that the pressure map presents a specific, non-horizontal isotherm at mid-radius (**Figure 3.179**). The region between 1.8 and 1.9 bar is two times larger at the wall compared to the centre, which could indicate cross-flows in this region, i.e. between 15 m and 18 m above TL. The readjustment of pressure would be followed by a readjustment in temperature a few meters above.

3.4.2.1.4.1.3 CHAUDRON'S DIAGRAMS

The Chaudron's diagrams obtained for the different points of the MPVP are presented in **Figure 3.180**. Based on these diagrams, it was possible to determine the point at which the first metallic iron was formed, which enabled for the calculation of the local gas consumption. The corresponding data and results are given in **Table 3.50**.

A few remarks concerning these results:

- the calculated specific consumption at the wall is quite low, which is in accordance with the slow heating rate of the burden, the delayed reduction of the burden in this area, and the low position of the root of the cohesive zone;

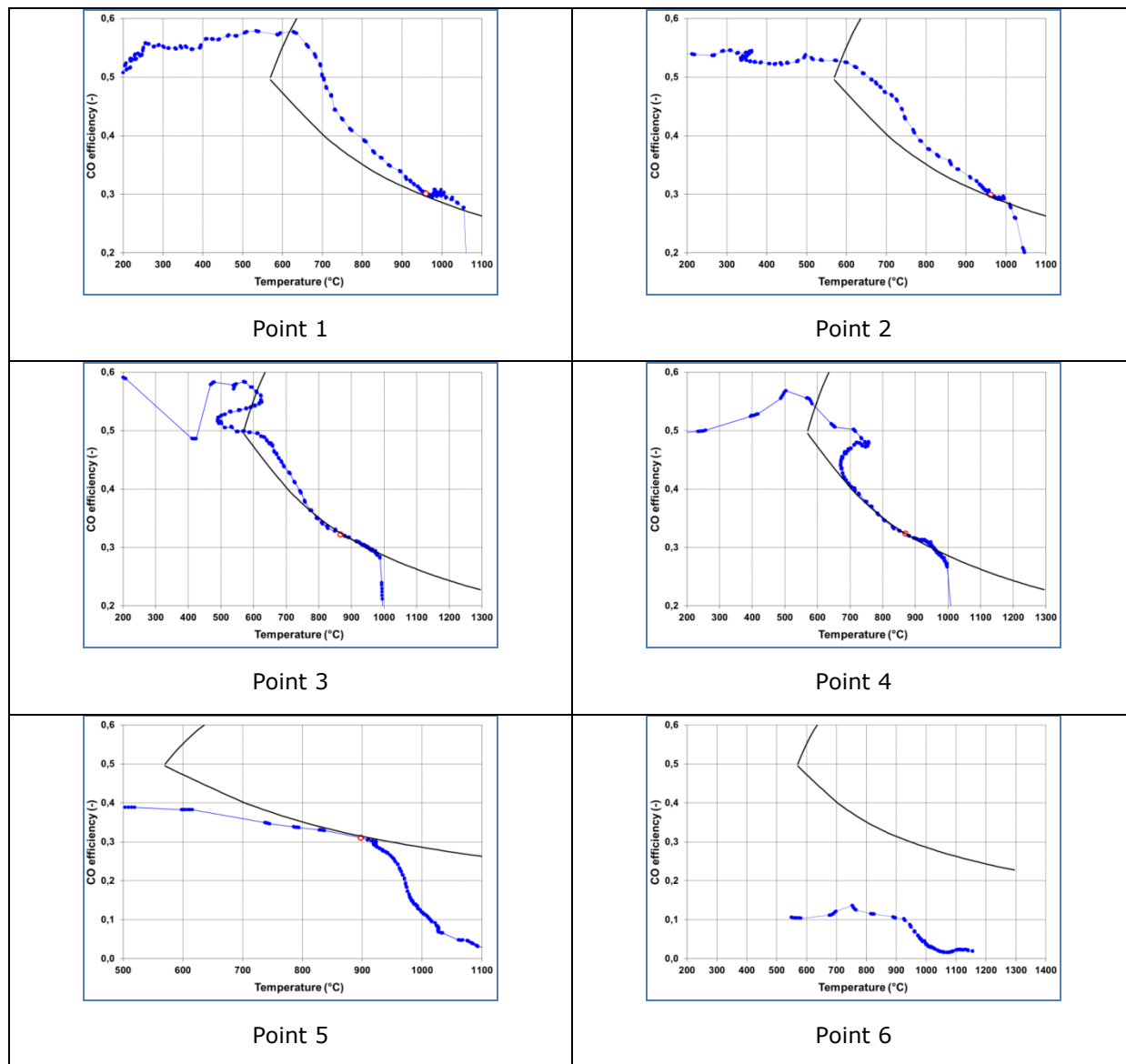


Figure 3.180: Chaudron's diagrams of the MPVP trial on 14/06/2016 at BF2. The red dots on the curves indicate the point selected for specific consumption calculation (μ) for the formation of the first metallic iron

Table 3.50: Conditions at the wustite-iron equilibrium and resulting local specific gas consumption

Point n°	Temperature	CO	CO ₂	H ₂	RCO	Calculated μ at(C+H ₂) / atFe
	°C	%	%	%	%	
1	959	31,49	13,56	6,71	0,301	1,533
2	965	32,59	13,90	6,13	0,299	1,908
3	866	30,92	14,70	6,03	0,322	1,899
4	869	31,90	15,27	7,76	0,324	2,747
5	897	32,24	14,53	5,05	0,311	4,803

- even if it was somewhat higher than at Point 1, the specific consumption at Point 2 and Point 3 was low, and in any case lower than the average specific gas consumption of the blast furnace (2,178 at(C+H₂) / atFe)
- the specific consumption at Point 5 was more than twice the average specific gas consumption of the furnace. This means that the centre was largely open to the gas, as this point was still located at a distance of ~2.0 m from the blast furnace axis.

3.4.2.1.4.2 MULTI-POINT VERTICAL PROBING ON 29/06/2017

3.4.2.1.4.2.1 DIRECT MEASUREMENTS AND THEIR PRELIMINARY INTERPRETATION

The information from the displacement sensor and the inclinometer, the thermocouples, and the

gas analyses are given in **Figure 3.181**, **Figure 3.182** and **Figure 3.183**, respectively.

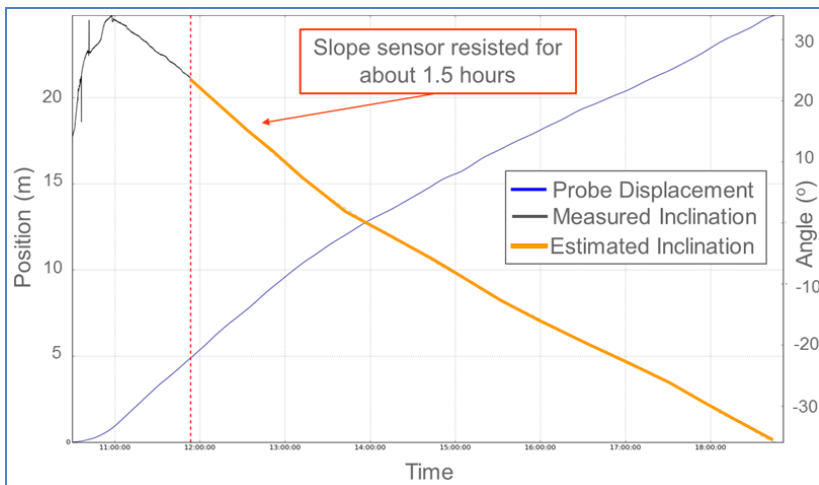


Figure 3.181: Displacement and measured and estimated inclination of the probe during the MPVP trial on 29/06/2017

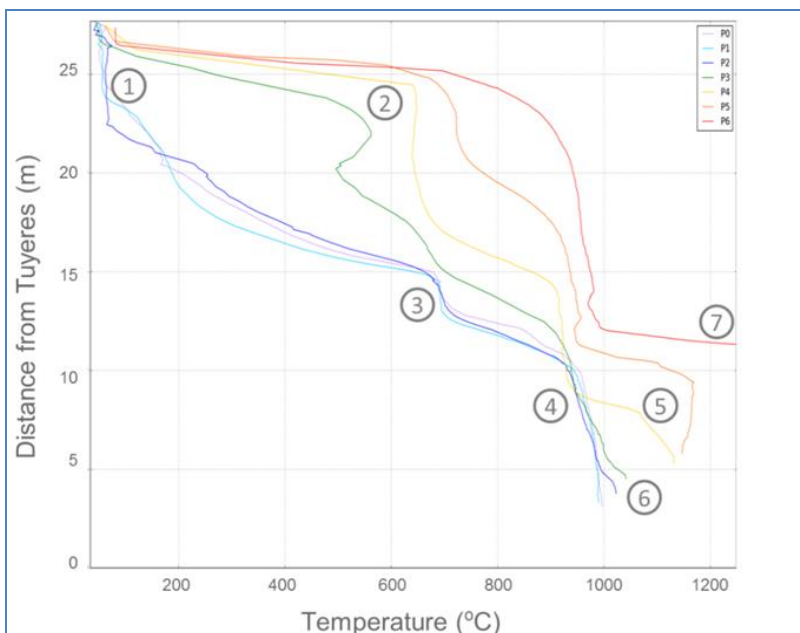


Figure 3.182: Temperature profiles measured during the MPVP trial of 29/06/2017 at AM Bremen BF2

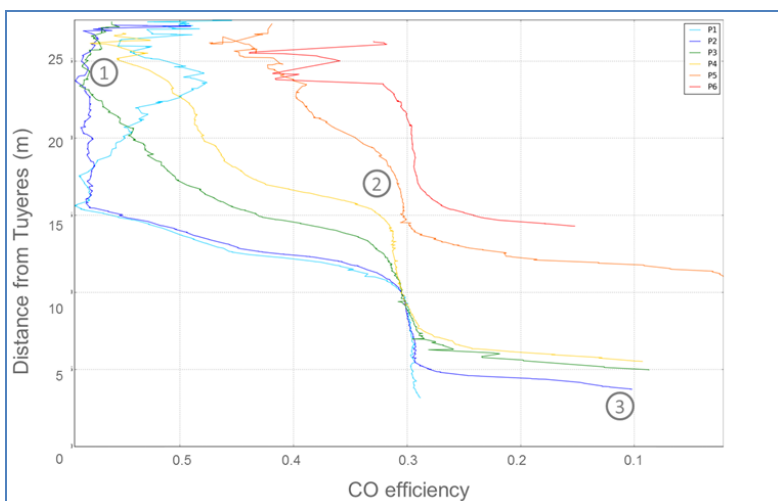


Figure 3.183: CO efficiency profiles measured during the MPVP trial of 29/06/2017 at AM Bremen BF2

The main comments that can be made are the following:

- the inclinometer was kept for 1.5 hours and finally broke at a temperature of ~ 200 °C, regarding the temperature profiles:
 - o ①: the extension of the drying zone is in the order of ~ 5 m, which corresponds to a high but still classical value. There is then no issue with the drying of the burden
 - o ②: a particular shape is observed in the heating profiles at Points 3 and 4, with either a peak or a hole between 20 m and 25 m above tuyère level (TL). This effect is less pronounced for Point 4. The same behaviour was observed in the previous MPVP
 - o ③: the intermediate plateau corresponding to the reduction of haematite into magnetite observed at Points 0, 1, 2 and 3 is quite narrow. At Point 4, a long plateau is observed that most likely also has to do with the reduction of haematite into magnetite. At Point 5, a plateau is also observed at a somewhat higher temperature, which could be the result of higher specific gas consumption at this location. For the central point, this intermediate plateau is not visible
 - o ④: a classical thermal reserve zone is observed between 900 and 1000 °C at all points
 - o ⑤: a small thermal reserve zone is observed at ~ 1170 °C at Points 4 and 5; this happens sometimes and could have to do with the recirculation of trace elements
 - o ⑥: a low position of the root of the cohesive zone is observed, lower than 3 m above TL. This might be put in relation with tuyère tilting problems sometime observed at BF2
 - o ⑦: the cohesive zone in the centre of the furnace is rather high. A classical inverted V shape of the cohesive zone is then expected
- regarding the CO efficiency profiles:
 - o ①: the reduction of the burden is significantly delayed at the wall of the furnace. More than 12 m are lost before it starts;
 - o ②: a chemical reserve zone is observed at all points;
 - o ③: the low position of the root of the cohesive zone is confirmed by the chemistry.

3.4.2.1.4.2.2 TEMPERATURE AND CO EFFICIENCY MAPS

This preliminary information is confirmed by the temperature and CO efficiency maps (**Figure 3.184**).

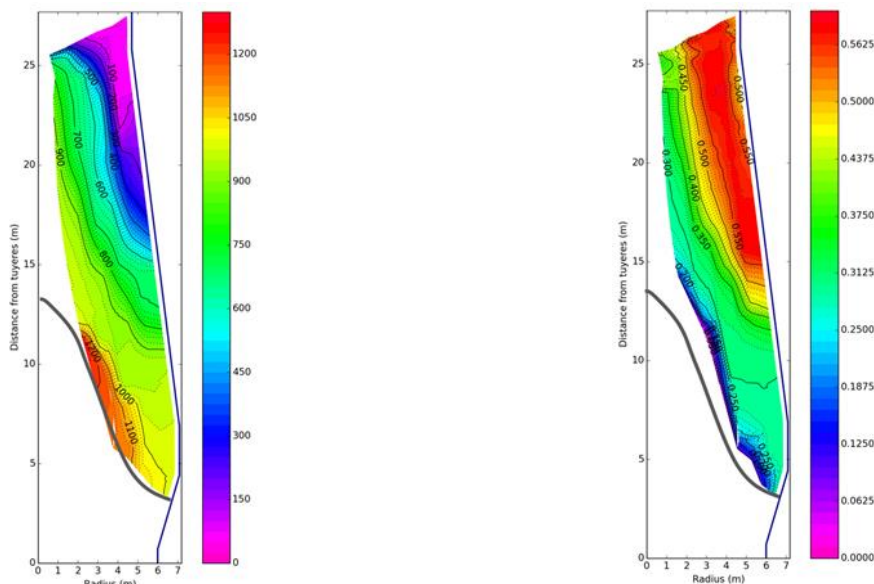


Figure 3.184: Thermal and CO efficiency maps resulting from the MPVP trial at BF2 on 29/06/2017

These maps make the following facts even more evident:

- a marked inverted V shape cohesive zone develops in the furnace. This is especially clear on the CO efficiency map;
- the periphery of the furnace (~70 % close to the top) is not concerned by the reduction of the ferrous burden. At the wall, the reduction starts 15 m above TL. This is something exceptional that was also observed during the previous MPVP trials at Bremen BF2;
- another special feature of this trial is the particular shape of the [400-700 °C] temperature range, which is almost vertical, and covers a significant height of the shaft. As a matter of fact, this zone develops at mid-radius (~1.5 m away from the wall) over a height of ~8 m (between 25 m and 17 m above TL) and has a width of ~1 m or more. In the same way as for the 2016 trial, this could have significantly affected the gas distribution within the furnace.

3.4.2.1.4.2.3 CHAUDRON'S DIAGRAMS

The Chaudron's diagrams obtained for the different points of the MPVP are presented in **Figure 3.185**.

Based on these diagrams, it is possible to determine the point at which the first metallic iron is formed, which in turn gives way to the calculation of the local gas consumption. The corresponding data and results are given in **Table 3.51**.

Table 3.51 : Conditions at the wustite-iron equilibrium and resulting local specific gas consumption for the MPVP trial on 29/06/2017

Point n°	Température °C	CO	CO2	H2	RCO	Calculated μ at(C+H2)/atFe
		%	%	%	%	
1	895	31,73	14,77	6,01	0,318	1,73
2	825	30,25	16,05	6,71	0,347	1,71
3	780	29,91	17,16	6,36	0,365	2,01
4	860	32,42	15,54	7,14	0,324	2,28
5	890	32,94	15,00	6,59	0,313	5,01

A few remarks concerning these results:

- the calculated specific consumption at the wall is quite low, which is in accordance with the slow heating rate of the burden, the delayed reduction of the burden in this area, and the low position of the root of the cohesive zone;
- the specific consumption at Point 2 and Point 3 is also low, and in both cases it is lower than the average specific gas consumption of the blast furnace (2,065 at(C+H2) / atFe);
- the specific consumption at Point 5 is more than twice the average specific gas consumption of the furnace. This means that the centre is largely open to the gas, as this point is still at a distance of ~2.0 m from the blast furnace axis.

3.4.2.1.4.3 CONCLUSIONS OF MPVP TRIALS

The MPVP trial performed on 29/06/2017 on AM Bremen BF2 confirms the previous results obtained during the MPVP performed on 14/06/2016. The conditions of the trials were almost identical and the conclusions of the first trial completely apply to the second one:

- the shaft appeared as split into two different zones, namely a wide open centre and a wall area lacking of gas, at least as far as burden heating and reduction were concerned;
- correlatively, the local specific gas consumptions in the wall area were significantly below the average specific gas consumption of the blast furnace;
- on the contrary, they were twice the average one already at 2 m from the BF centre
- the main consequences of this situation are:

- the existence of a well-developed inverted V shape cohesive zone;
- a low position of the root of the cohesive zone (less than 3.0 m above tuyère level). This might explain tuyère tilting issues at this furnace.

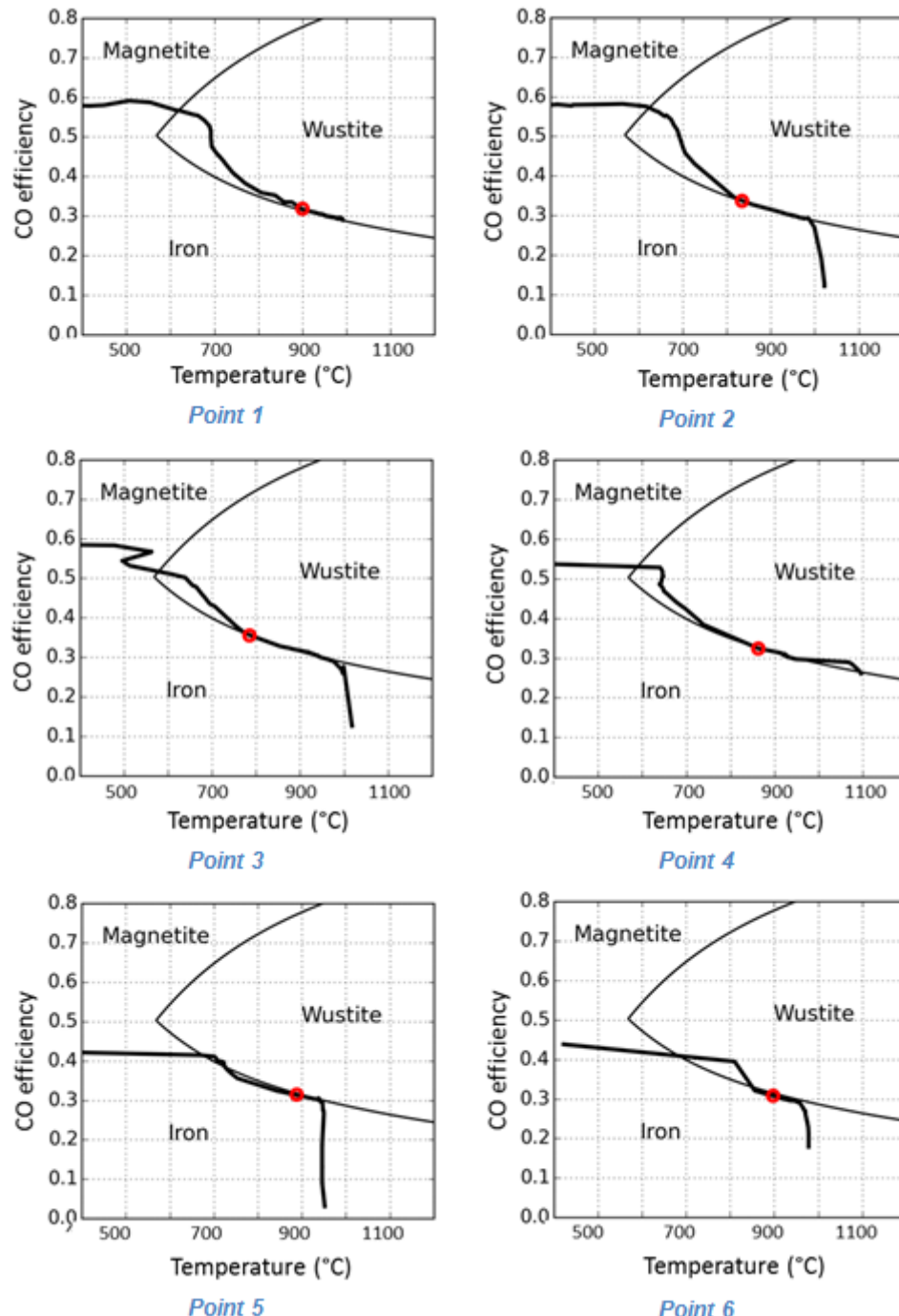


Figure 3.185: Chaudron's diagrams of the MPVP trial of 29/06/2017 at BF2. The red dots on the curves indicate the point selected for specific consumption calculation (μ) for the formation of the first iron atoms:

- at the wall, reduction starts more than 12 m below charging level, and a large part of the shaft is not used for the reduction of the ferrous burden;
- a secondary effect is that the critical temperature range for the burden reduction (400 - 700°C) develops abnormally over the shaft, especially in the vertical direction. This could also contribute to the split of the shaft into an active centre and a non-active wall area;
- however, it is somewhat surprising to see that the lack of gas at the wall does not impair the global reduction of the furnace. It looks like the reducibility of the raw material is high enough to make profit of the slow heating rate to reach the wustite-iron equilibrium at

lower temperatures than the classical 950 °C, paving the way for the obtaining of negative values of the defect to ideality of the reduction, called omegaP in AM heat and mass balance model. OmegaP measures the amount of oxygen in excess to wustite when the gas composition reaches the wustite iron equilibrium at 950 C. The oxidation degree of the ore at this stage is then $1,056 + \text{omegaP}$ (in atO/atFe).

- heating rate to reach the wustite-iron equilibrium at lower temperatures than the classical 950 °C, paving the way for the obtaining of negative values of omegaP.

Additionally, some complementary information can be derived from the trial, taking into account the reproducibility of the situation:

- from the MMHF calculations for the 2017 trial (**Table 3.55**) and taking Case 2 as a reference, it can be seen that the global heat losses of the furnace are in the range of standard values [400-450 MJ/t_{hm}]. But at the same time, the heat losses of the elaboration zone are quite low and those of the preparation zone quite high. It seems then possible that this situation is linked with the position of the isotherms in the shaft of the furnace and especially at the wall. As most of the shaft wall is at a temperature below 950 °C, the heat losses of the complete shaft are affected in the preparation zone. This is a critical situation because the high heat losses in the preparation zone cannot be compensated by some additional energy input, as it is the case with additional coke combustion in the elaboration zone. This explains the low top gas temperature (81 °C);
- from the coke core boring experiment, it could be seen that unreduced pellets may reach the tuyère zone. The pending question is then: what is the extent of this phenomenon during normal operation? If it is significant, the direct reduction of these pellets below the cohesive zone will necessitate a huge amount of energy that will be taken off the enthalpy of the raceway gas;
- moreover, it is likely that these pellets arrive below the cohesive zone due to percolation at the furnace wall. Then, this heat will be consumed essentially at the wall of the furnace. The melting of the ore will be delayed, which would explain the low position of the root of the cohesive zone.

The fact that the same thermo-chemical conditions could be observed in the shaft at a one year time interval gave some insight for changing the burden distribution conditions. This can be done in two directions at least:

- the most important point will be to distribute some of the central coke more towards the wall of the furnace. This will:
 - o reduce the extent of the drying zone;
 - o promote the development of a significant thermal and chemical reserve zone;
 - o avoid the build-up of a vertical zone in the critical temperature range for the degradation of sinter at mid-radius of the furnace;
- additionally, some attention should be paid to the location where the pellets are charged into the furnace, to see whether some improvement in their discharge position is possible with regard to percolation phenomena. As an example, an attempt of charging the pellets at mid-radius could be done.

3.4.3 TASK 3.3 DATA ANALYSIS

3.4.3.1 EVALUATION OF HIGH PCI OPERATION AT AM BREMEN BF2

3.4.3.1.1 COKE CORE BORING AND COKE SCRAPPING EXERCISE OF 31/05/2016

Among other information, the coke core boring exercise and the coke scrapping exercise give way to the degradation of the coke between the BF screens and the raceway. This degradation can be evaluated based on the cumulative size distributions of both cokes presented in **Figure 3.193**. The average of the two lots corresponding to the raceway coke of the coke core boring trial is also added to this graph. The estimated d₅₀ values of all three cokes are given in **Table 3.52** and **Figure 3.186**.

Table 3.52: Measured d₅₀ of all three cokes sampled on 31/05/2016

	Charged coke	Raceway coke	Scrapped coke
d ₅₀	67,0	30,5	34,0
Size decrease		36,5	33,0

The main points to be mentioned are the following:

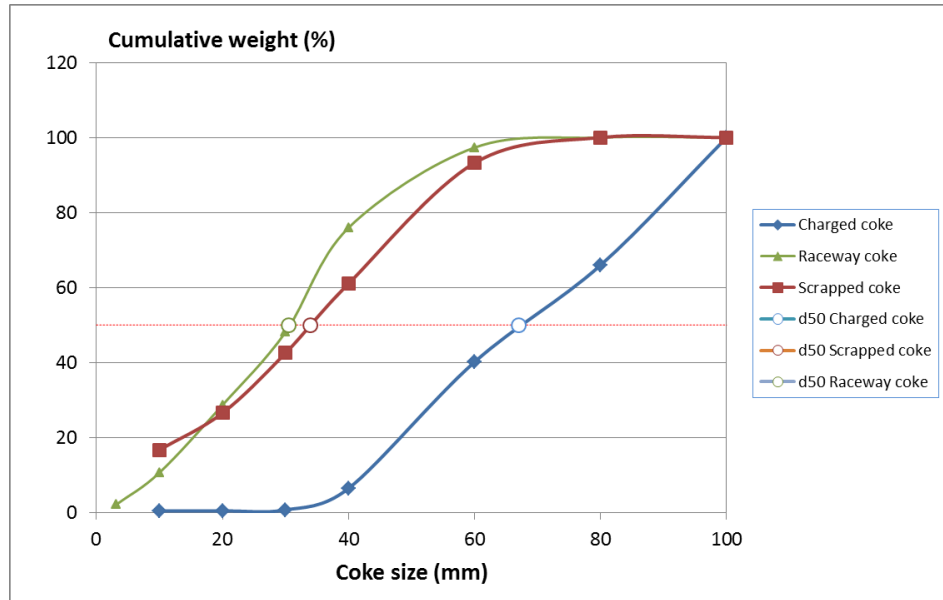


Figure 3.186: Size distributions of charged coke, raceway coke and scrapped coke during coke core boring and coke scrapping exercises on the 31/05/2016

- when arriving at the bosh, the mean size of the coke decreased by 33 mm down to 34 mm. Note that the corresponding I40 and CSR indexes were 53.3 % and 65 %, respectively the day before the coke core boring experiment;
- the raceway coke is in general finer than the scrapped coke. This could be put in relation with the degradation and combustion of the coke inside the raceway;
- however, it contains less fines lower than 10 mm, which can be explained either by a preferential combustion, or by the fact that these lighter particles are preferentially carried away by the blast issued from the tuyère, and should then be found mainly in the bird nest.

3.4.3.1.2 COKE CORE BORING AND COKE SCRAPPING EXERCISE OF 20/06/2017

Similarly, the information related to the coke core boring exercise and coke scrapping exercise done of the 20/06/2017 are given in **Figure 3.187** and **Table 3.53**.

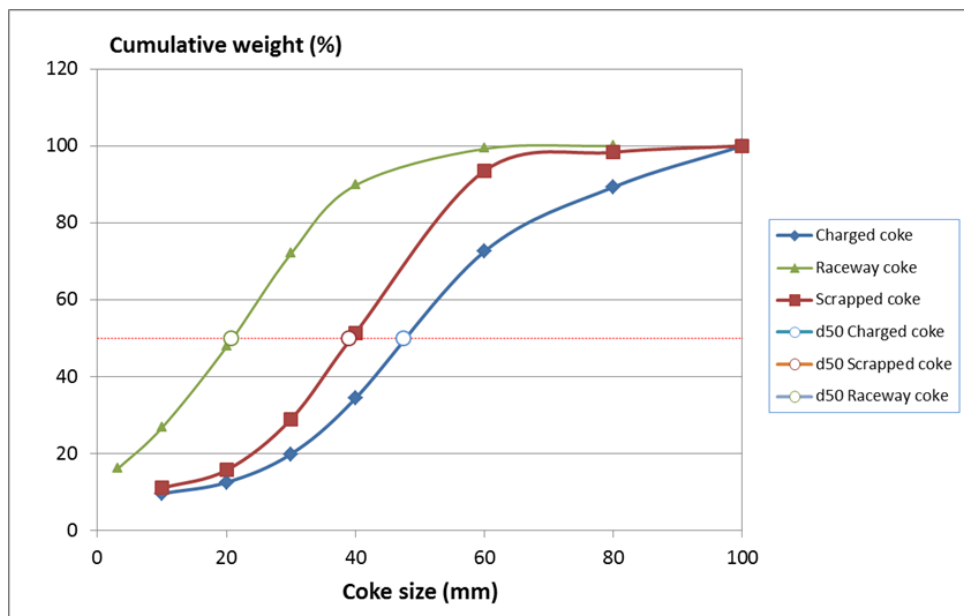


Figure 3.187: Size distributions of charged coke, raceway coke and scrapped coke during coke core boring and coke scrapping exercises on the 20/06/2017

Table 3.53: Measured d50 of all three cokes sampled on 20/06/2017

20/06/2017	Charged coke	Raceway coke	Scrapped coke
d50	47,5	20,7	39,0
Size decrease	CSR=67,3 %	26,8	8,5

As can be seen, there are significant differences between the two periods regarding the size distributions of the coke sampled at the three different locations. The scrapped coke is rather consistent, while a large discrepancy exists between the charged cokes on the one hand and the raceway cokes on the other hand. As mentioned before, the size of the raceway coke from the 2017 trial could be affected by the fact that the core was drilled under specific conditions (long delay between stoppage and core drilling). Regarding the charged coke, the low d50 value is questionable and puts some doubt on the representativeness of the sample.

3.4.3.1.3 MULTI-POINT VERTICAL PROBING PERFORMED ON 14/06/2016

3.4.3.1.3.1 GENERAL OPERATING CONDITIONS

AM Bremen BF2 was selected as the test facility of ArcelorMittal for the CharFoCo trials because the plant regularly operates at coal + lignite injection rates of 240 kg/tHM and over (75 % coal / 25 % lignite).

The main characteristics of the charging pattern of the blast furnace just after the trial are given in **Figure 3.188**.

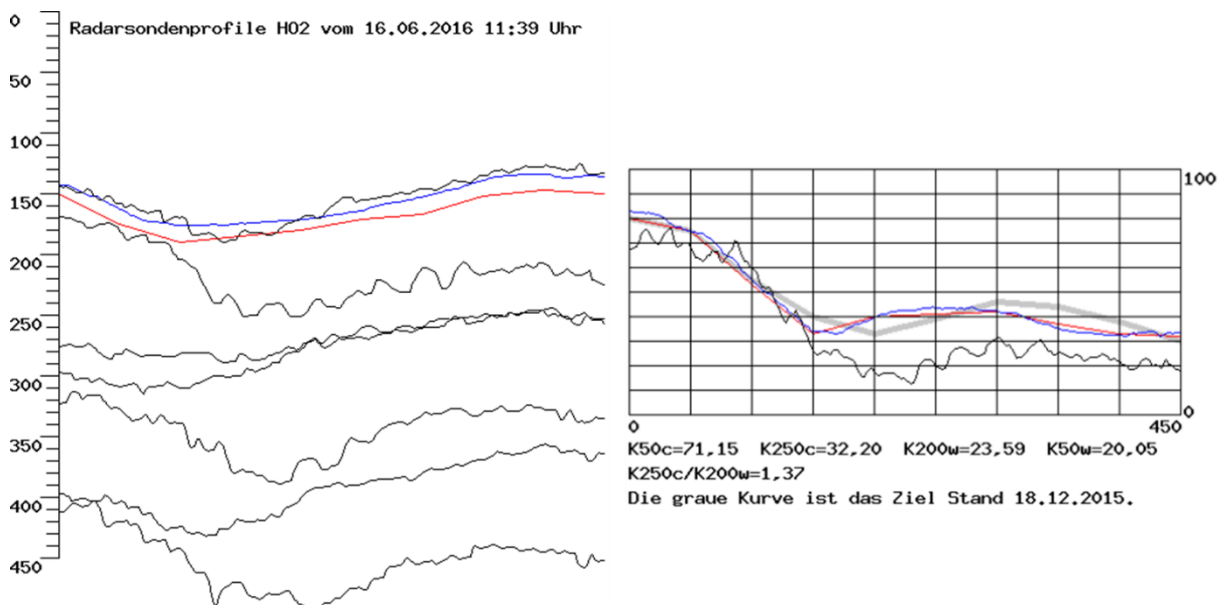


Figure 3.188: Measured charging pattern just after the MPVP trial on the 14/06/2016

The operational data of BF2 provided by the plant are presented in **Figure 3.189**. Key hot metal and slag quality indexes are given in **Figure 3.190**. As can be seen, the trial was performed under very stable conditions.

Table 3.54 gives some of the operating ratios of the blast furnace at the time of the trial.

Table 3.54: Main operating ratios of AM Bremen BF2 during the MPVP trial on 14/09/2016

Parameter	Unit	Date MPVP
		14/06/2016
Hot metal production (from burden)	t/d	6 284
Hot metal production (from EC model)	t/d	6 070
Coke rate (dry)	kg/thm	269,6
PCI rate (total)	kg/thm	236,8
incl. hard coal	kg/thm	168,2
incl. lignite	kg/thm	68,6
Equivalent coke rate	kg/thm	434,6
Natural blast flow rate	kNm ³ /h	217,6
Oxygen flow rate	Nm ³ /h	16 257
Blast temperature	°C	1 240
Adiabatic Flame Temperature (EC model)	°C	2 137
Top gas temperature	°C	104

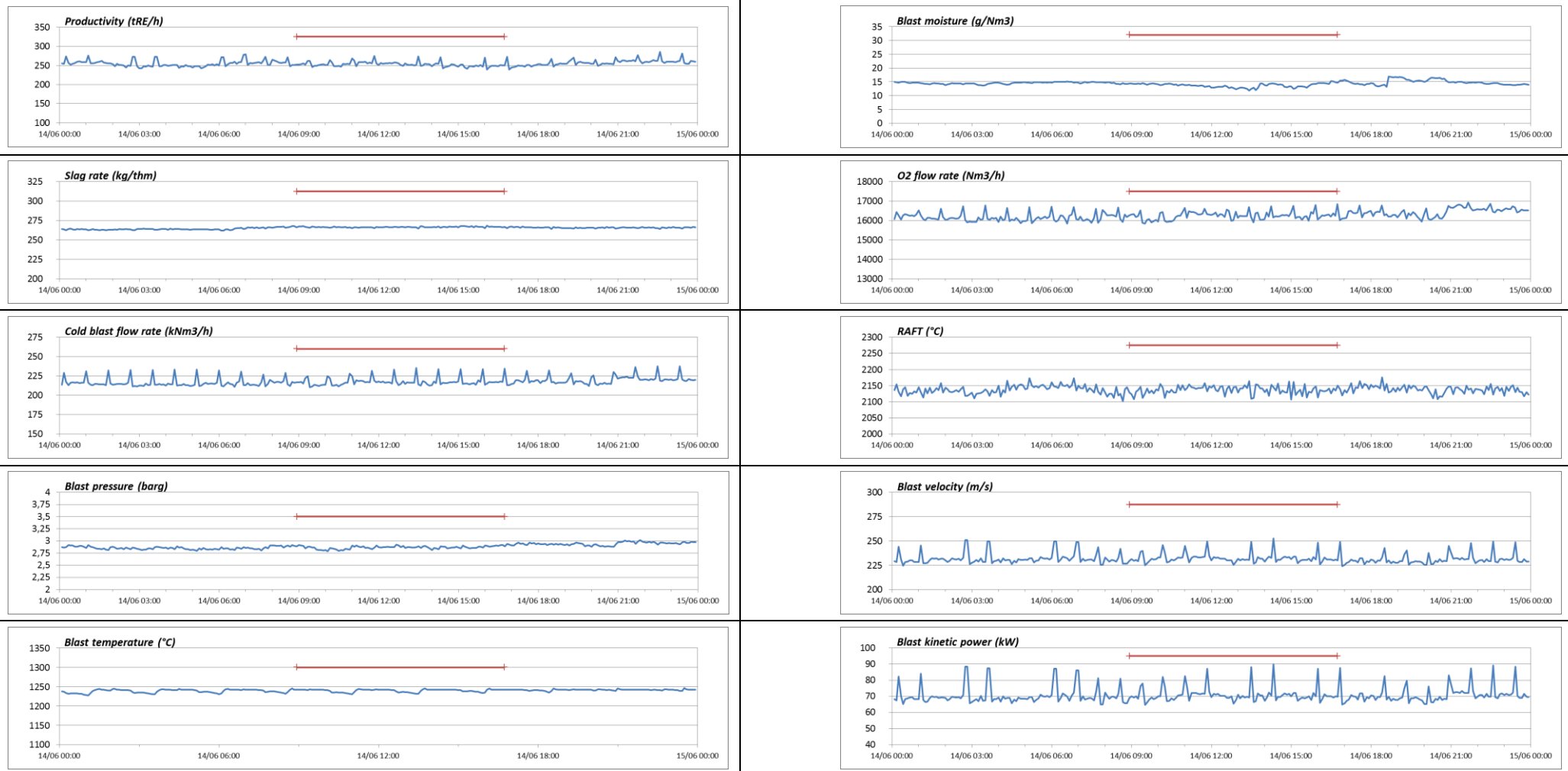


Figure 3.189: Operational data of AM Bremen BF2 during the 2016 MPVP trial, with indication of the period of the test (red line)



Figure 3.190: Hot metal and slag quality at the time of the MPVP trial

3.4.3.1.3.2 RESULTS OF HEAT AND MASS BALANCE MODEL (HMBM) CALCULATIONS

The operational data of the furnace was analysed by means of heat and mass balances, MMHF. The objective was to check the consistency of the data and to evaluate the operation in terms of reducing efficiency. The corresponding results of the model are given in **Table 3.55**.

Table 3.55: Main results of MMHF calculations and their comparison with the measurements (1)

		Measured	MMHF				
			Based on Gas Analysis				
			Case 01	Case 02	Case 03	Case 04	
Productivity	t/d	6 070	6 166	6 070	6 070	6 070	
Dry coke rate	kg/thm	269,6	275,6	276,9	282,3	284,0	
Wet coke rate	kg/thm	275,8	282,3	283,6	289,1	290,9	
Blast Rate	km ³ /h	217,6	217,6	214,9	219,2	218,5	
Blast Temperature	°C	1 240,0	1 240	1 240	1 240	1 240	
Blast moisture	g/Nm ³	13,7	13,7	13,7	13,7	13,7	
Oxygen flow rate	Nm ³ /h	16 257	16 257	16 257	16 257	16 257	
N ₂ in top gas	%	47,37	47,37	47,37	47,46	47,46	
CO in top gas	%	23,72	23,72	23,72	23,55*	23,72*	
CO ₂ in top gas	%	24,44	24,44	24,44	24,27*	24,44*	
H ₂ in top gas	%	4,47	4,47	4,47	4,81	4,46	
Injection 1 - Coal	kg/thm	168,2	168,2	168,2	168,2	168,2	
Hydrogen Content	%	3,81	3,81	3,81	3,81	3,30	
Injection 2 - Lignite	kg/thm	68,6	68,6	68,6	68,6	68,6	
Reserve zone gas rate	Nm ³ /thm		1 491	1 496	1 461	1 509	
OmegaP	atO/atFe	-	0,008	-	0,002	0,003	
μ, spec. gas consumption	mole (CO+H ₂)/mole Fe		2,147	2,153	2,177	2,159	
H ₂ yield	%		49,8	49,7	45,0	45,0	
Global heat losses	MJ/thm		599	629	693	677	
incl. preparation zone	MJ/thm		257	262	291	279	
incl. elaboration zone	MJ/thm		341	367	403	398	

*: fixed CO efficiency

Input
Output

In this table, Case 1 corresponds to the classical analysis of the operation on-line, based on the blast conditioning and the top gas analysis. As the calculated productivity was higher than the one calculated based on the burden – which is considered as the reference productivity – the latter was imposed in Case 2, leading to a different value of the blast flow rate. In both cases, the calculated and measured coke rates are 6 to 7 kg/t_{HM} higher than the measured one. Also, the H₂ efficiency was relatively high compared to the classical value of 45 %. The next case was then calculated assuming an H₂ efficiency of 45 %. In Case 4, it was assumed that there was an error on the H₂ analysis of the auxiliary reducing agents injected at tuyère. In order to match the measured and calculated analyses, it was necessary to assume a hydrogen content of the hard coal of 3.30 % instead of 3.81 % (which was already significant). Both led to an even higher coke rate compared to the measured one (difference over 10 kg/t_{HM}). So Case 2 was considered as the reference operation for further analysis.

The main conclusions derived from this calculation are the following:

- the ideal defect of the reduction is better than ideality (-0,008 atO/atFe);
- the calculated heat losses are relatively high (~630 MJ/t_{HM}), with higher values than usual observed in both zones. The reason for that is not clear.

3.4.3.1.4 MULTI-POINT VERTICAL PROBING PERFORMED ON 29/06/2017

3.4.3.1.4.1 GENERAL OPERATING CONDITIONS

The charging pattern used during the second test campaign is given in **Figure 3.191**.

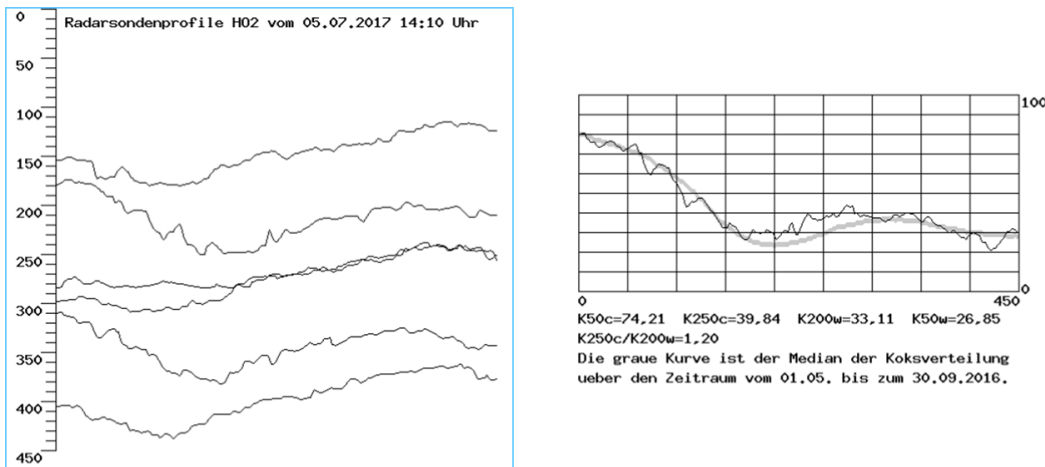


Figure 3.191: Measured charging pattern just after the MPVP trial on 29/06/2017

As can be seen, this charging pattern was quite similar to the one used at the time of the first MPVP trial.

The operational data of BF2 provided by the plant are presented in **Figure 3.189**. Key hot metal and slag quality indexes are given in **Figure 3.190**. Despite a process disturbance the day before, still visible in the hot metal quality (slightly higher temperature, carbon and silicon content of hot metal a shortly before midnight on 28/06/2017), it can be seen that the blast furnace had totally recovered and was stable at the time of the trial. Only the blast velocity and kinetic power were different due to an increase in the tuyère diameter between 2016 and 2017.

Table 3.54 compares the operating conditions of the furnace for the two periods. As can be seen, the operating conditions for both of them were comparable.

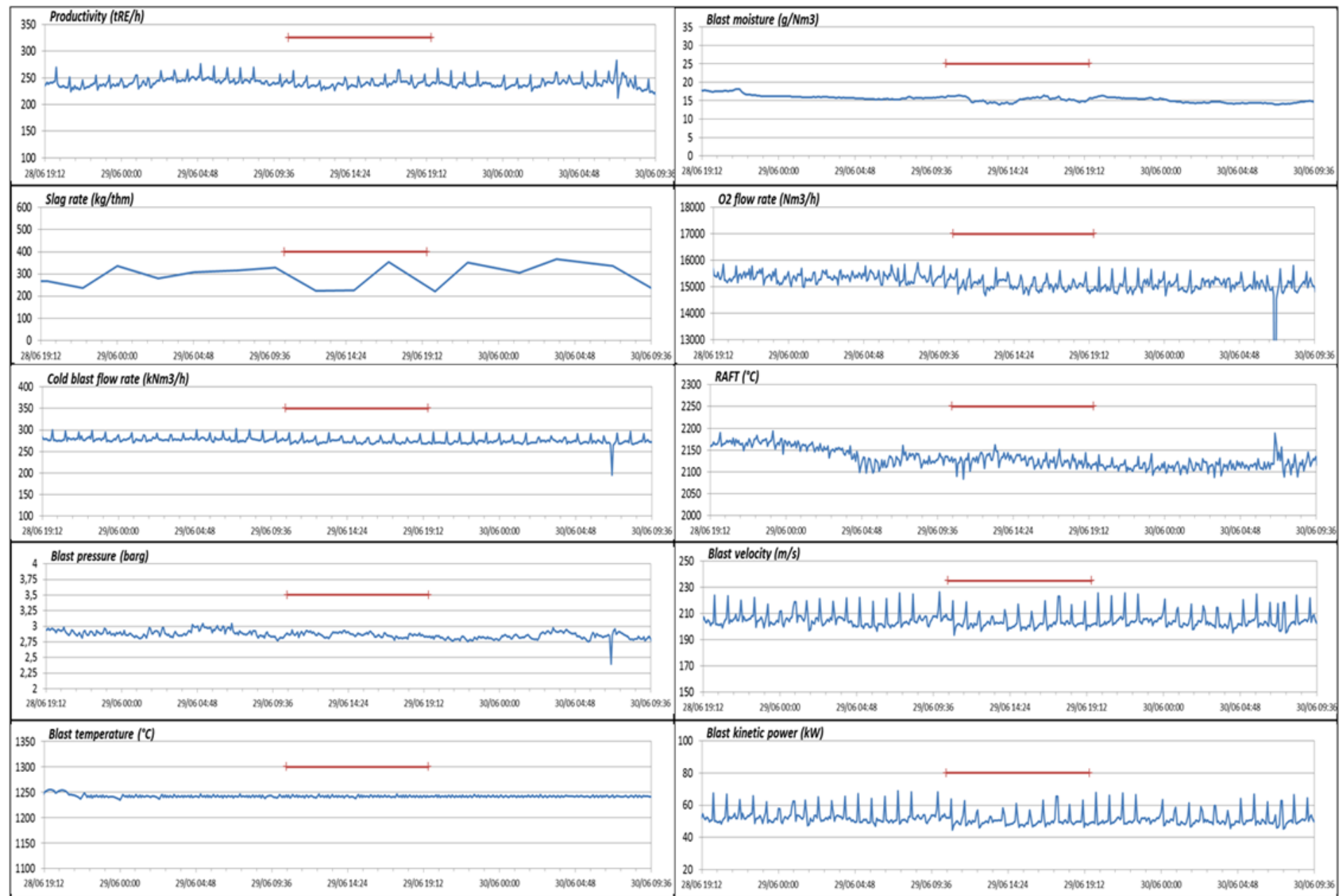


Figure 3.192: Operational data of AM Bremen BF2 at the time of the MPVP trial done on 29/06/2017, with indication of the test period(red line)



Figure 3.193: Hot metal and slag quality at the time of the MPVP trial on 29/06/2017

Table 3.56: Comparison of the main ratios of AM Bremen BF2 at the time of the MPVP trials

Parameter	Unit	Date MPVP	
		06/2016	06/2017
Hot metal production (from burden)	t/d	6 284	6 116
Hot metal production (from EC model)	t/d	6 070	5 734
Coke rate (dry)	kg/thm	269,6	257,0
PCI rate (total)	kg/thm	236,8	230,8
incl. hard coal	kg/thm	168,2	173,1
incl. lignite	kg/thm	68,6	57,7
Equivalent coke rate	kg/thm	434,6	422,2
Natural blast flow rate	kNm ³ /h	217,6	202,5
Oxygen flow rate	Nm ³ /h	16 257	15 091
Blast temperature	°C	1 240	1 242
Adiabatic Flame Temperature (EC model)	°C	2 137	2 127
Top gas temperature	°C	104	81

3.4.3.1.4.2 RESULTS OF HEAT AND MASS BALANCE MODEL (HMBM) CALCULATIONS

In addition to the monitoring of the main parameters of the blast furnace, BF2 operation at the time of the trial was also characterized by means of heat and mass balances using MMHF.

As for the 2016 MPVP trial, the first calculation done while imposing the blast conditioning and the top gas analysis led to a high value of the hydrogen efficiency. Different approaches were then used for better understanding, **Table 3.57**

Table 3.57: Main results of MMHF calculations and their comparison with the measurements (1)

		MMHF								
		Based on Gas Analysis				Based on Coke Rate				
		Measured	Case 01	Case 02	Case 03	Case 04	Case 05	Case 06	Case 07	Case 08
Productivity	t/d	6 116	5 917	6 116	6 116	6 116	5 868	6 116	6 116	6 116
Dry coke rate	kg/thm	257,0	258,1	255,4	263,6	266,2	258,0	258,0	258,0	258,0
Wet coke rate	kg/thm	269,9	269,9	267,1	275,7	278,4	269,9	269,9	269,9	269,9
Blast Rate	km ³ /h	202,5	202,5	208,0	214,6	213,5	202,5	213,9	212,0	209,7
Blast Temperature	°C	1 242,0	1 242	1 242	1 242	1 242	1 242	1 242	1 242	1 242
Blast moisture	g/Nm ³	14,4	14,4	14,4	14,4	14,4	14,4	14,4	14,4	14,4
Oxygen flow rate	km ³ /h	15 091	15 091	15 091	15 091	15 091	15 091	15 091	15 091	15 091
N ₂ in top gas	%	47,46	47,46	47,46	47,46	47,46	47,66	47,97	47,76	47,50
CO in top gas	%	22,91	22,91	22,91	22,66*	22,91*	22,51	22,36	21,56	21,98
CO ₂ in top gas	%	25,11	25,11	25,11	24,83*	25,11*	25,31	25,15	26,16	26,00
H ₂ in top gas	%	4,52	4,52	4,52	5,05	4,51	4,52	4,52	4,52	4,52
Injection 1 - Coal	kg/thm	173,1	173,1	173,1	173,1	173,1	173,1	173,1	173,1	173,1
Hydrogen Content	%	3,91	3,91	3,91	3,91	3,17	3,91	3,91	3,17	3,17
Injection 2 - Lignite	kg/thm	57,7	57,7	57,7	57,7	57,7	57,7	57,7	57,7	57,7
Reserve zone gas rate	Nm ³ /thm		1 449	1 441	1 475	1 462	1 455	1 464	1 444	1 383
Omega _P	atO/atFe	-	0,039	-	0,037	-	0,021	-	0,049	-
μ , spec. gas consumption	mole (CO+H ₂)/mole Fe		2,077	2,065	2,101	2,075	2,077	2,078	2,040	2,040
H ₂ yield	%		51,8	52,0	45,0	45,0	51,6	51,4	45,6	45,9
Global heat losses	MJ/thm		516	456	556	531	579	590	586	520
ind. preparation zone	MJ/thm		266	256	298	280	279	290	286	270
ind. elaboration zone	MJ/thm		250	200	259	251	300	300	300	250

*: fixed CO efficiency

Input
Output

In this table, Case 1 corresponds to the classical analysis of the operation on-line, based on the blast conditioning and the top gas analysis. As the calculated productivity was lower than the one calculated based on the burden – which is considered as the reference productivity – the latter was imposed in Case 2, leading to a different value of the blast flow rate. In both cases, the calculated and measured coke rates were similar. The only particular point was the H₂ efficiency, which was quite high compared to the classical value of 45 %. The two next cases were then calculated assuming this H₂ efficiency. Both led to higher coke rate than measured. Also for Case 3, the difference between the measured and calculated gas analysis became significant and close or even higher than what seemed acceptable for a well maintained gas analysis. So in Case 4, it was assumed that there was an error in the H₂ analysis of the auxiliary reducing agents injected at tuyère. In order to match the measured and calculated analyses, it was necessary to assume a hydrogen content of the hard coal of 3.17 % instead of 3.91 % (which was already significant). But at the same time, the difference between the measured and calculated coke rate increased further.

In a second stage, it was assumed that both the measured productivity and coke rate were correct and that the elaboration zone heat losses of the furnace were underestimated (Case 5 to Case 7).

The result was a calculated top gas analyses, too different from the measured ones, considering the acceptable error in this measurement. In Case 8, the effect of the assumption on the elaboration zone heat losses value was tested, without more success.

The conclusion of the heat and mass balance calculation is that the data set is not fully consistent. The best fitting between measured and calculated values is obtained for Case 2, so all further reasoning was based on this.

The main outcomes of this calculation are:

- the distance to ideality of the reduction, which is remarkably negative;
- the calculated heat losses, which are globally at a standard value but with a particular distribution between the preparation and elaboration zones, with elaboration zone heat losses are only two third of the classical ones.

3.5 Work Package 4: Blast furnace modeling

There has been intensive research regarding modelling of the blast furnace. MOGADOR (Model for Gas Distribution and Ore Reduction) is a steady-state mathematical BF model developed by CRM since 1995. It aims at monitoring the gas distribution in order to control the BF inner state with a proper burden distribution. MOGADOR is nowadays extensively used in ironmaking plants and was proved to be a valuable research tool in former projects.

Such models use built-in combustion routines in which the combustion kinetics can be tuned by the operator. Modelling of single coal particle conversion has been done by RWTH.

The objective of WP4 is the implementation of char impact in a comprehensive BF model with two objectives: to find bottlenecks in further PCI rate increase and to improve the model with input data gained by experiments (CRM: MOGADOR integrating new knowledge from WP1 and WP3). The work of CRM focuses on the implementation of effects of char on the Blast Furnace in the comprehensive BF model MOGADOR.

The obtained data from the laboratory and BF trials will be used in the MOGADOR model to investigate changes in BF performance and process parameters. The unburnt coal particles (char) are expected to be consumed through the following two mechanisms:

- Small particles of char transported by the gas out of the raceway are projected against coke and burden pieces where they can be trapped inside the pores affecting the coke reactivity and burden properties
- At the boundary of the raceway, due to the high temperature, char will stick on coke pieces and coat them. Those coated coke pieces together with liquids will create the bird's nest
- In order to study the influence of char with MOGADOR, the two mechanisms will be integrated in the model
 - Based on the softening tests results, the kinetics of Boudouard reaction would be modified taking into account the higher reactivity of coal char compared to coke
 - The changes of permeability would be simulated, in the raceway boundary and BF shaft. A local clogging of the raceway by char was attempted in a former project [8] without conclusive results. Therefore it was concluded that more research was necessary which would be addressed in the proposed project

The results will be validated with coke core borings of WP3 and MPVP (Multi Point Vertical Probing).

The combustion calculations by means of the CFD model will be used for the evaluation of the actual amounts of char leaving the raceway depending on the characteristics of the injected coal. The intention there is to use the results issued from the laboratory investigations on the kinetics of coal devolatilisation and char oxidation and gasification in WP1 to investigate the amount of char transferred to the coke reserve.

The modelling of char formation and gasification mechanism and kinetics as well as its interaction with coke and burden, particularly at the simulation conditions of dripping zone, will provide better knowledge and inputs to the further development and validation of the MOGADOR model. The OpenFOAM software (CFD code with well-developed multi-phase capabilities) is intended to be used.

3.5.1 TASK 4.1 IMPLEMENTATION OF CHAR BEHAVIOUR IN THE SHAFT IN MOGADOR

3.5.1.1 OBJECTIVES

The unburnt coal particles (char) are expected to affect the BF process through the following two mechanisms:

- Char particles will be transported by high velocity gas, then accumulate in the Blast Furnace where the velocity is lower, thus affecting the permeability.
- Small particles of char transported by the gas are projected against coke and burden pieces where they can be trapped inside the pores affecting the coke reactivity and burden properties.

3.5.1.2 CONDUCTED WORK

The MOGADOR model modification was defined (**Figure 3.194**). The permeability changes (in the raceway boundary and BF shaft) due to the presence of char would be included in the model. This accumulation would be calculated based on the gas flow and the new permeability map would be introduced into the model through an iterating procedure.

Kinetic data of char conversion by Boudouard reaction in the blast furnace shaft would be modified in the MOGADOR model using the results obtained within the WP1 (reducibility and softening tests, coke volatilisation and gasification rate, etc) taking into account the higher reactivity of coal char compared to coke.

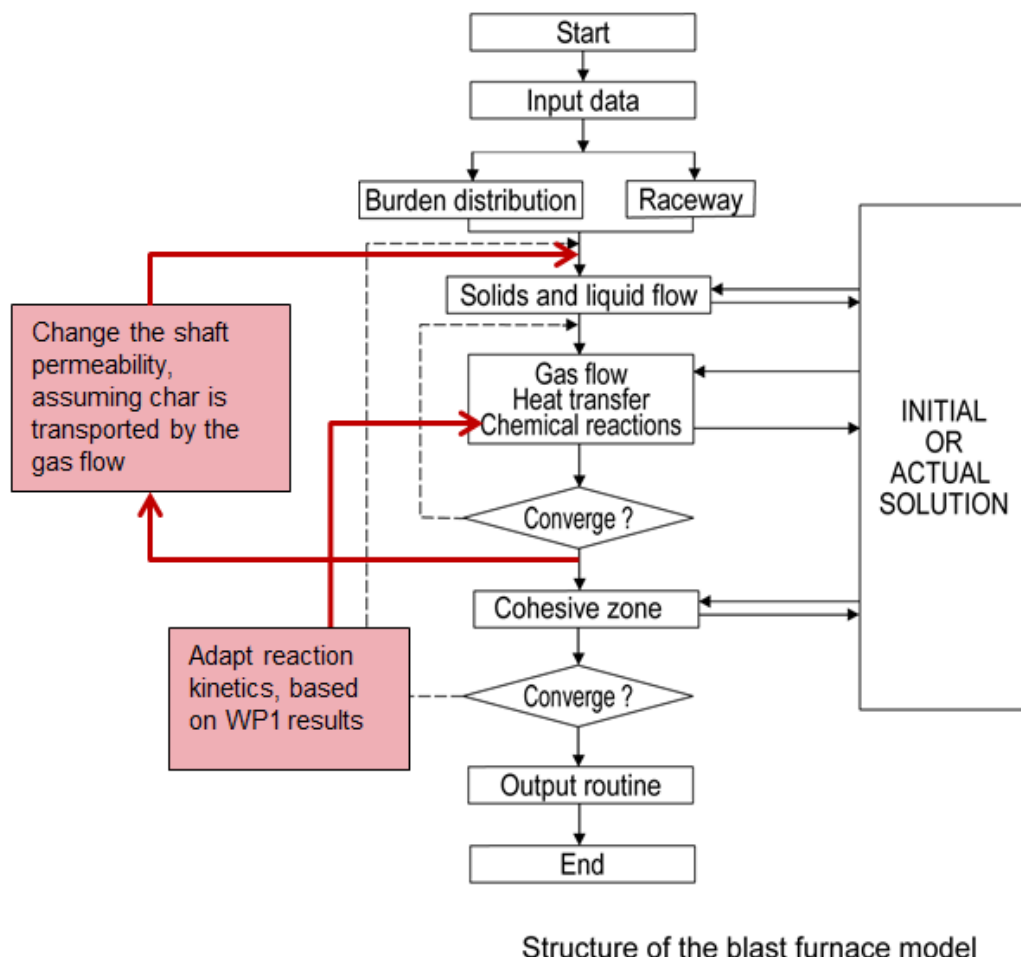


Figure 3.194: Proposed modifications to MOGADOR structure

3.5.1.3 RESULTS

Effect of char on BF permeability

In order to have a strategy on how we could modify the MOGADOR model, the effect of char on BF permeability was investigated.

By reproducing the conditions along a BF trajectory in an experimental apparatus, Iwanaga et al [9] concluded that the unburnt coal generated in the raceway moves upwards with the gas flow and the amount in the fused zone increases rapidly. The amount of unburnt pulverised coal (PC) collected is maximum at about the 1400°C zone (**Figure 3.195**), decreasing gradually as the

temperature decreased further. This may be because of the decreased contraction ratio and the increased void ratio. Although the retention of unburnt PC is not observed in the lumpy zone corresponding to the 600-800°C zone, the fines of unburnt PC start to reside again owing to the decrease in gas flowrate.

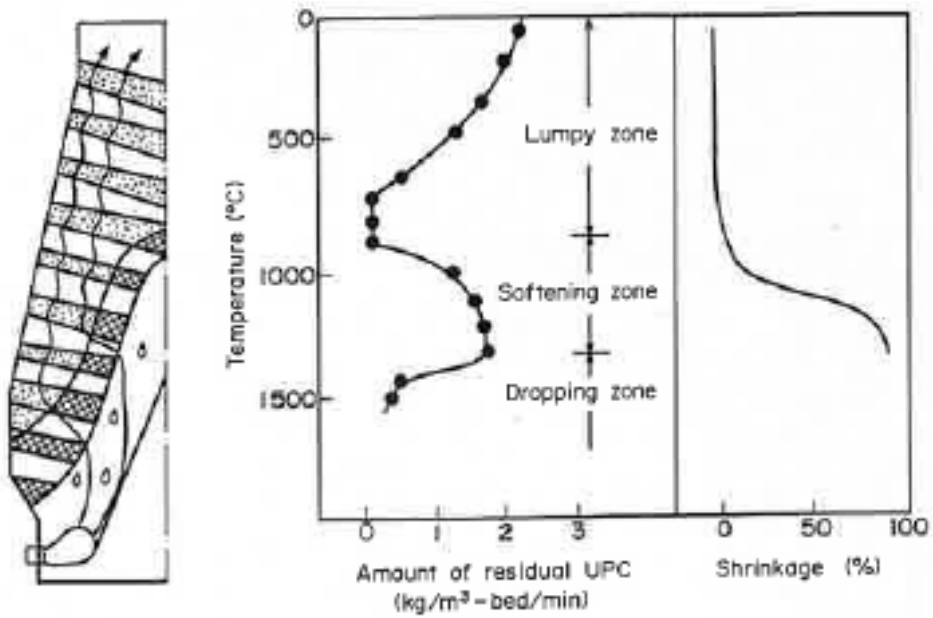


Figure 3.195: Change of amount of residual unburnt PC in hypothetical blast furnace [10]

To quantify the location of char inside the blast furnace (**Figure 3.196**), Dong et al [10] considered powder static holdup and dynamic holdup. For the static holdup, the equation of Hidaka was modified to consider that there is a maximum powder holdup ε_f^{\max} that corresponds to the situation when the voids among packed particles are fully occupied by powder particles

$$\varepsilon_{fs} = \text{Min} \left\{ 1.6 \times 10^{-4} \left[1 + 0.006 \left(U_g / d_s^{0.4} \right)^{2.5} \right] G_g^{-3.0}, \varepsilon_f^{\max} \right\}.$$

Where :

U_g superficial velocity of gas (m/s)

d_s particle diameter of solids (m)

G_g mass load gas (kg/m².s)

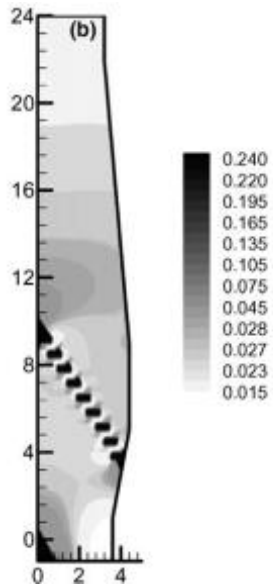


Figure 3.196: Computed powder total holdup [10]

MOGADOR simulations were done with reference geometry of Bremen BF-2. This blast furnace has the geometrical characteristics presented in **Table 3.58**.

Table 3.58: Selected geometry: Bremen BF-2

	BF-2
Hearth radius (m)	6.0
Bosh height (/tuy lvl)	4.4
Belly height (/tuy lvl)	6.8
Belly radius (m)	7.1
Shaft height (/tuy lvl)	25.8
Top radius (m)	4.7

The temperature maps and void fraction of the reference are plotted in **Figure 3.197**.

MOGADOR simulations : reference BF2

Solid Temp(°C) / Gas Temp(°C) / Void fraction

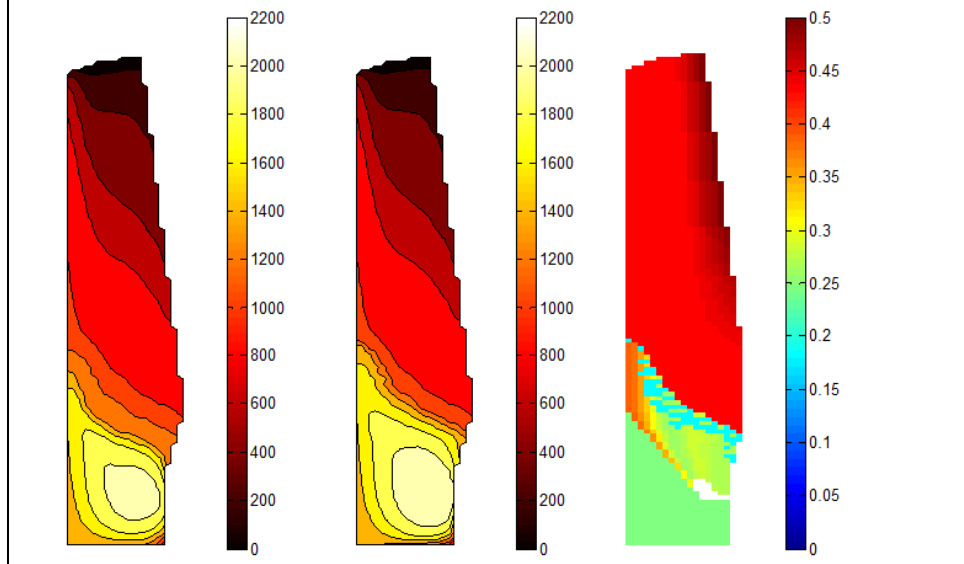


Figure 3.197: Reference MOGADOR simulation

By introducing in MOGADOR, the static holdup formula (Dong et al), we tried to take into account the presence of char accumulation that will block some of the burden void and decrease the global permeability.

Resulting figures are shown in **Figure 3.198**. It can be observed where the char powder can accumulate: its presence is mainly in cohesive zone, dead man and hearth. Those zones are the ones where the gas speeds decreases to a low value, a situation favourable for particle deposition. The temperature maps are impacted.

A maximal value for powder holdup is considered as total filling of the void is unrealistic. After MOGADOR convergence, the cohesive zone is not fully blocked: the gas flow is avoiding the less permeable parts thus the local velocity increases in the remaining coke windows, a less favourable condition for particle deposition.

Note that, at this stage, char is considered as an inert powder accumulating inside the BF and blocking permeability, and is not reacting within the blast furnace.

MOGADOR simulations with static holdup

Solid Temp(°C) / Gas Temp(°C) / Void fraction / Char holdup

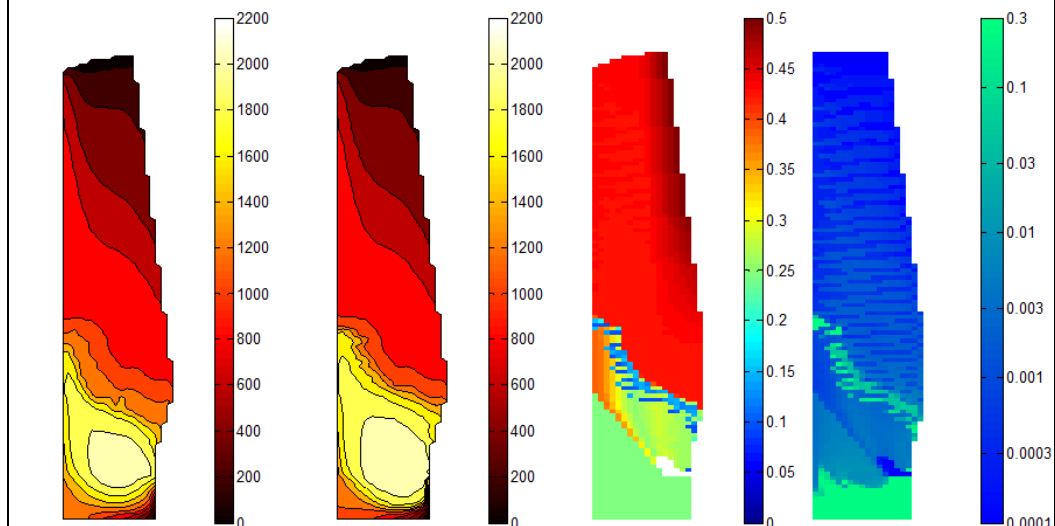


Figure 3.198: MOGADOR simulation with static holdup formula

Effect of char on coke reactivity

The effect of char and ash on the coke reaction rate was first investigated in literature [11] and can be seen as the combination of different phenomena. On one hand, residues of coal combustion act as catalysts and accelerate the solution loss reaction above about 1100°C. On the other hand, char and ash spheres observed on the coke surface after reaction may also protect coke from degradation. It can be summarised as a possible dual effect: the negative catalytic effect and the positive effect of preventing coke from degradation.

Incomplete conversion of injectants leads to char generation and may cause drop in the gas permeability, dirtying of the deadman and finally a decrease in BF productivity and increase in the coke rate. It may result in accumulation of unburned particles in the cohesive zone, deadman and slag. Char reactivity towards CO₂ is much higher than coke reactivity and therefore is consumed preferentially in the furnace. However, more rapid gasification of unburned PC particles compared with lump coke may inhibit coke degradation in the raceway. Coal ash attached on the surface of coke revealed that ash acts as a catalyst for coke reactivity [12].

Two complementary approaches were considered for MOGADOR implementation, one for each of the two different identified behaviours of char particles: stick on burden or transported with the gas.

According to a recent study [1], blast furnaces operating a 100% pellet burden show a higher amount of dust in top gas compared to a burden consisting of a mixture of sinter and pellets. The sinter can retain dust up to four times more than the pellet bed can and this is due to the sinter's rough surface and larger pores as compared with pellets and its size distribution.

Approach 1: particles stick on burden

Small particles of char transported by the gas are projected against coke and burden pieces where they can be trapped inside the pores affecting the coke reactivity and burden properties. To simulate this, we consider Coke and Char together and modify coke reactivity.

In MOGADOR model, the rate of solution loss reaction (Boudouard) is calculated based on an equilibrium law. The presence of char changes the coke reactivity, thus a new law could be implemented in MOGADOR, based on experimental data from RWTH.

This data is assuming a first-order reaction for the Boudouard reaction CO₂ + C = 2 CO

$$r = k * [\text{CO}_2]$$

with:

r	[mol/l.s]	reaction rate
k	[1/s]	reaction rate constant $k = A * e(-E_a/RT)$
[CO ₂]	[mol/l]	concentration in gas
E _a	[J/mol]	energy of activation

The experimental data can be sorted by Energy of activation

Char	20 - 39 kJ/mol
Coal	36 - 50 kJ/mol
Coke+char	50 - 62 kJ/mol
Coke	103 kJ/mol

To compute the equilibrium law from kinetic data, one has to remember the link between equilibrium and kinetics. Equilibrium occurs when the rates of the forward (A → B) and reverse (B → A) reactions are exactly equal. At equilibrium, the constant of equilibrium can be calculated as a ratio of reaction rate constants [13]. As the reaction rate constants for the two forward reaction C_{coke} + CO₂ → 2 CO and C_{char} + CO₂ → 2 CO were measured by RWTH and assuming the same reverse kinetics, the calculation of the equilibrium constant for coke with char gave: ΔG° = 35422 - 34.58 * Tsolids(K)

This new formula implemented in MOGADOR was used only if the char static holdup was higher than a defined value of 0.1% in volume, below that value we considered that the char amount was negligible and would not impact the coke equilibrium.

The effect of this modification can be observed comparing **Figure 3.199** and **Figure 3.200** with coke and char equilibrium the cohesive zone is slightly higher in the blast furnace.

Indeed, char being more reactive than coke, the gasification can start early.

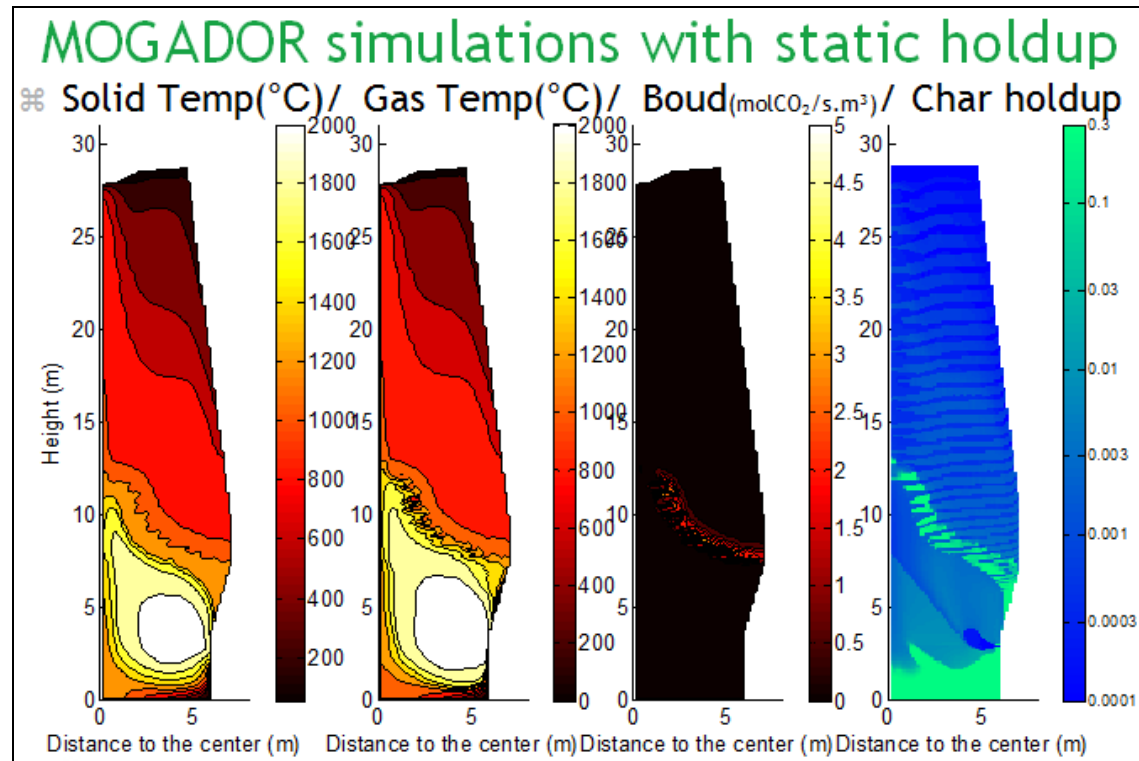


Figure 3.199: MOGADOR simulation with static holdup, with coke equilibrium

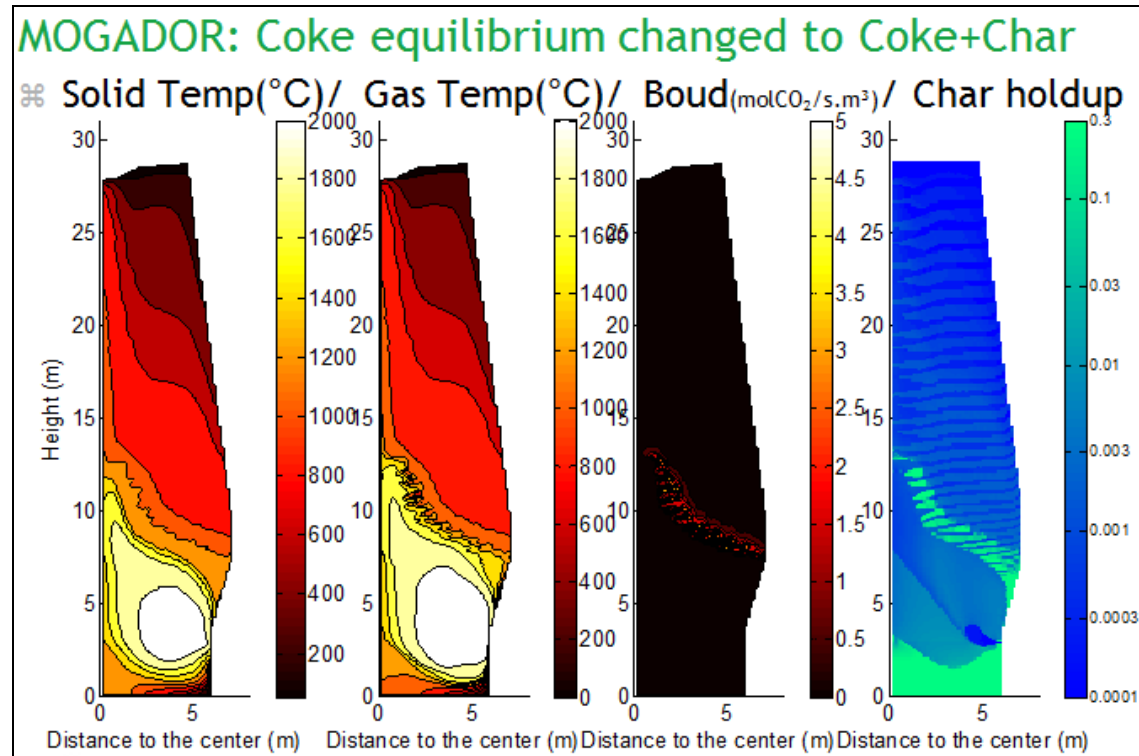


Figure 3.200: MOGADOR simulation with static holdup, with coke and char equilibrium

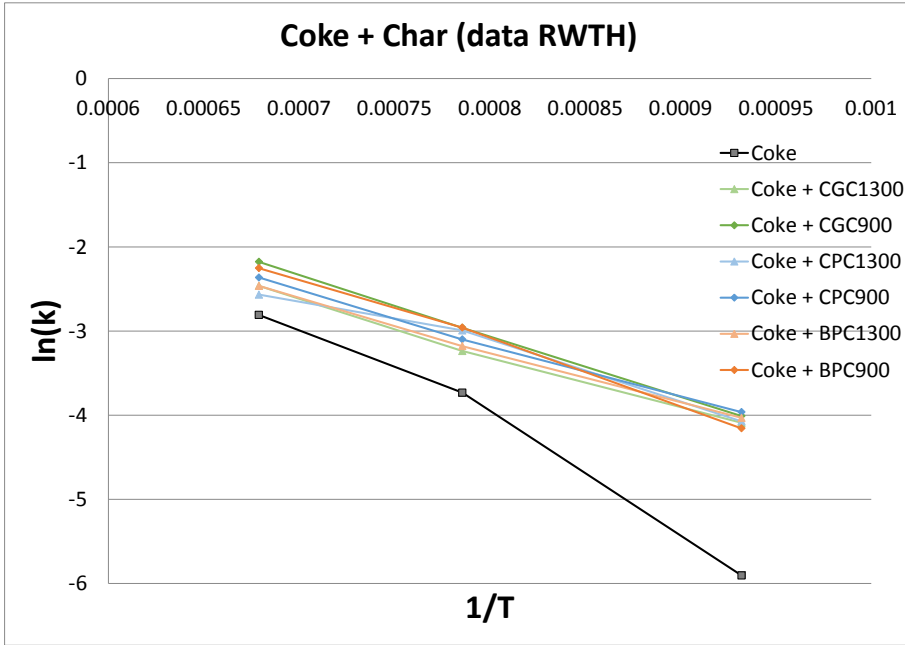


Figure 3.201: RWTH experimental data for coke and coke+char kinetics

Approach 2: particles transported with gas

Char particles will be transported by the high velocity gas, then accumulate into the Blast Furnace shaft where the velocity is lower, thus affecting the permeability.

To simulate this, we consider char particles independently and create a competition.

This approach gives the possibility to compute the consumption of char inside the BF, and to establish an equilibrium between char holdup and consumption.

In order to compute this competition in MOGADOR, experimental kinetic data of char alone will be compared to experimental coke kinetics, both data provided by RWTH.

a) Coke kinetics

In the MOGADOR model, kinetics of coke gasification by CO₂ is expressed by BOUD (kmolCO₂/s.m³ bed) and calculated by a simple gasification model applied to porous spherical particles [14]:

$$\text{BOUD} = \frac{\text{FACTB} \cdot \text{FACT4} \cdot [(\text{CO}_2) - (\text{CO}_2 \text{ eq})] \cdot P}{3600 \cdot \left(\frac{1}{k_f} + \frac{6}{d_c \cdot \rho_c \cdot E_f \cdot k_2} \right)}$$

where

- FACTB (-): multiplying factor (to be tuned)
- (CO₂) (-): CO₂ gas concentration
- (CO₂eq) (-): CO₂ gas concentration at the equilibrium
- P (atm): absolute gas pressure
- k_f (m/h): mass transfer coefficient through the gaseous film
- d_c (m): average particle diameter of coke
- ρ_c (kg/m³ coke): apparent specific mass of the coke
- E_f (-): efficiency factor
- k₂ (m³/kg.h): reaction rate constant

To be able to compute the competition between char and coke, first we replaced the calculation of BOUD with the experimental rate of reaction from RWTH. Note that the tuning factor FACTB was kept, as it was needed by MOGADOR to match with blast furnace probings.

MOGADOR - Reference BF2

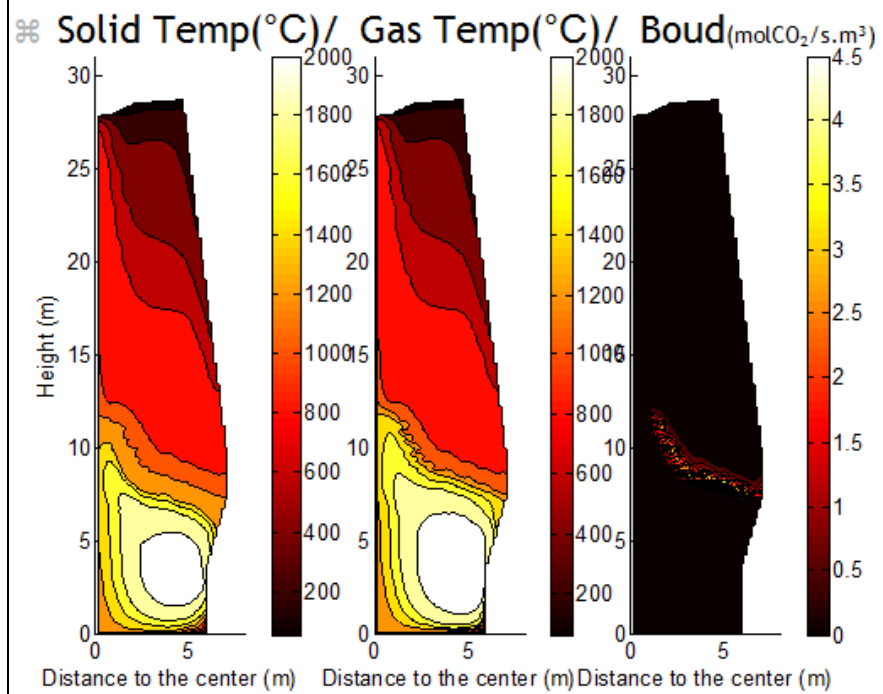


Figure 3.202: MOGADOR simulation of Reference case, Bremen BF2, 300x50 meshes

With experimental coke gasification kinetics

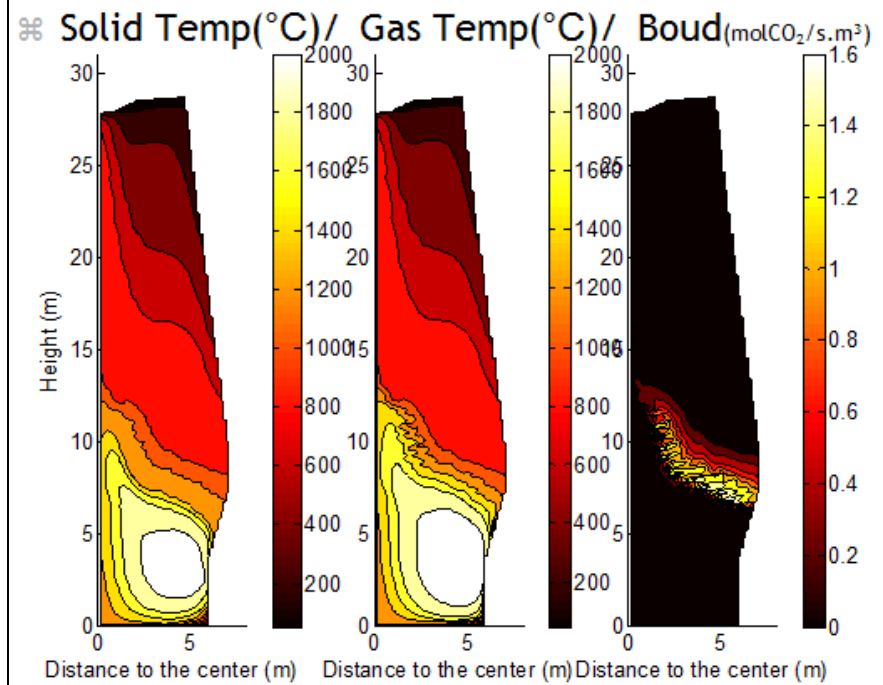


Figure 3.203: MOGADOR simulation with coke gasification kinetics from RWTH experimental data

The new formula for the coke gasification reaction rate is $r = k * [\text{CO}_2]$ in [mol/l.s] with

$$k = 280 * \exp(-102985/(8.314 * T_{\text{sol}}))$$

Changing the kinetics of coke gasification in MOGADOR has an impact on the calculation results, as can be seen on **Figure 3.205** and **Figure 3.206**. In the modified case, the Boudouard reaction takes place on a larger zone compare to the reference, impacting the

shape of the cohesive zone.

b) Char kinetics

The kinetic data of char gasification received from RWTH to be incorporated in MOGADOR are plotted in **Figure 3.204**.

For the next simulations, char "CPC900" was taken as it has the fastest kinetics. The formula for char PC900 gasification reaction rate is $r = k * [\text{CO}_2]$ in [mol/l.s] with

$$k = 6 * \exp(-35655/(8.314 * T_{\text{sol}}))$$

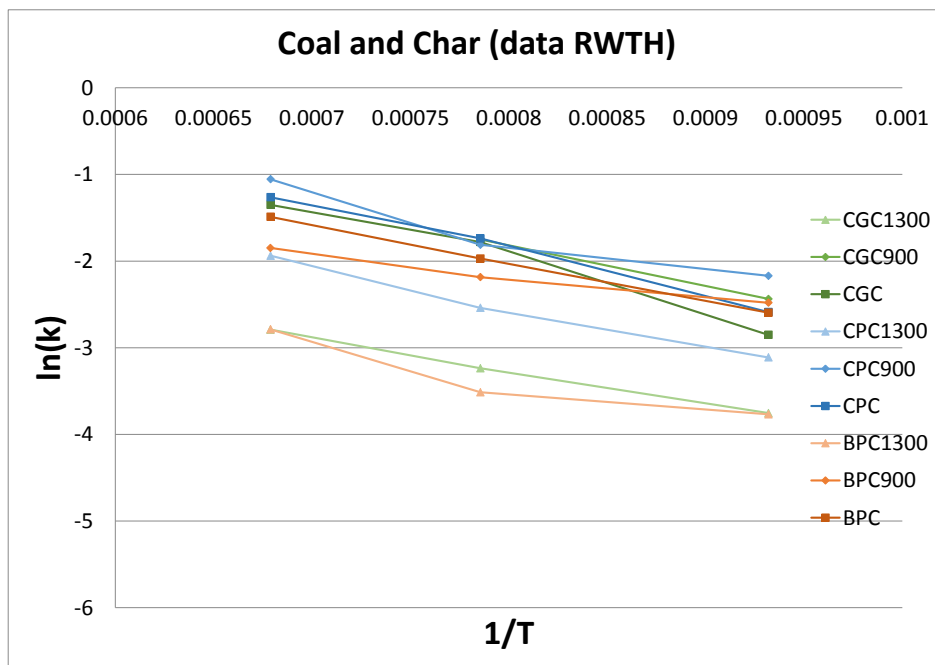


Figure 3.204: RWTH experimental data for coal and for char kinetics

Two philosophies are tested for consumption of char:

- Proportional to the Boudouard reaction rate

In this case, we considered the char is participating to the Boudouard reaction at the rate given by the experimental data. The char is consumed, but at the same time new char is generated in the raceway, so the overall figure is the image of the competition between generation and consumption.

Comparing **Figure 3.205** and **Figure 3.206** shows that with char consumption, Boudouard reaction rate is more important in the cohesive zone, that the shape of cohesive zone being slightly modified and that char is not going higher than cohesive zone where it is consumed.

- Total consumption of char if char participates in Boudouard reaction

In this case, we took a different approach, considering that char holdup is initially present, then is gradually consumed by the Boudouard reaction, giving at the end a total consumption of char where there is Boudouard reaction. This could correspond to a situation where the combustion of coal in the raceway is suddenly improved, no new char is produced anymore and the char already present inside the blast furnace is being consumed.

Comparing **Figure 3.206** and **Figure 3.207** shows that with total char consumption, above cohesive zone, no char is to be found anymore and the same is observed for the coke windows in the cohesive zone. However, with the hypothesis considered, at cohesive zone, char is remaining in the ore layer, those layers being impermeable to gas, the CO_2 is not able to go through and react with char.

MOGADOR: static holdup, no char consumption

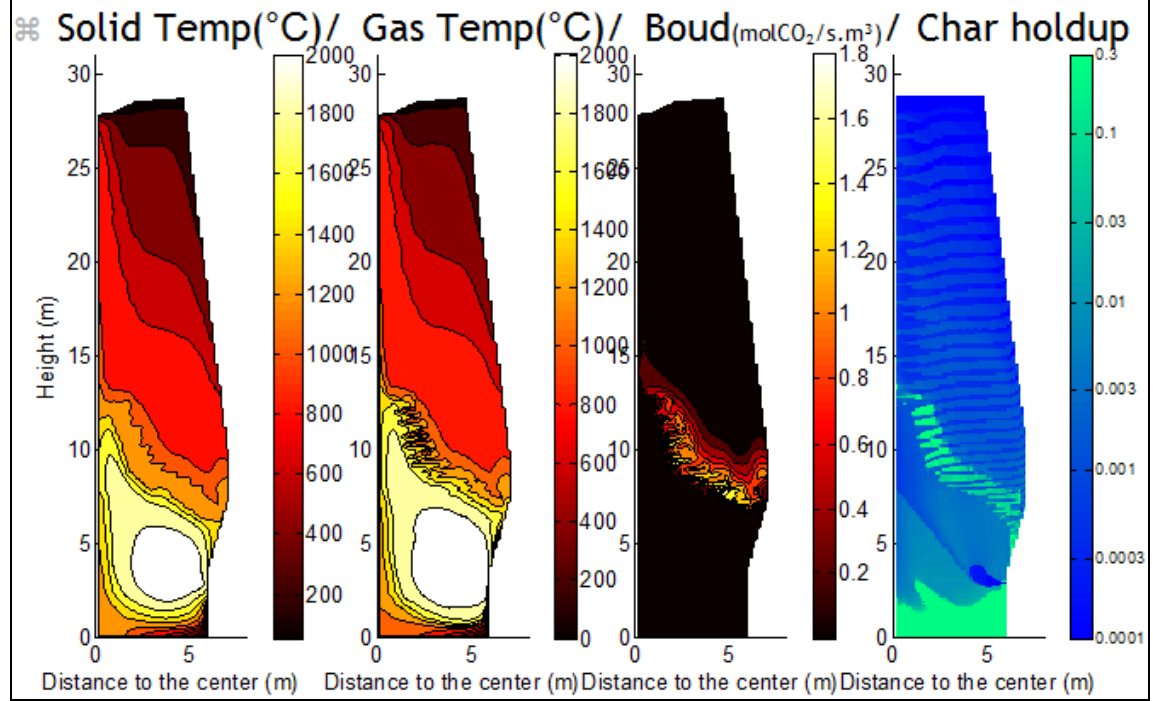


Figure 3.205: MOGADOR simulation with static holdup and coke gasification kinetics from RWTH experimental data

MOGADOR: Proportional char consumption

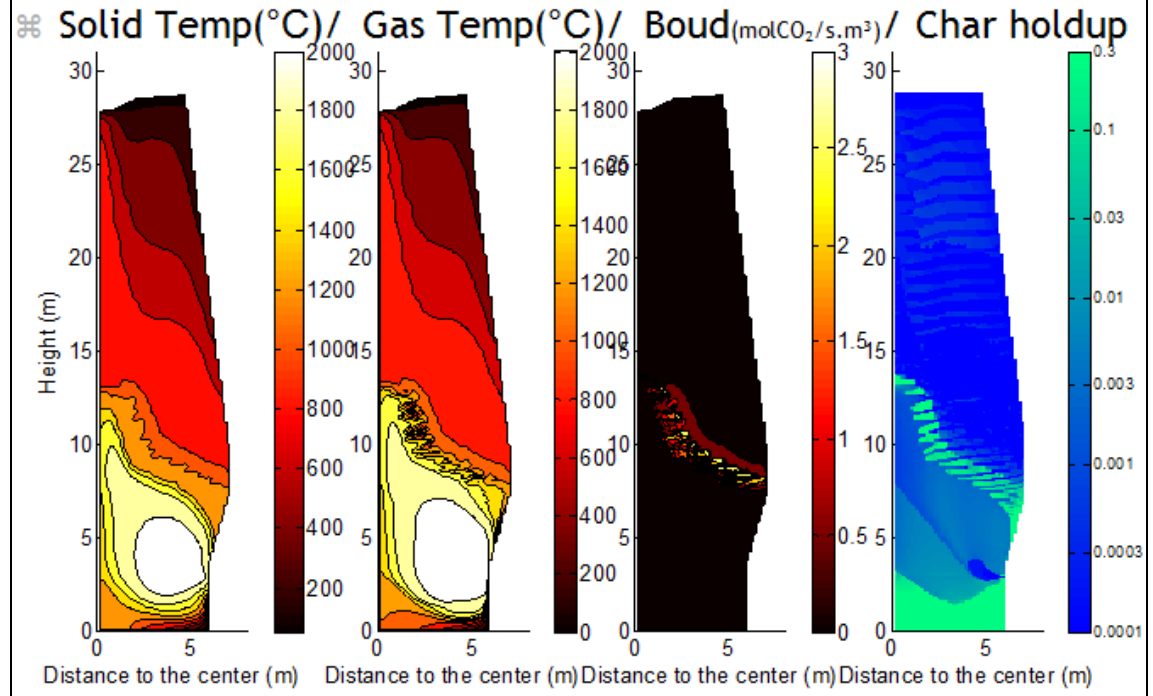


Figure 3.206: MOGADOR simulation with char consumption proportional to Boudouard reaction rate

MOGADOR: Total char consumption

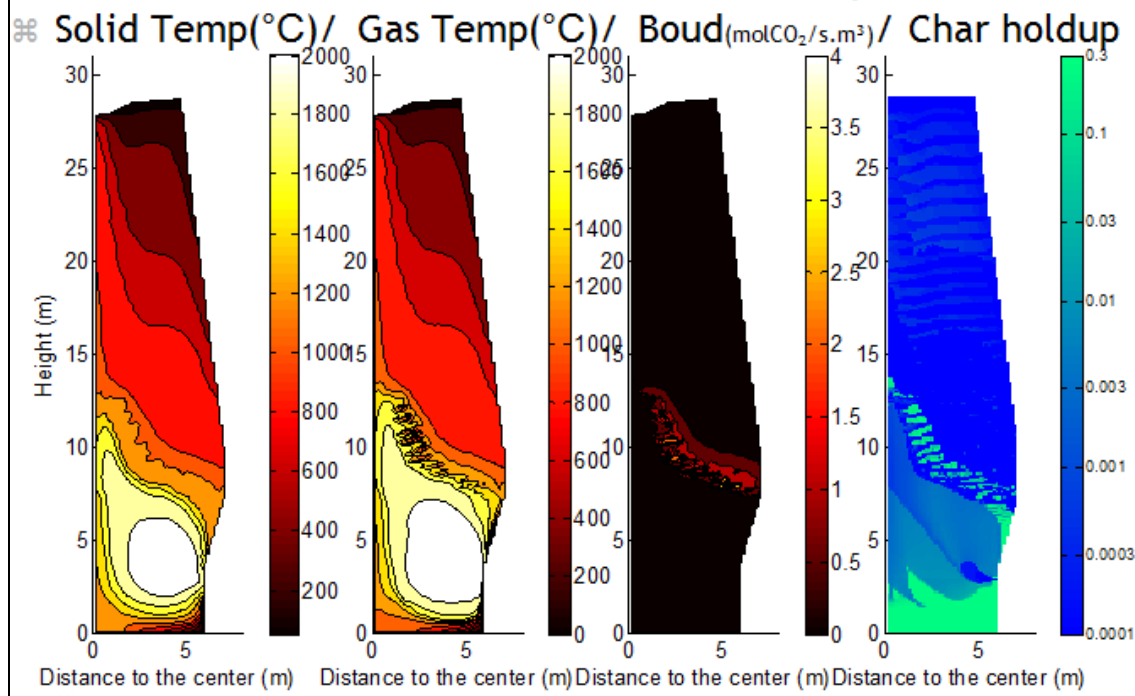


Figure 3.207: MOGADOR simulation with total consumption of char where Boudouard reaction takes place

Effect of char on BF performances

Among the previous simulations, the scenario with char consumption proportional to the Boudouard reaction rate was selected for further investigation.

The first investigation was to test the relative effect of the different char kinetics on BF performances. To this extent, the 6 chars plotted in **Figure 3.208** were considered for MOGADOR simulation.

Then, the second investigation was to update the temperature of beginning of softening relative to each different char, and experimentally measured in the IJSST softening test in WP1.

Main results are plotted in **Figure 3.208 - Figure 3.210**, and compared to the reference (green) and the case with char static holdup but no consumption (grey). Addition of char consumption kinetics increases the HM temperature compared to reference, this is because the char enters in competition with the coke, and in our simulations the coke rate was kept constant. Pressure drop is increased due to the presence of char that fill the voids and decrease permeability and the fact that the char consumption will increase the thickness of cohesive zone **Figure 3.210**), being more reactive than coke to the Boudouard reaction.

Effect of char on HM temperature

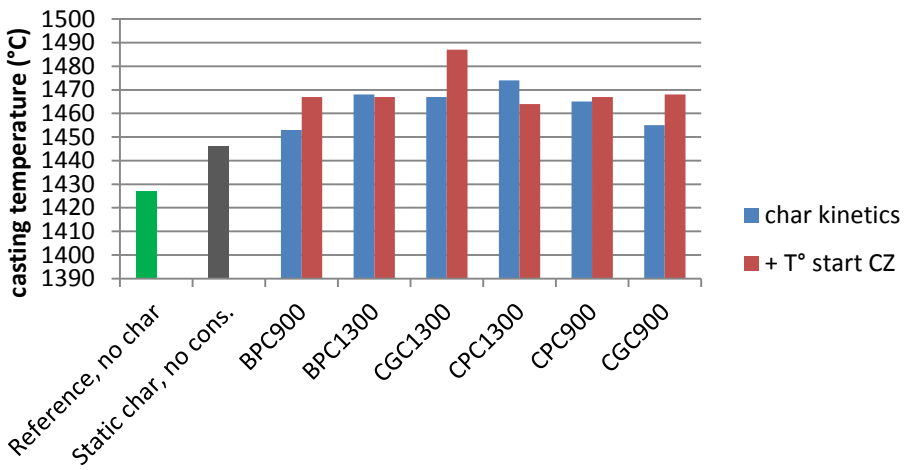


Figure 3.208: MOGADOR simulations with different char kinetics: effect on HM temperature

Effect of char on pressure drop

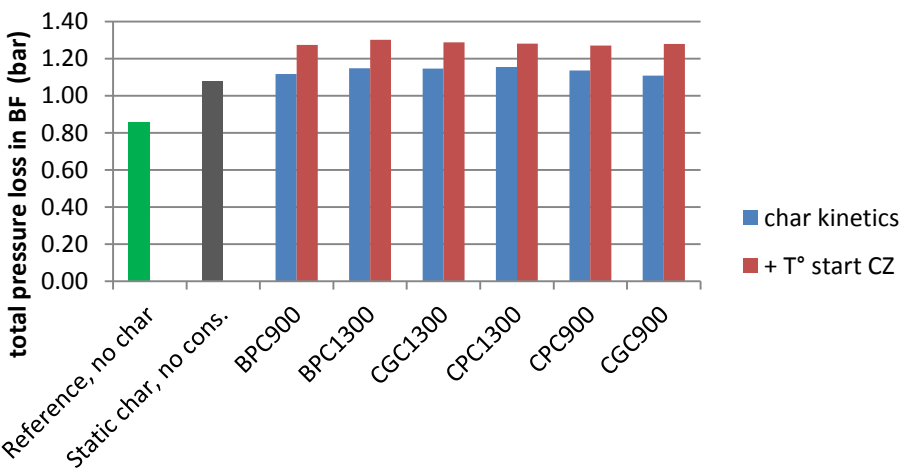


Figure 3.209: MOGADOR simulations with different char kinetics: effect on pressure drop

Effect of char on cohesive zone thickness

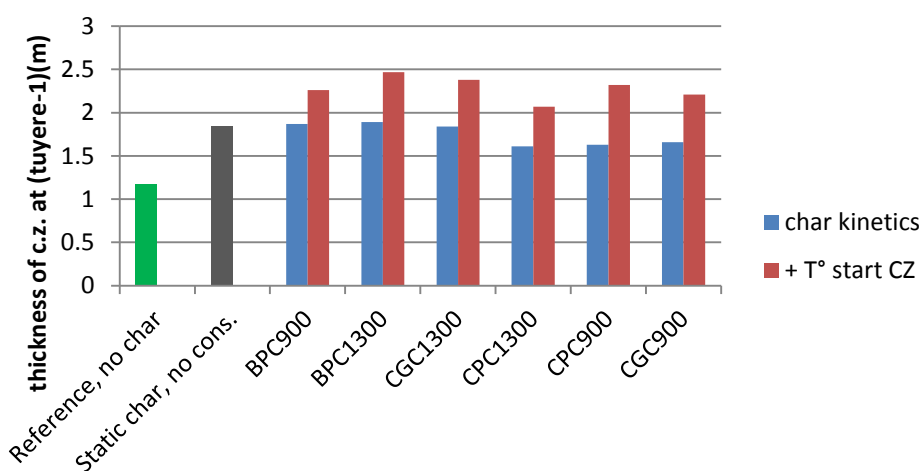


Figure 3.210: MOGADOR simulations with different char kinetics: effect on CZ thickness

3.5.2 TASK 4.2 EVALUATION OF THE AMOUNT OF CHAR LEAVING THE RACEWAY

The objective of Task 4.2 is to evaluate the amount of coal that is not converted in the raceway and leaves it as char by means of calculations performed with the CFD code ANSYS FLUENT®.

It was initially planned to use AM Bremen BF2 tuyeres conditions for performing these calculations. Unfortunately, it came out that due to the specific design of the tip of the lance used in Bremen, the calculations could never be converged despite several attempts. The amount of char leaving the raceway was then investigated based on the situation at GENT blast furnaces.

The arrangement of the two injection lances inside blowpipe and tuyere is given in **Figure 3.211**.

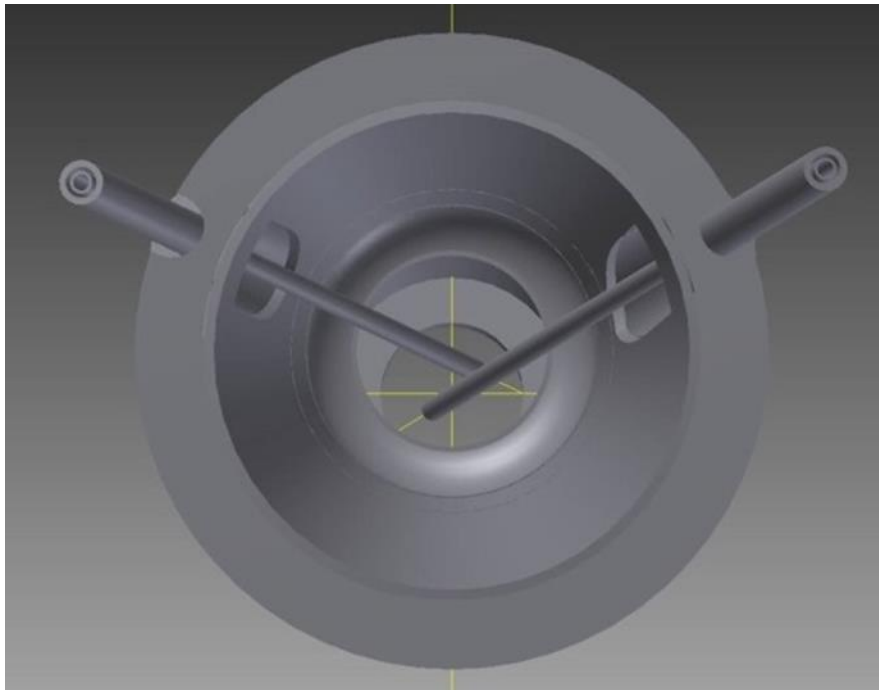


Figure 3.211: Lances arrangement at Gent blast furnaces

The conditions used for the calculations are given in **Table 3.60**. They correspond to $240 \text{ kg/t}_{\text{hm}}$ PCI.

Some pictures presenting the results of the calculations are given in **Figure 3.212**.

The results of the burnout evaluation are given in **Table 3.59**.

Table 3.59: Results of burnout calculations

		Particle size			Global
		35 µm	150 µm	250 µm	
De-volatilization	%	99,0	66,0	16,8	87,0
Char conversion	%	65,3	0,5	0,0	35,0
Burnout	%	76,0	20,0	5,0	51,0

From this table, it can be seen that approximately 50 % of the coal is leaving the raceway unburnt. This could of course depend on the assumptions made for the calculations (shape and porosity of the raceway, selected combustion model etc.). But this calculation gives a preliminary figure that can eventually be used for the implementation of the char behaviour in MOGADOR.

Table 3.60: Injection conditions used in the calculations

Wind rate /tuyere	Nm ³ /h	7 543
Oxygen rate /tuyere	Nm ³ /h	940
Wind Temperature	°C	1 139
PCI rate /tuyere	kg/s	0,69
RAFT	°C	2 185
Coal characteristics		
. Volatiles	%	17,3
. Fixed carbon	%	74,1
. Ash	%	8,5
. > 250 µm	%	5
. > 75 µm	%	30

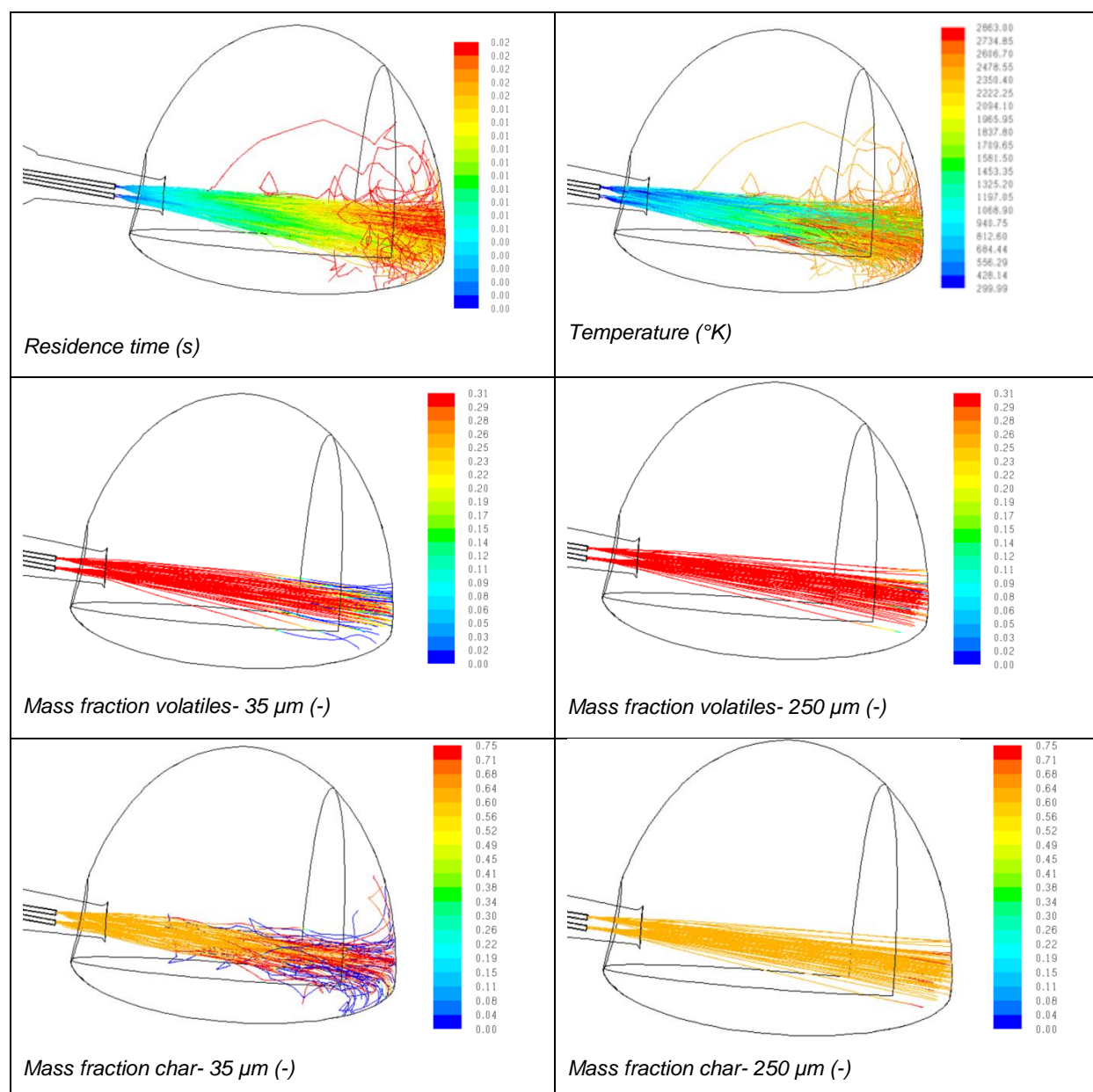


Figure 3.212: Evolution of residence time, temperature, volatiles and char fraction of the coal in the raceway

3.5.3 TASK 4.3 PROCESS MODELLING WITH MOGADOR INCLUDING CHAR PHENOMENA

The reference case of Bremen BF2 considered in the task 4.1 is based on operational conditions of February 2009 (**Figure 3.213**). This operation shows a rather flat operation, in concordance with the previous Multi-Point Vertical Probing (MPVP) realised in May 2008.

During the project, two new MPVP trials were done within WP3; showing a very central operation with a well-developed inverted V shape cohesive zone and a low position of the root of the cohesive zone.

MOGADOR simulation with the new charging pattern also shows a similar trend (**Figure 3.214**). The simulation results are in good accordance with the MPVP.

A simulation of MOGADOR with proportional char consumption was done with the new charging pattern of 2017 (**Figure 3.215**). This shows a straight inclined cohesive zone.

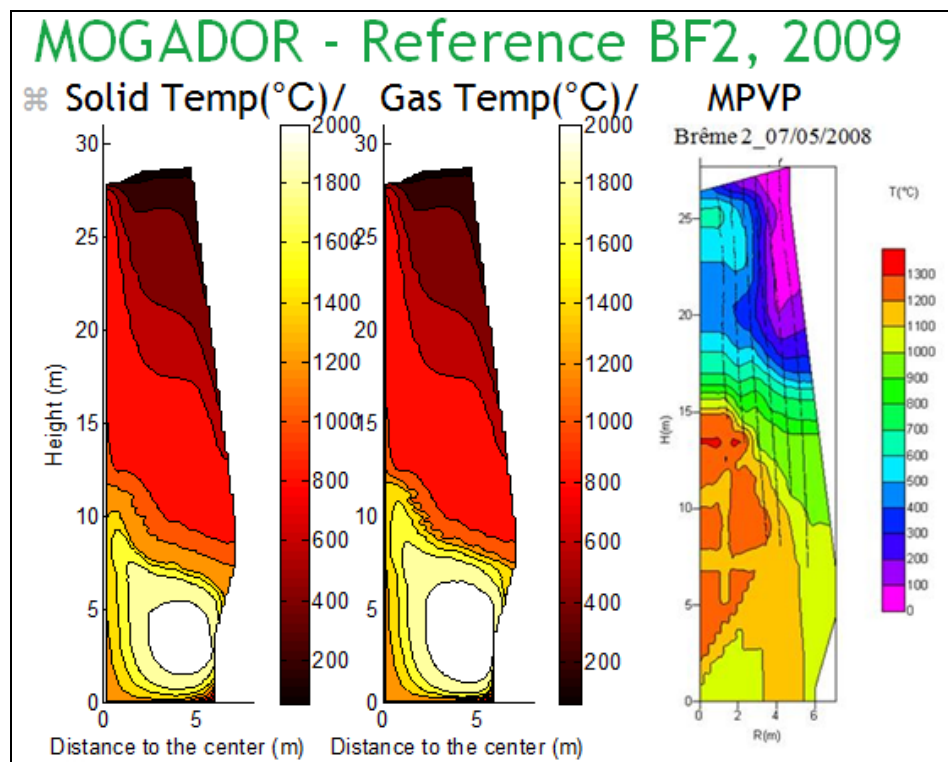


Figure 3.213: MOGADOR simulation of Bremen BF2 - 2009 operation (reference) + MPVP

MOGADOR - BF2, 2017 operation

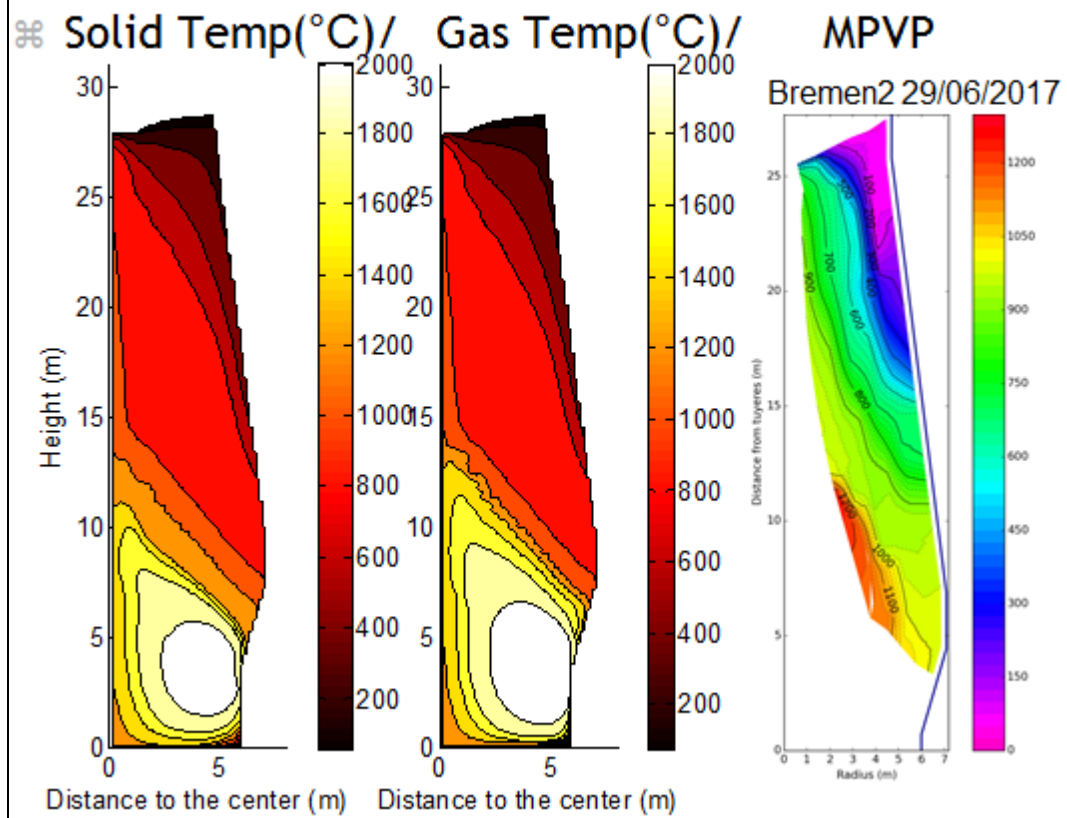


Figure 3.214: MOGADOR simulation of Bremen BF2 - 2017 operation + MPVP

Proportional char consumption, charging 2017

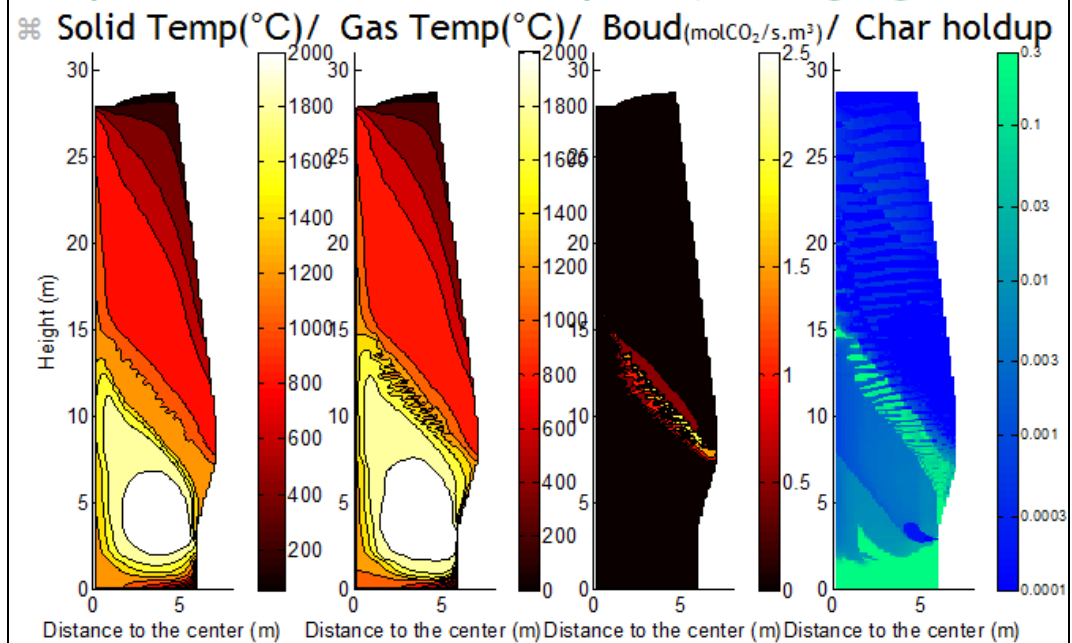


Figure 3.215: MOGADOR simulation with char consumption proportional to Boudouard reaction rate, with 2017 charging pattern

3.5.4 TASK 4.4 SIMULATION OF CHAR FORMATION AND CONVERSION ON THE MICRO LEVEL

Micro-level simulation of drainage behavior was realized through a single droplet model. This model was developed to simulate the passing behavior of a hot metal droplet through a coke. The simulation consisted of three phases. The droplet, which has a liquid form, passes through the void of a solid coke bed. Gas/char streams up while the droplet moves downwards. The dimensions of this model segment were set at 100 x 100 mm. A single droplet ($d=11$ mm) is being added to the system and passed through a coke channel. The amounts of mass which passes coke channel is referred as the collector zone. The amount that reaches the collector zone per time is being used as characteristic values to compare different conditions. The simulation time in the below presented example was set at 0.12 s.

Two different minimum coke channels were analysed. The channel was increased from 9.92 mm to 10.56 mm shown in **Figure 3.216**. Based on the results, an increase of voidage by 6.5 % led to increase of 7.39% in the collector zone. However the increase was not linear since a 10% led to 16 % increase in mass in the collector zone. The results indicate that a single droplet may separate into multiple smaller droplets passing through minimum spaced coke channels. The right side of **Figure 3.216** shows the distribution of the velocity. The part of the droplet in the center, which has no contact with the coke shows the highest velocity since the center is not slowed down through phenomena such as friction of the coke particle.

Furthermore the influence of the upstreaming gas/char phase was simulated. The reference velocity was set a 0.1 m/s. An increase to 0.5 showed a small decrease of the mass in the collector zone after 0.12 s. However a gas velocity of 1.3 decreased the mass collected by 13.13 %.

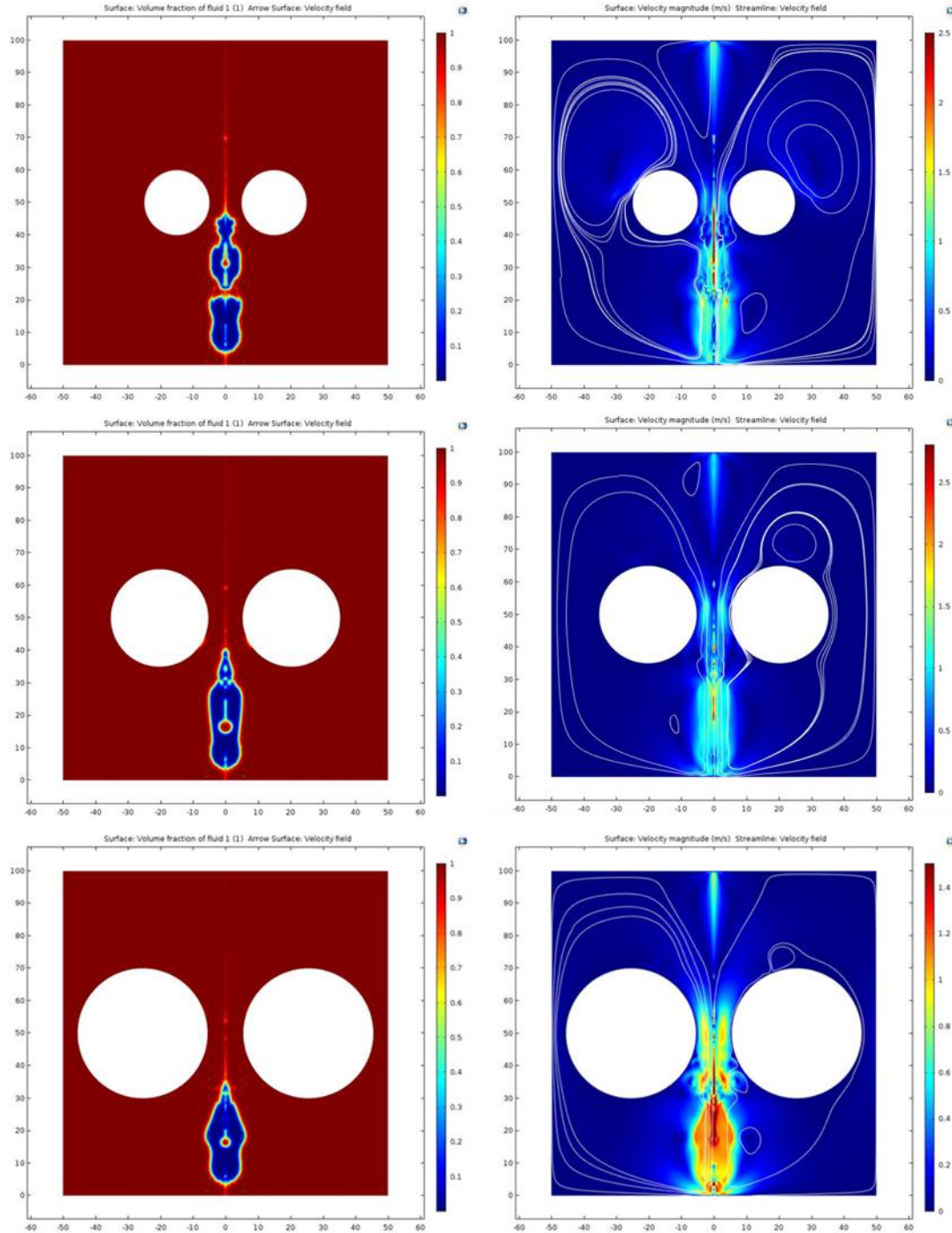


Figure 3.216: Simulation of dripping behaviour on microlevel with various minimum coke channel diameters

In addition, a model was developed which simulated multiple hot metal droplets as well as slag droplets dripping through a coke bed. A reference voidage of 0.51 was generated using a coke diameter of 11 mm. However, no upstreaming gas was simulated in this model. **Figure 3.217** shows the behaviour of droplets at different time steps. Grey circled areas present slags. During the initial time steps, the liquid flow of the droplets was disturbed by the coke bed. Droplets merge and cover the top coke bed layer. In the following time steps, the liquid enters and spreads through the other layers of the coke bed. Due to its lower density, slag ascends much slower through the coke bed than the hot metal. When huge amounts of droplets enter the coke bed, no upwards gas flow is possible which is simulated in the initial time steps of the simulation. However as soon as the liquid phases distribute through the coke bed, gas can pass.

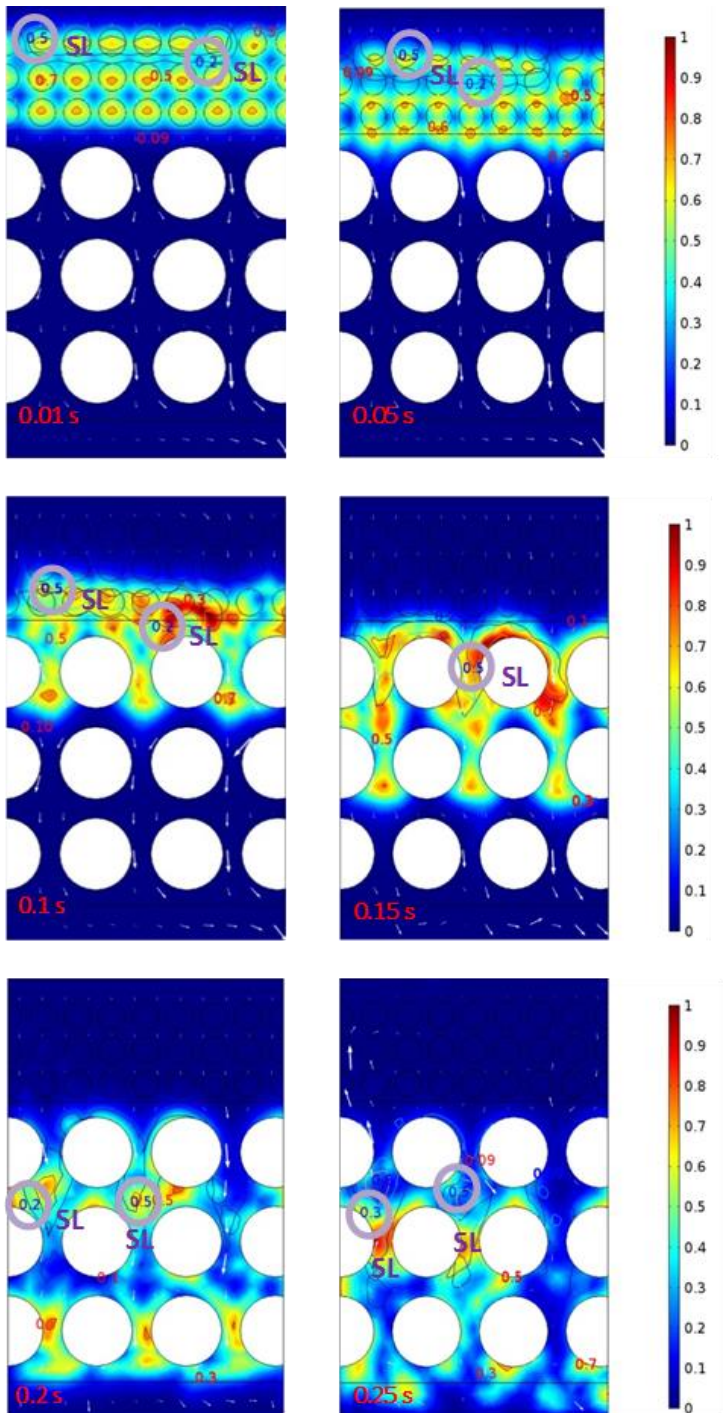


Figure 3.217: Dripping behaviour of multiple droplets through a coke bed

In conclusion, the voidage of the coke bed is important for the dripping behaviour. The single droplet model shows that when reaching a critical minimum spaced coke channel (voidage), the passing speed of incoming droplets may be accelerated significantly. Thus the drainage can be improved significantly. However voidage of coke bed cannot be increased indefinitely by varying coke particle size.

3.6 Work Package 5: Coordination, documentation, reporting

The kick-off meeting was held in Port Talbot on 24./25.09.2014. During this, a workshop on coal injection and coal and char research was done. The workshop was seen as very beneficial for the project. Therefore, such a workshop will be regularly organised as part of specific WP meetings.

Coordination meetings and work package meetings and visits were organised in IJmuiden, Port Talbot and Liege, Maizières on a regular basis.

4. LIST OF FIGURES

Figure 3.1: Interaction between work packages	16
Figure 3.2: Size distribution curves of Coal C-GC form prepared under various grinding conditions and final size distribution of Coal C-GC form sample after screening at 1 mm; cumulative wt. %..	18
Figure 3.3: Schematic drawing of MIRI experimental setup.....	19
Figure 3.4: Average pore diameter (left) and cross-sectional porosity (right) of raw coal.....	20
Figure 3.5: Particle size distribution (left) and shape factor of PC coals (90 - 125 µm)	20
Figure 3.6: LOM images of GC coal (50% <250 µm) (x50)	21
Figure 3.7: SEM images of GC coal (50 <250 µm) (x100)	21
Figure 3.8: Occurrence of inhomogeneous char (left), char particle by SEM (right top) and ash particles by SEM (right bottom).....	22
Figure 3.9: Location of coal ash in ternary system (CaO-SiO ₂ -Al ₂ O ₃).....	23
Figure 3.10: LOM image of PC char (90 -125 µm) (x50).....	24
Figure 3.11: SEM image of PC char (90 -125 µm) (x100)	24
Figure 3.12: LOM images of GC char (50% <250 µm) (x50)	25
Figure 3.13: SEM images of GC char (50% <250 µm) (x50)	25
Figure 3.14: Microscopic analysis of char collected in the MIRI	27
Figure 3.15: Sketch of the testing procedure with coal X for the different techniques	28
Figure 3.16: Sketch of the sample holder and picture of sample holder in the gleeble before test .	29
Figure 3.17: Results of devolatilisation tests at the Gleeble.....	29
Figure 3.18: Sketch of the SILIMELT test facility in Limoges	30
Figure 3.19: Evolution of temperature during the trial 100 mm (T103) and 200 mm (T102) below confinement box	30
Figure 3.20: Results of devolatilisation tests at the plasma torch.....	30
Figure 3.21: Sketch of the experimental set-up of the PCI Test Rig at CANMET	31
Figure 3.22: Picture of the CANMET test rig facility	31
Figure 3.23: Results of devolatilisation and conversion tests at the CANMET test rig	32
Figure 3.24: Evolution of temperature at the outlet of the reactor (O/C decreasing from left to right).....	34
Figure 3.25: Effect of O/C ratio in injection rig on burnout of Coal C GC	35
Figure 3.26: Volatile matter content of parent coal C and char as a function of the O/C ratio	35
Figure 3.27: BET surface area of initial Coal GC and residue vs O/C ratio in injection rig	36
Figure 3.28: Temperature at rig outlet during Coal C, PC form test 1. O/C ratio from left to right: 1.44, 1.85, 2.02, 2.32. 25918: test under 100 % N ₂	36
Figure 3.29: Temperature at rig outlet during Coal C, PC form test 2. O/C ratio from left to right: 2.02,2.13, 2.35, 1.78, 1.72. 25966: test under 100 % N ₂	36
Figure 3.30: Temperature at rig outlet during Coal C, PC form test 3. O/C ratio from left to right: 1.91, 2.35, 1.5, 1.68. 25981: test under 100 % N ₂	37
Figure 3.31: Burnout rate of Coal C, PC form as a function of the O/C ratio	37
Figure 3.32: Comparison of burnout rates of Coal C PC and GC form	37
Figure 3.33: BET surface area of residue vs O/C ratio in injection rig for Coal C PC form	38
Figure 3.34: BJH cumulative micropore volume of residue vs O/C ratio in injection rig for Coal C PC form	38

Figure 3.35: Blockage of the reactor pipe during experiment with Coal B PC	38
Figure 3.36: Scheme of Tammann furnace-based DT-setup	39
Figure 3.37: Comparison of synthetic char produced by Tammann furnace DT setup and MIRI plant	40
Figure 3.38: Comparison of LOM images of coal and char in PC size fraction (x500).....	41
Figure 3.39: Comparison of SEM images of coal and char in PC size fraction (x1000).....	42
Figure 3.40: Comparison of LOM images of coal and char in GC size fraction (x500)	43
Figure 3.41: Comparison of SEM images of coal and char in GC size fraction (x1000)	44
Figure 3.42: Char structure identified from Task 1.2	45
Figure 3.43: Porosity of various char types	45
Figure 3.44: Particle size distribution of Char C _{PC} with its parent coal	46
Figure 3.45: Tammann furnace AE setup.....	47
Figure 3.46: Typical TGA gasification curve and gasification rate determination.....	50
Figure 3.47: Independence of char gasification rate on the O/C ratio	50
Figure 3.48 : COBESI scheme	52
Figure 3.49: Temperature profile and gas composition at different positions during COBESI trial without coal injection.....	53
Figure 3.50: Temperature profile and gas composition at different positions during COBESI trial with injection of coal C _{PC}	53
Figure 3.51: Temperature profile and gas composition at different positions during COBESI trial with injection of coal C _{GC}	53
Figure 3.52: Temperature profile and gas composition at different positions during COBESI trial with injection of coal B _{PC}	54
Figure 3.53: TVC image during injection of coal C _{PC}	54
Figure 3.54: TVC image during injection of coal C _{GC}	54
Figure 3.55: TVC image during injection of coal B _{PC}	55
Figure 3.56: LOM images of coke sample sampled after COBESI trials	55
Figure 3.57: Schematic illustration of Tammann furnace DZ setup and magnification of crucible ..	57
Figure 3.58: Collected hot metal passing through the synthetic coke bed	57
Figure 3.59: Experimental Scheme for laboratory investigations for study of impact of char on burden	58
Figure 3.60: Schematic representation of HOSIM experimental test setup	60
Figure 3.61: Char volatile matter and reduction time in HOSIM	61
Figure 3.62: O/Fe ratio in HOSIM for tests with sinter and sinter coated with char.....	62
Figure 3.63: Cross sections of sinter and sinter with BPC900 char after reduction from full HOSIM and interrupted Q-HOSIM	63
Figure 3.64: Microstructure of sinter and sinter with BPC900 after reduction from full HOSIM	63
Figure 3.65: Presence of char BPC900 along the sinter pores and boundaries	64
Figure 3.66: Effect of char weight % on the volume increase after free swelling test at 1050 °C for 90 minutes	65
Figure 3.67: Image of pellets (L) and pellets with BPC1300 char (R) before and after swelling at 1050 °C for 90 min	66
Figure 3.68: Comparison of volume increase for pellets and char coated pellets in char layer in crucible after swelling at 1050 °C and 30 min.....	67

Figure 3.69: Pellets in a layer of char BPC1300 and char CPC900 before and after swelling at 1050 °C for 30 min	67
Figure 3.70: Microscopic analysis of pellet in BPC1300 char exposed predominantly to CO and char	68
Figure 3.71: Schematic representation of IJSST experimental setup	68
Figure 3.72: Reactivity of char in DTA and reduction time in IJSST	69
Figure 3.73: Char porosity in relation to reduction time in IJSST	70
Figure 3.74 Weight loss with time in IJSST	71
Figure 3.75: Pressure drop increase with temperature in IJSST	72
Figure 3.76: Comparison of pressure drop increase with bed shrinkage	73
Figure 3.77: Comparison of the magnitude of bed shrinkage	74
Figure 3.78: Full mosaic cross sections of softened pellets and pellets coated with varying char % by weight	74
Figure 3.79: Pellet boundary after softening	75
Figure 3.80: Pellet boundary after softening in the presence of char CPC1300.....	75
Figure 3.81: Pellet boundary after softening in the presence of char CGC900 with separate boundaries	75
Figure 3.82: Pellet boundary after softening indicating the presence of char after softening	76
Figure 3.83: CRM Softening test apparatus (l); Simplified sketch of CRM softening (r)	77
Figure 3.84: Sample in the crucible and punch.....	77
Figure 3.85: Interpretation of softening curves	78
Figure 3.86: Port Talbot ferrous burden reduction degree in function of reduction time	79
Figure 3.87: Reference softening trials results for Port Talbot sinter	80
Figure 3.88: Pressure drop of reference trials for Port Talbot sinter	80
Figure 3.89: Reference softening curves for Tata Steel Port Talbot pellets	81
Figure 3.90: Softening results for sinter mixed with char.....	82
Figure 3.91: Softening results for sinter mixed with char taking into account complimentary reduction due to char.....	83
Figure 3.92: Softening results for sinter-char mixes and trend line	83
Figure 3.93: Sinter particles after softening trial without char addition	84
Figure 3.94: Sinter particles after softening trial with addition of char	84
Figure 3.95: Softening (left) and melting (right) temperature of samples processed in HOSIM	84
Figure 3.96: Softening results for pellets mixed with char	85
Figure 3.97: Softening results for pellets mixed with char taking into account complementary reduction due to char.....	85
Figure 3.98: Softening results for pellets-char mixes and trend line	86
Figure 3.99: Crushed pellet particles after softening trial without char addition	87
Figure 3.100: Crushed pellet particles after softening trial with addition of char	87
Figure 3.101: Softening (left) and melting (right) temperature of samples processed in IJSST	87
Figure 3.102: Circulation in the body of the cooler.....	90
Figure 3.103: Camera views from the additional lance	91
Figure 3.104: View from the peep sight (blue circle), orange circle is the exit of the tuyere	91

Figure 3.105: Relation between particle size, field of view and maximum particle speed for selected camera (illustrated on the right)	93
Figure 3.106: Fast camera installed on the CRM melting furnace	93
Figure 3.107: Images acquired on the CRM melting furnace with the selected camera: moving coke dust (top left and middle); flame, fume and sparks (top right); particle moving at 0.7m/s (bottom)	94
Figure 3.108: Method used to measure the depth of the raceway	94
Figure 3.109 : Schematic of the raceway depth measurement	95
Figure 3.110: Thermal radiation emitted from a black-body	96
Figure 3.111: Cooling water streamlines and copper temperatures of tuyere cooler	97
Figure 3.112: COBESI instrumentation.....	98
Figure 3.113: COBESI Description	99
Figure 3.114: Bright Particle	99
Figure 3.115: Dark Particle.....	99
Figure 3.116: Raceway Depth measurement system at COBESI	100
Figure 3.117: Depth evolution during COBESI Trial.....	100
Figure 3.118: Laser Dots.....	101
Figure 3.119: Alkalies emission peaks	101
Figure 3.120: Alkalies intensity before first injection during COBESI trial	102
Figure 3.121: Alkalies intensity after first injection during COBESI trial.....	102
Figure 3.122: Temperature variation before injection during COBESI trial.....	103
Figure 3.123: Images of TVC at different coal injection rates (scenario 1)	107
Figure 3.124: Overview of regions of interest for temperature measurement at a Port Talbot BF tuyère.....	108
Figure 3.125: Temperature development at tuyère 9 with change of injection rate at tuyère 9 ...	108
Figure 3.126: Temperature development at tuyère 9 with increasing hot blast rate at tuyère 9 and 15	109
Figure 3.127: Fibres at Port Talbot	109
Figure 3.128: Temperature evolution at tuyere 12 in BF4 PT.....	110
Figure 3.129: Comparison between Temperature & PCI T12 BF4	110
Figure 3.130: Comparison between Temperature & PCI T12 BF4; Second measurement from 12:06 to 15:35.....	111
Figure 3.131: Alkali contents at T12 BF4	112
Figure 3.132: Ratio/Ratio	112
Figure 3.133: Comparison between Ratios & Process coal injection rates.....	112
Figure 3.134: Raceway depth measurement system at Port Talbot	113
Figure 3.135: Two dots without PCI injection	114
Figure 3.136: Pictures with coal injection	114
Figure 3.137: Comparison between Raceway depth and PCI/Hot Blast Flow	115
Figure 3.138: Radar placed behind a peep-hole at BF 4, Port Talbot	115
Figure 3.139: Radar raceway size data (l); histogram of measured data points for the according period (r)	115
Figure 3.140: Additive raceway length	116

Figure 3.141: Comparison of raceway data for two tuyère at 0, 100 and 200 kg/t _{HM} GC injection rate.....	116
Figure 3.142: Raceway size BF 4 in Port Talbot; measured with radar sensor.....	117
Figure 3.143: Raceway size BF 4 in Port Talbot; measured with radar sensor.....	117
Figure 3.144: Raceway size PT BF 4 based on complete time interval (!); Raceway size based on two distinct levels (larger 1 m: high level; smaller 1 m: low level).....	118
Figure 3.145: Raceway size PT BF 4 based on high levels.....	118
Figure 3.146: High (orange) and low (blue) raceway level at tuyère 1-30; PT BF 4	119
Figure 3.147: Raceway sizes for different tuyère diameters	119
Figure 3.148: Gas velocity field in the assumed raceway	121
Figure 3.149: Results of simulation; comparison of different cases	122
Figure 3.150: Relation hot blast amount and raceway depth	122
Figure 3.151: Correlation between kinetic energy and insertion length of raceway measurement [3]	123
Figure 3.152: Calculated relationship between the kinetic energy and the raceway depth.....	123
Figure 3.153: Raceway depth simulations compared with the radar measurements	124
Figure 3.154: Hot blast per tuyère, minimum and maximum values	124
Figure 3.155: Temperature at 0.7 m from the tuyère, seen from the peep sight.....	125
Figure 3.156: Sketch of the FVP bullet used for sampling dust in the shaft of the furnace.....	127
Figure 3.157: Sketch of the introduction system of the Flexible Vertical Probe	127
Figure 3.158: Schematic of the dust sampling system used during the FVP trial	127
Figure 3.159: Characteristics of the FVP trial of 14/04/2016 at BF2.	128
Figure 3.160: Different filters taken during the FVP trial.....	128
Figure 3.161: KCl crystals observed by SEM on the filter corresponding to sample 8.....	129
Figure 3.162: General aspect of the dust collected in the FVP pipe. Details of carbon particles morphologies.....	129
Figure 3.163: Analysis of some of the dust particles collected in the FVP pipe	130
Figure 3.164: Design of the heated probe based on heating wire.....	130
Figure 3.165: Pictures of coke sampling at tuyère level.....	132
Figure 3.166: Determination of the actual positioning of the different lots over the radius	133
Figure 3.167: Characterisation procedure of each lot of the core	133
Figure 3.168: Characteristics of the core sampled at AM Bremen BF2 on 31/05/2016	134
Figure 3.169: Characteristics of the core sampled at AM Bremen BF2 on 20/06/2017	135
Figure 3.170: SEM observation of fines < 125 µm of Lot 1 – Top left 1 st picture: structural aspect; 2 nd picture: chemical contrast	136
Figure 3.171: SEM observation of fines 125-250 µm of Lot 1 – Top left 1 st picture: structural aspect; 2 nd picture: chemical contrast.....	137
Figure 3.172: Pellets as prepared for SEM analysis	138
Figure 3.173: Chemical map of pellet G1 close to its surface obtained by SEM analysis	138
Figure 3.174: Chemical composition of the sample showing that it still contains ~95 % of hematite	138
Figure 3.175: Sketch of the Multi-Point Vertical Probe system.....	139

Figure 3.176: Displacement and measured and estimated inclination of the MPVP probe during the trial	139
Figure 3.177: Temperature profiles measured during the MPVP trial of 14/06/2016 at AM Bremen BF2	140
Figure 3.178: CO efficiency profiles measured during the MPVP trial of 14/06/2016 at AM Bremen BF2	140
Figure 3.179: Thermal and CO efficiency maps, and pressure map resulting from the MPVP trial at BF2 on 14/06/2016	141
Figure 3.180: Chaudron's diagrams of the MPVP trial on 14/06/2016 at BF2. The red dots on the curves indicate the point selected for specific consumption calculation (μ) for the formation of the first metallic iron	142
Figure 3.181: Displacement and measured and estimated inclination of the probe during the MPVP trial on 29/06/2017	143
Figure 3.182: Temperature profiles measured during the MPVP trial of 29/06/2017 at AM Bremen BF2	143
Figure 3.183: CO efficiency profiles measured during the MPVP trial of 29/06/2017 at AM Bremen BF2	143
Figure 3.184: Thermal and CO efficiency maps resulting from the MPVP trial at BF2 on 29/06/2017	144
Figure 3.185: Chaudron's diagrams of the MPVP trial of 29/06/2017 at BF2. The red dots on the curves indicate the point selected for specific consumption calculation (μ) for the formation of the first iron atoms:	146
Figure 3.186: Size distributions of charged coke, raceway coke and scrapped coke during coke core boring and coke scrapping exercises on the 31/05/2016	149
Figure 3.187: Size distributions of charged coke, raceway coke and scrapped coke during coke core boring and coke scrapping exercises on the 20/06/2017	149
Figure 3.188: Measured charging pattern just after the MPVP trial on the 14/06/2016	150
Figure 3.189: Operational data of AM Bremen BF2 at the time of the MPVP trial, with indication of the period of the test (red line)	152
Figure 3.190: Hot metal and slag quality at the time of the MPVP trial	153
Figure 3.191: Measured charging pattern just after the MPVP trial on 29/06/2017.....	155
Figure 3.192: Operational data of AM Bremen BF2 at the time of the MPVP trial done on 29/06/2017, with indication of the test period(red line).....	156
Figure 3.193: Hot metal and slag quality at the time of the MPVP trial on 29/06/2017	157
Figure 3.194: Proposed modifications to MOGADOR structure.....	160
Figure 3.195: Change of amount of residual unburnt PC in hypothetical blast furnace [].....	161
Figure 3.196: Computed powder total holdup [10]	162
Figure 3.197: Reference MOGADOR simulation.....	163
Figure 3.198: MOGADOR simulation with static holdup formula	163
Figure 3.199: MOGADOR simulation with static holdup, with coke equilibrium	165
Figure 3.200: MOGADOR simulation with static holdup, with coke and char equilibrium	165
Figure 3.201: RWTH experimental data for coke and coke+char kinetics.....	166
Figure 3.202: MOGADOR simulation of Reference case, Bremen BF2, 300x50 meshes	167
Figure 3.203: MOGADOR simulation with coke gasification kinetics from RWTH experimental data	167
Figure 3.204: RWTH experimental data for coal and for char kinetics.....	168

Figure 3.205: MOGADOR simulation with static holdup and coke gasification kinetics from RWTH experimental data	169
Figure 3.206: MOGADOR simulation with char consumption proportional to Boudouard reaction rate	169
Figure 3.207: MOGADOR simulation with total consumption of char where Boudouard reaction takes place	170
Figure 3.208: MOGADOR simulations with different char kinetics: effect on HM temperature	171
Figure 3.209: MOGADOR simulations with different char kinetics: effect on pressure drop	171
Figure 3.210: MOGADOR simulations with different char kinetics: effect on CZ thickness	171
Figure 3.211: Lances arrangement at Gent blast furnaces	172
Figure 3.212: Evolution of residence time, temperature, volatiles and char fraction of the coal in the raceway.....	173
Figure 3.213: MOGADOR simulation of Bremen BF2 - 2009 operation (reference) + MPVP	174
Figure 3.214: MOGADOR simulation of Bremen BF2 - 2017 operation + MPVP	175
Figure 3.215: MOGADOR simulation with char consumption proportional to Boudouard reaction rate, with 2017 charging pattern.....	175
Figure 3.216: Simulation of dripping behaviour on microlevel with various minimum coke channel diameters.....	177
Figure 3.217: Dripping behaviour of multiple droplets through a coke bed	178

5. LIST OF TABLES

Table 3.1: Coals and size fractions used for preliminary trials	17
Table 3.2: Chemical analysis for coals chosen for preliminary trials (wt.-%) (db)	17
Table 3.3: Coal conversion degrees based on MIRI trials	22
Table 3.4: Ash composition of coals and calculation of pseudo ash composition	23
Table 3.5: Results of injection trials with various oxygen enrichments	26
Table 3.6: Characteristics of Coal X used for evaluating the experimental techniques	28
Table 3.7: Typical experimental conditions of Gleebel trials	29
Table 3.8: Experimental conditions during the CANMET test rig trials	31
Table 3.9: Comparison of the results obtained on the different test facilities	32
Table 3.10: Standard experimental parameters and conditions at CANMET test rig	33
Table 3.11: Analysis of Coal C, GC form by CANMET	33
Table 3.12: Main results of Run 1 on Coal C-GC form	34
Table 3.13: Main results of Run 2 on Coal C-GC form	34
Table 3.14: Analysis of Coal C, PC form by CANMET	36
Table 3.15: Analysis of Coal B, PC form by CANMET	38
Table 3.16: Fusibility Properties of Ash under Oxidizing Atmosphere for Coal B (PC) (ASTM D1857)	38
Table 3.17: Parameters used for production of synthetic char	39
Table 3.18: Char structure classification based on Bailey et. al and Menendez et al. (3)	40
Table 3.19: Chemical analysis of synthetic char produced by Tammann furnace DT setup	46
Table 3.20: Results of physical properties of coal and char	47
Table 3.21: Kinetic reaction values	48
Table 3.22: TGA-scenario for determining char conversion	48
Table 3.23: TGA-results of coal and char under various atmospheric conditions [%min ⁻¹]	49
Table 3.24: Conditions of the trials at the Thermo Gravimetric Analyser (TGA)	49
Table 3.25: Calculated char volumes leaving the raceway	51
Table 3.26: Analysis of coke	51
Table 3.27: Activation energy of coke and coke with char	51
Table 3.28: COEBSI trial scenario	52
Table 3.29: Chemical composition of pellets wt.-%	56
Table 3.30: Reduction degree of pellets and pellets covered with char	56
Table 3.31: Scenario for dripping zone trials	56
Table 3.32: Metallurgical Test conditions and parameters	58
Table 3.33: Chemical composition of sinter in weight %	59
Table 3.34: Reduction time in HOSIM to attain end O/Fe of 0.5	60
Table 3.35: Fraction of reduced sinter below 3.15 mm after tumbling	62
Table 3.36: XRD Analysis on Sinter and Sinter with char BPC900 for interrupted (Q-HOSIM) and full HOSIM	64
Table 3.37: Chemical analysis of pellets after free swelling test for 90 minutes	66

Table 3.38: Reduction time in IJSST	69
Table 3.39 Comparison of temperatures for the onset of cohesive zone	73
Table 3.40: Evolution of sinter reduction degree during softening trials	82
Table 3.41: Evolution of pellets reduction degree during softening trials	86
Table 3.42: Camera specifications	92
Table 3.43: Time scheduling of the trial at COBESI	98
Table 3.44: Properties of the particles	99
Table 3.45: Scenarios for TVC at Port Talbot	106
Table 3.46: ROI for TVC and its purpose	107
Table 3.47: Alkaline boiling points	113
Table 3.48: Average of raceway sizes of tuyères, dependant on diameter	120
Table 3.49: Pressure drop across the tuyère simulations	121
Table 3.50: Conditions at the wustite-iron equilibrium and resulting local specific gas consumption	121
Table 3.51 : Conditions at the wustite-iron equilibrium and resulting local specific gas consumption for the MPVP trial on 29/06/2017	145
Table 3.52: Measured d50 of all three cokes sampled on 31/05/2016	148
Table 3.53: Measured d50 of all three cokes sampled on 20/06/2017	150
Table 3.54: Main operating ratios of AM Bremen BF2 during the MPVP trial on 14/09/2016	151
Table 3.55: Main results of MMHF calculations and their comparison with the measurements (1)	154
Table 3.56: Comparison of the main ratios of AM Bremen BF2 at the time of the MPVP trials	158
Table 3.57: Main results of MMHF calculations and their comparison with the measurements (1)	158
Table 3.58: Selected geometry: Bremen BF-2	162
Table 3.59: Results of burnout calculations	172
Table 3.60: Injection conditions used in the calculations	173

6. LIST OF ACRONYMS AND ABBREVIATIONS

BET: Brunauer-Emmett-Teller
BF: Blast Furnace
BJH: Barret-Joyner-Halenda
CAD: Computer aided design
CFD: Computational fluid dynamics
COBESI: Coke bed simulator
CR: camera resolution
CS: camera speed
CSR: coke strength after reaction
DTF: drop-tube furnace
FOV: field of view
FVP: Flexible Vertical Probing
GC: Granular Coal
HGI: Hardgrove grindability index
HMBM: heat and mass balance model
HVC: High volatile coal
IID: Image inter distance
LOM: Light optical microscopy
LVC: Low volatile coal
MIRI: Multifunctional injection rig for ironmaking
MPVP: Multi-Points Vertical Probing
NDIR: nondispersive infrared sensor
PC: Pulverised Coal
PSP: particle speed
PSZ: particle size
PVA: Polyvinyl alcohol
RAFT: Raceway adiabatic flame temperature
RDI: Reduction disintegration index
ROI: Region of interest
SEM: Scanning electron microscope
SFCA: silico-ferrite of calcium and aluminium
STA: Simultaneous Thermal Analyzer
TGA: Thermogravimetric analysis
TGRBF: Top gas recycling blast furnace
TL: tuyere level
TVC: Thermo vision camera
ULCOS: ultra-low CO₂ steelmaking
VM: Volatile matter
WP: Work Package

7. REFERENCES

- [1] Vikman, R.;
Reduction of dust in fully pellet charged blast furnaces
Jernkontoret
2017
- [2] Liu, X.: Honeyands, T.; O'Dea, D.
New techniques to measure softening and melting properties of mixed burdens of lump ore and sinter, Proceedings of China Society for Metals Congress, December 2017
- [3] Peters, M.
Untersuchungen zu den physikalischen Vorgängen im Unterofen unter besonderer Berücksichtigung des Koksverhaltens vor den Blasformen
Ph.D. thesis, RWTH Aachen, Germany, 1988
- [4] Bailly, J-L; Bolsigner, J-P; Picard, M; Sert, D; Succurro, A; Petit C.; Eymond J-L.
Design and utilization of the multi-points vertical probing on SOLLAC blast furnaces
60th Ironmaking Conference; Baltimore, MD; USA; 25-28 Mar. 2001.
- [5] RFSR-CT-2007-00001, HEARTHEFFIENCY-Improvement of hearth drainage efficiency and refractory life for high BF productivity and a well adjusted reductant injection rate at varying coke quality
31.12.2010
- [6] EUR20172EN, Assessing the internal state of the raceway/dead man part of the blast furnace at low coke rate
30.06.1999
- [7] EUR 20940 EN, Injectant coal gasification, char formation and char utilisation at high injection rates
31.12.2004
- [8] Powson, J.
Coal injection applications to optimise productivity
MPT international, (2006), No. 1, p. 28-32
- [9] Iwanaga, Y.
Behaviour of unburnt pulverised coal in blast furnace
Ironmaking and Steelmaking 1992 Vol 19 N°1
- [10] Dong, X. F.:
Gas-powder flow in blast furnace with different shapes of cohesive zone
Applied Mathematical Modelling 30 (2006)
- [11] Babich, A.
Effect of coke reactivity and nut coke on blast furnace operation
Ironmaking and Steelmaking 2009 vol 36 n°3
- [12] Gudenau, H. W.
Coke, char and organic waste behaviour in the blast furnace with high injection rate
Revista de metalurgia, 2003
- [13] https://www.chem.uci.edu/~lawm/chemical_equilibrium_part_1.pdf (slides 29 – 30)
- [14] Modelling of gas and char flows at high PCI through experimental and theoretical studies of the raceway and the dead man, EUR 20094, 1995-1998

Getting in touch with the EU

In person

All over the European Union there are hundreds of Europe Direct information centres. You can find the address of the centre nearest you at: https://europa.eu/european-union/contact_en

On the phone or by email

Europe Direct is a service that answers your questions about the European Union. You can contact this service:

- by freephone: 00 800 6 7 8 9 10 11 (certain operators may charge for these calls),
- at the following standard number: +32 22999696 or
- by email via: https://europa.eu/european-union/contact_en

Finding information about the EU

Online

Information about the European Union in all the official languages of the EU is available on the Europa website

at: https://europa.eu/european-union/index_en

EU publications

You can download or order free and priced EU publications at:

<https://publications.europa.eu/en/publications>. Multiple copies of free publications may be obtained by contacting Europe Direct or your local information centre (see https://europa.eu/european-union/contact_en).

EU law and related documents

For access to legal information from the EU, including all EU law since 1952 in all the official language versions,

go to EUR-Lex at: <http://eur-lex.europa.eu>

Open data from the EU

The EU Open Data Portal (<http://data.europa.eu/euodp/en>) provides access to datasets from the EU. Data can be downloaded and reused for free, for both commercial and non-commercial purposes.

In the past, blast furnace coal injection research mainly focused on combustion of injection coal in the raceway. However, it could be assumed that coal is anyway not able to fully combust, particularly at high injection rates, and unburnt residues leave the raceway as char.

The char evolution and subsequent consumption depends on the raceway characteristics, which depend on coal conversion. Both groups of factors were investigated with conversion tests, as well as raceway measurements. Generally, the char evolution is seen to manifest itself as a negative impact, but this may depend on the blast furnace conditions and injection coal characteristics. Char effects might deteriorate the blast furnace operation and stability (i.e. lower burden permeability or higher carbon losses in the flue dust). Nonetheless, char could also be advantageous by contributing toward the increase in coke reactivity thereby lowering the thermal reserve zone temperature. It was shown that the coal combustion highly depends on coal grain size and only marginally on oxygen enrichment. Effects of oxygen enrichment on maximum coal injection rate might be more related to char consumption, rather than coal conversion. Despite low conversion of granular coal under blast furnace raceway simulation conditions, granular coal injection is possible at high rates, obviously due to its consumption outside the raceway. Blast furnace operation experience with coals, like operational benefits or transport behaviour could be confirmed. Char impact on ferrous burden behaviour highly depends on temperature and gas composition and is difficult to predict from the performed tests.

Several raceway measurement techniques were successfully developed and applied at pilot scale and at a real blast furnace. Raceway size, temperature and changes in the gas composition could be shown. The raceway size depends on the location of the tuyère in relation to blast inlet and tap hole and changes significantly over time, indicating raceway collapses.

Gas and temperature measurements of the BF interior were performed: New insights regarding the impact of high coal injection rates on the blast furnace inner state were gained by gas and temperature measurements of the blast furnace inside and confirmed with mathematical modelling.

Studies and reports

